306319490Z

The Synthesis and Characterisation of some Hexagonal Perovskites

A thesis submitted to the
Board of the Faculty of Physical Sciences
in partial fulfilment of the requirements
for the degree of Doctor of Philosophy

by

Josephine J. Adkin

Worcester College
Hilary Term 2008

RADCLIFFE SCIENCE LIBRARY OXFORD
DEPOSITED
18 SEP 2008
THESIS

The Synthesis and Characterisation of some Hexagonal Perovskites

Josephine Adkin, Worcester College, University of Oxford
Submitted for the degree of Doctor of Philosophy, Hilary Term 2008

Abstract

The structural chemistry and magnetic properties of a number of manganese containing hexagonal perovskites have been studied by X-ray diffraction, neutron diffraction and magnetometry. Trends in the magnetic properties are investigated as a function of the hexagonal stacking sequence and manganese oxidation state.

The synthesis of the series of $BaMnO_{3-x}$ hexagonal perovskites is discussed. By varying both the partial pressure of oxygen and the firing temperature, stacking sequences with a range of hexagonal to cubic layer ratios can be synthesised. Factors which increase the structural tolerance factor are found to increase the proportion of hexagonal layers in the stacking sequence. The crystallographic properties of the $BaMnO_{3-x}$ compounds are discussed, and the oxide vacancies are found to be exclusively located in the face-sharing hexagonal (*h*) layers, particularly those which are adjacent to two apex-sharing cubic (*c*) layers. The preferential localisation of oxide vacancies in *chc* sites can be used to rationalise the observed stacking sequences, as well as the limiting stoichiometries of $BaMnO_{3-x}$ structures.

The magnetic behaviour of the $BaMnO_{3-x}$ phases is investigated, both individually and as a function of the stacking sequence. A strong direct exchange interaction between face-sharing cations couples all magnetic moments antiferromagnetically above ambient temperature. A slightly weaker interaction (utilising the 180° superexchange pathways between apex-sharing MnO_6 octahedra) results in three-dimensional antiferromagnetic order at a temperature in the range $230 \leq T\ (K) \leq 280$. The strength of this interaction is found to be dependent on the length of the face-sharing chains. A third interaction occurs at $T \sim 45K$, believed to represent a canting transition. Low temperature neutron diffraction data reveal that the magnetic moments order in a simple antiferromagnetic manner. The magnitude of the ordered moment shows a dependence on the length of the face sharing chains, where phases with shorter chains have a larger ordered moment. Long-range magnetic order is disrupted by charge disorder in the mixed Mn(III)/Mn(IV) system $4H\text{-}BaMnO_{2.65(1)}$.

The hexagonal $BaMn_{1-z}Ti_zO_{3-x}$ and $BaMn_{1-z}Zr_zO_{3-x}$ systems were also studied. Synthesis under argon atmospheres allows a range of new phases to be accessed. These include a novel manganese-zirconium phase, $6H\text{-}BaMn_{0.8}Zr_{0.2}O_{2.81(1)}$, and $BaMn_{0.55}Ti_{0.45}O_{3-x}$, which adopts the rare 15R' stacking sequence. The $BaMn_{1-z}Ti_zO_{3-x}$ system confirms that although the tolerance factor controls the proportion of cubic layers, it does not control the arrangement of these layers. This is controlled by the size of the B cations and the proportion of oxide vacancies. Partial cation order occurs in $6H\text{-}BaMn_{0.8}Zr_{0.2}O_{2.81(1)}$, which can be rationalised on the basis of the size difference between manganese and zirconium ions.

Topotactic reductions using binary hydrides are carried out in order to decouple the manganese oxidation state from the adopted stacking sequence. Using hydride reductions, $4H\text{-}Ba_{0.5}Sr_{0.5}MnO_{3-x}$ can be topotactically reduced to $4H\text{-}Ba_{0.5}Sr_{0.5}MnO_{2.02(1)}$. This increases the strength of the 180° superexchange interaction, and antiferromagnetic order is achieved above ambient temperature. Using the same techniques, $4H\text{-}BaMnO_{3-x}$ can be reduced to $4H\text{-}BaMnO_{2.47(1)}$ or $4H\text{-}BaMnO_{2.06(1)}$. These phases undergo a distortion to an orthorhombic unit cell.

Acknowledgements

First and foremost, I would like to thank my supervisor Mike Hayward for all his advice, encouragement and enthusiasm over the course of this project. I would also like to thank Dr. Joke Hadermann for collecting electron diffraction data and the beam scientists both at ISIS and the ILL for their assistance in collecting neutron data. I am also grateful to the EPSRC, the ICL and Worcester College for funding.

I would like to thank all the members of the Hayward group, past and present for making the last few years very enjoyable. Monday lunchtimes and Thursdays will never be the same again. In particular, thanks to Tom Parsons, Ian Saratovsky, Ed Dixon, Jo Clark, Andy Overton, Michelle Lockett and Sarah Dunstone. Additional thanks to all those who helped with the proof reading, namely Ed, Tom, Ian, James Best, James Casey and James Seddon.

Thanks also to all my friends, especially Daniel Goodman and Rebecca Hoath for living with me for the last couple of years, and broadening my horizons with a number of unusual discussions. Especial thanks to Dan for writing helpful computer programs as and when required. Lastly, thanks to my family, to George for both the proof reading and the supply of entertainment, and especially to my parents for their constant support and interest.

Contents

Chapter 1: Introduction **1**

1.1. The tolerance factor 1

1.2. Hexagonal Nomenclature 4

1.2.1. Defining the stacking sequence 5

1.3. Known hexagonal perovskite phases 7

1.3.1. 2H and related structures 8

1.3.2. Simple hexagonal perovskite structures 10

1.3.3. Complex hexagonal perovskite structures 12

Chapter 2: Experimental techniques **16**

2.1. Ceramic synthesis 16

2.2. Hydride reductions 16

2.3. Powder diffraction 17

2.3.1. X-ray powder diffraction 19

2.3.1.1. Philips PW1710 diffractometer 19

2.3.1.2. Siemens D5000 diffractometer 20

2.3.1.3. PANalytical X'pert PRO diffractometer 20

2.3.2. Neutron powder diffraction 21

2.3.2.1. D2B at the ILL 23

2.3.2.2. Isis 24

2.3.3. Electron diffraction 26

2.4. Structural Analysis 27

2.4.1. Peak shapes 27

2.4.2. Rietveld Refinement 28

2.4.3. Interpretation of profile coefficients 30

2.4.4. Fitting statistics 30

2.5. Bond Valence Sums 31

2.6. DC SQUID magnetometry 32

2.6.1. Magnetic measurements and units 33

2.6.2. Magnetic behaviour 34

2.7. Iodiometric titrations 35

2.8. Thermogravimetric analysis 37

Chapter 3: Synthesis of $BaMnO_{3-x}$ phases **38**

3.1. Introduction 38

3.2. Thermodynamic considerations 40

3.3. Experimental 42

3.3.1. Initial synthesis of $BaMnO_{3-x}$ 42

3.3.2. Altering the stacking sequence 42

3.4. Results and discussion 43

3.4.1. Phase diagram for $BaMnO_{3-x}$ 43

3.4.2. 8H-$BaMnO_{3-x}$ 45

3.4.2.1. Previous work 45

3.4.2.2. Attempted synthesis of 8H-$BaMnO_{3-x}$ in air 46

3.4.2.3. Synthesis under oxidising atmospheres 50

3.4.3. 9R-Ba(Sr)MnO_{3-x} 51

3.4.3.1. Introduction 51

3.4.3.2. Results 52

Chapter 4: Structural characterisation of $BaMnO_{3-x}$ phases 54

4.1. Introduction 54

4.2. Experimental 55
4.2.1. Synthesis 55
4.2.2. Topotactic oxidation 56
4.2.3. Neutron diffraction 57
4.2.4. Chemical analysis 57

4.3. Results 58
4.3.1. Chemical analysis 58
4.3.2. Structural refinement 60
4.3.2.1. Refinement procedure for 10H-$BaMnO_{3-x}$ 60
4.3.2.2. Deviations for other $Ba(Sr)MnO_{3-x}$ phases 62

4.4. Discussion 78
4.4.1. The tolerance factor 78
4.4.2. Oxide vacancies 81
4.4.2.1. Location of oxide anion vacancies 81
4.4.2.2. Rationalisation of oxide anion vacancy location 82
4.4.2.3. Manganese ion repulsion 90

4.5. Conclusion 92

Chapter 5: Magnetic characterisation of $BaMnO_{3-x}$ phases 94

5.1. Introduction 94
5.1.1. 4H-$SrMnO_3$ 95
5.1.2. 2H-$BaMnO_3$ and 2H-$BaCoO_3$ 97

5.2. Experimental 99

5.3. Results and discussion 99
5.3.1. The magnetic model of 6L-$BaMnO_{2.92(1)}$ 99
5.3.1.1. Results 99
5.3.1.2. Discussion 104
5.3.2. Deviations in magnetic behaviour for the remaining $BaMnO_{3-x}$ phases 105
5.3.2.1. Susceptibility data 105
5.3.2.2. The magnetic event at T ~ 250K 108
5.3.2.3. Cause of the event at T ~ 45K 111
5.3.2.4. 1.8K neutron diffraction 114

5.4. Conclusion 122

Chapter 6: The effect of disorder on magnetic behaviour 124

6.1. Introduction 124

6.2. Structural disorder 125
6.2.1. 15R-$BaMnO_{2.99(1)}$ and 9R-$Ba_{0.875}Sr_{0.125}MnO_{3.00(1)}$ 126
6.2.2. 2H-$BaMnO_3$ 132

6.3. Charge disorder in 4H-$BaMnO_{2.65(1)}$ and 4H-$Ba_{0.5}Sr_{0.5}MnO_{2.79(1)}$ 135

6.4. Conclusion 141

Chapter 7: Synthesis and characterisation of $Ba(Sr)Mn_{1-z}B'_zO_{3-x}$ 143

7.1. Introduction 143
7.1.1. B cation order 143
7.1.2. B cation order in the hexagonal perovskite system 144

7.1.3. The $Ba(Sr)Mn_{1-z}Ti_zO_{3-x}$ system *147*

7.2. Experimental 148

7.3. Results 149

7.3.1. Synthesis *149*

7.3.1.1. $BaMn_{1-z}Zr_zO_{3-x}$ 149

7.3.1.2. $Ba_{1-y}Sr_yMn_{1-z}Ti_zO_{3-x}$ 150

7.3.2. Structural refinement *152*

7.3.2.1. $BaMn_{1-z}Zr_zO_{3-x}$ 152

7.3.2.2. $BaMn_{1-z}Ti_zO_{3-x}$ 155

7.3.3. Electron diffraction *164*

7.3.4. Chemical characterisation *165*

7.3.5. Magnetometry *166*

7.4. Discussion 169

7.4.1. Structure *169*

7.4.2. Susceptibility data *170*

7.4.2.1. Similarities with the $BaMnO_{3-x}$ series 170

7.4.3. Differences from the $BaMnO_{3-x}$ series *171*

7.4.4. Cation ordering *173*

7.5. Conclusion 175

Chapter 8: Topotactic reduction of 4H-$Ba(Sr)MnO_{3-x}$ 176

8.1. Introduction 176

8.2. Experimental 177

8.2.1. Synthesis *177*

8.2.2. Characterisation *178*

8.3. 4H-$Ba_{0.5}Sr_{0.5}MnO_{2+x}$ 178

8.3.1. Results *178*

8.3.1.1. Structural refinement 179

8.3.1.2. Magnetometry data 183

8.3.2. Discussion *184*

8.3.2.1. Structure 184

8.3.2.2. Magnetism 185

8.4. 4H-$BaMnO_{2+x}$ 187

8.4.1. Results *187*

8.4.1.1. Synthesis 187

8.4.1.2. Structural analysis 188

8.4.1.3. Magnetometry 193

8.4.2. Discussion *194*

8.4.2.1. $BaMnO_{2.47(1)}$ 195

8.4.2.2. $BaMnO_{2.06(1)}$ 196

8.5. Conclusion 197

Bibliography 199

Appendix A i

Appendix B v

Appendix C viii

Appendix D ix

Chapter 1: Introduction

1.1. The tolerance factor

The cubic perovskite structure (Figure 1.1a) represents a simple and highly symmetric arrangement of elements in the ratio ABX_3. In this structure AX_3 layers are close packed along the [111] axis in the cubic ABCABC stacking sequence. The smaller B cations occupy octahedral holes between the layers. The BX_6 octahedra and AX_3 layers are shown in Figure 1.1b.

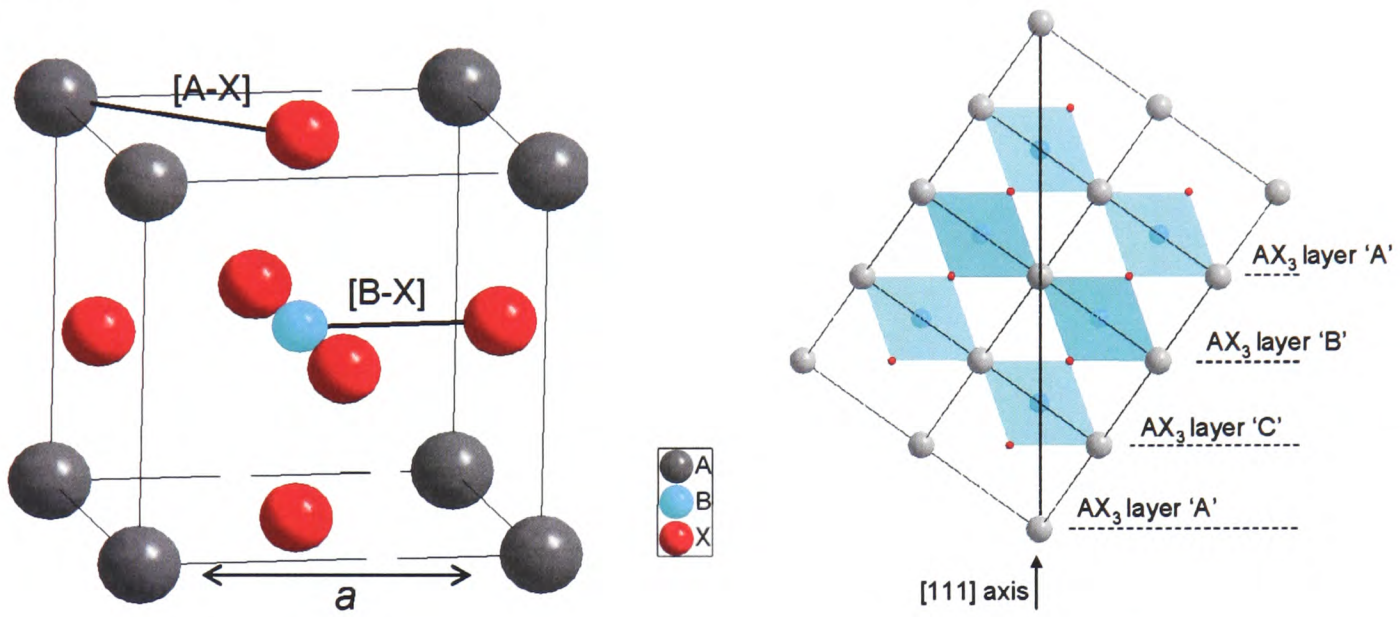


Figure 1.1 a) Cubic perovskite unit cell showing the relationship of the lattice parameter *a* to the A-X and B-X bond lengths and b) projection of the cubic perovskite unit cell showing the stacking sequence of the AX_3 layers.

The cubic geometry of the unit cell ensures a specific relationship exists between the A-X bond length, the B-X bond length and the cell parameter (a), described by Equation 1.1. This relationship may be rearranged to Equation 1.2, which defines the Goldschmidt tolerance factor (t) where $t = 1$ for the cubic perovskite structure. In non-cubic systems or those which are distorted from the ideal cubic geometry t does not equal 1. The value of t provides an indication of the nature and extent of deviation from the ideal cubic system.

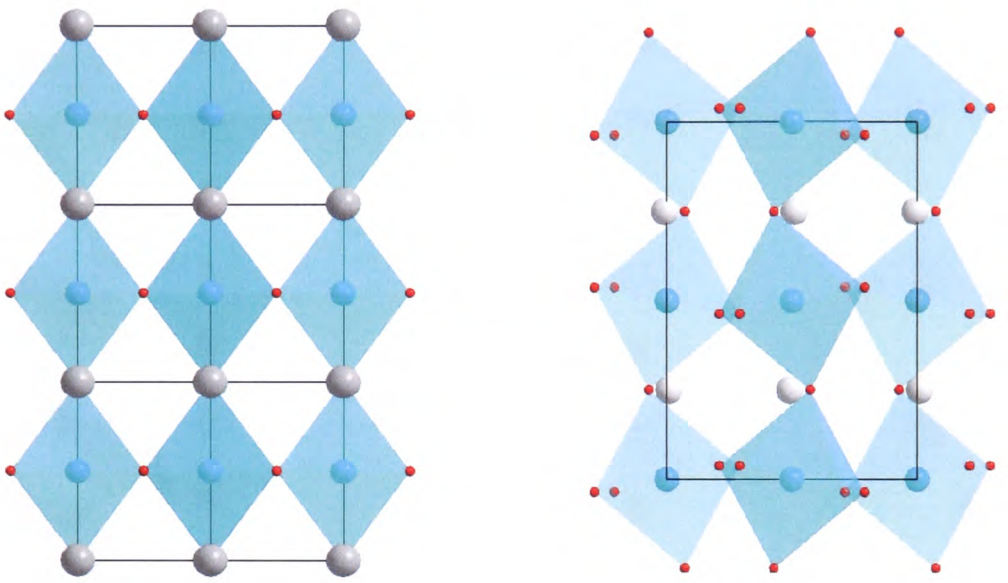
$$a = 2[\mathrm{B}-\mathrm{X}] = \sqrt{2}[\mathrm{A}-\mathrm{X}]$$

Equation 1.1

$$t = \frac{[\mathrm{A}-\mathrm{X}]}{\sqrt{2}[\mathrm{B}-\mathrm{X}]}$$

Equation 1.2

If the B-X bond length is increased relative to the A-X bond length then $t < 1$. Tolerance factors less than 1 can be accommodated by cooperative twisting of the BX_6 octahedra, which alters the B-X-B bond angles such that they are no longer equal to 180°. Figure 1.2 shows the structures of the two titanates, $SrTiO_3$ and $CaTiO_3$. These have different structures because of the different A cation sizes. $SrTiO_3$ adopts the ideal cubic perovskite structure where $t = 1$ and all Ti-O-Ti bond angles are 180°.[1] Calcium is smaller than strontium and $t = 0.791$ for $CaTiO_3$.[2] The reduced tolerance factor is accommodated by twisting of the TiO_6 octahedra, resulting in Ti-O-Ti bond angles which are not equal to 180°.



$SrTiO_3$ $t = 1.000$ $CaTiO_3$ $t = 0.791$

Figure 1.2 The ideal cubic perovskite structure of $SrTiO_3$ (t = 1) and distorted cubic perovskite structure of $CaTiO_3$ (t = 0.791).

If the A-X bond length is increased relative to the B-X bond length, tolerance factors greater than 1 are achieved. This indicates that the A cations are too large for the available sites in the cubic perovskite. No twisting can accommodate this, but in order to increase the average A site hexagonal close packing can be introduced into the stacking sequence of the AX_3 layers. Hexagonal close packing stacks the AX_3 layers in an ABAB sequence. The larger the value of t, the greater the proportion of AX_3 layers which are stacked using hexagonal close packing. This is exemplified by the $AMnO_3$ phases where A = Ca, Sr or Ba. As the size of the A cation increases, so does the tolerance factor and therefore so does the proportion of AX_3 layers which are stacked using hexagonal close packing. $CaMnO_3$ has a tolerance factor of 0.987 and adopts

a distorted cubic perovskite structure with only cubic close packing of the CaO_3 layers (and slight twisting of the MnO_6 octahedra).[3] The barium cation is much larger than the calcium cation and this is reflected in the tolerance factor of $BaMnO_3$ (1.089). A hexagonal perovskite structure is adopted, in which the BaO_3 layers are all hexagonally close packed.[4] In hexagonal perovskite structures the AX_3 layers are stacked along the *c* axis rather than the [111] stacking direction in the cubic system. The strontium cation is intermediate in size and the hexagonal perovskite structure adopted by $SrMnO_3$ contains 50% hexagonal close packing and 50% cubic close packing.[5] The three structures are shown in Figure 1.3.

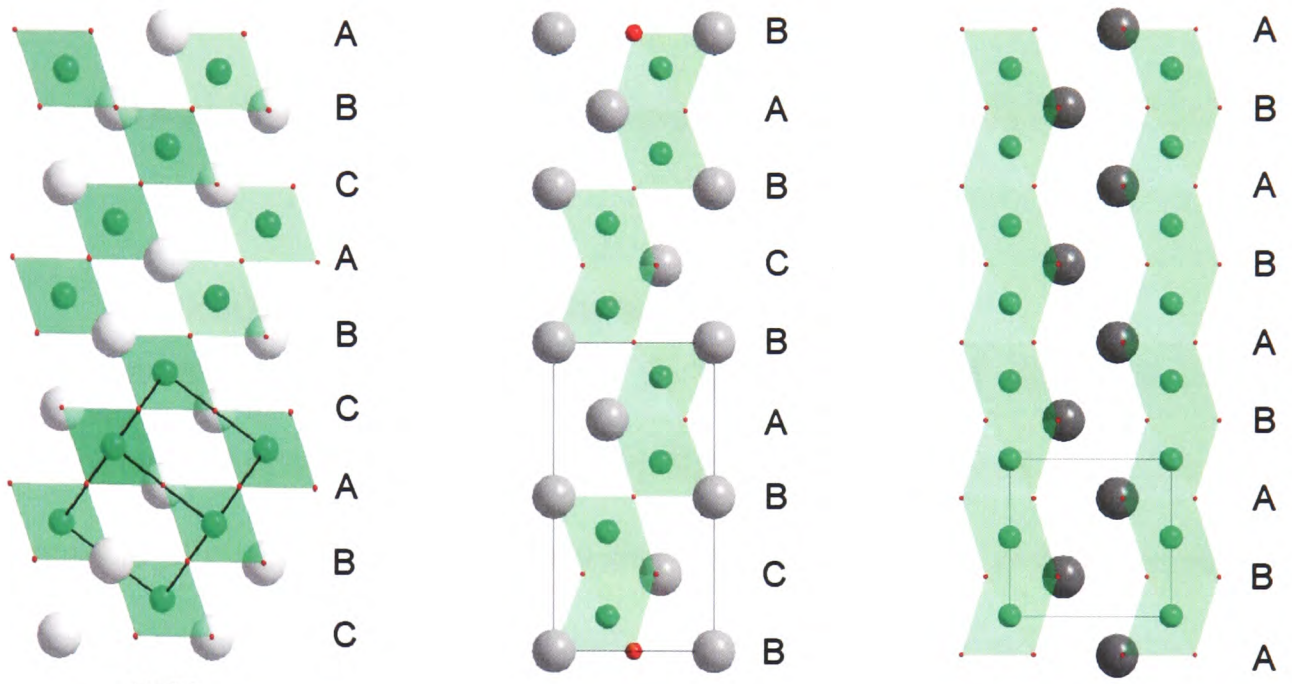


Figure 1.3 Structures adopted by $AMnO_3$ (A = Ca, Sr or Ba). A perfect cubic perovskite structure is shown for ease of comparison with the two hexagonal perovskites. The structure adopted by $CaMnO_3$ is actually distorted.

As well as changing the A cation (and so the average A-X bond length) the B-X bond length can be altered. This can be achieved by changing the B cation. For example $SrTiO_3$ in Figure 1.2 has a tolerance factor of 1 indicating it adopts the cubic perovskite structure, whereas the smaller manganese cation in $SrMnO_3$ increases the tolerance factor to 1.033, and the structure adopted by $SrMnO_3$ incorporates 50% hexagonal close packing (Figure 1.3). The B-X bond

can also be altered by oxidation or reduction. Increasing the average B cation oxidation state will reduce the average B-X bond length (and so increase the tolerance factor); reduction of the B cations will reduce the tolerance factor.

The cubic perovskite structures, along with their modifications, are among the most widely studied families of oxides. Of especial interest are those in which the dimensionality of the B-O network is lowered, allowing access to materials with two-dimensional characteristics. This occurs in structures such as the Ruddlesden-Popper series, $A_{n+1}B_nO_{3n+1}$ in which blocks of cubic perovskite are isolated from one another by rock salt AO layers. Hexagonal perovskites can have a still lower dimensionality. In the structure adopted by $BaMnO_3$ (with solely hexagonal stacking) chains of face-sharing MnO_6 octahedra are isolated from one another by Ba cations.

1.2. Hexagonal Nomenclature

There are a number of descriptions used to label the crystal structures of hexagonal perovskites. The first systematic description by Katz and Ward named structures according to the total number of close packed AX_3 layers stacked along the *c* axis in the unit cell.[6] Thus the structure containing two layers in the unit cell was referred to as the two-layer structure and the structure containing four manganese ions as the four-layer structure (both shown in Figure 1.3, labelled 2H and 4H). Chamberland [7] added a symbol dependent on the symmetry of the crystal system to the structure name: for structures with a hexagonal space group, such as the two-layer and four-layer structures in Figure 1.3, the letter H was added to the number of layers in the unit cell; for those described by a rhombohedral space group (in the hexagonal setting), the letter R was added.

Hexagonal perovskite structures each contain a specific sequence of AX_3 layers with cubic and hexagonal stacking, but the number of layers in this stacking sequence (*L*) need not be identical to the number of layers in the unit cell (*N*). In many cases, as in the 4H sequence discussed

above, the stacking sequence of cubic and hexagonal layers is repeated several times within the unit cell. The number of repeat units of the stacking sequence in the unit cell (r) is related to N and L as follows:

$$N = L \times r \qquad L = \frac{N}{r}$$

Equation 1.3

The value of r is always 1, 2 or 3 and can be determined from the stacking sequence (see Appendix A). Values of $r = 2$ or 3 contain inherent symmetry due to the repeat of the stacking sequence, and Chamberland's *N*R/*N*H notation can be extended to reflect this. Unit cells where $r = 1$ are described as *N*L. If $r = 2$ the unit cell is always hexagonal and such structures are described as *N*H. If $r = 3$ the unit cell is rhombohedral (in the hexagonal setting) and these cells are described as *N*R.

The 2-layered (2H) and 4-layered (4H) labels describe unique sequences of AX_3 layers, but the naming system becomes ambiguous for unit cells containing many AX_3 layers. There are two different 8H hexagonal perovskite unit cells, for example, both of which are adopted by known phases (shown in Figure 1.4). These differ both in the ratio of cubic to hexagonal close packed layers and in the sequence of these layers within the cell. In order to unambiguously describe compounds with larger unit cells the sequence in which the AX_3 layers are stacked must be defined, along with the number of layers in the unit cell.

1.2.1. Defining the stacking sequence

Most hexagonal perovskite systems incorporate both hexagonal and cubic close packing of the AX_3 layers (the 2H sequence is an exception). Each AX_3 layer can be described as a cubic (c) or hexagonal (h) layer, depending on whether it stacks with the neighbouring layers using cubic (ABC) or hexagonal (ABA) close packing. The type of stacking is also relevant for the connectivity of the BX_6 octahedra, as is apparent in the structures shown in Figure 1.3. BX_6

octahedra share apexes when connected by cubic layers and faces when connected by hexagonal layers.

The full stacking sequence of cubic and hexagonal layers in the unit cell may be defined by listing all AX_3 layers according to the close packing sequence (e.g. ABCB for the 4 layered sequence shown in Figure 1.3). Although the ABC notation for the stacking sequence can be used to name the structure unambiguously, little information about the named structure is immediately obvious. More commonly, each AX_3 layer is described by either *c* for a cubic layer or *h* for a hexagonal layer. Using this notation, the first 8H sequence is described as a *chhh* sequence and the second, 8H', is described as *ccch*. Both are shown in Figure 1.4.

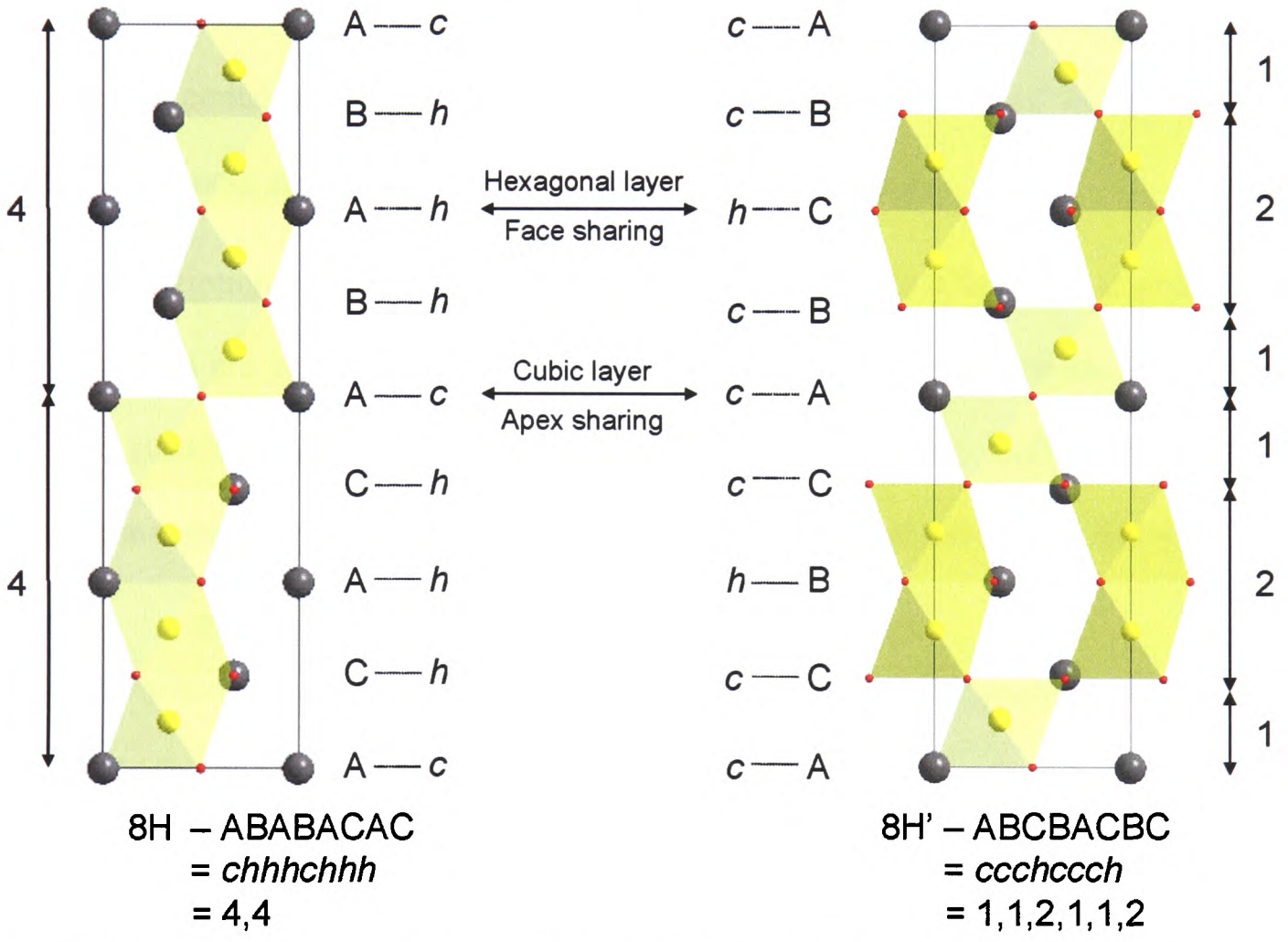


Figure 1.4 Stacking sequences for the two 8H unit cells, 8H - 4 (*chhh*) and 8H' - 2,1,1 (*ccch*).

The *ch* notation highlights structural features that may be missed using the ABC notation. From the full 8H sequence, *chhhchhh*, it is immediately obvious that the true stacking sequence contains only four layers with a *chhh* sequence which is repeated twice within the unit cell

(hence the H label). This information is less apparent in the alternative notation of ABABACACA.

The *ch* notation also facilitates calculation of the ratio of cubic to hexagonal layers, but the long sequences become unwieldy for large unit cells. A further disadvantage is the focus on the AX_3 layers, when often the connectivity of the BX_6 octahedra is more important. An alternative description which defines the stacking sequence simply lists the number of face-sharing BX_6 octahedra connected into chains between the cubic layers. Thus a BX_6 octahedra connected solely by apex-sharing would be represented by the number 1 (as there is only 1 octahedron between cubic layers) and a pair of face-sharing BX_6 octahedra would be represented by the number 2. The 8H sequence is simply '4' using this notation, and immediately indicates that the structure contains chains of 4 face-sharing BX_6 octahedra, linked by apexes. Different stacking sequences are shown for both forms of 8H in Figure 1.4.

The two descriptions of the stacking sequence, according to the AX_3 layers or according to the BX_6 octahedra are both equally valid, as the connectivity of the B cations is predetermined from the stacking sequence of the AX_3 layers (and visa versa). Both the *ch* and the 1,2 notations are useful in different situations, and both will be used throughout this work.

1.3. Known hexagonal perovskite phases

Hexagonal perovskite and related structures may be split into three groups: the 2H and related structures contain no cubic layers; simple stacking sequences contain cubic layers which are distributed as evenly as possible throughout the structure; and complex stacking sequences contain cubic layers that are not distributed as evenly as possible throughout the structure. An example of each group is shown in Figure 1.5.

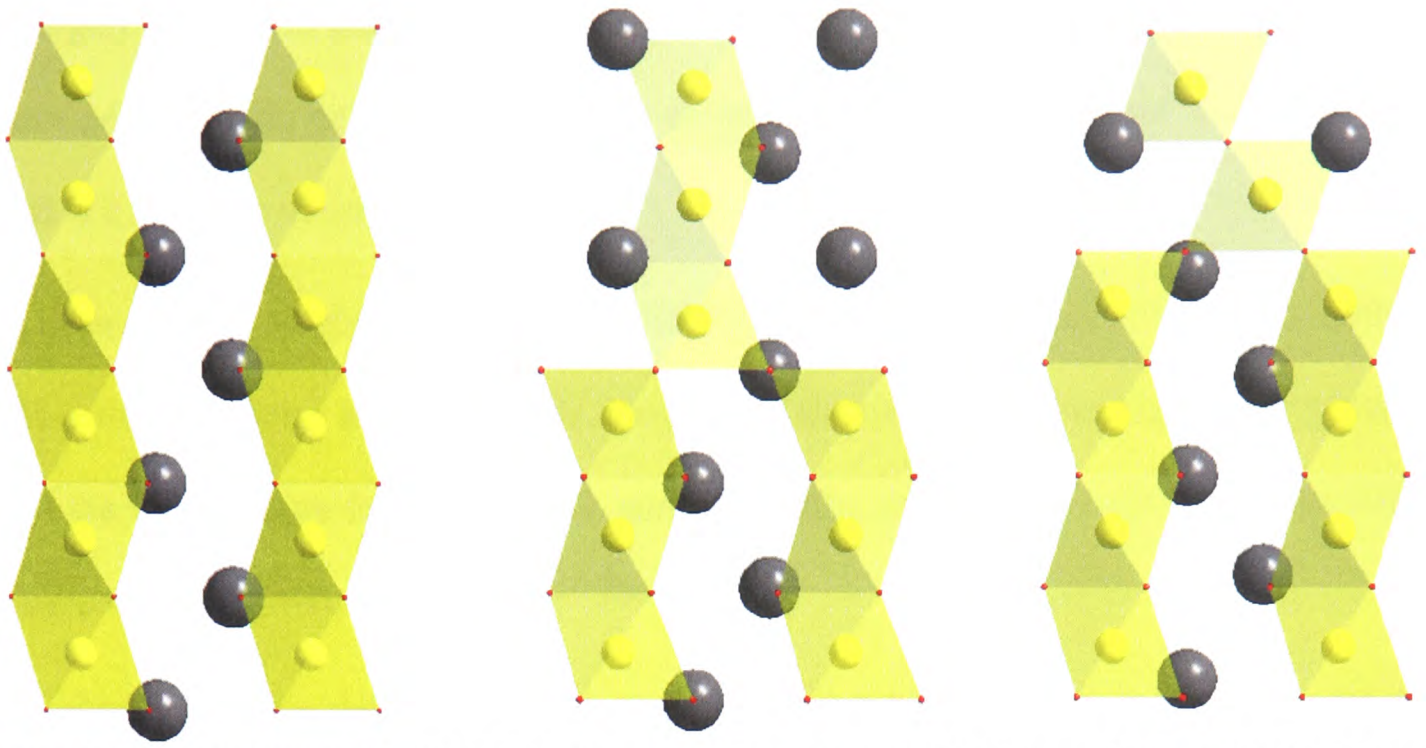


Figure 1.5 From left to right: the 2H stacking sequence, with no cubic layers; the simple 9R stacking sequence in which the cubic layers are uniformly distributed; the repeat unit of the complex 12H stacking sequence where the cubic layers cluster together.

As discussed in Section 1.1, the ratio of cubic to hexagonal layers is dictated by the tolerance factor. Thus either reducing the average A-X bond length or increasing the average B-X bond length (by substitution for B or an increase in the B cation oxidation state) will increase the proportion of cubic layers. High pressure synthesis also favours an increased proportion of cubic layers. This can be rationalised on the basis of the increased density achieved by incorporating more cubic layers into the stacking sequence.

1.3.1. 2H and related structures

The first group consists of 2H and related stacking sequences which have no cubic layers. These structure types, with the B cations connected into isolated chains, can be described as one-dimensional structures. In order for any hexagonal layers to be incorporated into the structure, it is necessary to have a tolerance factor larger than 1. For the 2H sequence (with solely hexagonal layers) to be adopted, the tolerance factor should be as large as possible. This requires both a large A cation and a small B cation. There are several suitably large A(I) cations, such as Rb, Cs and Tl. These form 2H-A(I)B(II)X_3 phases, where X is a halide or hydride ion. The requirement for a small B cation means that compounds with the 2H structure

are largely limited to phases where B is a first row transition element. Most known ABX_3 phases adopt the 2H hexagonal perovskite structure where A = Rb, Cs or Tl, X = Cl, Br or I and B is a first row transition element.[8-19]

If X is an oxide or sulphide anion, 2H-A(II)B(IV)X_3 phases are formed. The only suitably large A(II) cation is barium and 2H-$BaBX_3$ compounds are relatively common. $BaBO_3$ compounds adopt the 2H structure for B = Mn, Co and Ni, $BaBS_3$ compounds adopt the 2H structure for systems such as B = Ti, V, Nb or Ta.[20-26]

Compounds adopting the 2H structure attracted considerable interest due to the possibility of one-dimensional electronic and magnetic behaviour as a result of the isolated chains of face-sharing BO_6 octahedra. In some compounds, such as the Group I ternary halides $RbVI_3$ and $KNiCl_3$, the face-sharing chains of BO_6 octahedra are incommensurate, suggesting the interchain forces are relatively weak.[12, 27]

Further interest was directed at compounds based on ordered intergrowth of A_3O_9 layers (such as are found in the 2H structure) and A_3BO_9 layers (found in the Sr_4PtO_6 structure).[28] The polyhedral chains of the 2H structure and Sr_4PtO_6 are compared in Figure 1.6.

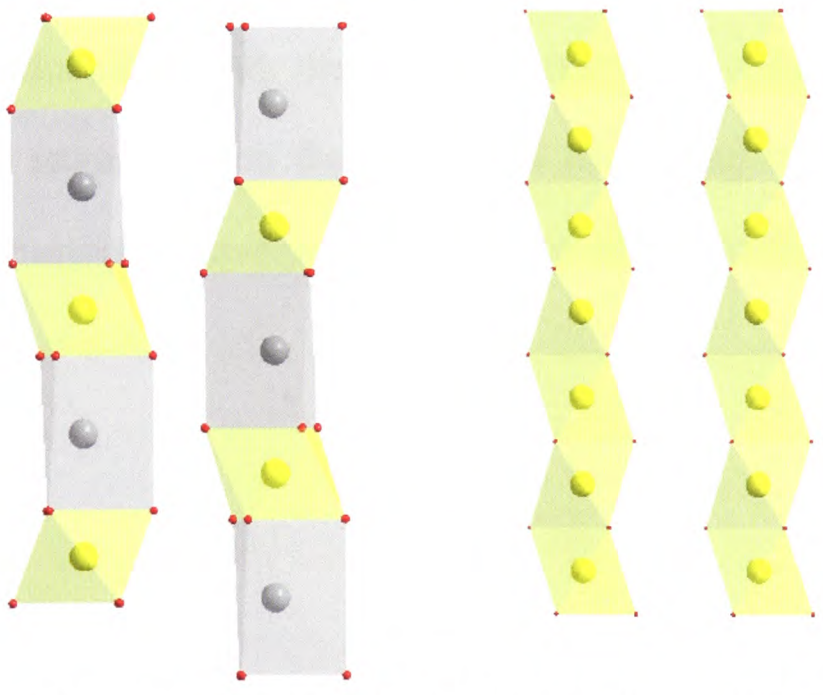


Figure 1.6 One dimensional polyhedral chains in the Sr_4PtO_6 structure and the 2H structure.

Sr_4PtO_6 (or Sr_3SrPtO_6) contains trigonal prismatic SrO_6 units, which alternate with PtO_6 octahedra within the face-sharing chains. The ratio of octahedra to trigonal prisms can be varied from 1 : 0 (the 2H structure) to 1 : 1 (the Sr_4PtO_6 structure) in phases of the form $AB_{1-n}O_{3(1-n)}$.

Studies have shown that although the one-dimensional interactions along the chain are generally much stronger than the two-dimensional interactions between the chains, the systems cannot be considered to be truly one-dimensional. There is often a relatively strong interaction between the chains despite the lack of B-O-B connectivity. Depending on the strength of the interchain interaction, the systems may be considered to be quasi-one-dimensional.[29] If the interaction between the chains is antiferromagnetic, the three-fold symmetry axis precludes typical long-range antiferromagnetic order, as not all of the antiferromagnetic pair-wise interactions can be satisfied.

1.3.2. Simple hexagonal perovskite structures

A wide range of hexagonal polymorphs are available as a result of introducing cubic layers into the hexagonal 2H stacking sequence. Rather than introducing trigonal prisms into isolated chains, as observed in the $AB_{1-n}O_{3(1-n)}$ phases discussed above, the cubic layers introduce apex-sharing BO_6 octahedra which link the chains together. The adoption of simple stacking sequences is easily rationalised on the grounds of minimising strain within the structure. Simple stacking sequences are common, and a review of the literature reveals the sequences listed in Table 1.1.

Stacking sequence		Name	*c*/(*c*+*h*)	Examples
5	*chhhh*	15R	0.200	$BaMnO_{3-x}$ [30]
4	*chhh*	8H	0.250	$BaMnO_{3-x}$ [30]
3	*chh*	9R	0.333	$Ba(Mn/Ru/Ir)O_3$, $BaMn_{1-x}Ru_xO_3$, $BaMn_{1-x}Ir_xO_3$ (x=0.3/4/5) [31-36]
2,3	*chchh*	10H	0.400	$BaMnO_{3-x}$, $BaFeO_{2.67}$, $BaCo_{0.7}Ir_{0.3}O_{2.84(1)}$, $BaCoO_{2.6}Cl_{0.2}$ [30, 37-39]
2	*ch*	4H	0.500	$Ba(Cr/Mn/Ru/Rh)O_{3-x}$, $Ba_{0.67}Sr_{0.33}IrO_3$, $SrMnO_3$, $Ba_{1-x}Sr_xRuO_3$ ($0.15<x<0.4$) [30, 40-45]
1,2,2,2,2	*cchchchch*	27R	0.556	$BaCrO_3$ [46]
1,2,2,2	*cchchch*	14H	0.571	$BaCrO_3$ [47]
1,2,2	*cchch*	15R'	0.600	$BaFe_{0.7}Ir_{0.3}O_{2.949(7)}$, $SrMn_{0.915(5)}Fe_{0.085(5)}O_{2.979(3)}$ [48, 49]
1,2	*cch*	6H	0.666	$Ba(Ti/Cr/Fe/Tc)O_3$, $Ba_3Ru_2(Mg/Sr/Fe/Co/Ni/Cu/Zn/In)O_3$, $BaCr_{0.67}(W,Mo)_{0.33}O_3$ [36, 37, 50-57]
1,1,2,1,2	*ccchcch*	21R	0.714	$BaRu_{0.571}Li_{0.428}O_{2.857}$ [58]
1,1,2	*ccch*	8H'	0.750	$BaCr_{0.5}(Nb/Ta)_{0.5}O_3$, $BaRu_{0.75}Na_{0.25}O_3$, $Ba(Nb/Ta)_{0.75}Li_{0.25}O_3$ [59-61]
1,1,1,2	*cccch*	10H'	0.800	$BaZr_{0.2}Al_{0.4}(Y/Gd/Dy/Ho/Tm/Yb/Lu)_{0.4}O_{2.6}$, $BaW_{0.6}Li_{0.4}O_3$, $SrMn_{0.72}Fe_{0.27}O_{2.87}$ [59, 62, 63]
1,1,1,1,2	*ccccch*	12H'	0.833	$Ba(Mn,V,As,P,Cr)_{0.33}(Ru/Nb/Ta)_{0.33}Na_{0.33}O_{2.83}$, $BaTi_{0.67}(Y,Nd)_{0.33}O_{2.83}$ [64, 65]

Table 1.1 Simple stacking sequences reported for known hexagonal perovskites.

A range of magnetic and electronic properties are observed for compounds adopting hexagonal perovskite structures. These obviously depend strongly on the nature of the B cation. The isostructural phases 4H-$BaCrO_3$, 4H-$SrMnO_3$ and 4H-$BaRuO_3$ show very different behaviour: 4H-$BaCrO_3$ is ferrimagnetic and semiconducting, 4H-$SrMnO_3$ is an antiferromagnetic insulator and 4H-$BaRuO_3$ is metallic.[43, 45, 46, 66-68]

More subtle variations in the magnetic and electronic behaviour are observed between different crystallographic forms of the same chemical composition. 4H-$BaRuO_3$ and 9R-$BaRuO_3$ display different transport properties: 4H-$BaRuO_3$ shows metallic resistivity which is maintained to low temperatures, whereas 9R-$BaRuO_3$ initially shows metallic resistivity but undergoes a

transition to a more resistive state at T ~ 50K (the transition is associated with the development of an extremely small ferromagnetic moment).[45]

The study of such polytypes is valuable for determining structure-property relationships, but relatively little work has been carried out on such phases in the hexagonal perovskite series. There are a large number of polymorphs are reported for the composition $BaCrO_3$.[7, 43, 46, 47, 53] The structures form a series in which an increasing proportion of cubic layers are inserted into the 4H stacking sequence. The stacking sequences of 4H, 27R, 14H and 6H unit cells are shown in Figure 1.7. 4H, 27R, 14H and 6H-$BaCrO_3$ are all are reported to be semiconducting and ferrimagnetic, but there are no reports of how properties such as the Néel temperature vary across the series with the ratio of face-sharing to apex-sharing B-O-B linkages.[46]

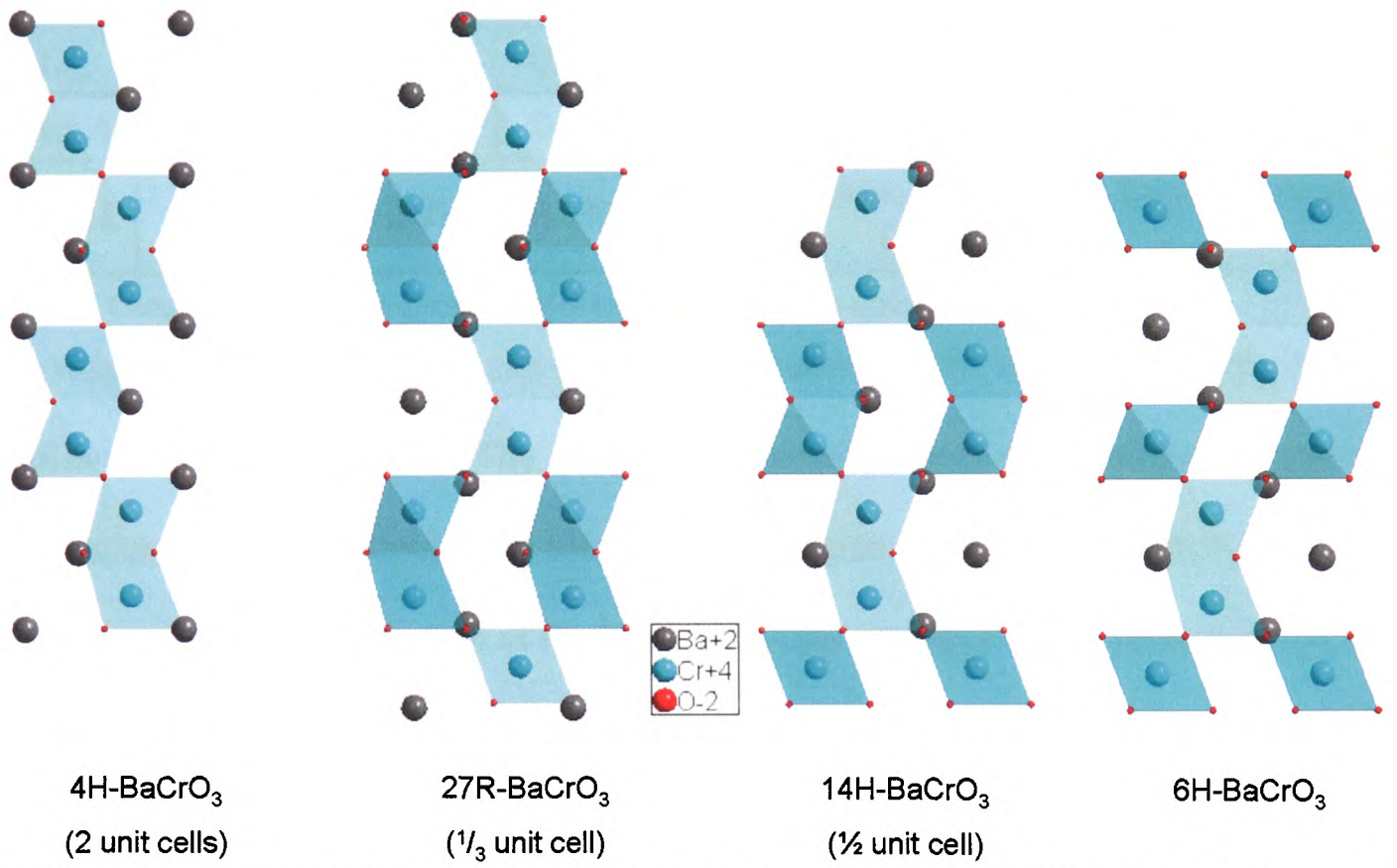


Figure 1.7 Stacking sequences of 4H (2) 27R (2,2,2,1), 14H (2,2,2,1) and 6H (2,1). The missing member of the sequence, 15R (2,2,1), is not known for $BaCrO_3$.

1.3.3. Complex hexagonal perovskite structures

The 6H (three layer repeat unit, *cch*) sequence is extremely common, reported for $BaTiO_3$, $BaCrO_3$ and $BaFeO_{3-x}$, along with a wide range of $BaB_{1-y}B'_yO_{3-x}$ phases. This has a ratio of 1 : 2 hexagonal to cubic layers, with the simplest (and therefore smallest) possible stacking

sequence for this ratio. A complex stacking sequence with the same ratio of 1 : 2 hexagonal to cubic layers but where the hexagonal (or cubic) layers are clustered together (for example, *cccchh*), necessarily contains a larger number of layers in the repeat unit. There are no reported observations of such structures containing 66% cubic layers. However, more complex stacking sequences are observed for a variety of other proportions of cubic layers. Observed stacking sequences of this type are listed in Table 1.2.

Stacking sequence		Name	*c*/(*c*+*h*)	Example
2,4	*chchhh*	6L	0.333	$BaMnO_{3-x}$, $BaMn_{0.767}Fe_{0.233}O_{2.87}$, $BaCoO_{2.666}Cl_{0.167}$ [30, 69, 70]
1,3	*cchh*	12R	0.500	$BaTi_{0.5}Mn_{0.5}O_{3.00}$, $BaMn_{0.5}Ca_{0.25}Mo_{0.25}O_3$, $BaMn_{0.75}(In,Ce,Pr)_{0.25}O_3$, $BaCo_{0.5}Ir_{0.5}O_{3.02(1)}$, $BaRu_{0.75}Zr_{0.25}O_{12}$ [38, 71-74]
1,1,4	*ccchhh*	12H	0.500	$BaCoO_{2.6}$, $BaMn_{1-x}Co_xO_{3.00}$ $0.62<x<0.45$ [75, 76]
1,1,3	*ccchh*	5L	0.600	$Ba(V,Co)O_{3-x}$, $BaCo_{0.8}Ir_{0.2}O_{2.83(1)}$ [38, 77]
1,1,1,1,4	*cccccchhh*	16H	0.625	$BaMn_{0.775}Ca_{0.225}O_{2.875}$ [78]
1,1,1,1,3	*Ccccchh*	21R	0.714	$BaY_{0.29}Mn_{0.42}Ti_{0.29}O_{2.85}$, $BaMn_{0.71}Ca_{0.29}O_{2.85}$, $BaMn_{0.71}Cr_{0.29}O_{2.85}$ [79-81]

Table 1.2 Complex stacking sequences reported for known hexagonal perovskites.

The complex stacking sequence can often be rationalised on the basis of different coordination requirements of the B cations. The hexagonal perovskite stacking sequences where the cubic (or hexagonal) layers do not simply maximise their separation necessarily incorporate different B cation sites. An illustrative set of stacking sequences are those which have 50% cubic layers, as shown in Figure 1.8. This ratio requires a repeat unit of at least 2 layers, 1 cubic and one hexagonal. The simple stacking sequence for this ratio is named 4H, which has a stacking sequence of *ch* (or 2) and contains only one B cation site. This is adopted for $BaCrO_3$ and $SrMnO_3$, shown in Figure 1.7 and Figure 1.3 respectively.

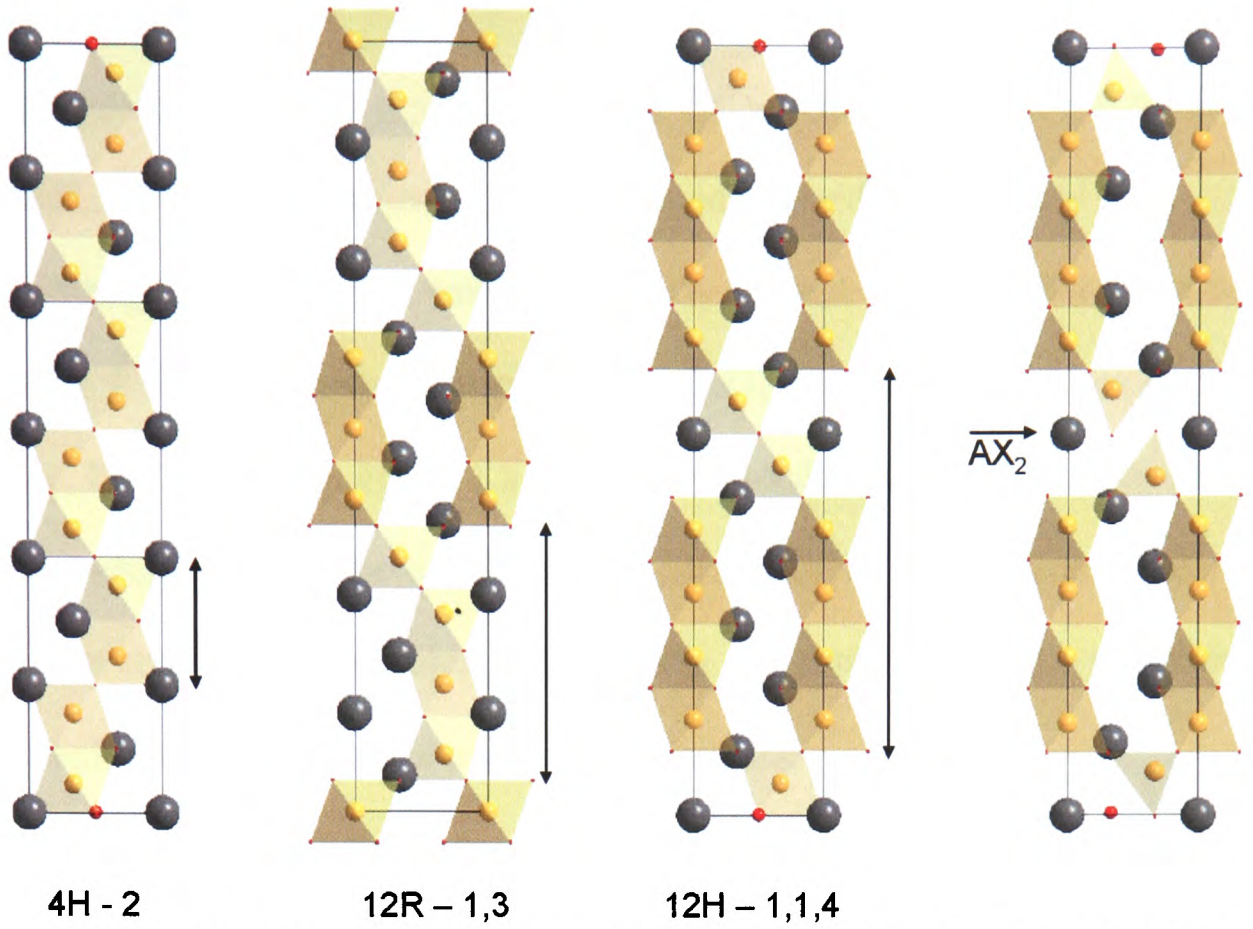


Figure 1.8 Stacking sequences with a 1:1 ratio of hexagonal to cubic layers. The unit cells are marked and length of the stacking sequence indicated by a double headed arrow. The fourth structure shows the inclusion of anion vacancies in the 12H structure, resulting in BX_4 tetrahedra.

Few compounds of the form $AB_{1-x}B'_xO_3$ adopt the 4H sequence as the different B cations generally have different coordination requirements and often cannot share the single crystallographic B cation site in the 4H sequence. $Ba_4Ru_3ZrO_{12}$, for example, adopts the 12R *cchh* (or 1,3) stacking sequence, which has the same 1 : 1 ratio of cubic to hexagonal layers.[74] The Zr(IV) ion ($r_{Zr(IV)}$ = 0.72 Å)[82] is too large to be accommodated in the face-sharing sites and instead occupies the apex-sharing site. The Ru(IV) ion ($r_{Ru(IV)}$ = 0.62 Å)[82] occupies the smaller face-sharing sites.

The third stacking sequence containing 50% cubic layers is called 12H and has a sequence of *ccchhh* (or 1,1,4). Hexagonal perovskites containing a 1,1 block in the stacking sequence are relatively common; these represent the vast majority of the complex stacking sequences. Many of the structures adopting these stacking sequences are oxygen deficient. If the oxide vacancies are accommodated in an ordered manner, this can redirect the stacking sequence. While $BaCoO_3$ adopts the 2H structure, reduction of the cobalt from Co(IV) to Co(III) reduces the

tolerance factor and a new 12H-$BaCoO_{2.61}$ phase is observed.[76] The 1,1 unit in the 12H stacking sequence represents a pair of adjacent CoO_6 octahedra which are connected only by apex-sharing. The oxygen vacancies are accommodated within the central layer separating this pair of octahedra, resulting in a composition AO_2 (instead of AO_3). This alters the Co cation connectivity from apex-sharing octahedra into CoO_4 tetrahedra which are not connected to each other. This is shown in Figure 1.8. These tetrahedral sites are favoured by small B cations. The relationship between the stoichiometric 12H stacking sequence and the reduced 12H structure incorporating tetrahedral coordination is similar to the relationship between brownmillerite phases and the cubic perovskite structure.

In the $BaCoO_{2.61}$ case, the introduction of tetrahedral coordination can be rationalised on the basis of the coordination requirements of the cobalt. Co(III) has a d^6 electronic configuration and thus a strong preference for octahedral coordination. Because of this, the oxide vacancies are located in the Co(IV) coordination spheres. In order to maintain the charge balance, these coordination spheres must contract relative to unreduced 2H-$BaCoO_3$. The extent of this contraction results in tetrahedral coordination. The 12H-1,1,4 stacking sequence is also observed for $BaMn_{0.4}Co_{0.6}O_{2.83}$ and $BaMn_{0.5}Co_{0.5}O_{2.87}$.[83, 84] In both cases the apex-sharing sites are believed to be occupied by Co(IV) in a tetrahedral coordination.

Thus the structure adopted by a given compound is predominantly dependent on the tolerance factor. This determines the ratio of hexagonal to cubic layers. The layers will generally be arranged in the simple stacking sequence. However, complex stacking sequences may occur when multiple B cations with different coordination requirements are present.

Chapter 2: Experimental techniques

2.1. Ceramic synthesis

The ceramic route was used to prepare thermodynamically stable products at high temperatures. The method involves heating binary metal oxides and carbonates to temperatures between 1000°C and 1500°C in order to overcome the high diffusion barrier between solids.

Stoichiometric quantities of high purity (> 99.95%) starting materials were thoroughly ground together in an agate pestle and mortar. The homogenous mixture was then fired for 24 hours in an alumina crucible at 900-950°C to decompose the carbonate starting materials. Following decarbonation the mixture was pressed into 1.5-2.5g pellets before firing at higher temperatures. The firing sequences are detailed in the appropriate chapters. The temperature was raised to the appropriate value at a rate of 10 °C min^{-1}. Crucibles were generally removed directly from the furnace to cool them. Reactions were considered complete when X-ray powder diffraction patterns showed no change after successive firings.

In some cases, air was not an appropriate reaction atmosphere for forming the desired product. Reactions under alternative atmospheres were carried out in flow furnaces. The appropriate gas was fed into the flow tube via a flow meter. The gases used included 2% H_2/N_2, Ar, O_2, and 1% O_2/Ar. Atmospheres of 10% - 40% oxygen were obtained by mixing oxygen and argon gases in the desired ratio using flow meters before flowing through the reaction furnace. This is discussed further in Chapter 3.

2.2. Hydride reductions

Binary metal hydrides were used in low temperature, topotactic reductions. The hydride reagents used (NaH, LiH) are oxygen and moisture sensitive, so any mixtures containing them were kept under an inert atmosphere. The manganate starting materials were mixed with the hydride in an argon filled glove box and sealed under vacuum in a glass ampoule prior to heating. The reaction with LiH produces hydrogen gas, so large samples containing LiH were

placed in alumina boats and fired in a silica tube containing a pressure release valve. The pressure was released into a flow of argon, previously passed through titanium heated to 800°C to remove any oxygen. The pressure release system (shown in Figure 2.1) ensured that any flow back of gas through the pressure release valve did not introduce oxygen into the system.

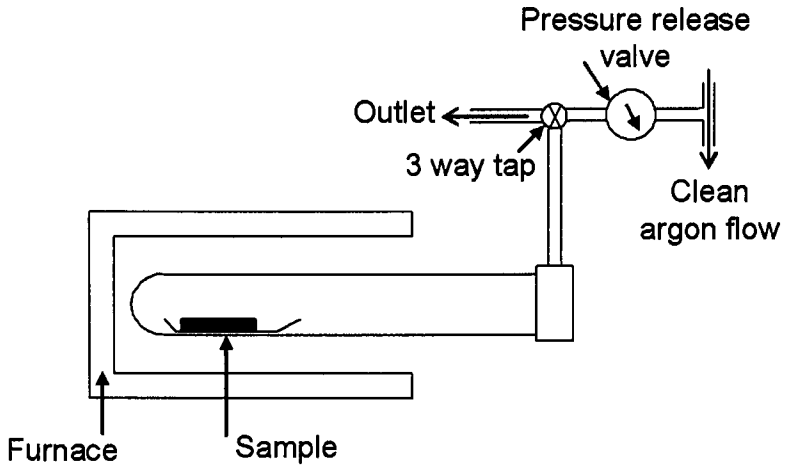


Figure 2.1 Experimental setup of the pressure release system.

Unless otherwise stated, a stoichiometric double excess of hydride was used. The sample was heated at a ramp rate of 1 - 2°C min^{-1} to ensure that the temperature of the furnace did not over-shoot the relatively low target temperatures (T < 500°C). The reaction progress was monitored using X-ray powder diffraction, with reactions were considered complete when X-ray powder diffraction patterns showed no change after successive firings. When the reaction had reached completion the products were washed on a Schlenk line, using methanol to remove the oxide or hydroxide by-product as well as any excess hydride. The methanol was then removed by drying samples under vacuum.

2.3. Powder diffraction

Diffraction methods are an extremely useful tool in solid state structure determination. Diffraction is a consequence of directing radiation at a periodic arrangement of lattice points when the lattice separation is of a similar order to the wavelength of the radiation. Three types of radiation were used in diffraction experiments on powdered samples: X-rays, neutrons and electrons, all of which possess wavelengths of the same order as the interatomic separations of a crystal. Diffraction occurs according to Bragg's law (Equation 2.1).[85] This can be derived by

considering the reflection of an incident beam from a series of lattice planes. Where coherent diffraction intensity is observed the angle (2θ) between the incident beam and the scattered beam is related to the interplanar spacing (d) by the wavelength of the incident beam (λ). The integer, n, can generally be taken as unity.

$$2d\sin\theta = n\lambda$$

Equation 2.1

Values of d may be obtained by monitoring the diffracted intensity as a function of θ for a fixed wavelength (angle dispersive scattering), or alternatively as a function of λ at a fixed angle (energy dispersive scattering). X-ray and electron diffraction techniques generally use angle dispersive scattering, whereas in the field of neutron diffraction both techniques are used.

Although Bragg's law determines whether coherent diffraction is possible, it does not determine the intensity (I) with which this will happen. This is dependent on a number of factors:

$$I_{hkl} \propto LmA\left|F_{hkl}\right|^2$$

Equation 2.2

where L is the sample-independent Lorentz-polarisation factor; m is the reflection multiplicity; A is the absorption factor and F_{hkl} is the structure factor. The structure factor relates the intensity of the reflection to the arrangement of atoms within the unit cell:

$$F_{hkl} = \sum_n f_n \exp\left[2\pi i\left(hx_n + ky_n + lz_n\right)\right]\exp\left(\frac{-8\pi^2 U_{iso}\sin^2\theta_{hkl}}{\lambda^2}\right)$$

Equation 2.3

where f_n is the atomic scattering factor (or the nuclear scattering length) and x_n, y_n and z_n are the fractional coordinates of the n^{th} atom in the unit cell. The exponential term corrects the structure factor for displacement of the atoms according to the parameter U_{iso} (for isotropically displaced atoms). This has a strong dependency on θ. Thus although the position of the Bragg peaks yields the interplanar spacings, it is the intensity which yields information about the arrangement of the atoms within the unit cell.

2.3.1. X-ray powder diffraction

X-ray powder diffraction is a widely employed technique in the study of solid state structures, in part due to the ready availability of monochromatic X-ray sources. There is a strong interaction between X-rays and the atomic electron clouds, which allows the rapid collection of data sets and thus easy monitoring of reaction progress. Longer collection times result in data sets suitable for refinement purposes. The disadvantage of X-ray diffraction is that as X-rays are scattered by the electron cloud of an element, the scattering factor f_n is proportional to the number of electrons the element possesses. This leads to the domination of the diffraction data by heavy elements.

2.3.1.1. Philips PW1710 diffractometer

The Philips diffractometer was routinely used to determine reaction completeness. It operates in Bragg-Brentano reflection geometry using both Cu $K\alpha_1$ and Cu $K\alpha_2$ radiation. Non-air-sensitive samples were generally loaded into a recess on an aluminium plate. The diffraction data obtained using this technique generally show additional reflections due to the aluminium holder, and occasionally intensity variation was observed due to preferred orientation effects. When the aluminium reflections overlapped with critical sample reflections, diffraction data were obtained from samples sprinkled on a glass slide which had been coated with a small amount of Dow-Corning high vacuum grease. The data from non-air-sensitive samples were collected over the range $3° < 2\theta < 70°$ using a continuous scan with a speed of 0.04 °2θ s^{-1}.

Samples which were potentially air-sensitive were placed on a glass slide using a small amount of Dow-Corning high vacuum grease in an argon filled glove box. This was placed in an aluminium holder containing a thin Mylar window (Figure 2.2). The holder was sealed using a screw cap and o-ring. The data for air sensitive samples were collected using a continuous scan over a range of $10° < 2\theta < 70°$ and with a scan speed of 0.02 °2θ s^{-1}. This longer scan allowed for the loss of intensity due to the sample holder.

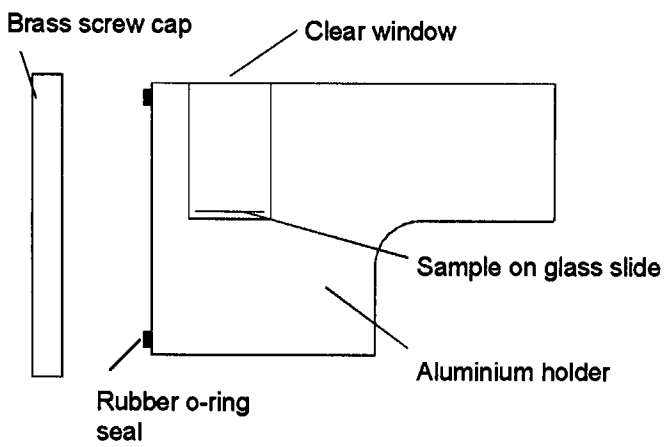


Figure 2.2 Schematic diagram of the air-sensitive X-ray cell for the Philips and X-pert diffractometer.

2.3.1.2. Siemens D5000 diffractometer

The Siemens D5000 Diffractometer was used to obtain high quality data sets suitable for refinement, often to ascertain sample quality prior to neutron powder diffraction measurements. The Siemens diffractometer operates in Bragg-Brentano geometry and the Ge monochromator selects Cu $K\alpha_1$ radiation only. The single wavelength radiation (λ = 1.5406 Å) allowed phases with near-identical lattice parameters to be distinguished from one another.

High resolution data suitable for refinement were collected in a step scan from $10° < 2\theta < 120°$, measuring each point for 20 s with a step size of 0.02°. Samples were sprinkled over the surface of a silicon wafer (cut along the systematically absent (110) plane) coated with Dow-Corning high vacuum grease. The silicon wafer was rotated at a speed of 30 rpm to minimise effects from a possible uneven coating of the diffracting surface.

2.3.1.3. PANalytical X'pert PRO diffractometer

The X'pert diffractometer was also used to obtain high quality data sets suitable for refinement. It operates in Bragg-Brentano geometry and the monochromator selects Cu $K\alpha_1$ radiation only, allowing increased resolution compared to the Philips data sets. The X'pert diffractometer allows some control over the balance between intensity and resolution. 0.02 mm Soller slits can be used in order to maximise the resolution of the measurement or to maximise the intensity, 0.04 mm Soller slits can be used. Unless otherwise stated, 0.02 mm Soller slits were used for all non-air-sensitive measurements and 0.04 mm Soller slits for all air-sensitive measurements.

Non-air-sensitive samples were spread over the surface of a silicon wafer cut along the systematically absent (110) plane which had been coated with Dow-Corning high vacuum grease. The data were collected in a continuous scan from $10° < 2\theta < 90°$, at a rate of $0.007846°s^{-1}$. The silicon wafer was rotated at a speed of 30 rpm to minimise effects from a possible uneven coating of the diffracting surface.

Data sets for air-sensitive samples were acquired using the same air-sensitive X-ray cell as the Philips scans. The data were collected from $10° < 2\theta < 80°$, with a slower scan speed of $0.007081°s^{-1}$.

2.3.2. Neutron powder diffraction

Neutron diffraction is a complimentary technique to X-ray diffraction as X-rays interact with the electron cloud via the electromagnetic force, whereas neutrons interact via the strong nuclear force with the nuclei of atoms. The different interaction provides certain advantages and disadvantages of neutron diffraction compared to X-ray diffraction.

- Since the scattering of neutrons is independent of the electron cloud, it does not vary in a systematic way with the atomic number as the X-ray form factor does. This means that unlike X-ray diffraction patterns, neutron diffraction patterns are not dominated by heavy atoms. Neutron diffraction therefore provides a useful technique for detecting and distinguishing between lighter elements in the presence of heavier ones. Using a combination of X-ray and neutron diffraction, most sets of elements can be distinguished.

- The neutron form factor can generally be regarded as being independent of the angle at which scattering occurs. Thus unlike X-ray diffraction data, there is no decay of the scattering intensity as the *d*-spacing increases. This is a result of the small size of the scattering nuclei, which approximate to a point source in comparison to the typical neutron wavelength and the interatomic separations.

- Neutrons interact with matter much more weakly than X-rays. This provides both advantages and disadvantages. While larger samples or longer measurement times are required to obtain acceptable diffraction data, the weak interaction with matter allows measurements in special environments (e.g. furnaces or cryostats) to be performed easily. A further advantage is that the mean free path of neutrons within a solid is much greater than the mean free path of X-rays within a solid. This allows neutron diffraction to probe the bulk material, avoiding some of the systematic errors associated with bulk studies performed using X-ray diffraction.

- Finally, the neutron has an intrinsic spin (I = ½) and so a magnetic dipole moment. Thus neutrons interact with magnetic fields generated by unpaired electrons distributed throughout the solid. If these are distributed in a periodic manner, diffraction from these will result in magnetic diffraction peaks. This diffraction intensity provides the only method of unambiguously determining magnetic structures. Since the unpaired electrons do not approximate to a point source, the intensity of magnetic reflections exhibits a strong angular dependence. In the event of magnetic ordering, the nuclear structure factor (F_{hkl}) in Equation 2.3 is modified by simply adding the magnetic structure factor (for an unpolarised neutron beam). The magnetic structure factor ($\mathbf{F}^{mag}$) is defined as follows:

$$\mathbf{F}_{hkl}^{mag} = \sum_{n} \mathbf{q}_n p_n \exp\left[2\ \pi\ i\ \left(hx_n + ky_n + lz_n\right)\right]$$

Equation 2.4

The sum is taken over the magnetic atoms. The magnetic interaction vector (**q**) is the projection of the magnetic moment vector on to the plane perpendicular to the scattering vector. The magnitude of the magnetic cross section (p) is proportional to the spin quantum number of the magnetic atom (S). The scattering power is thus proportional to S^2.

2.3.2.1. D2B at the ILL

The ILL is a nuclear reactor based neutron source, where neutrons are produced as a by-product of the nuclear fission process. This process produces high-energy neutrons with a range of wavelengths. These are passed through a moderator in order to reduce their energy. The neutrons are then passed through a single crystal monochromator before being diffracted from the sample.

The D2B diffractometer at the ILL is a high resolution two-axis diffractometer.[86] The instrument is located in the reactor core shell to take advantage of a high neutron flux. A D_2O moderator produces neutrons with thermal energies, which are monochromated using a Ge crystal. The monochromator has a high take-off angle (135°) to increase the resolution. A schematic of the instrument is shown in Figure 2.3.

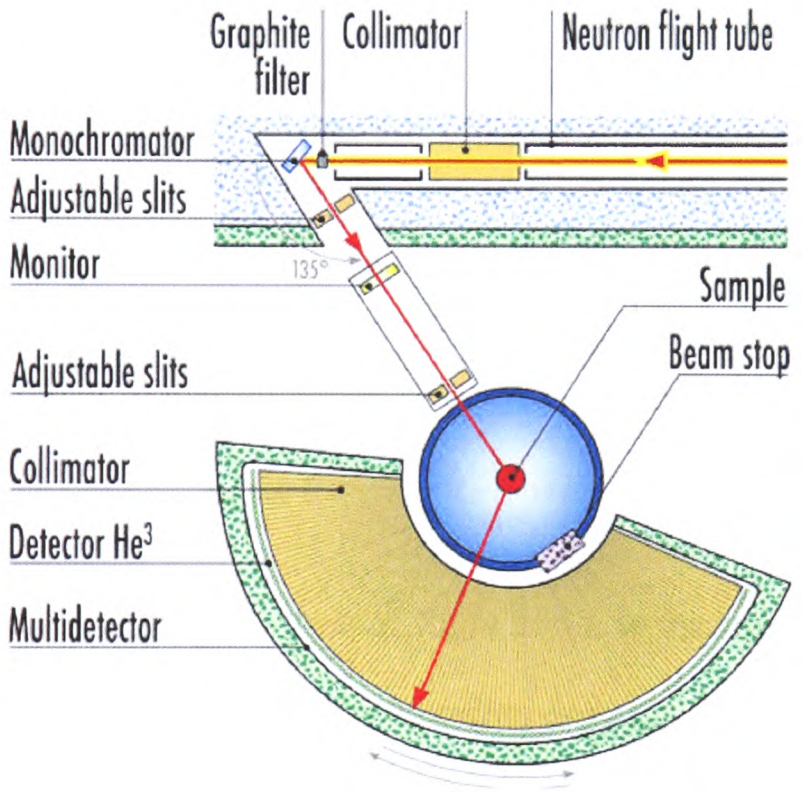


Figure 2.3 Schematic representation of the D2B diffractometer (Figure reproduced from reference [87]).

Data were collected over the range $5 < 2\theta\ (°) < 160$ using a 64 counter multidetector. The counters are spaced at 2.5° intervals, so a complete diffraction pattern is obtained in 100 steps of 0.025 °2θ. Typically, several scans are collected and summed to produce the final data set. The optimal wavelength of $\lambda = 1.594$ Å was used for all measurements. Samples of typically 3

– 4 g were contained in vanadium cans. Measurements made at low temperatures were carried out in an ILL 'orange' cryostat.

2.3.2.2. Isis

The ISIS facility in the UK produces neutrons using a spallation process. High energy protons are accelerated in a synchrotron and then fired in pulses at a tungsten target. This bombardment drives intense pulses of high energy neutrons from the nuclei of the target. In order to lower the speed of the neutrons such that it is suitable for neutron scattering measurements, the neutrons are passed through a moderator. The moderator is composed of small hydrogen-containing molecules such as methane or water. Repeated collisions with hydrogen (which has a large scattering cross-section) transfer the excess energy from the neutrons. The pulsed neutrons from spallation sources such as ISIS are analysed using time of flight (energy dispersive) techniques. The detectors are at a fixed scattering angle and the time of flight for the neutrons is measured. This corresponds to the energy and so the wavelength of the neutrons. The wave nature of neutrons is described by the de Broglie relation which defines the wavelength from the momentum of a free particle mv (where m is the mass, v is the velocity). Bragg's law can be modified as shown in Equation 2.5:

$$2d\sin\theta = n\lambda = n\frac{h}{mv} = n\frac{h}{m}\frac{t}{L}$$

Equation 2.5

where h is Planck's constant; t is the time of flight and L is the length of the flight path. The resolution of a time of flight diffractometer therefore depends on three major components: an angular uncertainty ($\Delta\theta$), and timing uncertainty (Δt) and a pathlength uncertainty (ΔL), as shown in Equation 2.6.

$$\frac{\Delta d}{d} = \left[\Delta\theta^2\cot^2\theta + \left(\frac{\Delta t}{t}\right)^2 + \left(\frac{\Delta L}{L}\right)^2\right]^{\frac{1}{2}}$$

Equation 2.6

The angular uncertainty is dependent on cot θ, which is equal to zero for $\theta = 90^{\circ}$. Thus the resolution is highest for detector banks close to $2\theta = 180^{\circ}$.

2.3.2.2.1. HRPD at ISIS

HRPD, the High Resolution Powder Diffractometer, is situated almost 100m from the ISIS target.[88] The long neutron flight path minimises the timing and pathlength uncertainty in Equation 2.6, maximising the achievable resolution. The ^{3}He and ZnS scintillator detectors on HRPD are separated into three banks. The backscattering bank at $160^{\circ} < 2\theta < 176^{\circ}$ provides the highest resolution ($\Delta d/d = 4\times10^{-4}$). The low angle bank ($28^{\circ} < 2\theta < 32^{\circ}$) covers a wide *d*-spacing range. The 90° bank at $87^{\circ} < 2\theta < 93^{\circ}$ is intermediate between the two.

2.3.2.2.2. Polaris at ISIS

The Polaris instrument is a medium resolution, high intensity diffractometer, using an ambient temperature water moderator.[89] There are a total of 434 ^{3}He and ZnS scintillator detectors arranged into four detector banks. The back scattering bank at $130^{\circ} < 2\theta < 160^{\circ}$ provides the highest resolution ($\Delta d/d = 5\times10^{-3}$), the 90° bank at $83^{\circ} < 2\theta < 97^{\circ}$ the greatest intensity, and the low angle ($28^{\circ} < 2\theta < 42^{\circ}$) and long *d*-spacing ($13^{\circ} < 2\theta < 15^{\circ}$) banks provide a wide *d*-spacing range (0.5-8.15 and 0.5-21.0 Å respectively). Data collected from the long *d*-spacing bank were not used in this work. A schematic of the Polaris diffractometer is shown in Figure 2.4.

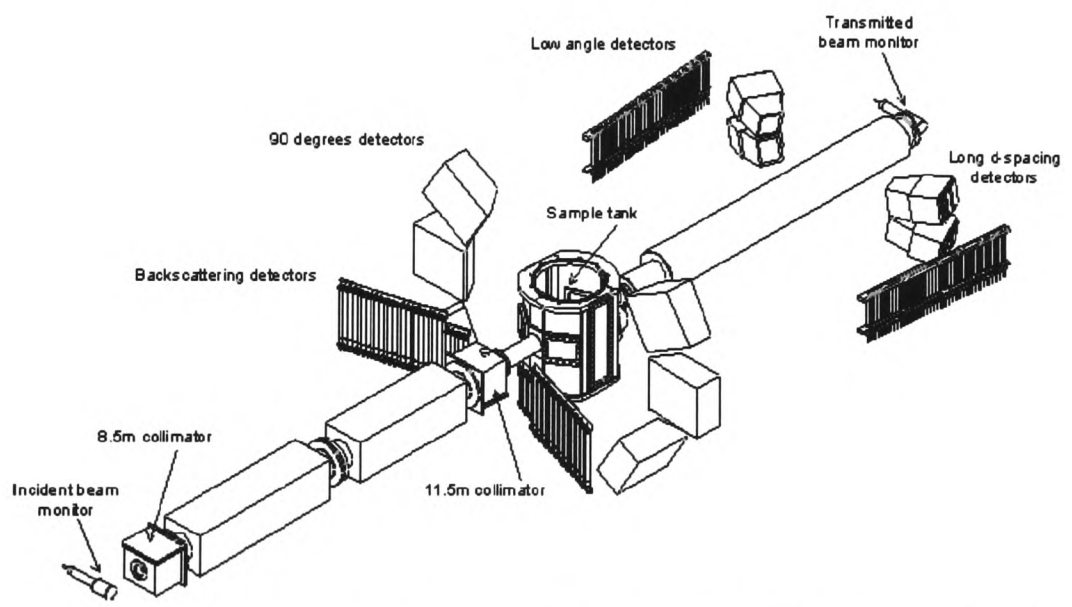


Figure 2.4 Schematic representation of the Polaris diffractometer. (Figure reproduced from reference [89]).

Samples were loaded into vanadium cans. Cans containing air-sensitive samples were sealed using indium wire for measurements carried out at ambient or low temperatures, and using a copper gasket for measurements carried out at higher temperatures.

2.3.3. Electron diffraction

The interaction of electrons with matter is very strong. Incident electrons are diffracted by periodic variations in potential within a crystal. This gives a high scattering efficiency and means that electron diffraction can be carried out on extremely small samples, such as individual crystallites. Additionally, the short wavelength of electrons achieves a high resolution. Thus electron diffraction is particularly useful for finding short-range order and cell expansions.

A JEOL JEM-2000FX electron microscope was used to collect data. The sample was prepared by mixing a small amount with methanol or chloroform to create a suspension. A drop of this was pipetted onto a carbon coated copper grid, which was inserted into the microscope. The electrons are accelerated towards the sample using a large voltage (200 kV) with a beam current of ~ 118 μA. The beam is focused using electric or magnetic fields. Electron diffraction patterns show a two-dimensional section of reciprocal lattice points. This contains information that would be missing if it were compressed to one-dimension (as in X-ray powder diffraction). The *d*-spacings (d_{hkl}) can be calculated using the following formula:

$$d_{hkl} = \frac{\lambda L}{R}$$

Equation 2.7

where λL is the camera constant (obtained by taking a silicon standard measurement) and R is the distance between centre spot and diffracted spot.

Further high resolution electron diffraction data were collected by Dr. Joke Hadermann at the University of Antwerp.

2.4. Structural Analysis

All neutron and X-ray diffraction data presented were analysed using the Rietveld method of profile refinement.[90] The use of diffraction profiles enables maximal information to be extracted from powder diffraction data and minimises the problems caused by reflection overlap (especially important in low symmetry crystal structures), d_{hkl} degeneracy and poor instrumental resolution.

The Rietveld method uses a least squares optimisation procedure where the difference between observed and calculated diffraction profiles is minimised.[91] The residual, S, in Equation 2.8 is minimised by adjusting I_C, the calculated profile intensity (which is based on Equation 2.2 and Equation 2.3).

$$S = \sum w_i (I_O - I_C)^2$$

Equation 2.8

I_O represents the observed profile intensity and w_i the weighing factor. The weighing factor ensures that the entire profile is fitted, not just the most intense peaks.

2.4.1. Peak shapes

The Rietveld method models the diffraction profile as a sum of a background function and the peak functions of each individual reflection. The peak shape functions describing individual reflections can be defined using peak width parameters. The peak width is dependent on three main factors.

Each reflection has an intrinsic width or Darwin width. This is a consequence of the uncertainty principle. Diffraction of radiation within a crystal requires the photon (or neutron) be restricted to a small volume. The uncertainty in the momentum (and therefore the wavelength) produces a diffraction peak with a finite width. The intrinsic peak width is generally negligible compared to other factors.

Peak widths may be increased by instrumental factors, such as geometric inaccuracies in the diffraction set up or spectral dispersion of the radiation. If the radiation is monochromated by diffraction through a crystal the wavelength profile is limited by the Darwin width of the monochromator. The Rietveld method was developed assuming reflections had a Gaussian peak shape, corrected for asymmetry, which accounts for instrumental peak broadening.

The Gaussian profile function is inaccurate, as peak broadening also occurs because of structural imperfections in the sample. These can include the dimensions of the crystallographic domains, microstrain and stacking faults. Peak broadening due to sample effects is described using a Lorentzian function. The overall peak shape is described by a pseudo-Voigt function, a linear combination of the Gaussian and Lorentzian functions as shown in Equation 2.9.[91, 92] A mixing parameter, η, determines the optimal contribution required from the Gaussian and Lorentzian components to fit the observed profile.[93]

$$V(\Delta T) = \eta\, L(\Delta T, \Gamma) + (1-\eta)\, G(\Delta T, \Gamma)$$

Equation 2.9

2.4.2. Rietveld Refinement

The Rietveld method was applied via the use of the GSAS suite of programs.[94] These were used to analyse X-ray and neutron powder diffraction data from both angular dispersive and time of flight sources. GSAS provides several different profile functions for modelling peak shapes. The second profile function was used to model constant wavelength data. This employs an integration of the pseudo-Voigt function discussed above.

The Gaussian and Lorentzian functions used to describe the peak profiles are dependent on the full width at a half maximum (FWHM), Γ, of the reflection. This is a function of the Gaussian FWHM (Γ_G) and the Lorentzian coefficient (γ). The Gaussian FWHM for diffraction using a constant wavelength is defined using the profile parameters U, V and W which account for instrumental peak broadening. An additional term, P, represents a contribution due to crystallite broadening (Scherrer broadening).

$$\Gamma_G = \sqrt{U\tan^2\theta + V\tan\theta + W + \frac{P}{\cos^2\theta}}$$

Equation 2.10

The Lorentzian parameter is defined for constant wavelength sources in Equation 2.11. The definition uses profile parameters representing Scherrer particle size broadening (X) and microstrain broadening (Y). Additional profile parameters account for the anisotropy of the sample with respect to particle size (X_e) or strain (Y_e). These parameters broaden reflections depending on the angle (ø) between a defined anisotropic broadening axis and the normal of the lattice planes giving rise to diffraction. An empirical expression of the microstrain anisotropy is given by γ_L.

$$\gamma = \left(Y + Y_e\cos\phi + \gamma_L d^2\right)\tan\theta + \frac{\left(X + X_e\cos\phi\right)}{\cos\theta}$$

Equation 2.11

An additional type of broadening can be included by defining a sublattice. For the reflections which lie on the sublattice, the anisotropic microstrain parameter, (X_e) is replaced by a new parameter, X_s. This allows the modelling of diffraction data collected from samples containing stacking faults. These faults will result in a set of sharp reflections due to diffraction from the sub-lattice, which are unaffected by the stacking fault. Reflections which do not lie on the sub-lattice will be broader.

Profile function 3 was chosen for refinement against the majority of time of flight experiments. This convolutes the pseudo-Voigt function in Equation 2.9 with a pair of back-to-back exponential functions. The Gaussian variance (σ^2) and Lorentzian parameter for time of flight experiments are defined in Equation 2.12 and Equation 2.13 respectively.

$$\sigma^2 = \sigma_0{}^2 + \sigma_1{}^2 d^2 + \sigma_2{}^2 d^4$$

Equation 2.12

$$\gamma = \gamma_0 + \left(\gamma_1 + \gamma_{1e}\cos\varphi\right)d + \left(\gamma_2 + \gamma_{2e}\cos\varphi\right)d^2 + \gamma_L$$

Equation 2.13

where σ_0, σ_1 and σ_2 are the Gaussian parameters; γ_1 and γ_{1e} account for microstrain broadening and γ_2 and γ_{2e} account for Scherrer broadening.

2.4.3. Interpretation of profile coefficients

As the peak shape functions are based on physical phenomena, the parameters which define the functions often have a physical meaning. As discussed above, the Lorentzian profile coefficients are dependent on both particle size and strain in the sample. This relationship allows estimations to be made of the microstrain and coherent particle size of the measured sample. The use of anisotropic profile parameters allows the microstrain and coherent particle size to be separated into that parallel and perpendicular to the anisotropic broadening axis. The relationships for estimating the microstrain are defined in Equation 2.14 and Equation 2.15. The relationship for constant wavelength data includes a term Y_i which represents an instrumental contribution to be subtracted. The time of flight relationship is dependent on the diffractometer constant C.[91]

$$S_{\parallel} = \frac{1}{C}(\gamma_1 + \gamma_{1e})100\% = \frac{\pi}{18000}(Y + Y_e - Y_i)100\%$$

Equation 2.14

$$S_{\perp} = \frac{1}{C}\gamma_1 100\% = \frac{\pi}{18000}(Y - Y_i)100\%$$

Equation 2.15

The anisotropic particle size can be estimated by similar relationships, using the alternative set of Lorentzian parameters. K is the Scherrer constant, related to crystal shape. This can generally be approximated as unity.[85]

$$p_{\parallel} = \frac{CK}{\gamma_2 + \gamma_{2e}} = \frac{18000K\lambda}{\pi(X + X_e)}$$

Equation 2.16

$$p_{\perp} = \frac{CK}{\gamma_2} = \frac{18000K\lambda}{\pi X}$$

Equation 2.17

2.4.4. Fitting statistics

The Rietveld method is designed to find the minimum residual for Equation 2.8, where the calculated pattern is the best possible match to the observed pattern. The quality of fit is clearly dependent on the model from which the calculated pattern is generated and so in order to compare different models it is necessary to have values which monitor the goodness of fit. This

can be measured using several functions. The profile Rp and the weighed profile wRp are expressed as percentages, dependent on the difference between the observed (y_O) and the calculated (y_C) intensity of each data point:

$$\mathrm{Rp} = 100 \times \frac{\sum |y_O - y_C|}{\sum y_O}$$

Equation 2.18

$$\mathrm{wRp} = 100 \times \left(\frac{\sum w (y_O - y_C)^2}{\sum w y_O^{\,2}} \right)^{½}$$

Equation 2.19

The reduced χ^2 is defined as:

$$\chi^2 = \frac{\sum w (y_O - y_C)^2}{(N_{obs} - N_{\mathrm{var}})}$$

Equation 2.20

where N_{obs} is the number of observables and N_{var} is the number of variables.

2.5. Bond Valence Sums

Bond valence sums provide a method of relating the valence of an ion to the bond lengths of the coordination sphere around it.[95-97] The valence, v_{ij} of a bond between two atoms i and j is defined such that the valence V_i of atom i is equal to the sum of the bond valences to atoms j in the coordination sphere (Equation 2.21).

$$V_i = \sum_j v_{ij} = \sum_j \exp\left(\frac{r_0' - r_{ij}}{B} \right)$$

Equation 2.21

The bond valence of a bond between two atoms i and j is inversely correlated with the bond length, r_{ij}. It is also dependent on a constant B (which is empirically determined and has a value of 0.37) and the nature of the atoms i and j involved in the bond. Each pair of atoms has a bond valence parameter, r_0, which describes the length of a bond of unit valence. Bond valence parameters have been empirically determined from comparison of known compounds involving the same ion pairs. Bond valence sums can therefore be considered to be a comparison of the bond lengths in a given coordination sphere with those of other known

phases involving the same ions. All parameters used in this work were taken from the paper by Brese and O'Keefe.[95]

2.6. *DC SQUID magnetometry*

Magnetometry characterises properties dependent on the magnetic moments associated with the spin and orbital motions of electrons. The most sensitive magnetometers contain a *S*uperconducting *Q*uantum *I*nterference *D*evice (SQUID), consisting of a closed superconducting loop with two Josephson junctions in the path taken by the current (Figure 2.5).

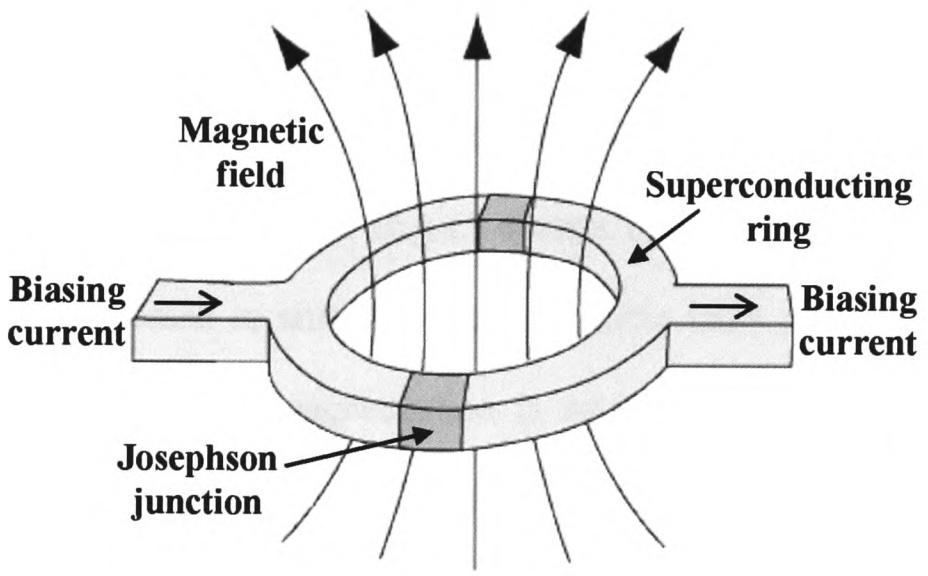


Figure 2.5 Schematic of SQUID (edited from diagram extracted from reference [98]).

A measurement is performed by moving the sample through superconducting detections coils at the centre of a superconducting magnet capable of generating fields up to 50000 Oe. As the sample rod moves through the detection coils, the magnetic moment of the sample induces a persistent electric current in the superconducting detection circuit. The detection coils couple inductively to the SQUID, which functions as an extremely sensitive current to voltage converter. When the current is greater then the critical current the ring no longer has zero resistance and a voltage is produced. Quantum interference of the wavefunctions at the two Josephson junctions produces oscillations in the critical current. Thus small changes in the magnetic field alter the critical current and hence the voltage across the ring. The instrument is

configured such that variations in the voltage output are proportional to the magnetic moment of the sample.

The magnetic data in this thesis were collected using either a Quantum Design MPMS-5 or MPMS XL magnetometer. Accurately weighted samples were contained in a gelatine capsule and mounted in a plastic drinking straw. Empty capsules were placed on either side to eliminate any background contribution from the sample capsule. The straw was attached to the sample rod using Kapton tape. Scans were typically performed four times both to improve the signal to noise ratio and obtain a value for the error.

2.6.1. Magnetic measurements and units

The output of the magnetometer is the magnetic moment, m, measured in electromagnetic units (emu) in the centimetre gram second (c.g.s.) system of units. This is easily converted into magnetisation, M, (expressed in units of electromagnetic units per mole) by division by the number of moles present. The magnetisation is related to the applied magnetic field, H, (measured in oersted (Oe) in c.g.s. units) and the flux density (B, measured in gauss (G) in c.g.s. units) as follows:

$$B = H + 4\pi M$$

Equation 2.22

Two types of magnetic measurement were carried out. The magnetic moment of a sample was measured as a function of temperature in the range $5 \leq T\ (K) \leq 300$ under an applied field of H = 100 Oe after cooling without an applied field and again after cooling in the measuring field. The magnetic data are presented in the form of molar magnetic susceptibilities (χ_{mol}) defined as:

$$\chi_{mol} = \frac{M}{H}$$

Equation 2.23

The magnetisation was also measured at a constant temperature as a function of field in the range $-50000 \leq H\ (Oe) \leq 50000$. These magnetisation-field isotherms were carried out at 6K

and 300K. Measurements at additional temperatures were carried out as required after inspection of the magnetisation vs. temperature data.

2.6.2. Magnetic behaviour

For a perfect paramagnet, the susceptibility is inversely proportional to the temperature. Paramagnetic susceptibilities can be modelled using the Curie law:

$$\chi_{mol} = \frac{Ng^2\mu_B^2 J(J+1)}{3k_B T} = \frac{C}{T}$$

Equation 2.24

where N is the number of atoms; g is the Landé factor; μ_B is the Bohr magneton; J is the angular momentum of the electrons; k_B is the Boltzmann constant; and C is the Curie constant. C is therefore given by:

$$C = \frac{Ng^2\mu_B^2 J(J+1)}{3k_B} \approx \frac{1}{8}\mu_{eff}^2$$

Equation 2.25

where μ_{eff} is the effective magnetic moment.

The Curie law is rarely obeyed as few magnetic systems are perfectly paramagnetic. Some interatomic interactions are expected, and can be accounted for using the Curie-Weiss law:

$$\chi_{mol} = \frac{C}{T-\theta} + K$$

Equation 2.26

where θ is the Weiss constant. A negative Weiss constant indicates the dominant magnetic interactions are antiferromagnetic, a positive value that they are ferromagnetic. A temperature independent constant K is sometimes included. K accounts for temperature-independent paramagnetism (TIP), which is caused by the mixing of excited states into the ground state.

Although the Weiss constant takes weak interatomic interactions into account, for systems with strong magnetic interactions the Curie-Weiss model is not valid. Strong magnetic interactions occur due to quantum mechanical exchange. If two orbitals containing single unpaired electrons overlap, the exchange interaction between the electrons favours an antiferromagnetic

interaction. This type of exchange is known as direct exchange. The strength of the interaction depends on the degree of orbital overlap, and so diminishes rapidly with the separation of the atoms. A longer range exchange coupling may occur between the metal ions through an indirect pathway involving the intervening anion (Figure 2.6). This is type of magnetic coupling is known as superexchange. The magnitude and sign of the superexchange interaction depends on the degree of overlap of the metal and anion orbitals, as well as on the geometry of the M-X-M bond and the number of electrons in the metal orbital. The sign of the interaction can be predicted using the Goodenough-Kanamori-Anderson rules.[99]

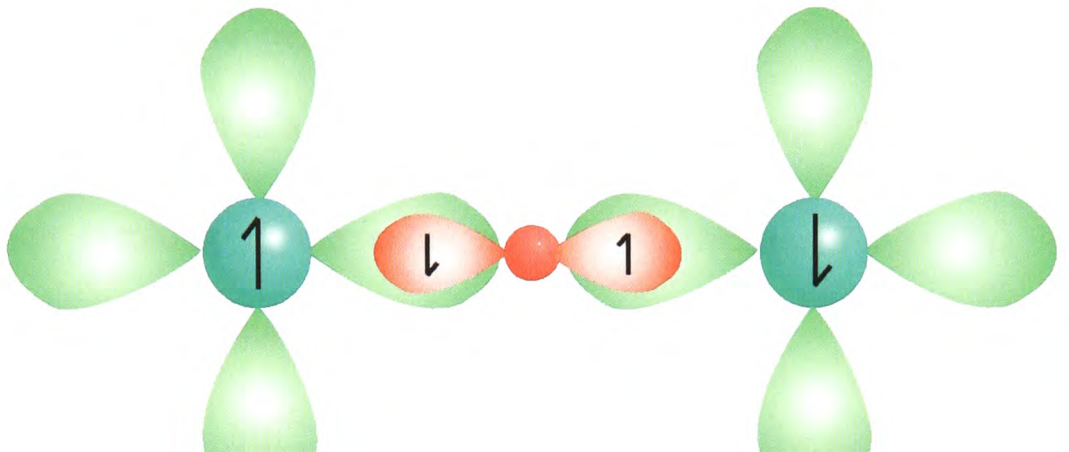


Figure 2.6 Superexchange interaction across a 180° M-X-M bond. The interaction is antiferromagnetic for two singly occupied metal orbitals.

2.7. *Iodiometric titrations*

Chemical analysis using iodiometric titrations relies on the liberation of iodine in solution. The iodine is typically liberated from KI due to oxidation by a transition metal. The iodine is removed by a precise volume of thiosulphate $S_2O_3^{2-}$ solution, which is standardised against a known concentration of KIO_3. This technique establishes the oxidation state of the transition metal cation by calculating the change in oxidation state between the starting transition metal ion and the stable ion in aqueous solution.

Approximately 40mg of well-ground powdered sample was placed in a three-necked, round-bottomed flask. For air-sensitive samples, this took place in a glove box and the flask was sealed prior to the start of the titration. The flask was flushed with argon before to the addition of the solutions, and a flow of argon over the solution was maintained during the titration.

Approximately 10ml of a solution of ~ 16% HCl was added to the flask, along with ~ 0.2g (an excess) of KI. In order to minimise errors, titrations against previously standardised thiosulphate were begun immediately after the additions of the solutions. At the approach of the end-point (corresponding to a loss of yellow colouration in the sample), a few drops of starch were added.

In order to ensure the accuracy of the titrations, the concentration of the thiosulphate solution was adjusted such that titres were typically between 15 – 35 cm^3. At least three titrations were performed for each sample. If the results of the three titrations showed significant variations, three more titrations were performed. If the inconsistency in the results was maintained, iodiometry was abandoned as a viable technique for calculating the manganese oxidation state.

The calculation resulting in the value of x for a compound $AMnO_{3-x}$ was obtained by considering the following relations:

$$Mn^{(4-2x)+} + (2-2x)I^- \rightarrow Mn^{2+} + (1-x)I_2$$

Equation 2.27

$$I_2 + 2S_2O_3^{2-} \rightarrow 2I^- + S_4O_6^{2-}$$

Equation 2.28

The relationship between the oxidation state of the manganese and the number of moles of iodine produced can be equated with the relationship describing the number of moles of thiosulphate required to reduce the iodine:

$$(2-2x) \times \text{Moles Mn} = \frac{(2-2x) \times m}{RMM(AMnO_{3-x})} = 2 \times \text{Moles } I_2 = \text{Moles } S_2O_3^{2-} = C \times V$$

Equation 2.29

where m is the mass of the sample; C is the concentration of the thiosulphate and V is the volume used in the titration (in litres). By noting that RMM ($AMnO_{3-x}$) = RMM ($AMnO_3$) - (x × AM(O)), the equation can be rearranged to find x.

$$x = \frac{(RMM(AMnO_3) \times C \times V) - 2m}{(AM(O) \times C \times V) - 2m}$$

Equation 2.30

The equations for compounds not of the form $AMnO_{3-x}$ can be adjusted accordingly.

2.8. Thermogravimetric analysis

Thermogravimetric analysis was also carried out to identify the chemical compositions. This technique measures the mass change on heating under a given atmosphere. If the final composition is known, the initial composition can be calculated from Equation 2.31 and vice versa.

$$\frac{Mass(initial)}{RMM(initial)} = Moles = \frac{Mass(final)}{RMM(final)}$$

Equation 2.31

Samples were generally oxidised, with the extent of the mass change used to calculate the oxygen uptake. Samples of typically 50 mg were heated under flowing oxygen at a rate of 10 °C min^{-1} to a final or holding temperature. This temperature was held for approximately 2 hours or until the mass gain reached a plateau. Precise details of the measurement programs will be given in the relevant chapters.

In order for thermogravimetric analysis to be used to identify the actual composition of samples, it is necessary to assume that the final product is fully oxidised. If this assumption is not valid, thermogravimetric analysis merely sets an upper bound on the range of compositions available. A problem with thermogravimetric analysis is the error introduced by the gas buoyancy. Heating the sample reduces the density of the surrounding gas which can cause the appearance of mass loss for a sample of constant mass. This can be accounted for by correcting the data according to a test measurement carried out on a constant mass.

Chapter 3: Synthesis of $BaMnO_{3-x}$ phases

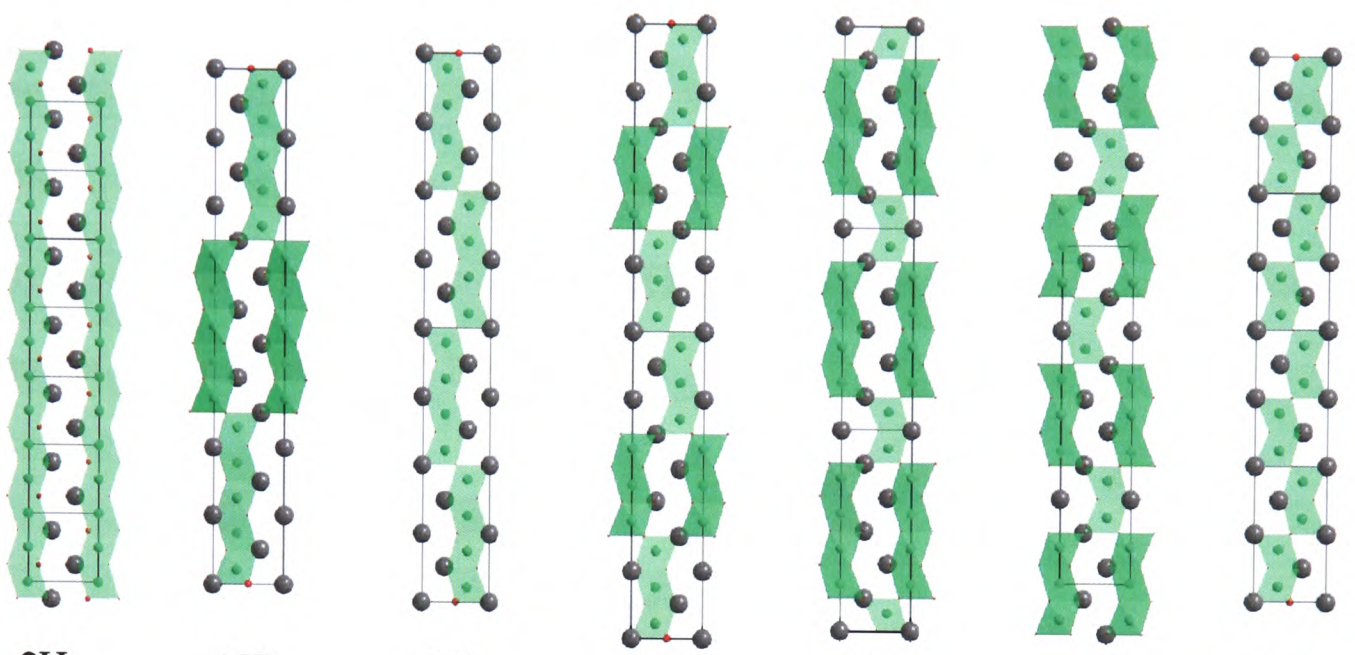
3.1. *Introduction*

$BaMnO_{3-x}$ ($x < 0.5$) phases adopt hexagonal perovskite structures. As discussed in Section 1.1, hexagonal perovskite structures occur when the tolerance factor (t) is greater than 1, in order to accommodate large A site cations in the presence of small B site cations. The adoption of hexagonal perovskite structures by $BaMnO_{3-x}$ can thus be rationalised by the large t, a necessary result of the combination of the large radius of barium radius ($r_{Ba(II)}$, 12 coordinate = 1.61 Å) and small radius of manganese ($r_{Mn(IV)}$, 6 coordinate = 0.53 Å or $r_{Mn(III)}$, 6 coordinate, high spin = 0.645 Å).[82] Section 1.1 described how the relative proportion of cubic (apex-sharing) to hexagonal (face-sharing) layers in the stacking sequence of hexagonal perovskite structures is determined by the extent of the deviation of t above 1. The closer t is to 1, the greater the proportion of cubic layers. The tolerance factor of $BaMnO_{3-x}$ is dependent on the average Mn-O bond length. Varying the ratio of Mn(IV) to Mn(III) (varying x) changes the average Mn-O bond length, therefore oxidation or reduction can be used to control the ratio of cubic to hexagonal layers.

The range of stacking sequences available is largely determined by the range of achievable tolerance factors. As there is a relatively large difference between the Mn(III)-O bond length and the Mn(IV)-O bond length, varying the ratio of Mn(III) to Mn(IV) results in a wide range of tolerance factors. Therefore $BaMnO_{3-x}$ phases can adopt a wide range of stacking sequences with different ratios of cubic to hexagonal layers. The stacking sequences of $BaMnO_{3-x}$ range from 2H-$BaMnO_3$ (no cubic layers) to 4H-$BaMnO_{3-x}$ (50% cubic layers).

The first reported $BaMnO_{3-x}$ phase was the fully oxidised end member, 2H-$BaMnO_3$. 2H-$BaMnO_3$ was synthesised by Gushee, Katz and Ward in 1957.[21] This phase was later characterised by Hardy, along with the most reduced end member, 4H-$BaMnO_{3-x}$ (2 or *ch* stacking sequence).[20] In 1970, Chamberland used a high pressure synthesis route which

resulted in the formation of 2H-$BaMnO_{3.00}$, 4H-$BaMnO_{2.85}$, and a new 9R-$BaMnO_{3.00}$ phase with an intermediate stacking sequence (3 or *chh*).[100] Following this, a systematic investigation into the $BaMnO_{3-x}$ phase diagram was performed by Negas and Roth in 1971.[30] Although they could not prepare the 9R-$BaMnO_{3.00}$ phase reported by Chamberland, they describe the preparation and phase relations of a number of other $BaMnO_{3-x}$ phases with stacking sequences intermediate between 2H and 4H. The reported stacking sequences of $BaMnO_{3-x}$ are shown in Figure 3.1.



2H	15R	8H	9R	6L	10H	4H
0% cubic	20% cubic	25% cubic	33% cubic	33% cubic	40% cubic	50% cubic
∞	5 (5,5,5)	4 (4,4)	3 (3,3,3)	2,4 (2,4)	2,3 (2,3,2,3)	2 (2,2)

Figure 3.1 Reported stacking sequences in the $BaMnO_{3-x}$ series, arranged according to the proportion of cubic layers. The percentage of cubic layers and stacking sequence is also shown. In parentheses is the stacking sequence within the unit cell.[30, 100]

Although the stacking sequences of phases in the $BaMnO_{3-x}$ series have previously been reported, many questions about the series remain unanswered. Despite the extensive synthetic study by Negas and Roth, they were unable to synthesise the 9R-$BaMnO_3$ phase reported by Chamberland. This raises the question of how the synthetic technique affects the stacking sequence adopted. Moreover, the location of the oxide vacancies within the structures has not been identified for any of the $BaMnO_{3-x}$ phases. Most importantly, with the exception of the end member, 2H-$BaMnO_3$, the physical properties of phases in the $BaMnO_{3-x}$ series have never been reported.

This work aims to study all phases in the $BaMnO_{3-x}$ system in order to gain a better understanding of the anion vacancy locations and magnetic ordering in these phases. The variation in magnetic properties with stacking sequence is also of interest. The different $BaMnO_{3-x}$ phases adopt a wide range of stacking sequences with near-identical chemical compositions, providing an ideal series in which to investigate the structure-property relationships of hexagonal perovskites.

3.2. *Thermodynamic considerations*

Hexagonal perovskite structures contain a certain proportion of hexagonal AO_3 layers which connect BO_6 octahedra by face-sharing. 2H-$BaMnO_{3.00}$ is necessarily an end member of the $BaMnO_{3-x}$ series as it contains only hexagonal layers. The composition $BaMnO_{3.00}$ favours a stacking sequence with a high proportion of hexagonal layers due to the large tolerance factor, a result of the small Mn(IV)-O bond length.

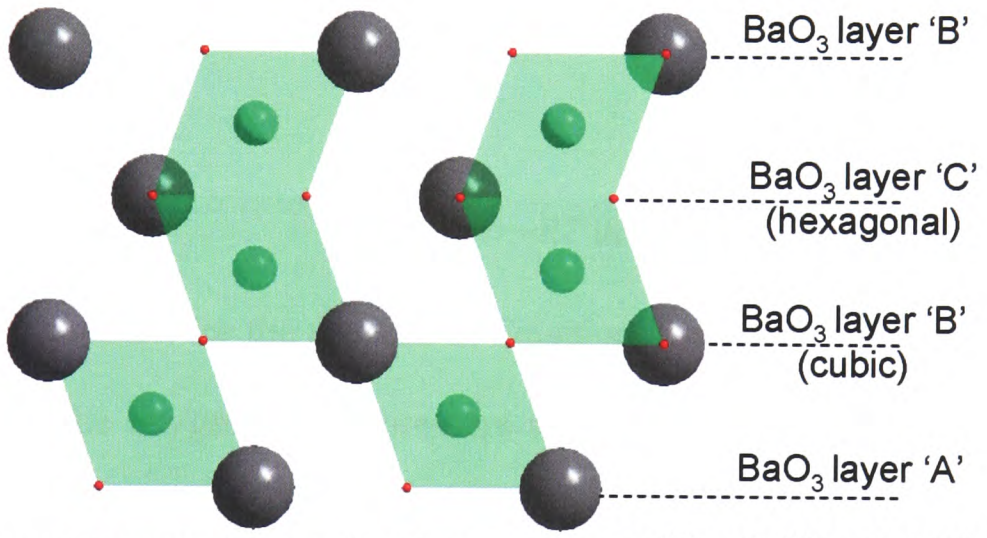


Figure 3.2 Cubic and hexagonal layers in a hexagonal perovskite stacking sequence. The two layers adjacent to a hexagonal layer are identical. The two layers adjacent to a cubic layer are displaced from one another in the *ab* plane by by x' = x + ⅓, y' = y - ⅓.

The remaining $BaMnO_{3-x}$ phases contain cubic layers in the stacking sequence. In order to introduce cubic layers into the 2H stacking sequence, the tolerance factor must be reduced. This can be achieved by the introduction of oxide vacancies, which reduce the manganese oxidation state and so increase the average manganese-oxygen bond length.

The chemical reaction leading to a reduced manganese oxidation state is shown in Equation 3.1. The extent of the reduction can be controlled by adjusting the Gibbs free energy (ΔG) of

this reaction. The dissociation of oxygen gas is entropically favourable and so the forward reaction of Equation 3.1 which produces free oxygen can be favoured by raising the reaction temperature (Equation 3.2).

$$BaMnO_{3.00} \rightleftharpoons BaMnO_{3-x} + \left(\frac{x}{2}\right)O_2$$

Equation 3.1

$$\Delta G = \Delta H - T\Delta S$$

Equation 3.2

At relatively low temperatures ($\leq$ 1000°C) many solid state reactions which involve a large structural change are extremely slow, due to the need for long-range ion diffusion. The reaction rate can be increased by raising the temperature, but as this also changes the Gibbs free energy the extent of reduction (x) is also likely to change.

In order to raise the temperature without altering the reaction product, the change in the Gibbs free energy must be offset. Equation 3.3 shows that the Gibbs free energy is dependent on the equilibrium constant (K) of the reaction in Equation 3.1, as well as the temperature (T) at which the reaction is carried out.

$$\Delta G^\circ = -RT \ln K$$

Equation 3.3

The equilibrium constant for the reaction in Equation 3.1 is affected by the partial pressure of oxygen. Altering the oxygen partial pressure therefore adjusts the Gibbs free energy of the reaction independently of the temperature, allowing a balance to be struck between the temperature and the extent of reduction. This allows the kinetic benefit of a high reaction temperature without altering the extent of reduction.

The manganese oxidation state (and so the tolerance factor) is maximised by low temperatures and high partial pressures of oxygen. The tolerance factor can be reduced by either increasing the temperature or lowering the partial pressure of oxygen. Alternatively, t can be maintained on firing under a higher temperature by raising the partial pressure of oxygen.

3.3. *Experimental*

3.3.1. Initial synthesis of $BaMnO_{3-x}$

2H-$BaMnO_3$ was prepared from $BaCO_3$ (99.997%, Alfa Aesar) and MnO_2 (99.999%, Alfa Aesar) by a standard ceramic route as described by Cussen and Battle.[4] These were mixed in the appropriate stoichiometric ratio in an agate mortar and then heated at 950°C in air to decompose the carbonate. The resulting powder was reground and pressed into 2-3g, 13 mm pellets at 5 tons of pressure before firing at higher temperatures. A relatively low firing temperature (1000°C) was utilised in the 2H synthesis in order to ensure that the final product was fully oxygen stoichiometric. However, this low temperature results in a slow rate of reaction, and a relatively long firing time was required to ensure the reaction was complete. Samples were fired at 1000°C for at least five periods of 3 days each and were reground and repelleted between heating periods. Reaction progress was monitored using X-ray powder diffraction.

4H-$BaMnO_{3-x}$ samples were also prepared directly from $BaCO_3$ and MnO_2. These were thoroughly mixed and decarbonated by firing at 950°C in air. Pellets of decarbonated starting materials were then fired under flowing argon at 1300-1350°C for two periods of two days each. Phase purity was confirmed using X-ray powder diffraction.

3.3.2. Altering the stacking sequence

The use of preformed 2H-$BaMnO_3$ eliminates the requirement for long-range cation diffusion and the reaction is reduced to a simple equilibration with the oxygen in the atmosphere (as shown in Equation 3.1), accompanied by structural rearrangement. The remaining $BaMnO_{3-x}$ phases were synthesised from preformed 2H-$BaMnO_3$ in order to increase the reaction rate. As the cations were already evenly distributed throughout the sample in these cases, samples were generally fired as a loose powder in order to speed the equilibration with atmospheric oxygen. Samples of 2H-$BaMnO_3$ were fired in oxygen partial pressures in the range $0 < pO_2\ (atm) \leq$

0.33 atm. Reactions under non-atmospheric conditions were carried out in a tube furnace. Oxygen partial pressures in the range 0.1-0.33 atm were achieved by mixing oxygen (99.5%) and argon (99.998%) prior to passing them over samples, using the experimental setup shown in Figure 3.3.

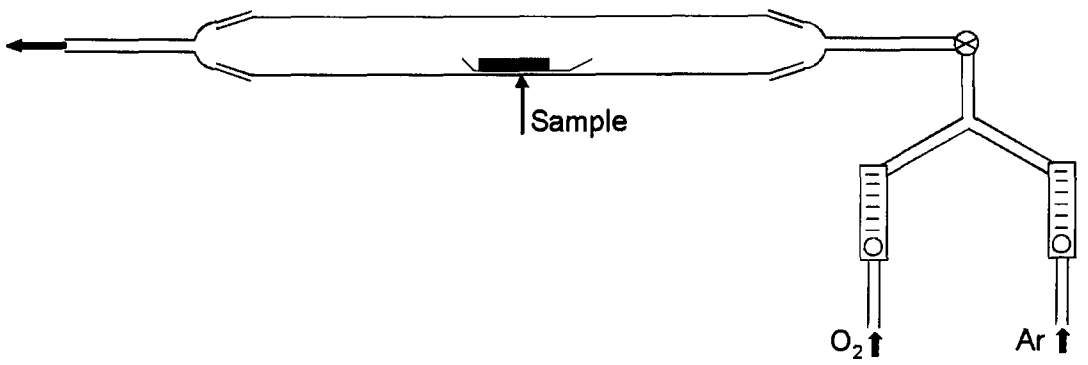


Figure 3.3 Experimental setup of the gas mixing system.

Flow rates of both gases were monitored using flow meters and adjusted to achieve the appropriate oxygen partial pressure. The error associated with adjusting the flow rate was too great to achieve atmospheres of $pO_2 \leq 5\%$ with any degree of accuracy. In order to achieve lower pO_2 atmospheres, a gas flow of 1% (±0.05%) (certified, BOC special gases) oxygen in argon was employed. For still lower pO_2 atmospheres, samples were fired under flowing argon ($pO_2 < 0.5\%$). Gases were typically passed over the sample at a rate of 20-60 cm^3s^{-1}. In all cases, samples were cooled to ambient temperature under the reaction atmosphere.

3.4. Results and discussion

3.4.1. Phase diagram for $BaMnO_{3-x}$

Reactions were carried out between $1200 \leq T\ (°C) \leq 1500$ at oxygen partial pressures of < 0.5% (flowing argon), 1%, 15%, 21% (air), 25%, 30% and 33%. A summary of the reactions performed is shown in the phase diagram in Figure 3.4. Only samples for which the firing time was sufficient to form a single phase sample are shown.

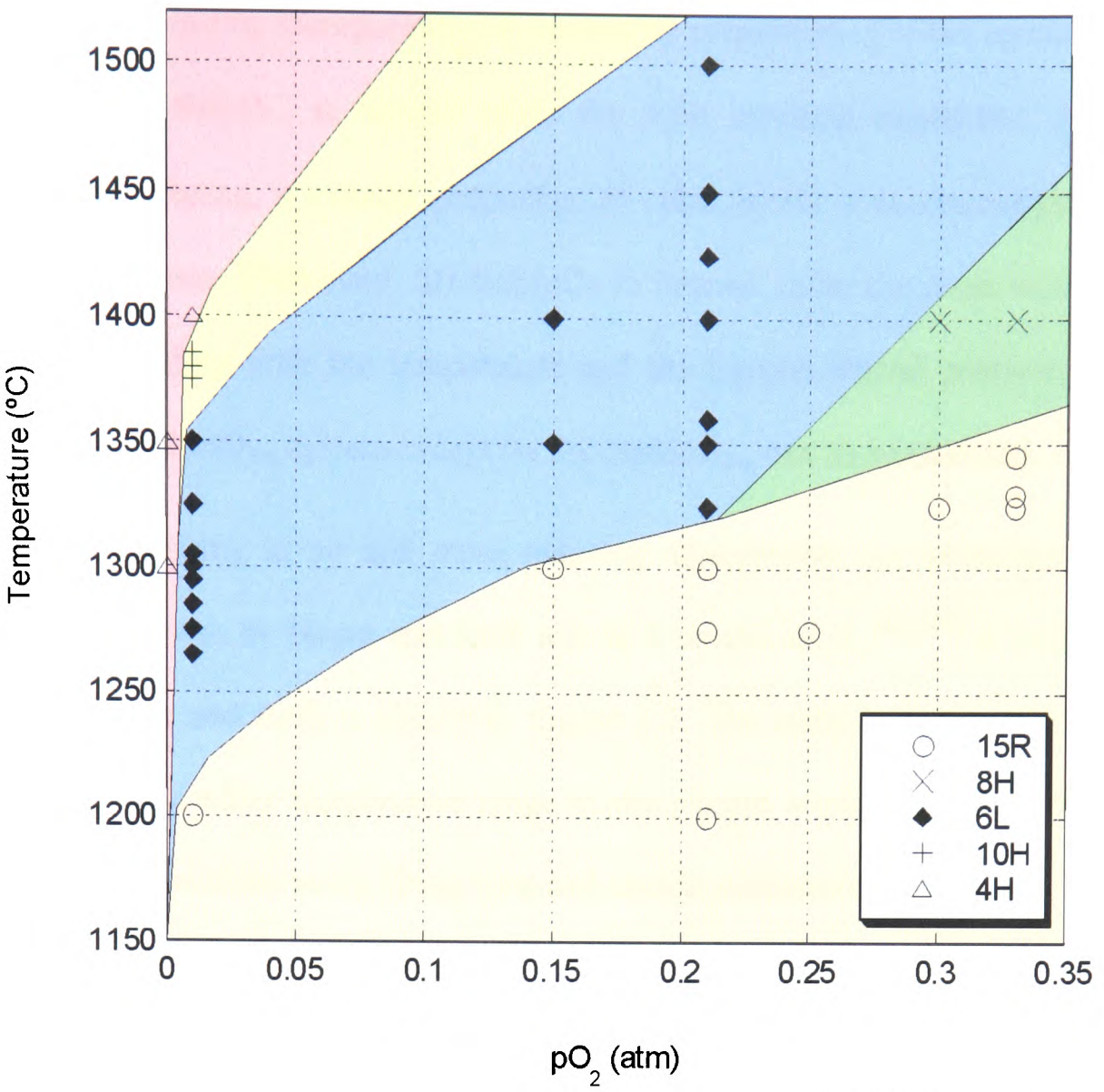


Figure 3.4 Phase diagram for $BaMnO_{3-x}$ phases produced from a 2H-$BaMnO_3$ starting material. The shaded regions represent approximate phase boundaries.

Prolonged heating at T ≥ 1400°C under reducing atmospheres (≤ 1% O_2) resulted in the formation of a purple impurity phase. This was identified from X-ray powder diffraction as $BaAl_2O_4$, formed by the substitution of manganese in the sample with aluminium in the alumina boat. In order to prevent this, the boat was lined with platinum foil. Under these conditions, prolonged heating at T ≥ 1400°C resulted in the formation of 4H-$BaMnO_{3-x}$.

As anticipated on the basis of thermodynamic relations, simultaneously increasing both the temperature and the partial pressure of oxygen in the reaction atmosphere can maintain a constant composition, resulting in similar tolerance factors and so identical stacking sequences. The tolerance factor can be reduced by shifting the equilibrium towards increased reduction of $BaMnO_{3-x}$, either by increasing the temperature at a constant partial pressure of oxygen or reducing the partial pressure of oxygen at a constant temperature. The $BaMnO_{3-x}$ system reacts

to the reduction in *t* by incorporating an increasing proportion of cubic layers into the stacking sequence. 4H-$BaMnO_{3-x}$ is formed under the most reducing conditions. As the conditions become less reducing, a reduced proportion of cubic layers is accommodated in the adopted stacking sequences. Ultimately, 2H-$BaMnO_3$ is formed under the most oxidising conditions. Thus by controlling both the temperature and the oxygen partial pressure, all the reported phases of the $BaMnO_{3-x}$ system except for 9R-$BaMnO_{3-x}$ can be synthesised.

The results on firing in air and more reducing atmospheres are essentially consistent with previous work, both by Negas and Roth and by Uematsu et al..[30, 101] A comparison with the results of Negas and Roth is shown in Figure 3.5. The stability range of 6L-$BaMnO_{3-x}$ was found to cover a wider temperature range in the current work. The differences are probably attributable to variations in the firing time and sample preparation technique.

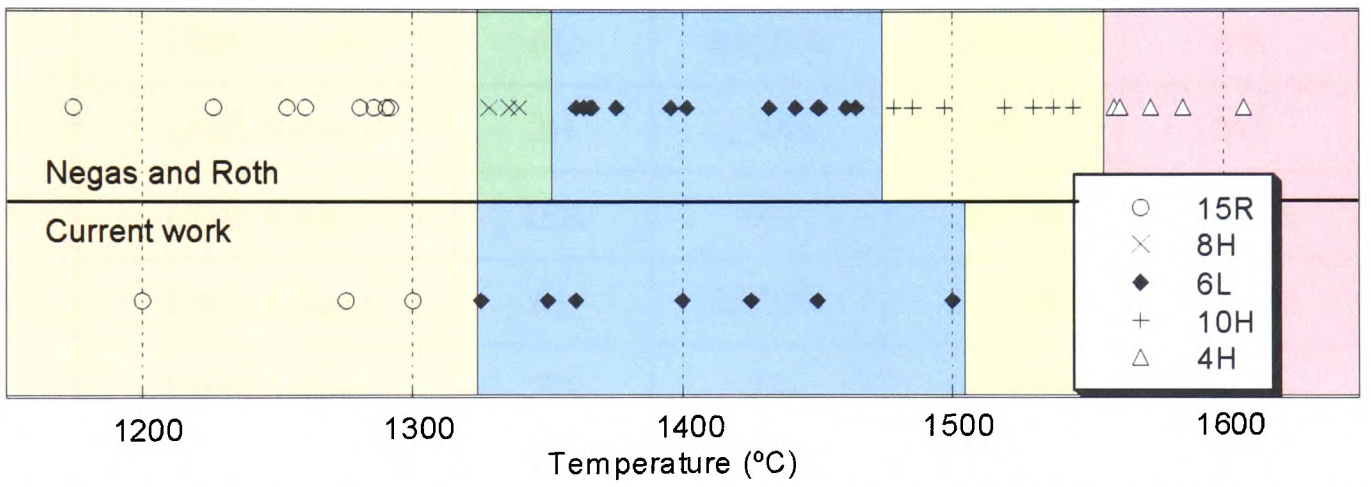


Figure 3.5 Comparison of current results with those of Negas and Roth.[30] All reactions were carried out in air.

The main interest lies in the region of the phase diagram in which 8H-$BaMnO_{3-x}$ can be formed and so the synthesis around this region will be discussed in more detail.

3.4.2. 8H-$BaMnO_{3-x}$

3.4.2.1. Previous work

Negas and Roth found that 8H-$BaMnO_{3-x}$ was the most synthetically challenging member of the $BaMnO_{3-x}$ series. Although 8H-$BaMnO_{3-x}$ was prepared in air in the narrow range $1312 \leq T$ (°C) ≤ 1341, the reaction was very slow.[30] Uematsu et al. also noted the formation of

8H-$BaMnO_{3-x}$ within this temperature range, generally as part of a two phase mixture with 15R-$BaMnO_{3-x}$, although a single phase sample of 8H-$BaMnO_{3-x}$ was reported for T = 1350°C under pO_2 = 0.2 atm.[101] Hydrothermal synthesis techniques can also be used to produce a small proportion of 8H-$BaMnO_3$ in the form of single crystals, although the majority of the sample prepared using this technique forms a microcrystalline powder of 9R-$BaMnO_3$.[102]

3.4.2.2. Attempted synthesis of 8H-$BaMnO_{3-x}$ in air

3.4.2.2.1. Results

Full details of the reactions carried out in air in the range 1300 ≤ T (°C) ≤ 1350 are listed in Table 3.1. The synthetic results are summarised in Figure 3.6.

Temperature (°C), firing time	Structure at start	6L	8H	15R
1350, 5 days	2H	100%	0%	0%
1325, 6 days	6L	87(2)%	13(2)%	0%
1325, 8 days	2H	100%	0%	0%
1320, 6 days	15R	0%	5(2)%	95(2)%
1300, 6 days	6L	19(3)%	58(3)%	23(2)%
1300, 6 days	2H	0%	56(3)%	44(3)%

Table 3.1 Relative proportions of 6L-$BaMnO_{3-x}$, 8H-$BaMnO_{3-x}$ and 15R-$BaMnO_{3-x}$ as a weight fraction of the sample after firing at various temperatures.

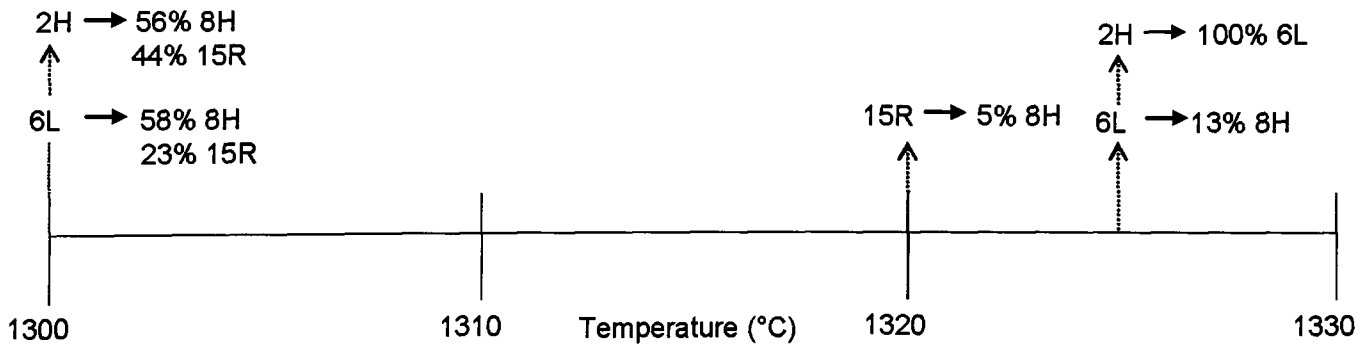


Figure 3.6 Representation of the information in Table 3.1, showing the percentage of the sample which adopts a new stacking sequence on firing at various temperatures.

A single phase 8H-$BaMnO_{3-x}$ sample proved extremely difficult to synthesise in air. Diffraction patterns collected from samples of 15R-$BaMnO_{3-x}$ fired in the reported temperature stability range of 8H-$BaMnO_{3-x}$ (T = 1320°C) showed weak reflections corresponding to

8H-$BaMnO_{3-x}$, but the conversion of 15R-$BaMnO_{3-x}$ to 8H-$BaMnO_{3-x}$ did not proceed to completion. After 6 days of firing, only 5% of a 0.3g 15R-$BaMnO_{3-x}$ sample had undergone the structural change to 8H-$BaMnO_{3-x}$. The behaviour suggests that the formation of 15R-$BaMnO_{3-x}$ kinetically traps the reaction and although it may be possible to prepare 8H-$BaMnO_{3-x}$ from 15R-$BaMnO_{3-x}$, an extremely long firing time would be required. This behaviour is consistent with that reported by Negas and Roth.[30] In order to obtain a phase-pure 8H sample in a realistic time scale, a different route must be employed.

2H-$BaMnO_3$ samples fired at 1300°C in air formed a two phase mixture composed of ~ 56% 8H and ~ 44% 15R-$BaMnO_{3-x}$. Thus using 2H-$BaMnO_3$ as the starting material instead of 15R-$BaMnO_{3-x}$ significantly enhanced the proportion of 8H-$BaMnO_{3-x}$. However the formation of phase-pure 8H-$BaMnO_{3-x}$ from a sample consisting of ~ 44% 15R-$BaMnO_{3-x}$ is still extremely slow.

In order to minimise the formation of 15R-$BaMnO_{3-x}$, a sample of 2H-$BaMnO_3$ was fired at the higher temperature of 1325°C. This resulted in the formation of 6L-$BaMnO_{3-x}$. The 6L stacking sequence has fewer hexagonal layers than the 8H stacking sequence (8H = 75% hexagonal layers, 6L = 66.6% hexagonal layers), suggesting that the tolerance factor too small for the formation of 8H-$BaMnO_{3-x}$. This indicates firing conditions of 1325°C in air are too reducing for the formation of 8H-$BaMnO_{3-x}$.

A further attempt was made to prepare 8H-$BaMnO_{3-x}$ by oxidising 6L-$BaMnO_{3-x}$. A sample of 6L-$BaMnO_{3-x}$ was fired at 1325°C for 6 days, however only 13% of the sample adopted the 8H structure. Although firing at 1300°C did increase the proportion of 8H-$BaMnO_{3-x}$, a significant proportion of 15R-$BaMnO_{3-x}$ was also produced.

These observations are consistent with previous work in indicating that under atmospheric conditions there is an extremely narrow temperature range in which 8H-$BaMnO_{3-x}$ can be formed. They also confirm that 15R-$BaMnO_{3-x}$ transforms very slowly to 8H-$BaMnO_{3-x}$.

3.4.2.2.2. Interpretation of results

The results can be rationalised by considering the reduction process more carefully. If a sample of $BaMnO_3$ is fired at a high enough temperature, some reduction of the manganese will occur. This produces a driving force for the introduction of cubic layers into the stacking sequence. However, a continuous increase in the proportion of cubic layers is not observed. Only discrete stacking sequences are seen suggesting that the structural transformation occurs in steps. If the driving force is not sufficient to drive the transformation to the next available stacking sequence, a two phase mixture is produced rather than a disordered intermediate phase.

If cubic layers were introduced in a disordered manner, the expected X-ray diffraction data should correspond to a single phase with a high degree of anisotropic broadening. However, a high degree of anisotropic broadening is not observed for samples of 15R-$BaMnO_{3-x}$, 8H-$BaMnO_{3-x}$ or 6L-$BaMnO_{3-x}$. Two phase mixtures of 15R-$BaMnO_{3-x}$ and 8H-$BaMnO_{3-x}$ are observed in certain diffraction patterns. This helps to confirms that the cubic layers are not introduced in a disordered manner, but are accommodated by the adoption of a new stacking sequence. The phase transformation is shown schematically in Figure 3.7.

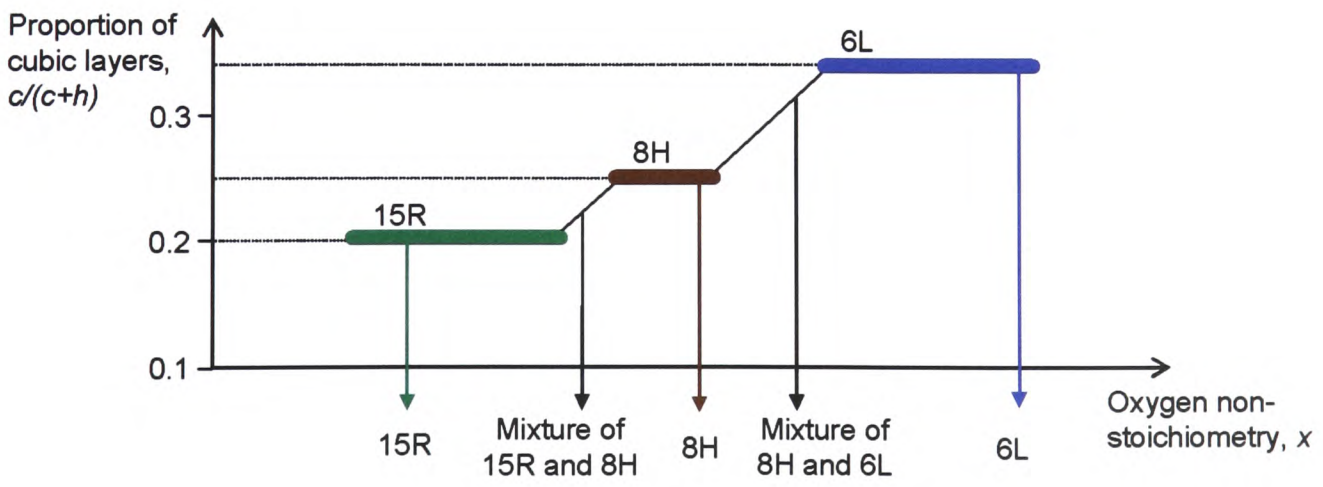


Figure 3.7 Representation of how the proportion of cubic layers may vary with the oxygen non-stoichiometry of the sample, *x*. A mixture of two phases could represent a true two phase system or (potentially) a single phase with an intermediate proportion of cubic layers in a disordered arrangement.

The stepwise transformation of the stacking sequence in order to introduce more cubic layers often requires a great deal of structural reorganisation. If the degree of structural reorganisation is too large compared to the driving force for more cubic layers, the transformation into a new stacking sequence is likely to be slow, possibly slow enough that effectively no transformation takes place. A small driving force is likely to occur close to phase boundaries, when the extent of reduction produces a tolerance factor marginally outside the bounds which favour the original stacking sequence.

These arguments can be used to rationalise the slow transformation of 15R-$BaMnO_{3-x}$ to 8H-$BaMnO_{3-x}$. A slight reduction of 15R-$BaMnO_{3-x}$ produces only a small driving force for increasing the proportion of cubic layers. The unit cells of 15R-$BaMnO_{2.99(1)}$ and 8H-$BaMnO_{2.95(1)}$ have a long incommensurate length, thus a relatively large degree of structural reorganisation is required to form 8H-$BaMnO_{3-x}$ from 15R-$BaMnO_{3-x}$. Therefore the transformation is slow at best, and can be stopped completely by a phase separation at worst. The driving force for an increased proportion of cubic layers can be increased by increasing x. This can be achieved by raising the temperature. On increasing the temperature to 1400°C, for example, 15R-$BaMnO_{3-x}$ readily adopts a new stacking sequence. However, this degree of reduction also increases the proportion of cubic layers required for thermodynamic equilibration, favouring the 6L stacking sequence. Likewise, when 6L-$BaMnO_{3-x}$ is oxidised sufficiently to overcome the barrier to structural reorganisation and drive the transformation to a new stacking sequence, the extent of oxidation results in the adoption of the 15R stacking sequence (in preference to the 8H stacking sequence). On firing 2H-$BaMnO_3$ at T = 1300°C, a different problem occurs. Although the driving force of reducing 2H-$BaMnO_3$ at this temperature is easily sufficient to alter the stacking sequence, 15R-$BaMnO_{3-x}$ is formed more rapidly than 8H-$BaMnO_{3-x}$. Once 15R-$BaMnO_{3-x}$ has been formed, this traps a portion of the sample which transforms extremely slowly to 8H-$BaMnO_{3-x}$.

This interpretation of the synthetic results suggests two possible methods for forming a phase-pure sample with the 8H stacking sequence. One is an extremely long firing time at a very precise temperature (the method used by Negas and Roth). This will allow the slow transformation of 15R-$BaMnO_{3-x}$ (or 6L-$BaMnO_{3-x}$) to 8H-$BaMnO_{3-x}$ to take place. The alternative is to increase the rate of this transformation, which can be achieved by increasing the temperature. This also increases the extent of manganese reduction, but as discussed in Section 3.2, this can be avoided by simultaneously increasing the partial pressure of oxygen in the atmosphere.

3.4.2.3. Synthesis under oxidising atmospheres

Firing $BaMnO_3$ at a temperature of 1400°C under an atmosphere of 33.3% O_2 resulted in a manganese oxidation state in the correct range for a tolerance factor which favours the formation of 8H-$BaMnO_{3-x}$. Table 3.2 lists the final products of firing 2H-$BaMnO_3$ samples under oxidising atmospheres.

T (°C)	pO_2 (atm)	Time (hr)	15R	8H	6L
1330	0.33(4)	200	100%	/	/
1360	0.33(4)	40	74(2)%	26(2)%	/
1400	0.33(4)	40	/	100%	/
1425	0.30(4)	40	/	62.9(8)%	37.1(8)%

Table 3.2 Relative proportions of 6L-$BaMnO_{3-x}$, 8H-$BaMnO_{3-x}$ and 15R-$BaMnO_{3-x}$ as a weight fraction of the sample after firing at various temperatures under oxygen rich conditions.

Under these conditions, reactions rates were greatly increased compared with the reactions carried out in air at lower temperatures. A phase-pure sample with the 8H stacking sequence could be readily prepared from samples of 2H-$BaMnO_3$ in 40 hours. At lower temperatures, a mixture of 15R-$BaMnO_{3-x}$ and 8H-$BaMnO_{3-x}$ was formed; at higher temperatures a mixture of 8H-$BaMnO_{3-x}$ and 6L-$BaMnO_{3-x}$ phases was formed. It is likely that increased firing times would have resulted in single phase samples of 8H-$BaMnO_{3-x}$ or 6L-$BaMnO_{3-x}$ respectively.

3.4.3. 9R-Ba(Sr)MnO_{3-x}

3.4.3.1. Introduction

9R-$BaMnO_3$ has been reported by Chamberland et al. using a high pressure synthesis route, as well as by Potoff et al. using hydrothermal techniques.[100, 102] However 9R-$BaMnO_3$ was not observed in the extensive study by Negas and Roth. Nor was it observed, even as a minority phase, under any of the conditions reported above. Notably, the 6L and 9R structures contain the same proportion of cubic layers. Based on previous arguments, they are therefore expected to have the same tolerance factors, the same oxygen stoichiometry and form under the same conditions. This being the case, it is clear that some factor other than the tolerance factor directs one structure to be adopted in preference to the other. A review of other known hexagonal phases reveals that the 9R stacking sequence is relatively common. This represents the simple stacking sequence for 33.3% cubic layers, according to the definitions set out in Section 1.3. The regular 9R structure is adopted by $BaRuO_3$ and a slightly distorted version is adopted by $BaIrO_3$. It is also found for several mixed B cation systems such as $BaMn_{0.644}Ru_{0.356}O_3$ and $BaMn_{1-x}Ir_xO_3$.[33-35, 103] The 6L stacking sequence, on the other hand, is a complex stacking sequence known only for $BaMnO_{3-x}$ and the closely related phases $BaMn_{0.767}Fe_{0.233}O_{2.87}$ and $Ba_{1-y}Sr_yMnO_{3-x}$ ($y \leq 0.15$, $x \sim 0.1$).[69, 104]

Complex stacking sequences are favoured over simple ones when they contain a particularly favourable structural feature. This was discussed in Section 1.3.3 for stacking sequences containing 50% cubic stacking, where the 12R sequence provides a large B cation site and the 12H sequence contains a small B cation site. The only difference between the chemical compositions of the reported 9R-$BaMnO_3$ and 6L-$BaMnO_{3-x}$ phases is in the proportion of oxide vacancies. 9R-$BaMnO_3$ contains no oxide vacancies and has only been synthesised under high pressure, whereas 6L-$BaMnO_{3-x}$ can only be synthesised under reducing conditions and so always contains oxide vacancies. The significance of the oxide vacancies is consistent with a previous study by Negas on the phase diagram of $Ba_{1-y}Sr_yMnO_{3-x}$.[104] This found that the 9R

structure was adopted for a composition of $Ba_{1-y}Sr_yMnO_{3-x}$ where $0.09 \leq y \leq 0.14$ and $x \leq 0.03$. As the temperature is increased above 1300°C, the proportion of oxide vacancies increases and the 6L stacking sequence is adopted, with typical values of $x \sim 0.11$. This suggests that the structural feature that results in the 6L sequence being favoured is associated with the vacant oxide sites. Thus in order to form 9R-$BaMnO_3$, the tolerance factor must be reduced without introducing oxide vacancies, which can be achieved if the average A-O bond length is the factor that adjusts the tolerance factor. High pressure synthesis reduces the tolerance factor by reducing the average size of the more compressible A cation, but an alternative method of reducing the average A cation size is to substitute barium for strontium and form the 9R-$Ba_{1-y}Sr_yMnO_{3-x}$ phase reported by Negas, where $0.09 \leq y \leq 0.14$ and $x \leq 0.03$.

3.4.3.2. Results

Following the procedure reported by Negas, samples of $Ba_{1-y}Sr_yMnO_{3-\delta}$ (y = 0.075, 0.125, 0.175, $\delta \sim 0$) were prepared using standard ceramic techniques. These were fired under air at T < 1200°C in order to prevent the introduction of any significant quantities of oxide vacancies. The firing temperatures and resultant phases are listed in Table 3.3.

y	T (°C)	Time (days)	Stacking sequences present
0.075	1000	31	9R + 2H
0.125	1000	7	9R
	1050	14	9R
	1100	9	9R
	1150	24	9R
0.175	1000	25	9R + 4H

Table 3.3 Results of firing $Ba_{1-y}Sr_yMnO_{3-x}$ phases in air.

The products were consistent with those observed by Negas.[104] The y = 0.075 sample segregated into two phases: a minority phase of 2H-$Ba_{1-y}Sr_yMnO_{3-\delta}$, and the desired 9R-$Ba_{1-y}Sr_yMnO_{3-\delta}$ phase. It is likely that the barium and strontium segregate, with the

strontium concentrated in the 9R phase. The best result was found for the $y = 0.125$ sample. The tolerance factor of $Ba_{0.875}Sr_{0.125}MnO_{3-\delta}$ is such that the 9R stacking sequence is adopted.

Chapter 4: Structural characterisation of $BaMnO_{3-x}$ phases

4.1. Introduction

The stacking sequence adopted by $BaMnO_{3-x}$ phases is related to the value of x. The variation of the stacking sequence with x can generally be rationalised on the basis of the tolerance factor. Gonzalez-Calbet et al. have performed a study of $BaMnO_{3-x}$ phases using high resolution electron microscopy (HREM), identifying several new stacking sequences as minority phases.[105-108] They also claim to have identified an empirical rule (Equation 4.1) relating the oxide anion non-stoichiometry, x, to the number of cubic (c) and hexagonal (h) layers in the unit cell.

$$x = \frac{c}{2(c+h)}$$

Equation 4.1

This empirical rule fails to account for the range of compositions found by other investigations. Table 4.1 lists the reported chemical compositions found for different $BaMnO_{3-x}$ samples by a variety of studies.

	Negas and Roth [30]	**Uematsu et al.** [101]	**Gonzalez-Calbet et al.** [105-108]	
Method	TGA under O_2 to 1000°C	TGA under O_2 to 700°C	TGA under H_2, standardised against 2H-$BaMnO_{3.00}$	Equation 4.1
2H	0	0	0 (by definition)	0.00
15R	0.018-0.03	0-0.03	0.08-0.10	0.100
8H	0.041	0.04-<0.1	/	0.125
6L	0.1-0.141	0.1-0.19	0.166	0.166
10H	0.174-0.195	0.17-0.19	/	0.200
4H	0.262-0.283	>0.245	0.23-0.4	0.250

Table 4.1 Previously reported magnitude of x for different stacking sequences of $BaMnO_{3-x}$. The method used to obtain a value for x is also listed.

Although the compositions of 6L and 10H-$BaMnO_{3-x}$ are consistently close to those predicted by Equation 4.1, 15R and 8H-$BaMnO_{3-x}$ invariably contain fewer oxide vacancies than are predicted, and 4H-$BaMnO_{3-x}$ often contains many more than predicted. Gonzalez-Calbet et al. also suggest a model which provides a rationalisation for the relationship in Equation 4.1. In this model the oxide vacancies are located in cubic layers of composition $BaO_{2.50}$, while the hexagonal layers retain a composition of $BaO_{3.00}$. This model is contradictory with the only neutron diffraction study of a Ba(Sr)MnO_{3-x} hexagonal perovskite, which found that the oxide vacancies were located in the hexagonal layers.[109]

The location of the oxide vacancies is important as this appears to affect the favoured stacking sequence. The 9R and 6L structures contain the same proportion of cubic layers, yet as discussed in Section 3.4.3, 9R-$BaMnO_{3.00}$ can be only prepared using high pressure synthesis techniques.[100] Conversely, 6L-$BaMnO_{3.00}$ cannot be prepared using high pressure synthesis methods, but is readily prepared under reducing conditions as 6L-$BaMnO_{3-x}$. The different synthesis conditions required suggest that the oxide vacancies play a crucial role in determining which structure is adopted.

In order to unambiguously locate the oxide anion vacancies within the $BaMnO_{3-x}$ structures and investigate the validity of the Gonzalez-Calbet model, neutron diffraction studies were carried out on samples of $BaMnO_{3-x}$ phases.

4.2. Experimental

4.2.1. Synthesis

The synthesis methods used to prepare the various $BaMnO_{3-x}$ phases are described in detail in Chapter 3. The firing conditions of samples prepared for neutron diffraction studies are fully detailed in Table 4.2. Two strontium containing phases were also prepared. 9R-$Ba_{0.875}Sr_{0.125}MnO_3$ was fired in air at $T \leq 1150°C$. 4H-$Ba_{0.5}Sr_{0.5}MnO_{3-x}$ was fired under flowing argon, using identical conditions to those used to prepare 4H-$BaMnO_{3-x}$. Phase purity

for all samples was confirmed using X-ray powder diffraction. Further X-ray powder diffraction data sets suitable for structural refinement were collected using the Siemens diffractometer, described in Section 2.3.1.2.

Sample	Atmosphere	Temperature (°C)	Time (Hours)
15R-$BaMnO_{3-x}$	2:1 argon: oxygen	1330	200
		1335	40
		1345	40
8H-$BaMnO_{3-x}$	2:1 argon: oxygen	1400	80
9R-$Ba_{0.875}Sr_{0.125}MnO_{3-x}$	Air	1000	48 (2 days)
		1050	336 (14 days)
		1100	216 (9 days)
		1150	552 (23 days)
6L-$BaMnO_{3-x}$	1% oxygen in argon	1300	60
10H-$BaMnO_{3-x}$	1% oxygen in argon	1400	80
4H-$BaMnO_{3-x}$	Argon	1300	96
4H-$Ba_{0.5}Sr_{0.5}MnO_{3-x}$	Argon	1300	96

Table 4.2 Reaction conditions for $BaMnO_{3-x}$ phases prepared for neutron diffraction experiments.

4.2.2. Topotactic oxidation

Further samples of 4H-$BaMnO_{3-x}$ and 4H-$Ba_{0.5}Sr_{0.5}MnO_{3-x}$ were prepared and oxidised, forming 4H-$BaMnO_{3.00}$ and 4H-$Ba_{0.5}Sr_{0.5}MnO_{3.00}$. The oxidation was carried out by heating samples under flowing oxygen to 600°C and holding the temperature for 6 hours. Samples were then cooled to ambient temperature under flowing oxygen before removal from the furnace. The completion of the oxidation was confirmed using iodiometric titrations and thermogravimetric analysis. High quality X-ray diffraction data suitable for refinement were collected from 4H-$BaMnO_{3.00}$ and 4H-$Ba_{0.5}Sr_{0.5}MnO_{3.00}$ using the Siemens diffractometer.

Small samples of 6L-$BaMnO_{3-x}$ and 10H-$BaMnO_{3-x}$ were also heated under oxygen at 600°C for 6 hours for the purposes of magnetic measurements, to be discussed in Section 6.3. High

quality X-ray powder diffraction data were collected from the oxidised samples using the Siemens diffractometer. Refinement of the 6L and 10H models against the relevant data sets resulted in a good fit. The lattice parameters obtained from these refinements are listed in Table 4.3. These show little difference to those obtained prior to oxidation, although a small reduction is observed, consistent with slight oxidation having taken place.

	10H-$BaMnO_{3-x}$		**6L-$BaMnO_{3-x}$**	
	a (Å)	*c* (Å)	*a* (Å)	*c* (Å)
Original lattice parameters	5.6547(1)	23.1936(5)	5.6623(1)	13.9993(3)
After firing under oxygen	5.6537(1)	23.1820(2)	5.6603(1)	13.9919(5)

Table 4.3 Lattice parameters before and after oxygen treatment for 10H and 6L-$BaMnO_{3-x}$.

4.2.3. Neutron diffraction

Neutron powder diffraction data for structural refinement were collected from all $Ba(Sr)MnO_{3-x}$ phases (except the four 4H samples) at ambient temperature (T ~ 295K) using the Polaris diffractometer at ISIS, UK (Section 2.3.2.2.2). Ambient temperature neutron powder diffraction data were collected from 4H-$BaMnO_{3-x}$ and 4H-$BaMnO_{3.00}$ using the HRPD diffractometer at ISIS, UK (Section 2.3.2.2.1). Neutron powder diffraction data were collected at 295K from 4H-$Ba_{0.5}Sr_{0.5}MnO_{3-x}$ and 4H-$Ba_{0.5}Sr_{0.5}MnO_{3.00}$ using the D2B diffractometer at the ILL, Grenoble (Section 2.3.2.1).

4.2.4. Chemical analysis

Thermogravimetric analysis was carried out as described in Section 2.8 in order to determine the composition of the samples. Approximately 50 mg samples were heated under flowing oxygen. The mass gain was monitored as the temperature was raised at 10°C min^{-1} to the final temperature ($350 \leq T$ (°C) ≤ 800). The final temperature was held for 90 minutes, or until the mass gain had reached a plateau.

Iodiometric titrations were also performed on all $BaMnO_{3-x}$ samples, using the experimental procedure described in Section 2.6. Titrations were carried out at least three times per sample, yielding highly consistent results.

4.3. Results

4.3.1. Chemical analysis

For the most reduced $BaMnO_{3-x}$ phase, 4H-$BaMnO_{3-x}$, thermogravimetric analysis revealed a mass gain between 0.48% (when the holding temperature was 350°C) and 2.06% (when the holding temperature was 600°C). No further mass gain was observed on raising the holding temperature from 600°C to 800°C. This is consistent with complete oxidation for $T \geq 600°C$. Plots showing the mass gain against time for a range of holding temperatures are shown in Figure 4.1. X-ray powder diffraction data were collected from the oxidised products of thermogravimetric analysis using the Philips diffractometer. These data confirm that the structure is retained during oxidation.

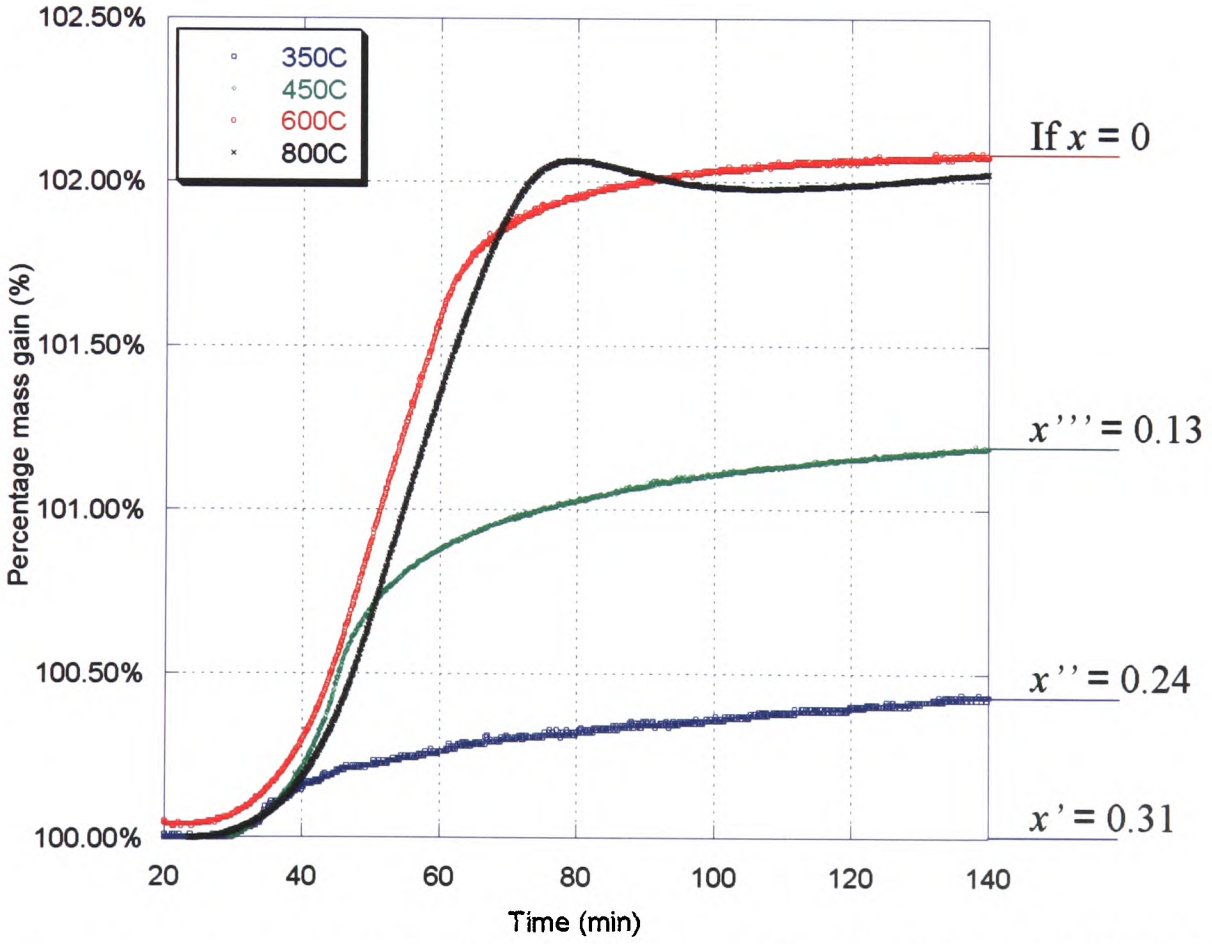


Figure 4.1 Thermogravimetric analysis of 4H-$BaMnO_{3-x}$ at 350, 450, 600, and 800°C. If the final composition is $BaMnO_{3.00}$, the initial composition is $BaMnO_{2.69}$. Oxidation takes place to $BaMnO_{2.76}$ at 350°C and $BaMnO_{2.87}$ at 450°C.

A mass gain of 2.06% at 600 - 800°C is consistent with a composition of $BaMnO_{2.69(1)}$, assuming that the final product of oxidation is the fully stoichiometric $BaMnO_{3.00}$. As the topotactic oxidation need not result in a fully oxidised product, thermogravimetric analysis sets an upper bound on the original oxygen stoichiometry, rather than determining the true value. Thus the true composition lies within the range $BaMnO_{3-x}$, $x \geq 0.31(1)$. Thermogravimetric analysis was also used to identify the lowest temperature at which no further oxygen uptake occurred. This temperature (600°C) was used to oxidise samples topotactically, as discussed in Section 4.2.2. The low temperature prevents cation rearrangement and so ensures the oxidation is topotactic.

The mass gain of 4H-$BaMnO_{3-x}$ was relatively large. For the remaining $BaMnO_{3-x}$ phases the maximum mass gain on oxidation was much smaller. Coupled with the slow rate at which oxidation occurred, this made the compositions found using thermogravimetric analysis unreliable, even if the measurement is corrected for the buoyancy effects as discussed in Section 2.8. Iodiometric titrations were therefore used to gain more reliable values for the composition. The compositions found using iodiometric titrations are detailed in Table 4.4. The composition of 4H-$BaMnO_{2.67(1)}$ yielded by iodiometric titration is consistent with that obtained using thermogravimetric analysis (4H-$BaMnO_{2.69(1)}$). Iodiometric titrations were also performed on the topotactically oxidised samples in order to confirm that full oxidation had taken place. Results for titrations carried out on oxidised samples are listed in Table 4.5

15R-$BaMnO_{3-x}$	**8H-$BaMnO_{3-x}$**	**6L-$BaMnO_{3-x}$**	**10H-$BaMnO_{3-x}$**	**4H-$BaMnO_{3-x}$**
0.01(1)	0.05(1)	0.07(1)	0.08(1)	0.33(1)

Table 4.4 Values of '*x*' obtained from iodiometric titration performed on $BaMnO_{3-x}$ phases.

4H-$BaMnO_{3-\delta}$	**4H-$Ba_{0.5}Sr_{0.5}MnO_{3-\delta}$**	**9R-$Ba_{0.875}Sr_{0.125}MnO_{3-\delta}$**	**6L-$BaMnO_{3-\delta}$**	**10H-$BaMnO_{3-\delta}$**
0.00(1)	0.01(1)	0.00(1)	0.01(1)	0.04(1)

Table 4.5 Values of 'δ' obtained from iodiometric titration performed on oxidised or stoichiometric Ba(Sr)$MnO_{3-\delta}$ phases.

4.3.2. Structural refinement

The details of the structural refinement against diffraction data are similar for all $Ba(Sr)MnO_{3-x}$ samples. The structural refinement of 10H-$BaMnO_{3-x}$ will therefore be discussed in detail in Section 4.3.2.1, followed by deviations from this procedure for other phases in Section 4.3.2.2.

4.3.2.1. Refinement procedure for 10H-$BaMnO_{3-x}$

High quality X-ray powder diffraction data were collected between $10° \leq 2\theta \leq 120°$. The data were fitted well by the 10H-$BaMnO_{3-x}$ model described by Negas and Roth,[30] with no additional diffraction features observed. All cationic positions and anisotropic displacement factors were refined against the X-ray powder diffraction data. Due to the lack of sensitivity of X-ray diffraction to light atoms in the presence of heavy atoms, the atomic positions of the oxide anions were not refined, oxide fractional occupancy numbers were fixed at unity and all oxide displacement factors were constrained to take the same isotropic value.

The anisotropic profile broadening parameters were refined to account for any particle size anisotropy or lattice strain arising from defects in the stacking sequence. The broadening axis was set as [001]. Details are shown in Table 4.6, along with the improvement to fitting statistics on refining the anisotropic profile broadening parameters. The anisotropy of 10H-$BaMnO_{2.91(1)}$ is very slight, but refinement of the parameter related to anisotropic microstrain results in a small improvement in the fit to the X-ray diffraction data. The parameter related to anisotropic particle size refined to zero, indicating any anisotropy is solely due to microstrain. The equations detailed in Section 2.4.1 allow the strain parallel and perpendicular to the anisotropic broadening axis to be calculated.

	Refined anisotropic broadening parameters	χ^2	Rp	wRp	Strain ⊥	Strain ||
X-ray	None	1.323	7.59%	5.99%	/	/
X-ray	Microstrain parameter	1.304	7.53%	5.96%	0.10%	0.17%
Neutron	None	2.88	4.17%	2.46%	/	/
Neutron	Microstrain parameter	2.64	3.94%	2.35%	0.13%	0.19%
Neutron	Microstrain parameter and particle size parameter	2.64	3.94%	2.34%	0.11%	0.17%

Table 4.6 Improvement to refinement of 10H-$BaMnO_{2.91(1)}$ model against X-ray and neutron powder diffraction data on refining anisotropic profile parameters.

The model obtained from refinement against the X-ray diffraction data was then refined against the neutron powder diffraction data. A dual refinement against both data sets was not carried out due to slight differences in the measuring temperature. Refinement against the neutron diffraction data allowed the accurate location and fractional occupancy of the oxide sites to be determined. All atomic coordinates and anisotropic displacement parameters were refined against the neutron diffraction data. Particular attention was paid to the fractional occupancies of oxide ions. Free refinement of the oxide occupation numbers yielded an overall stoichiometry in good agreement with that obtained via iodiometric titration (Refined stoichiometry = $BaMnO_{2.91(1)}$, Titrated stoichiometry = $BaMnO_{2.92(1)}$).

Anisotropic profile parameters were also refined against the neutron diffraction data, with the same broadening axis of [001]. The anisotropic profile parameters were constrained across the three neutron diffraction histograms obtained from the Polaris diffractometer such that the values for the sample microstrain were self consistent. Again, a small improvement to the fitting statistics was noted, related to a small difference in the strain parallel and perpendicular to the broadening axis. The absolute values for the microstrain are similar to those observed via X-ray diffraction.

The observed and calculated neutron diffraction profile for 10H-$BaMnO_{2.91(1)}$ is shown in Figure 4.11, the refined structure is detailed in Table 4.17 and depicted in Figure 4.12. Selected bond lengths and angles are listed in Table 4.18. Anisotropic displacement factors are detailed in Appendix B.

4.3.2.2. Deviations for other Ba(Sr)MnO_{3-x} phases

Some deviations from the refinement procedure described above were necessary for the other samples. Structural models based on those reported by Negas and Roth were also refined against neutron powder diffraction data collected from 15R, 8H, 6L and all 4H-Ba(Sr)MnO_{3-x}.[30] The starting model for refinement against the data collected from 9R-$Ba_{0.875}Sr_{0.125}MnO_{3-x}$ was based on that described by Chamberland et al. for 9R-$BaMnO_{3.00}$ prepared under pressure.[100]

The refinements against data collected from the 15R, 8H and 9R samples yielded unrealistically low oxygen occupancies and so these models were constrained such that the total stoichiometry was consistent with the values obtained chemically. Iodiometric titration indicated that the 9R-$Ba_{0.875}Sr_{0.125}MnO_{3-x}$ sample was fully oxygen stoichiometric, so all oxygen occupancies were fixed at unity in the refinement. Details of the chemical compositions and the oxygen occupancy numbers yielded by free refinement are listed in Table 4.7.

Phase	Composition from free refinement	Composition from titration	Free refinement of oxygen occupancies		
15R	$BaMnO_{2.909(9)}$	$BaMnO_{2.99(1)}$	O1 - *hch*	O2 - *chh*	O3 - *hhh*
			0.979(4)	0.958(3)	0.977(3)
8H	$BaMnO_{2.908(9)}$	$BaMnO_{2.95(1)}$	O1 - *hch*	O3 - *chh*	O2 - *hhh*
			0.995(4)	0.958(4)	0.962(2)
9R	$Ba_{0.875}Sr_{0.125}MnO_{2.924(8)}$	$Ba_{0.875}Sr_{0.125}MnO_{3.00(1)}$	O1 - *hch*	O2 - *chh*	/
			0.984(3)	0.970(2)	/

Table 4.7 Oxygen site occupancies and compositions obtained from free refinement against neutron powder diffraction data.

The constrained refinement against the neutron diffraction data resulted in the occupancy numbers for some oxide sites taking values greater than unity. Occupancy numbers for these sites were fixed such that they were fully occupied.

For $Ba_{1-y}Sr_yMnO_{3-x}$ phases where $y \neq 0$, the distribution of strontium over the A cation sites was also refined. This was constrained such that total cation stoichiometry remained constant and each site remained fully occupied.

Examination of the neutron diffraction data collected from the 4H-$BaMnO_{2.65(1)}$ sample revealed an additional reflection that was unaccounted for by the 4H model. This was assigned to the presence of a small amount of MnO. MnO was added as a second phase to the refinement, resulting in an improvement to the fit. The refined mole fraction of MnO was 0.01379(3).

In some cases, the refined displacement ellipsoids representing the barium ions were greatly elongated along the c axis. This occurs for barium ions located in the cubic layers of 4H-$BaMnO_{2.65(1)}$ and 4H-$Ba_{0.5}Sr_{0.5}MnO_{2.79(1)}$, but is reduced for comparable ions in 4H-$BaMnO_{3.00(1)}$ and 4H-$Ba_{0.5}Sr_{0.5}MnO_{2.99(1)}$. Therefore the elongation of the displacement ellipsoids is probably related to disorder originating from the introduction of an oxide vacancy into the barium coordination sphere. An attempt was made to model this by splitting the barium site. Two split-site models were refined against the data and compared to the original displacement ellipsoid model. For the first split-site model (model 1), barium ions located in the cubic layers were displaced from the mirror plane. The occupancy numbers were adjusted such that the cation ratio remained constant and anisotropic displacement factors were used to model the scattering. In the second model, a barium site located on the mirror plane (as in the original model) was added to model 1. This models a situation in which barium ions may be displaced from the mirror plane, or may be undisturbed. Isotropic displacement factors were used to model the barium ions in model 2. Examples of the different models are shown in

Figure 4.2. Table 4.8 lists the refinement statistics and equivalent displacement parameters for the three models (U_{iso} for isotropic ellipsoids or U_{equiv} for anisotropic ellipsoids).

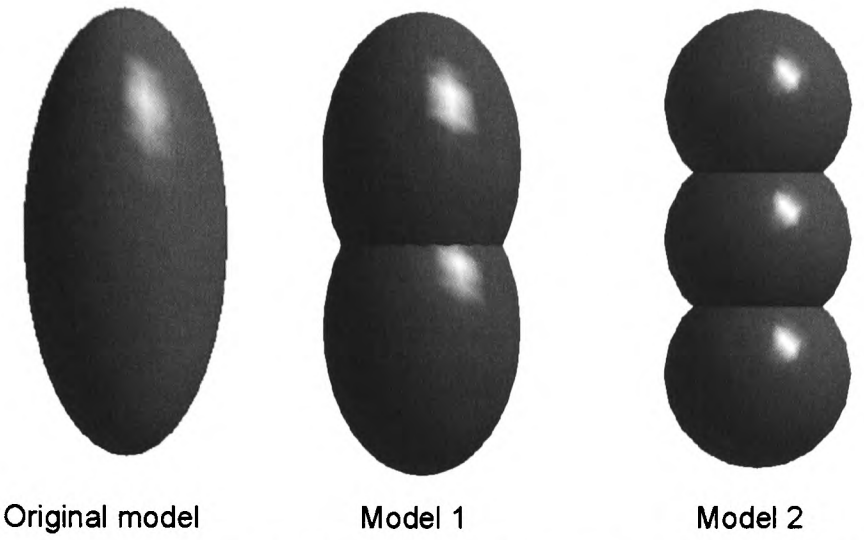


Figure 4.2 Examples of models for the displacement of barium ions in the cubic site of 4H-Ba(Sr)MnO_{3-x} samples.

Sample	Model	U_{iso} or U_{equiv} (Å^2)	Rp	wRp	χ^2
4H-$BaMnO_{2.65(1)}$	Original	1×0.024	5.04%	5.53%	1.693
	Model 1	2×0.015	5.04%	5.53%	1.692
	Model 2	3×0.011	5.04%	5.53%	1.692
4H-$Ba_{0.5}Sr_{0.5}MnO_{2.79(1)}$	Original	1×0.028	3.35%	4.53%	4.070
	Model 1	2×0.017	3.37%	4.55%	4.100
	Model 2	3×0.012	3.37%	4.56%	4.108

Table 4.8 Goodness of fit parameters for different anisotropic displacement parameters used to model the cubic barium site.

The displacement ellipsoids of barium ions occupying the cubic site are found to span approximately the same volume regardless of the model used. As there was no significant improvement in the fit for the two split site models, the simpler original model was retained for the final refinement.

The refined structural parameters and selected bond lengths for Ba(Sr)MnO_{3-x} samples are detailed in Table 4.9 - Table 4.21. Observed and calculated plots of refinements against the neutron diffraction data and the refined models are shown in Figure 4.3 - Figure 4.13. Tables of anisotropic displacement parameters can be found in Appendix B.

Atom	x	y	z	Fractional Occupancy	U_{equiv} (Å^2)
Ba1	0	0	0	1	0.0057
Ba2	0	0	0.13369(5)	1	0.0080
Ba3	0	0	0.26527(4)	1	0.0047
Mn1	0	0	½	1	0.0052
Mn2	0	0	0.36177(4)	1	0.0016
Mn3	0	0	0.43157(6)	1	0.0032
O1	½	0	0	1	0.0072
O2	0.18603(6)	-0.18603(6)	0.06421(2)	0.9875(1)	0.0051
O3	0.48332(6)	-0.48332(6)	0.13281(2)	1	0.0063
Space group : R $\bar{3}$ m, a = 5.6791(1) Å, c = 35.345(1) Å					
χ^2=2.18, wRp = 3.01%, Rp = 4.90%					
Titrated stoichiometry = $BaMnO_{2.99(1)}$					

Table 4.9 Structural parameters refined against neutron powder diffraction data collected from 15R-$BaMnO_{2.99(1)}$.

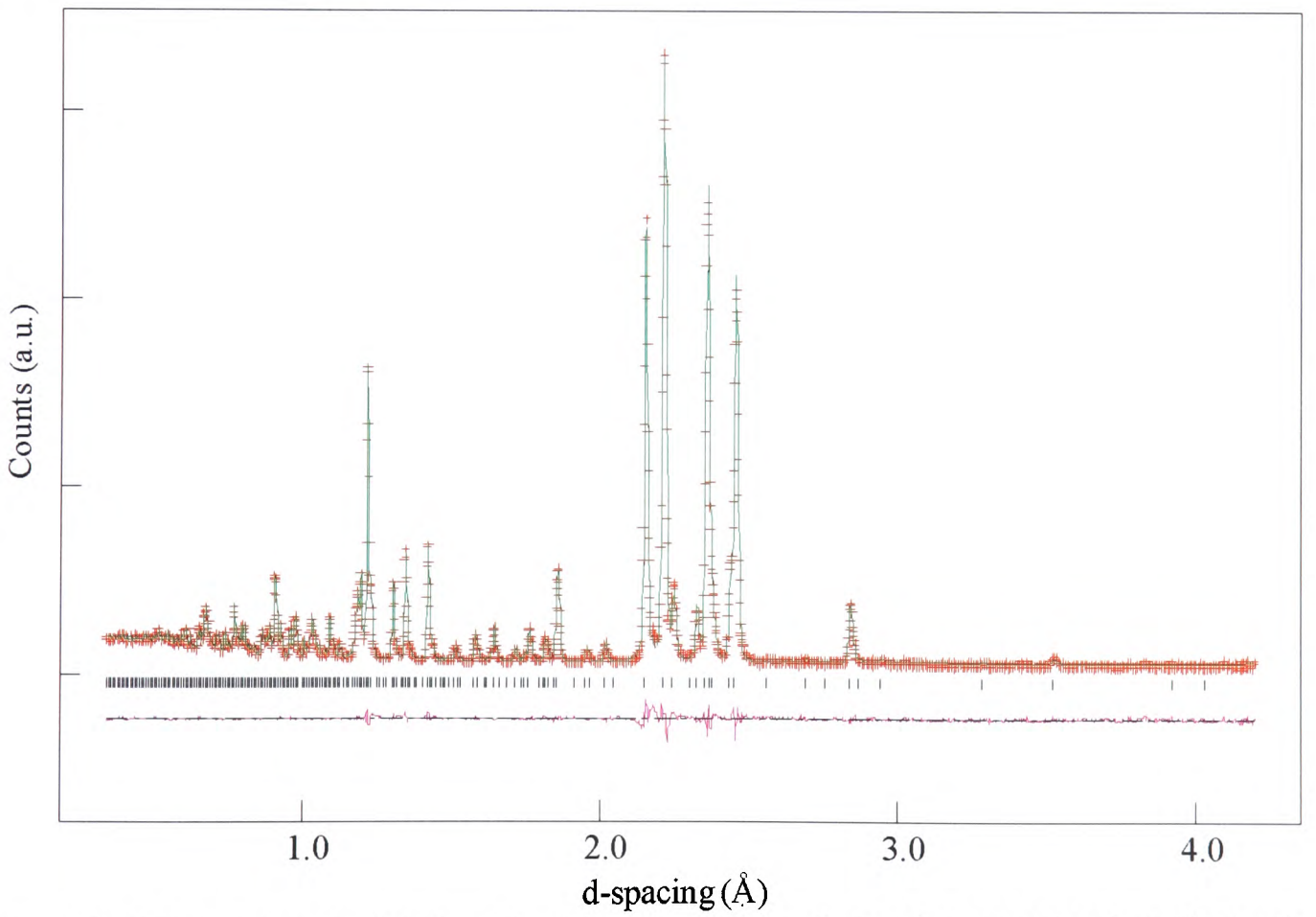


Figure 4.3 Observed, calculated and difference plots from the structural refinement of 15R-$BaMnO_{2.99(1)}$ against neutron powder diffraction data collected at 298K.

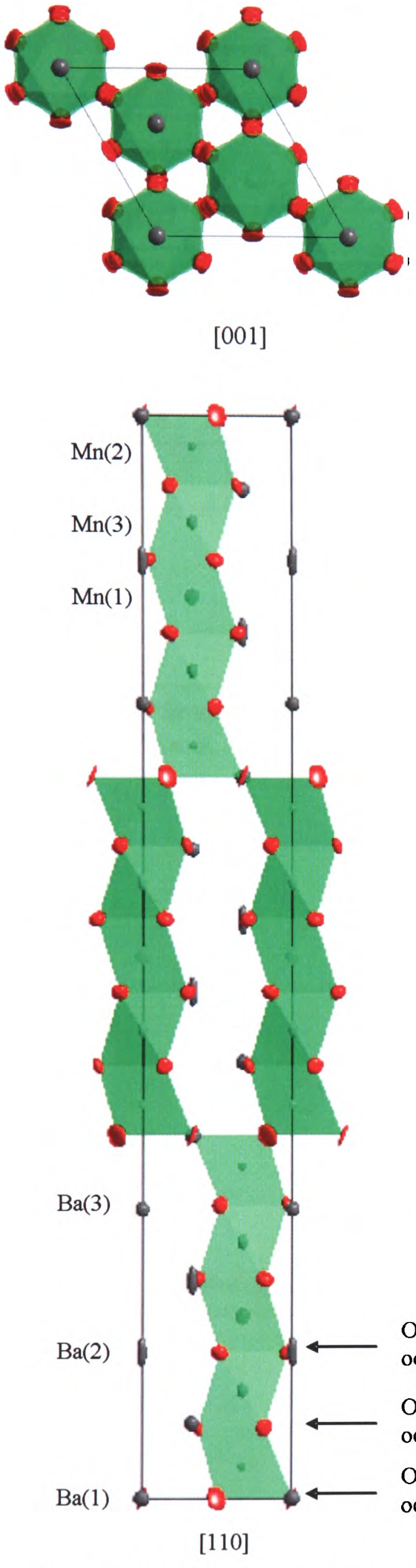


Figure 4.4 Refined structural model of 15R-$BaMnO_{2.99(1)}$.

Bond	Bond Length(Å)/angle(°)
Ba1-O1	2.83956(8)
Ba1-O2	2.9153(7)
Ba2-O2	3.062(2)
Ba2-O3(3x)	2.972(2)
Ba2-O3(6x)	2.84445(9)
Ba3-O1	2.911(1)
Ba3-O2	2.8492(1)
Ba3-O3	2.914(1)
Mn1-O3	1.8999(6)
Mn2-O1	1.9229(8)
Mn2-O2	1.923(1)
Mn3-O2	1.882(2)
Mn3-O3	1.917(2)
Mn1-Mn3	2.420(2)
Mn2-Mn3	2.466(3)
Mn1-O3-Mn3	78.71(5)
Mn2-O2-Mn3	80.77(6)

Table 4.10 Selected bond length and angles extracted from the structure of 15R-$BaMnO_{2.99(1)}$.

Atom	x	y	z	Fractional Occupancy	U_{equiv} (Å^2)
Ba1	0	0	0	1	0.0079
Ba2	0	0	¼	1	0.0094
Ba3	⅓	⅔	0.12839(4)	1	0.0055
Mn1	⅓	⅔	0.55338(5)	1	0.0032
Mn2	⅓	⅔	0.68562(5)	1	0.0041
O1	½	0	0	1	0.0070
O2	0.51668(6)	0.0333(1)	¼	0.979(2)	0.0062
O3	0.81450(3)	0.62899(7)	0.12106(2)	0.977(1)	0.0056

Space group : $P6_3/mmc$, a = 5.6736(1) Å, c = 18.7550(4) Å

χ^2=2.20, wRp = 2.34%, Rp = 4.05%

Titrated stoichiometry = $BaMnO_{2.95(1)}$

Table 4.11 Structural parameters refined against neutron powder diffraction data collected from 8H-$BaMnO_{2.95(1)}$.

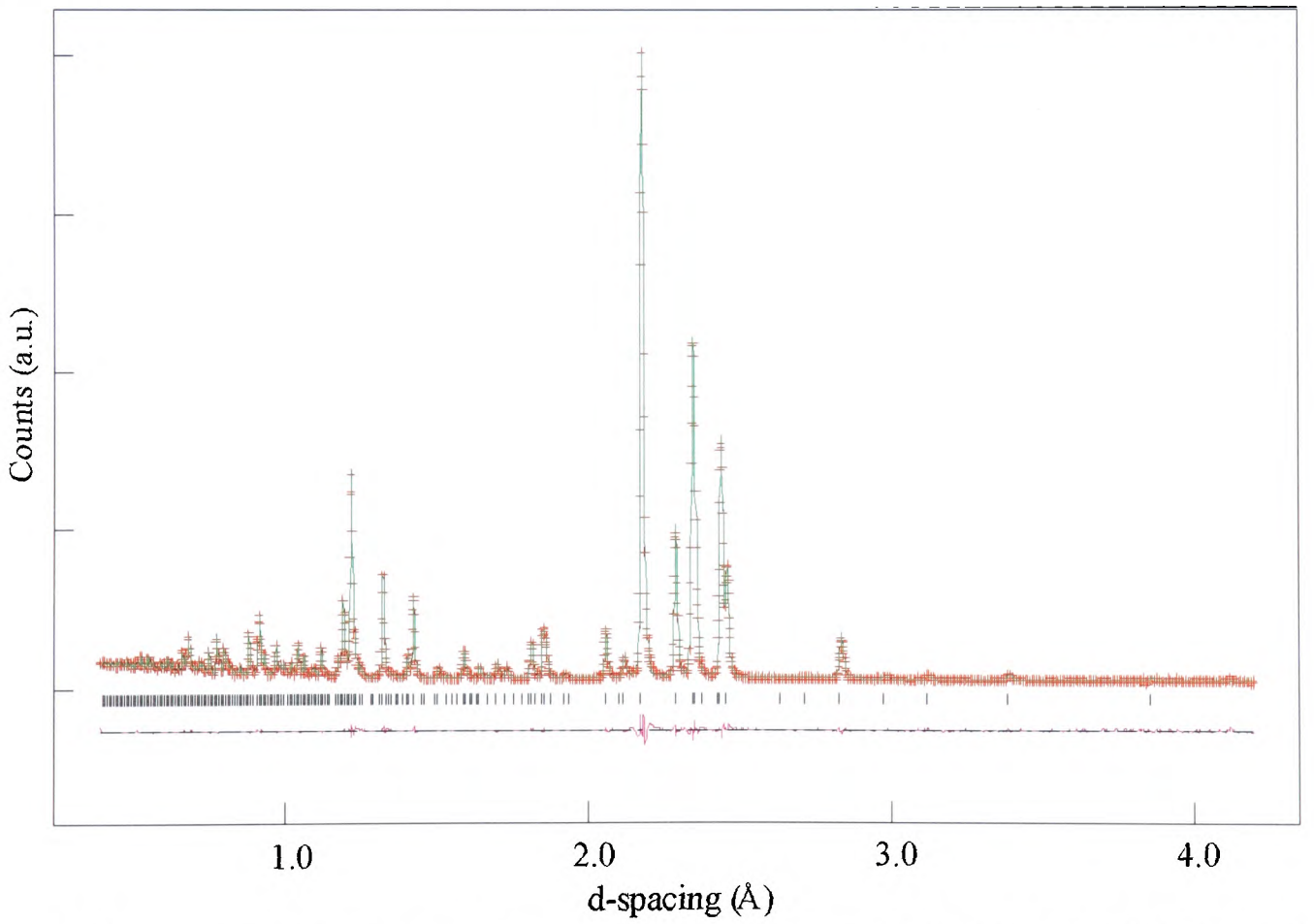
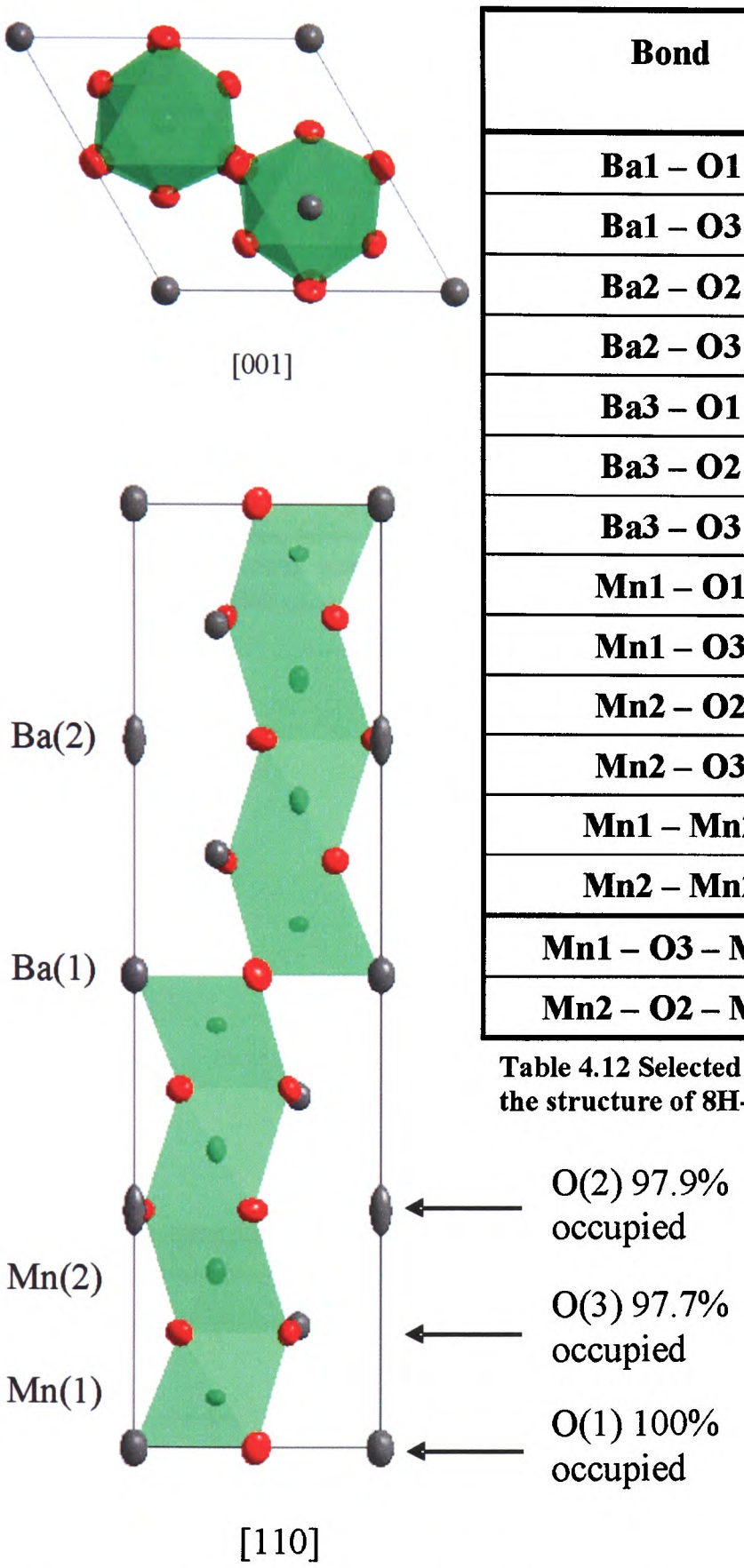


Figure 4.5 Observed, calculated and difference plots from the structural refinement of 8H-$BaMnO_{2.95(1)}$ against neutron powder diffraction data collected at 298K.



Bond	Bond Length(Å)/angle(°)
Ba1 – O1	2.83680(5)
Ba1 – O3	2.9117(4)
Ba2 – O2	2.84153(6)
Ba2 – O3	3.0285(4)
Ba3 – O1	2.9122(7)
Ba3 – O2	2.9065(8)
Ba3 – O3	2.84616(7)
Mn1 – O1	1.9195(5)
Mn1 – O3	1.9291(7)
Mn2 – O2	1.9054(8)
Mn2 – O3	1.8912(7)
Mn1 – Mn2	2.480(1)
Mn2 – Mn2	2.415(2)
Mn1 – O3 – Mn2	80.96(3)
Mn2 – O2 – Mn2	78.65(5)

Table 4.12 Selected bond lengths and angles extracted from the structure of 8H-$BaMnO_{2.95(1)}$.

Figure 4.6 Refined structural model of 8H-$BaMnO_{2.95(1)}$.

Atom	x	y	z	Fractional Occupancy	U_{equiv} (Å^2)
Ba1/Sr1	0	0	0	0.77(1)/0.23(1)	0.0066
Ba2/Sr2	0	0	0.21940(3)	0.926(5)/0.074(5)	0.0060
Mn1	0	0	½	1	0.0033
Mn2	0	0	0.38173(4)	1	0.0033
O1	½	0	0	1	0.0074
O2	0.14867(3)	-0.14867(3)	0.55830(2)	1	0.0058
Space group : R-3m, a = 5.6397(1) Å, c = 20.8973(6) Å					
χ^2=3.935, wRp = 2.81%, Rp = 4.76%					
Titrated stoichiometry = $Ba_{0.875}Sr_{0.125}MnO_{3.00(1)}$					

Table 4.13 Structural parameters refined against neutron powder diffraction data collected from 9R-$Ba_{0.875}Sr_{0.125}MnO_{3.00(1)}$.

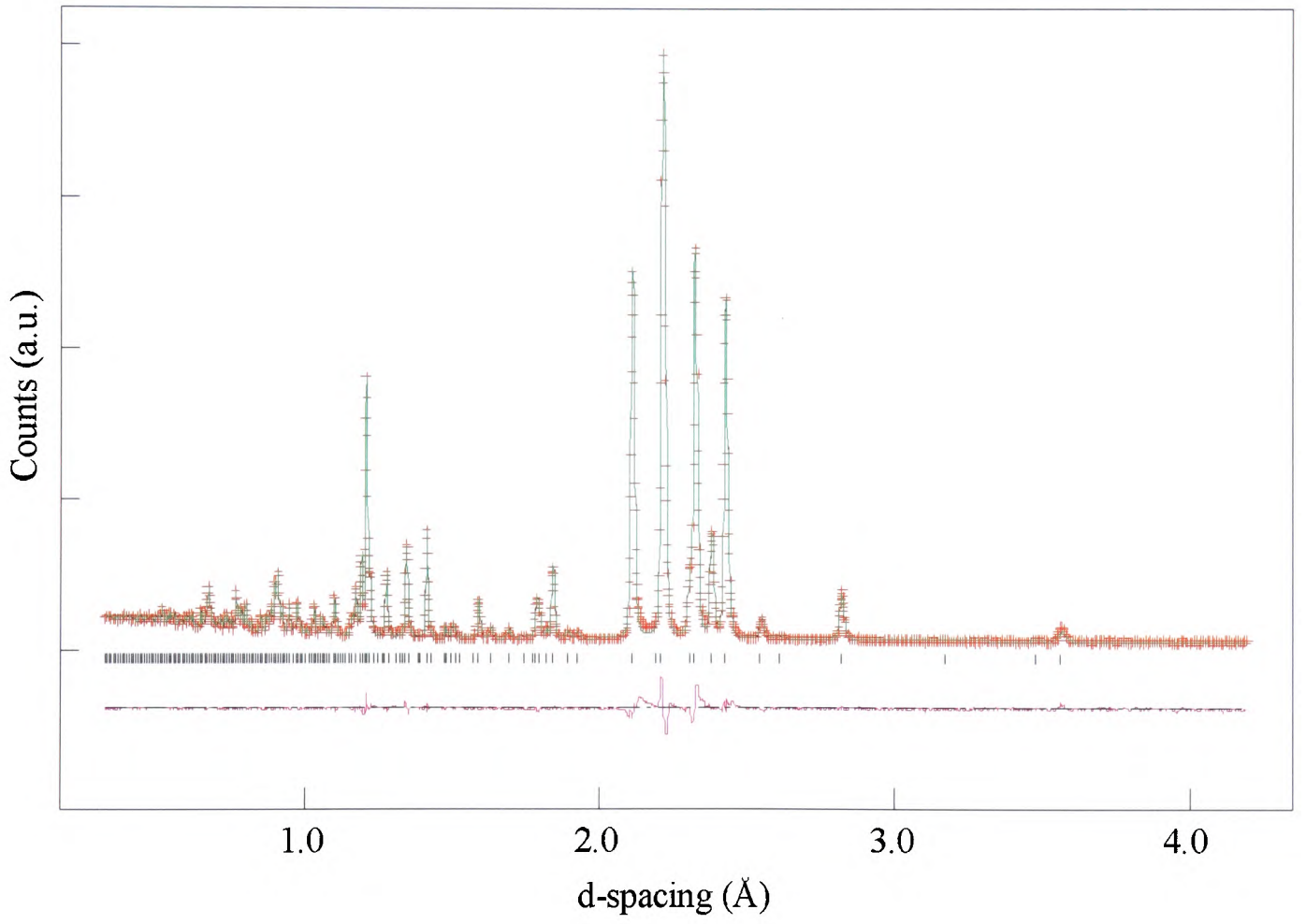


Figure 4.7 Observed, calculated and difference plots from the structural refinement of 9R-$Ba_{0.875}Sr_{0.125}MnO_{3.00(1)}$ against neutron powder diffraction data collected at 298K.

Bond	Bond Length(Å)/angle(°)
Sr/Ba1 – O1	2.81985(7)
Sr/Ba1 – O2	2.8953(3)
Sr/Ba2 – O1	2.8843(6)
Sr/Ba2 – O2(3x)	2.9393(5)
Sr/Ba2 – O2(6x)	2.82775(8)
Mn1 – O2	1.8954(3)
Mn2 – O1	1.9164(4)
Mn2 – O2	1.9181(6)
Mn3 – O2	1.884(1)
Mn3 – O3	1.915(1)
Mn1 – Mn2	2.4720(7)
Mn1 – O2 – Mn2	80.81(2)

Table 4.14 Selected bond lengths and angles extracted from the structure of 9R-$Ba_{0.875}Sr_{0.125}MnO_{3.00(1)}$.

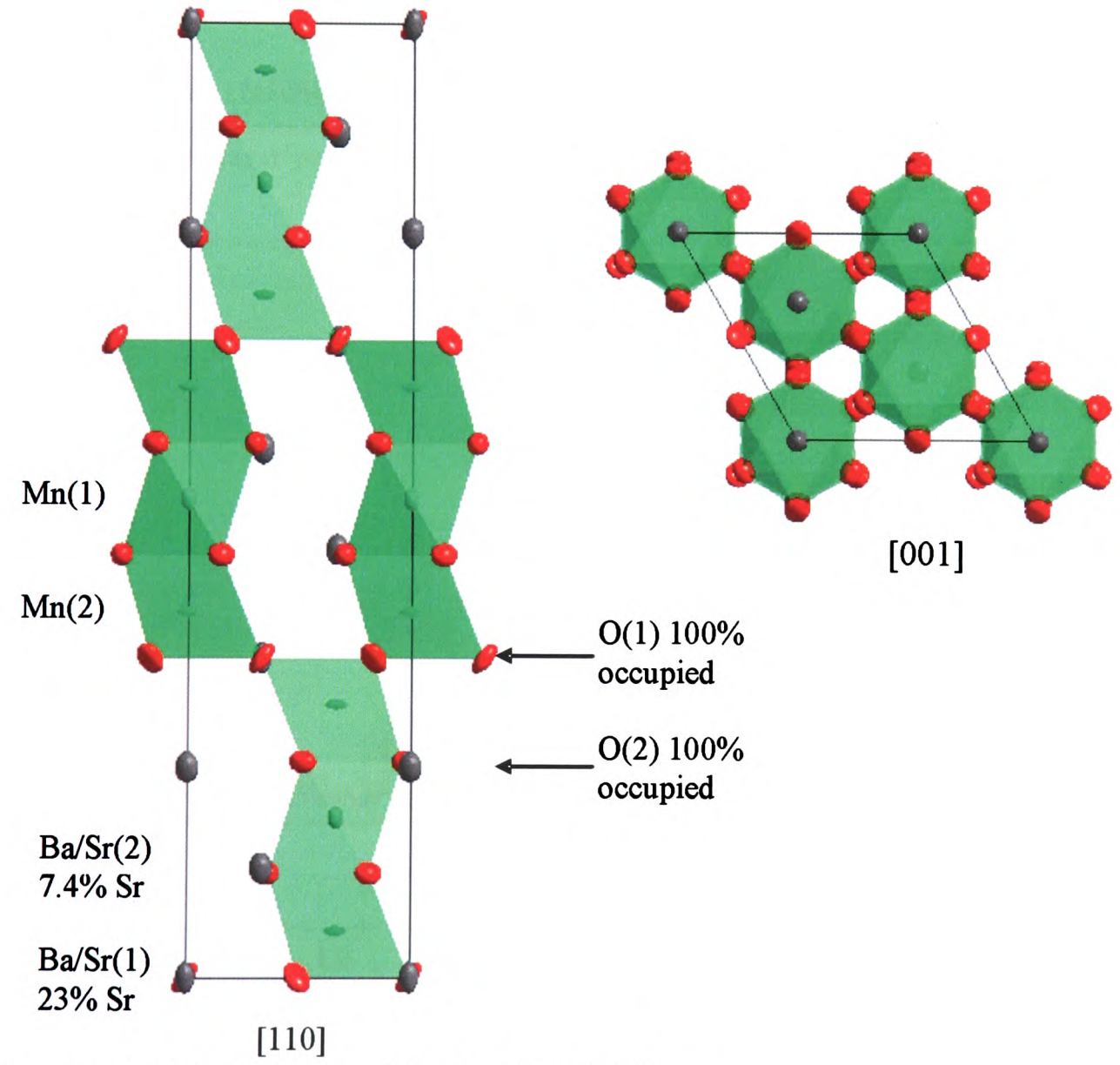


Figure 4.8 Refined structure of 9R-$Ba_{0.875}Sr_{0.125}MnO_{3.00(1)}$.

Atom	*x*	*y*	*z*	Fractional Occupancy	U_{equiv} (Å^2)
Ba1	0	0	0	1	0.0056
Ba2	⅓	⅔	½	1	0.0109
Ba3	⅓	⅔	0.1667(2)	1	0.0067
Ba4	⅔	⅓	0.3365(1)	1	0.0058
Mn1	0	0	0.2364(1)	1	0.0024
Mn2	0	0	0.4135(2)	1	0.0047
Mn3	⅔	⅓	0.0906(1)	1	0.0041
O1	0.5215(1)	0.4785(1)	0	0.927(6)	0.0045
O2	0.8503(1)	0.8503(1)	½	0.952(8)	0.0054
O3	0.8330(1)	0.8330(1)	0.16487(9)	0.998(4)	0.0070
O4	0.1486(1)	0.1486(1)	0.32730(4)	0.984(6)	0.0051

Space group : P $\bar{6}$ m2, a = 5.6623(1) Å, c = 13.9993(3) Å

χ^2=1.74, wRp = 2.59%, Rp = 4.91%

Refined stoichiometry = $BaMnO_{2.92(2)}$, Titrated stoichiometry = $BaMnO_{2.93(1)}$

Table 4.15 Structural parameters refined against neutron powder diffraction data collected from 6L-$BaMnO_{2.92(2)}$.

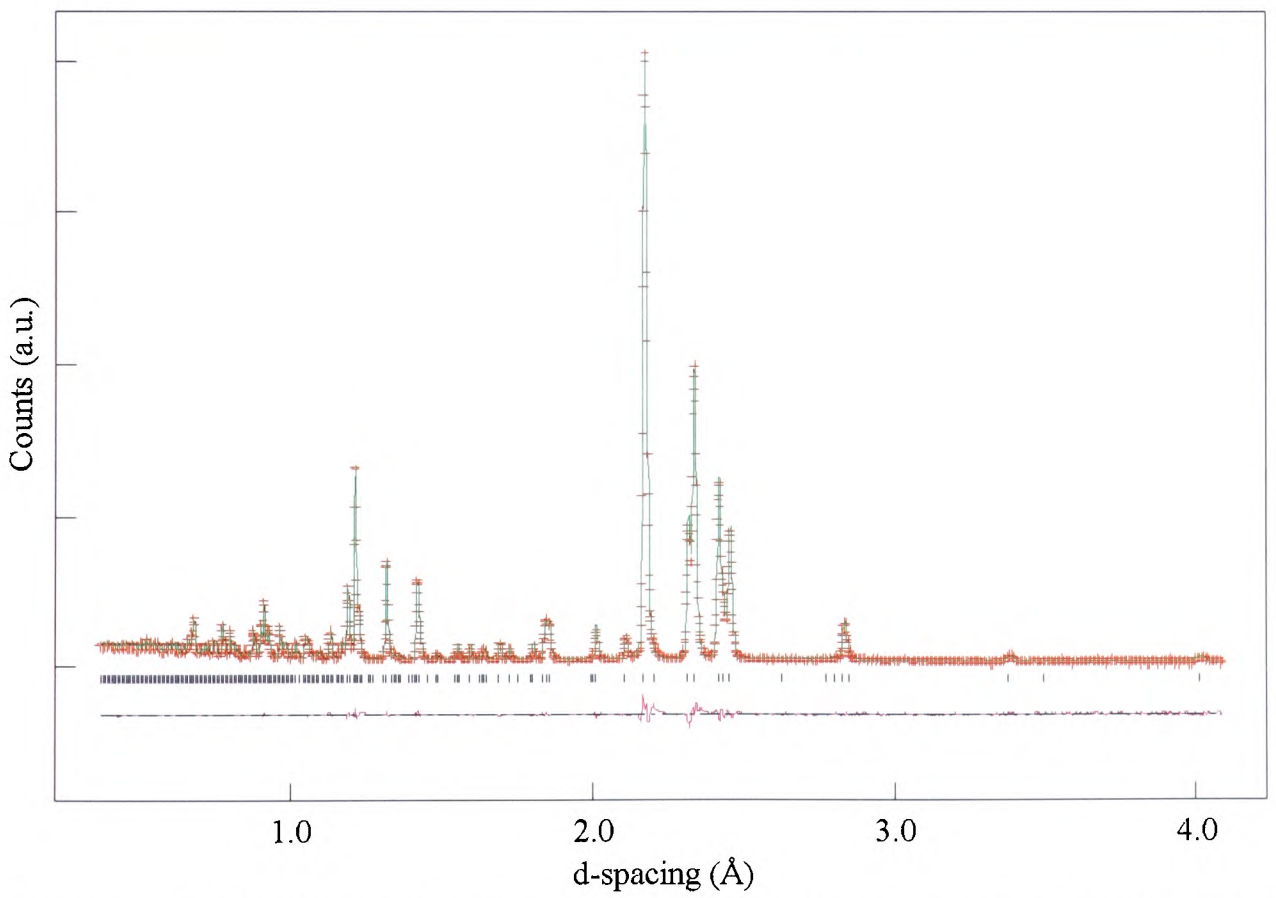


Figure 4.9 Observed, calculated and difference plots from the structural refinement of 6L-$BaMnO_{2.92(2)}$ against neutron powder diffraction data collected at 298K.

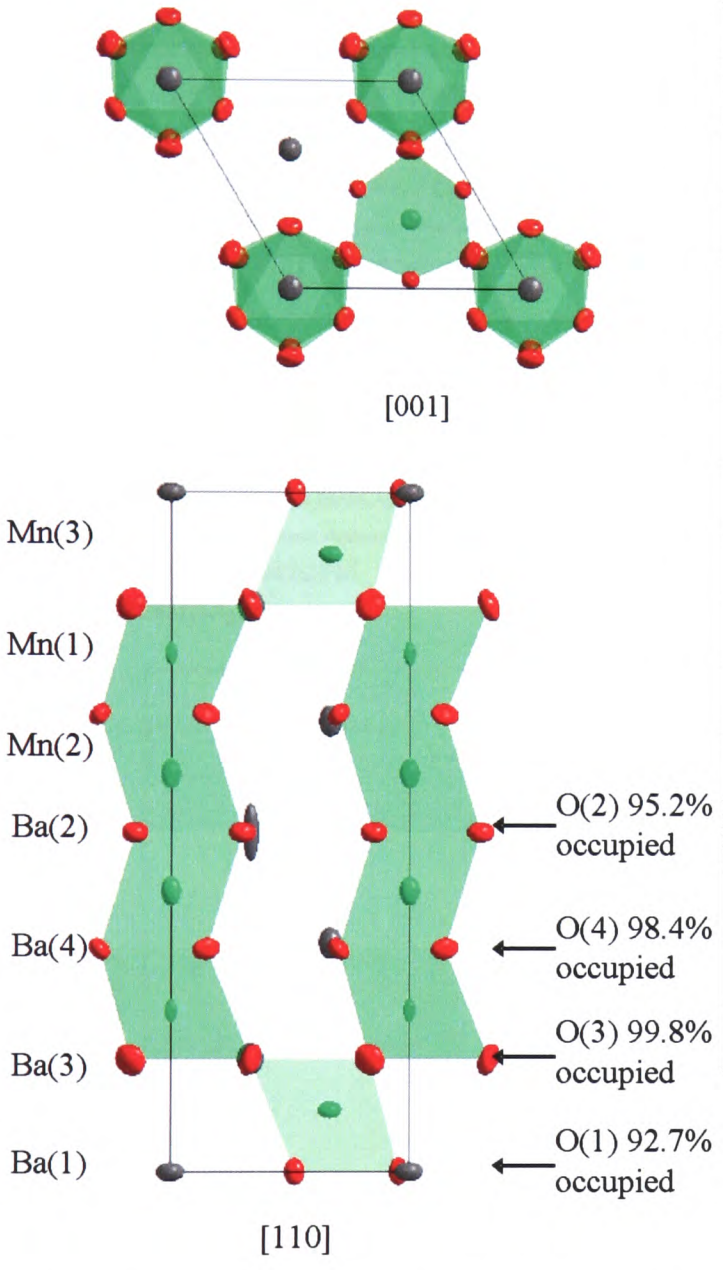


Figure 4.10 Refined structure of 6L-$BaMnO_{2.92(1)}$.

Bond	Bond Length(Å)/angle(°)
Ba1 – O1	2.8390(1)
Ba1 – O3	2.830(1)
Ba2 – O2	2.8361(1)
Ba2 – O4	3.0210(8)
Ba3 – O1	2.975(2)
Ba3 – O3	2.83129(7)
Ba3 – O4	2.887(2)
Ba4 – O2	2.912(2)
Ba4 – O3	2.904(2)
Ba4 – O4	2.8396(1)
Mn1 – O3	1.920(2)
Mn1 – O4	1.935(2)
Mn2 – O2	1.903(2)
Mn2 – O4	1.893(2)
Mn3 – O1	1.908(2)
Mn3 – O3	1.934(2)
Mn3 – Mn3	2.538(4)
Mn1 – Mn2	2.480(4)
Mn2 – Mn2	2.422(5)
Mn1 – O4 – Mn2	80.75(9)
Mn3 – O1 – Mn3	83.4(1)
Mn2 – O2 – Mn2	79.0(1)

Table 4.16 Selected bond lengths and angles extracted from the structure of 6L-$BaMnO_{2.92(2)}$.

Atom	x	y	z	Fractional Occupancy	U_{equiv} (Å^2)
Ba1	0	0	¼	1	0.0056
Ba2	⅓	⅔	0.14939(5)	1	0.0076
Ba3	⅓	⅔	0.54722(4)	1	0.0057
Mn1	0	0	0	1	0.0037
Mn2	0	0	0.10714(4)	1	0.0035
Mn3	⅓	⅔	0.69509(4)	1	0.0044
O1	0.52108(6)	0.0422(1)	¼	0.933(2)	0.0055
O2	0.14828(4)	0.29655(8)	0.05254(2)	0.984(2)	0.0060
O3	0.83309(5)	0.6662(1)	0.15054(2)	0.979(2)	0.0068
Space group : $P6_3/mmc$, a = 5.6547(1) Å, c = 23.1936(5) Å					
χ^2=2.64, wRp = 2.35%, Rp = 3.94%					
Refined stoichiometry = $BaMnO_{2.91(1)}$, Titrated stoichiometry = $BaMnO_{2.92(1)}$					

Table 4.17 Structural parameters refined against neutron powder diffraction data collected from 10H-$BaMnO_{2.91(1)}$.

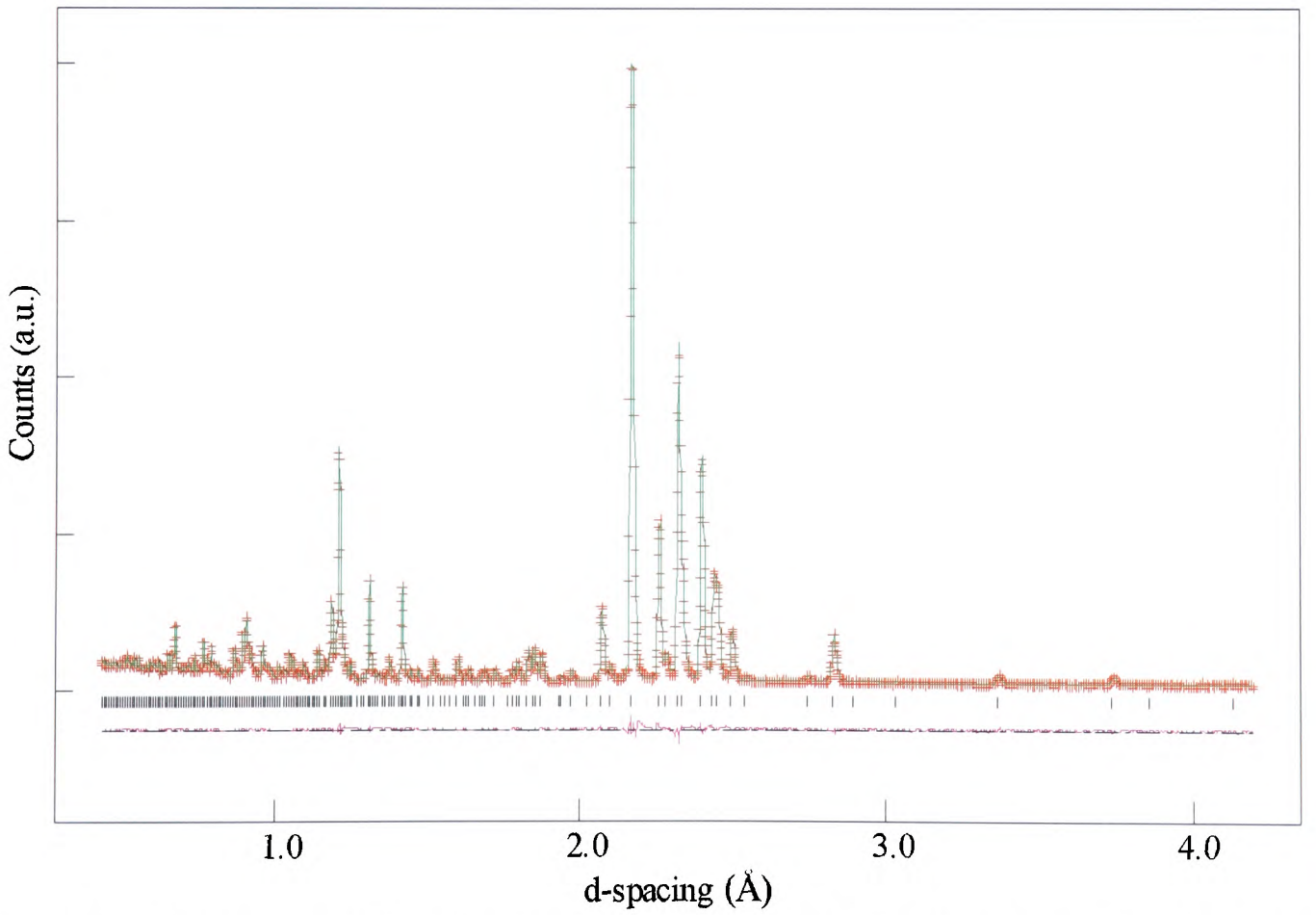


Figure 4.11 Observed, calculated and difference plots from the structural refinement of 10H-$BaMnO_{2.91(1)}$ against neutron powder diffraction data collected at 298K.

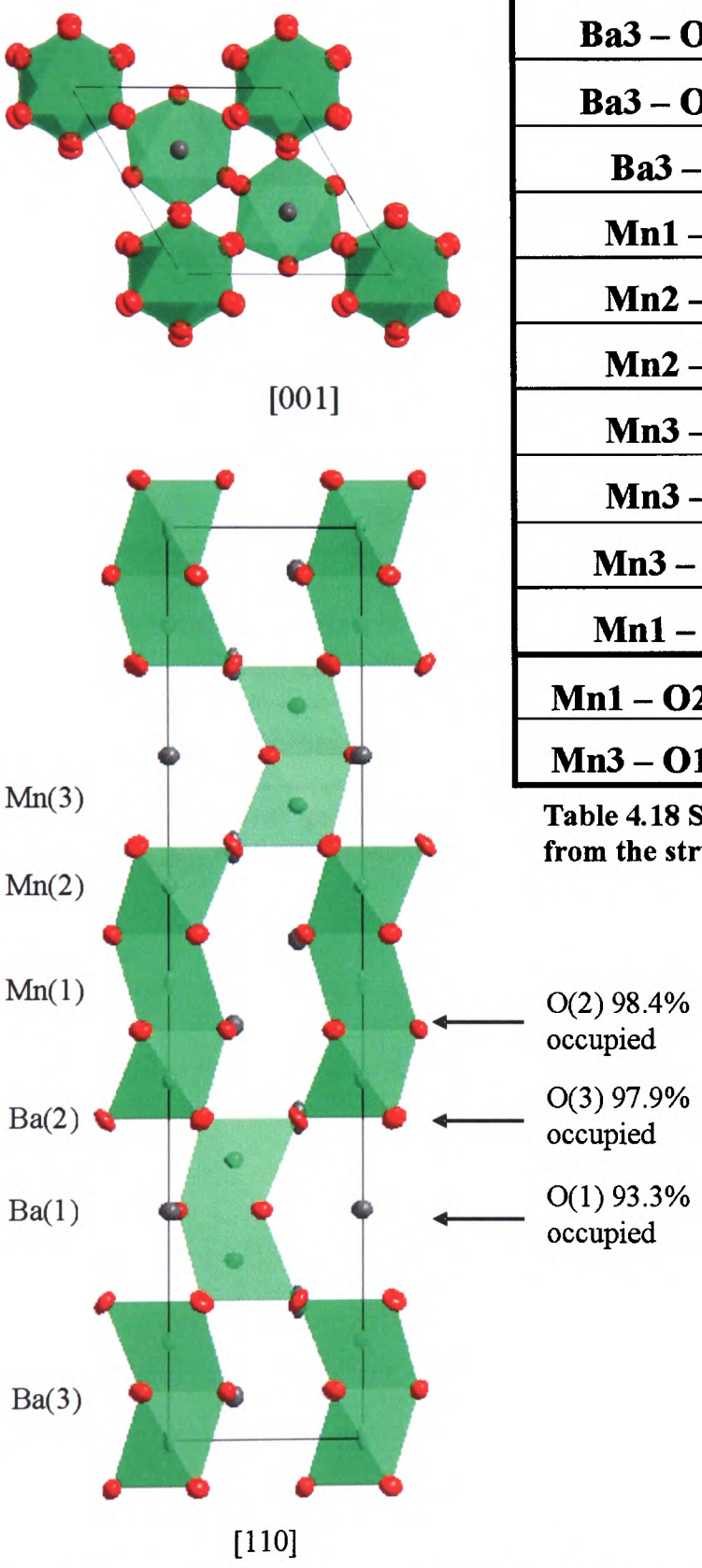


Figure 4.12 Refined structure of 10H-$BaMnO_{2.91(1)}$.

Bond	Bond Length(Å)/angle(°)
Ba1 – O1	2.83489(8)
Ba1 – O3	2.8275(4)
Ba2 – O1	2.971(1)
Ba2 – O2	2.886(1)
Ba2 – O3	2.82751(6)
Ba3 – O2(6x)	2.83578(8)
Ba3 – O2(3x)	2.9393(8)
Ba3 – O3	2.8979(9)
Mn1 – O2	1.8959(4)
Mn2 – O2	1.9268(8)
Mn2 – O3	1.9199(7)
Mn3 – O1	1.9118(8)
Mn3 – O3	1.9298(8)
Mn3 – Mn3	2.547(2)
Mn1 – Mn2	2.4865(1)
Mn1 – O2 – Mn2	81.09(3)
Mn3 – O1 – Mn3	83.54(5)

Table 4.18 Selected bond lengths and angles extracted from the structure of 10H-$BaMnO_{2.91(1)}$.

Atom	Position	Variable	$BaMnO_{2.65(1)}$	$BaMnO_{3.00(1)}$
Ba1	2a (0,0,0)	U_{equiv} ($Å^2$)	0.00241	0.00112
Ba2	2c (⅓,⅔,¼)	U_{equiv} ($Å^2$)	0.00112	0.00088
Mn	4f (⅓,⅔,z)	z	0.60855(9)	0.61274(8)
		U_{equiv}	0.00085	0.00082
O1	6g (½,0,0)	Fractional Occupancy	0.971(3)	0.980(2)
		U_{equiv} ($Å^2$)	0.00145	0.00110
O2	6h (x,2x,¼)	x	-0.18961(5)	-0.18715(3)
		Fractional Occupancy	0.760(2)	0.987(2)
		U_{equiv} ($Å^2$)	0.00152	0.00107
***a* (Å)**			5.6833(2)	5.6376(2)
***c* (Å)**			9.3556(4)	9.2241(3)
χ^2			1.693	1.730
wRp			5.53%	5.83%
Rp			5.04%	5.04%
Refined stoichiometry			$BaMnO_{2.59(1)}$	$BaMnO_{2.95(1)}$
Titrated stoichiometry			$BaMnO_{2.65(1)}$	$BaMnO_{3.00(1)}$

Table 4.19 Structural parameters refined against neutron powder diffraction data collected from 4H-$BaMnO_{2.65(1)}$ and 4H-$BaMnO_{3.00(1)}$. The model is in the space group $P6_3/mmc$.

Atom	Position	Variable	$Ba_{0.5}Sr_{0.5}MnO_{2.79(1)}$	$Ba_{0.5}Sr_{0.5}MnO_{2.99(1)}$
Ba/Sr1	2a (0,0,0)	Fractional Occupancy	0.67(1)/0.33(1)	0.68(1)/0.32(1)
		U_{equiv} ($Å^2$)	0.00259	0.00115
Ba/Sr2	2c (⅓,⅔,¼)	Fractional Occupancy	0.33(1)/0.67(1)	0.32(1)/0.68(1)
		U_{equiv} ($Å^2$)	0.00146	0.00110
Mn	4f (⅓,⅔,z)	z	0.6091(2)	0.6112(2)
		U_{equiv} ($Å^2$)	0.00081	0.00080
O1	6g (½,0,0)	Fractional Occupancy	1	1
		U_{equiv} ($Å^2$)	0.00191	0.00123
O2	6h (x,2x,¼)	x	-0.1861(1)	-0.1839(1)
		Fractional Occupancy	0.852(4)	0.978(5)
		U_{equiv} ($Å^2$)	0.00159	0.00088
***a* (Å)**			5.58539(8)	5.5528(1)
***c* (Å)**			9.2123(1)	9.1471(2)
χ^2			4.070	5.168
wRp			4.11%	5.26%
Rp			3.10%	4.03%
Refined stoichiometry			$Ba_{0.5}Sr_{0.5}MnO_{2.77(1)}$	$Ba_{0.5}Sr_{0.5}MnO_{2.96(1)}$
Titrated stoichiometry			$Ba_{0.5}Sr_{0.5}MnO_{2.79(1)}$	$Ba_{0.5}Sr_{0.5}MnO_{2.99(1)}$

Table 4.20 Structural parameters refined against neutron powder diffraction data collected from 4H-$Ba_{0.5}Sr_{0.5}MnO_{2.79(1)}$ and 4H-$Ba_{0.5}Sr_{0.5}MnO_{2.99(1)}$. The model is in the space group $P6_3/mmc$.

Bond	Bond Length(Å)/angle(°)			
	$BaMnO_{2.65(1)}$	$Ba_{0.5}Sr_{0.5}MnO_{2.79(1)}$	$BaMnO_{3.00(1)}$	$Ba_{0.5}Sr_{0.5}MnO_{2.99(1)}$
Ba/Sr1 – O1	2.8417(1)	2.793(1)	2.8188(1)	2.776(1)
Ba/Sr1 – O2	2.9924(4)	2.923(1)	2.9424(2)	2.891(1)
Ba/Sr2 – O1	2.8570(9)	2.811(1)	2.82249(9)	2.793(1)
Ba/Sr2 – O2	2.8506(1)	2.799(1)	2.8259(1)	2.781(1)
Mn – O1	1.9295(5)	1.900(1)	1.9313(4)	1.898(1)
Mn – O2	1.9372(7)	1.927(2)	1.9081(6)	1.917(1)
Mn – Mn	2.647(2)	2.596(3)	2.532(2)	2.539(3)
Mn – O2 - Mn	86.17(4)	84.69(1)	83.14(4)	82.93(1)

Table 4.21 Selected bond lengths and angles extracted from the structures of 4H-$BaMnO_{2.65(1)}$, 4H-$BaMnO_{3.00}$, 4H-$Ba_{0.5}Sr_{0.5}MnO_{2.79(1)}$ and 4H-$Ba_{0.5}Sr_{0.5}MnO_{2.99(1)}$.

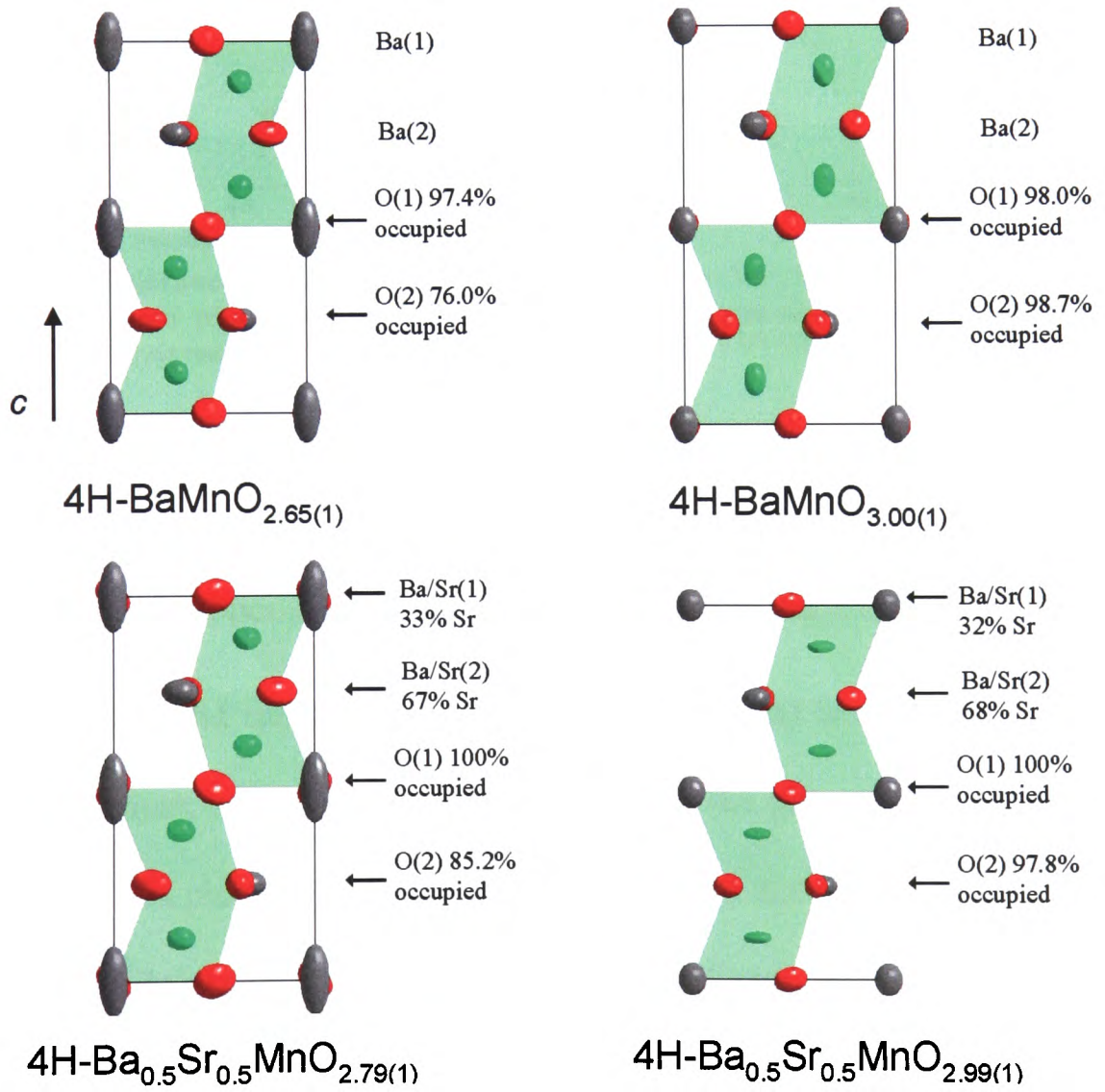


Figure 4.13 Refined structures of 4H-$BaMnO_{2.65(1)}$, 4H-$BaMnO_{3.00}$, 4H-$Ba_{0.5}Sr_{0.5}MnO_{2.79(1)}$ and 4H-$Ba_{0.5}Sr_{0.5}MnO_{2.99(1)}$.

4.4. *Discussion*

4.4.1. The tolerance factor

Neutron diffraction experiments confirm the stacking sequences reported by Negas and Roth and allow the location of the oxide anions and oxide anion vacancies to be determined. This gives accurate metal-oxygen bond lengths (detailed in Table 4.10 - Table 4.21) from which the tolerance factor *(t)* can be calculated. Figure 4.14a plots *t* for the $Ba(Sr)MnO_{3-x}$ phases against the proportion of cubic layers. A linear relationship is observed.

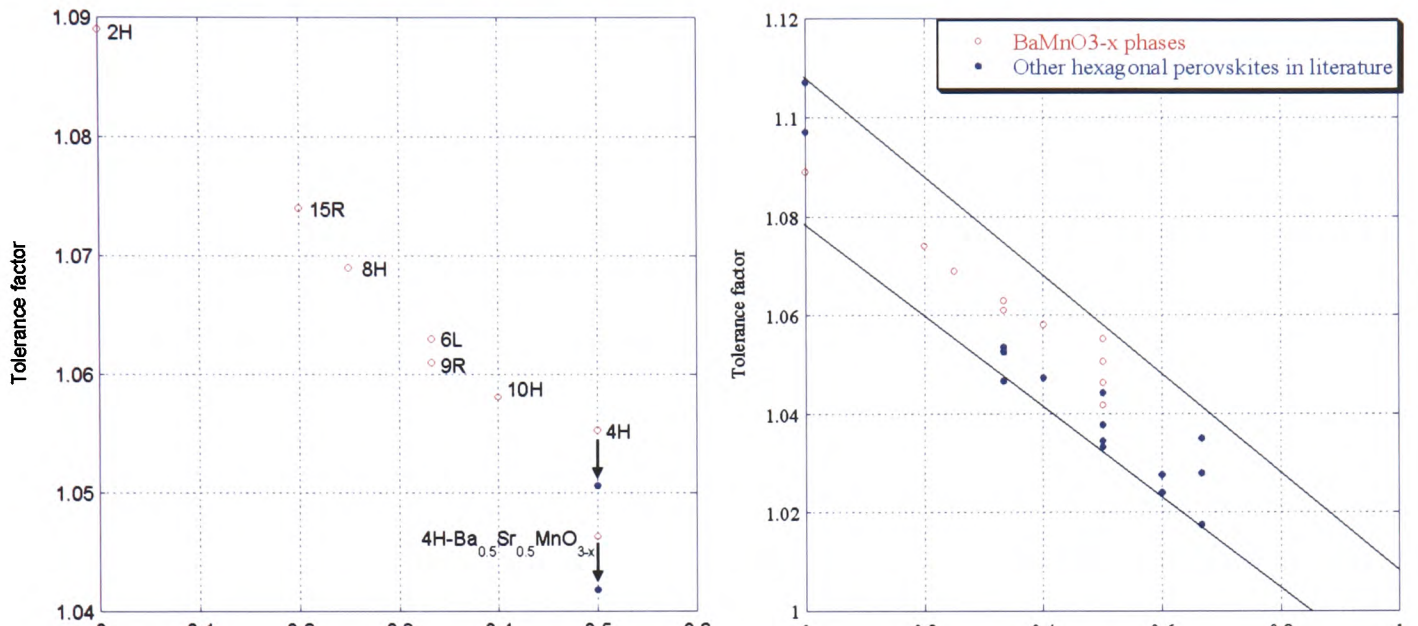


Figure 4.14 a) Tolerance factor of $Ba(Sr)MnO_{3-x}$ phases vs. the proportion of cubic layers. Topotactically oxidised phases are in blue. b) Tolerance factors obtained from neutron diffraction studies of known hexagonal perovskite phases.[5, 35, 37, 38, 48, 49, 69, 72, 110, 111]

Figure 4.14b shows the same data along with comparable data extracted from published models of other hexagonal perovskite phases. This shows the linear relationship between tolerance factor and proportion of cubic layers is valid beyond the $Ba(Sr)MnO_{3-x}$ series.

The average A-O bond length (and so the tolerance factor) is reduced by the substitution of strontium for barium, so for the $Ba_{1-y}Sr_yMnO_3$ series the proportion of cubic layers increases with *y*. Figure 4.15a plots the average Mn-O bond length against the oxygen non-stoichiometry in the 2H → 4H-$BaMnO_{2.65(1)}$ series. There is a clear linear increase in the Mn-O bond length as *x* is increased. The average Mn-O bond length has a direct effect on the value of the tolerance factor (as shown in Equation 1.2). The increase in Mn-O bond length on reduction

reduces the tolerance factor, so the proportion of cubic layers for the $BaMnO_{3-x}$ series increases with x. Thus the magnitude of x is also related to the proportion of cubic layers.

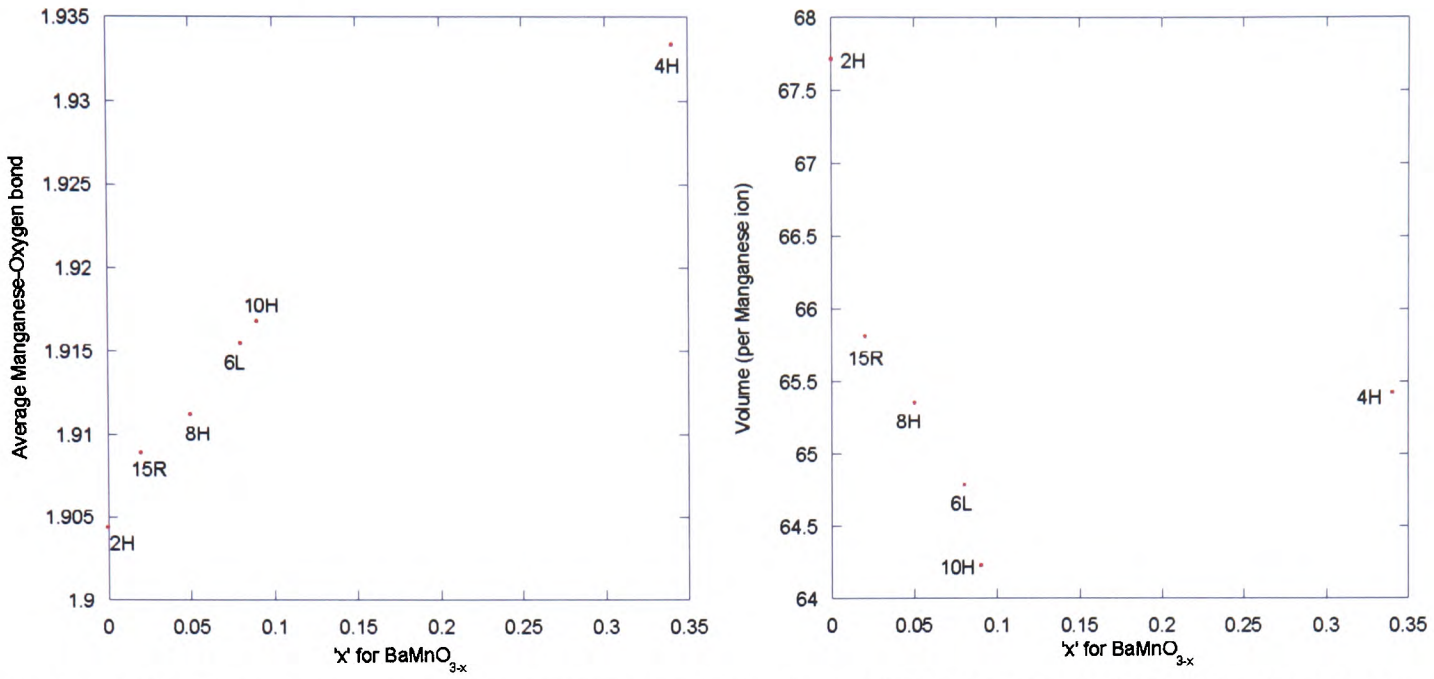


Figure 4.15 a) Average manganese-oxygen bond length or b) Volume per manganese ion vs. oxygen non-stoichiometry.

Figure 4.15b plots the volume of the unit cell (per manganese ion) against x for $BaMnO_{3-x}$. The unit cell volume increases on reduction of 10H-$BaMnO_{2.91(1)}$ to 4H-$BaMnO_{2.65(1)}$, as expected considering the increase in the average Mn-O bond length on reduction. However the volume decreases on reduction from 2H-$BaMnO_{3.00}$ → 10H-$BaMnO_{2.91(1)}$, despite the increase in the Mn-O bond length, implying that the introduction of cubic layers reduces the volume (and so increases the density) of the unit cell.

In the 2H → 4H-$BaMnO_{2.65(1)}$ series, reduction is clearly associated with a change in the stacking sequence. This makes it impossible to separate effects caused by the change in manganese oxidation state from effects caused by the change in the stacking sequence. However the influence of the oxidation state can be isolated from alterations in the stacking sequence using low temperature topotactic oxidations. The average bond lengths of the isostructural pair 4H-$BaMnO_{2.65(1)}$ and 4H-$BaMnO_{3.00(1)}$ are listed in Table 4.22, along with those of 2H-$BaMnO_3$, extracted from reference [4].

	Volume per manganese ($Å^3$)	Average Ba-O bond length (Å)	Average Mn-O bond length (Å)	Tolerance factor
2H-$BaMnO_{3.00}$	67.715(5)	2.9347(2)	1.9044(4)	1.0896
4H-$BaMnO_{3.00(1)}$	63.473(1)	2.8524(2)	1.9197(5)	1.0507
4H-$BaMnO_{2.65(1)}$	65.425(1)	2.8854(4)	1.9334(6)	1.0553

Table 4.22 Average bond lengths and tolerance factors for 4H-$BaMnO_{3-x}$ and 2H-$BaMnO_3$.

Increasing the proportion of hexagonal layers while conserving the manganese oxidation state (changing 4H-$BaMnO_{3.00(1)}$ to 2H-$BaMnO_{3.00}$) increases the unit cell volume and the average Ba-O bond length (so the tolerance factor is increased), but has little effect on the average Mn-O bond length. Conversely, topotactic oxidation in which the manganese oxidation state is increased while the structure is conserved (changing 4H-$BaMnO_{2.65(1)}$ to 4H-$BaMnO_{3.00(1)}$) reduces the average Mn-O bond length. This reduces the unit cell volume and thus the average Ba-O bond length. If oxidation is carried out at a high temperature, the system will adjust in order to relieve the strain introduced by the contraction of the Ba-O bonds. This is achieved by increasing the proportion of hexagonal layers. Competition between the increasing cell volume due to reduction and decreasing volume due to the increased proportion of cubic layers can account for the non-linear relationship between x and the cell volume observed in Figure 4.15b.

The relationships between x, t and the proportion of cubic layers in the stacking sequence are relatively well understood, but often the proportion of cubic layers in the stacking sequence does not unambiguously determine the stacking sequence. The formation of 9R-$BaMnO_3$ and 6L-$BaMnO_{3-x}$ suggests that the nature of the stacking sequence is dependent on the presence and location of oxide vacancies.

4.4.2. Oxide vacancies

4.4.2.1. Location of oxide anion vacancies

The oxide vacancy location can be analysed across the $Ba(Sr)MnO_{3-x}$ series by separating the oxide sites according to their environment. The coordination sphere of each oxide ion spans three layers of the stacking sequence. There are only four three layer stacks which are possible, as there are never two adjacent cubic layers within the structures adopted by $BaMnO_{3-x}$ phases. These four environments are shown in Figure 4.16, labelled A if the oxide ion in the central layer of a *chc* stack, B for the *hch* stack, C for the *hhc* stack and D for the *hhh* stack. The description of the environment is valid for barium ions as well as for oxide ions.

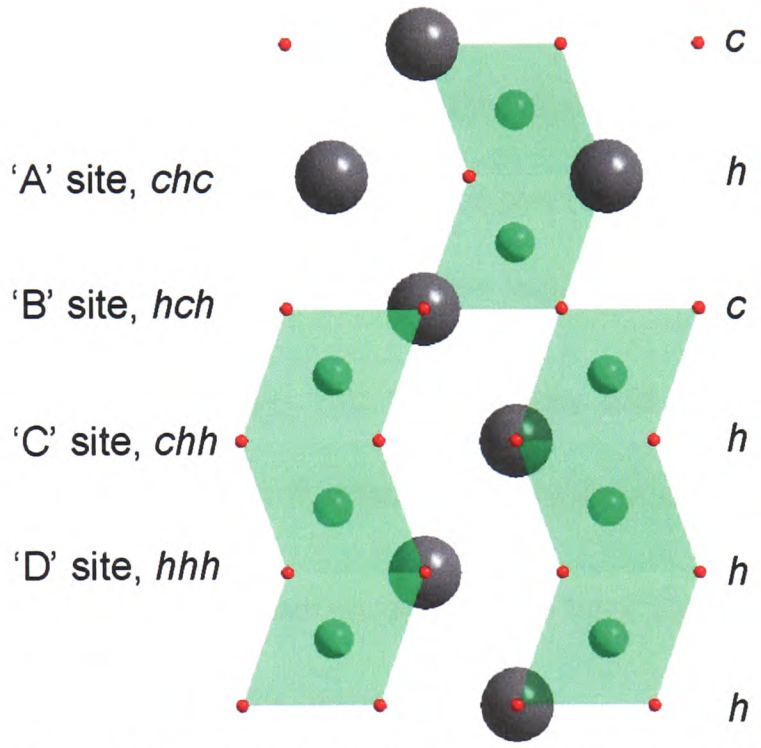


Figure 4.16 Available oxide environments in $BaMnO_{3-x}$ hexagonal perovskite structures.

The oxide occupancy numbers for each environment (A, B, C and D) are listed in Table 4.23. By organising the occupancy numbers by environment, several trends are observed. The cubic layer (containing B oxide sites) generally has the highest occupancy. This contradicts the Gonzalez-Calbet model described in Section 4.1, but is consistent with the neutron diffraction investigation of oxide anion distribution in 4H-$Ba_{0.5}Sr_{0.5}MnO_{2.84}$.[109] In fact site A (describing the layer in the centre of a dimer of face-sharing MnO_6 octahedra) appears to be the most favoured location for an oxide anion vacancy.

Oxide anion environment	4H	10H	6L	9R	8H	15R	Average
A - *chc*	0.760(2)	0.933(2)	0.927(6)	/	/	/	0.873
B - *hch*	0.971(3)	0.979(2)	0.998(4)	1	1	1	0.991
C - *hhc*	/	0.984(2)	0.984(6)	1	0.977(1)	0.988(1)	0.987
D - *hhh*	/	/	0.952(8)	/	0.979(2)	1.000(1)	0.977

Table 4.23 Oxygen occupancies by oxide anion environment for Ba(Sr)MnO_{3-x} phases. The oxide anion environments are depicted in Figure 4.16.

4.4.2.2. Rationalisation of oxide anion vacancy location

In order to rationalise the location of the oxide anion vacancies in the hexagonal layers and particularly in the A site, it is necessary to consider the coordination requirements of the entire structure.[112, 113] The most energetically favourable sites for oxide vacancies are likely to be those where the effect of removing an oxide ion causes the least disruption to the structure. On introducing oxide vacancies, three major effects are expected:

- For every oxide anion vacancy, two Mn(IV) ions will be reduced to Mn(III). This will result in an increase in the Mn-O bond length, as discussed in Section 4.4.1.
- The coordination spheres of barium ions which have lost an oxide ion will contract, so as to balance the valence of the barium ions.
- If a vacancy is introduced to the shared face joining two MnO_6 octahedra, the manganese ions will have an increased repulsion, due to the loss of shielding anions between them.

The location of the oxide vacancies depends on the requirements of both the barium and the manganese ions. The valence of the manganese ions is reduced, but that of the barium ions is not. Therefore in order to minimise the disruption to the structure the oxide anions removed should be those which have the greatest effect on the manganese coordination sphere and the

smallest effect on the barium coordination sphere. These oxide sites may be identified by considering the bond valence sums about the oxide anions.

Bond valence sums, described in Section 2.5 represent a comparison of the number and length of bonds in the coordination sphere of a specific site with those of other phases containing the same ions. Bond valence sums are generally used to identify the valence of the central atom, but also useful for indicating the relative strengths of bonding interactions.

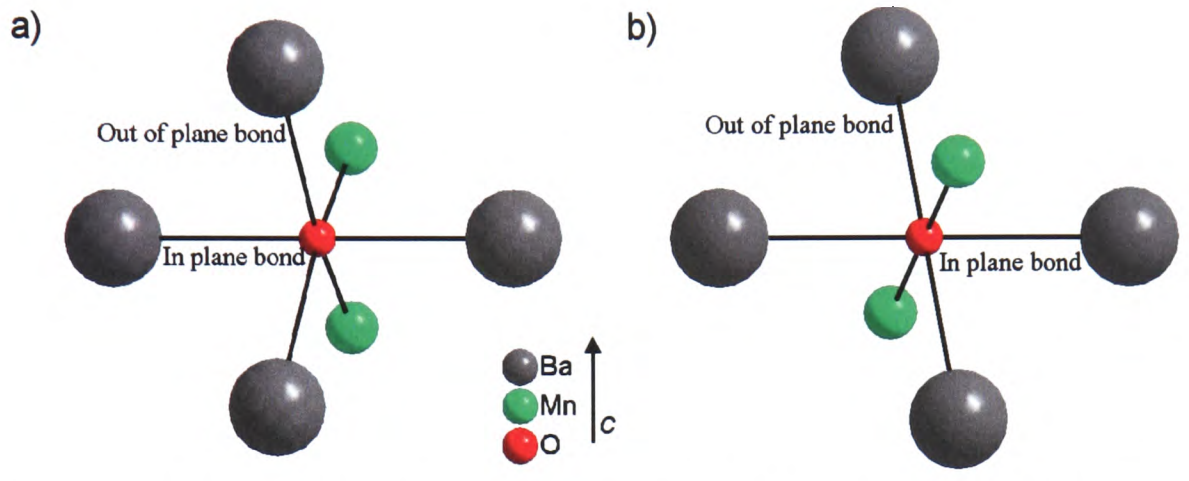


Figure 4.17 Coordination spheres of oxide ions in a) a hexagonal layer and b) a cubic layer.

The coordination spheres of oxide anions in hexagonal perovskite structures, shown in Figure 4.17, are approximately octahedral, containing four Ba-O bonds and two Mn-O bonds. The bond valence sum of an oxide ion is thus composed of two parts: a contribution from four Ba-O bonds, and a contribution from two Mn-O bonds. The oxide anions which have the greatest effect on the manganese coordination spheres will have the shortest Mn-O bonds, and so the greatest contribution to the bond valence sum from manganese bonds. Similarly, those with the smallest effect on the barium coordination spheres will have the longest Ba-O bonds, indicated by the smallest contribution to the bond valence sum from barium. These oxide anions are most easily identified by calculating the difference between the bond valence sum contribution from manganese and the contribution from barium, where a larger number represents a more favourable site for a vacancy. Contributions to the bond valence sum of the oxide ion from barium and manganese, along with the difference between them, are listed according to oxide anion environment in Table 4.24. The total bond valence sum about each

oxide anion is slightly greater than 2, as expected considering the valence of oxygen. Average values of the contribution to the bond valence sum of oxide ions are listed in Table 4.25.

		A - *chc*	**B - *hch***	**C - *hhc***	**D - *hhh***
15R	Contribution from Ba	/	0.825	0.750	0.791
	Contribution from Mn	/	1.263	1.336	1.318
	Difference	/	***0.438***	**0.586**	0.527
8H	Contribution from Ba	/	0.829	0.767	0.828
	Contribution from Mn	/	1.277	1.310	1.325
	Difference	/	***0.448***	**0.543**	0.497
9R	Contribution from Ba	/	0.879	0.835	/
	Contribution from Mn	/	1.286	1.321	/
	Difference	/	***0.407***	**0.486**	/
6L	Contribution from Ba	0.768	0.886	0.791	0.830
	Contribution from Mn	1.315	1.250	1.296	1.333
	Difference	**0.547**	***0.364***	0.505	0.503
10H	Contribution from Ba	0.776	0.895	0.865	/
	Contribution from Mn	1.327	1.282	1.327	/
	Difference	**0.551**	***0.387***	0.462	/
4H	Contribution from Ba	0.739	0.882	/	/
	Contribution from Mn	1.216	1.241	/	/
	Difference	**0.477**	***0.359***	/	/
4H (oxidised)	Contribution from Ba	0.813	0.953	/	/
	Contribution from Mn	1.315	1.235	/	/
	Difference	**0.502**	***0.282***	/	/

Table 4.24 Contribution to the bond valence sums about oxygen anions from barium and from manganese and the difference between the contributions. The site with the greatest difference for each sample is in bold; the site with the smallest difference is in bold and italics.

	A - *chc*	**B - *hch***	**C - *hhc***	**D - *hhh***
Average contribution from Mn	1.293	1.262	1.318	1.325
Average contribution from Ba	0.774	0.878	0.802	0.816

Table 4.25 Average values of the contribution to the oxide bond valence sum from manganese and barium.

Table 4.24 and Table 4.25 show that the B site oxide ions, O_{cub}, have both the smallest contribution from manganese (indicating they have the longest Mn-O bonds, and thus the smallest effect on the manganese coordination spheres) and the largest contribution from barium (indicating they have the shortest Ba-O bonds, and thus the largest effect on the barium coordination spheres). Both factors suggest that the B site is the worst site in which to locate an oxide vacancy. This is confirmed by the data in Table 4.23, in which the oxygen occupancies are listed according to environment and the B site is always close to full occupancy.

The A, C and D oxide ions located in hexagonal layers (O_{hex}) have similar contributions from manganese, but oxide anions located in the A site (O(A)) have a smaller contribution from barium. Thus O(A) anions always have the largest difference between the contribution to the bond valence sum from manganese and the contribution from barium. This suggests that O(A) anions are the most likely to be replaced with a vacancy. Table 4.23 confirms that the majority of the oxide vacancies are located in the A site.

Thus analysis of the contribution of manganese and barium to the bond valence sum of the oxide ions can account for the observed vacancy distribution. This analysis produces two main observations: firstly, that there is a much larger difference in the contribution to the bond valence sum to O_{cub} from barium and from manganese than to O_{hex}; secondly, that of the O_{hex} anions, O(A) anions have the smallest contribution from barium.

4.4.2.2.1. Comparison of O_{cub} with O_{hex}

The difference between the hexagonal and cubic layers (and thus O_{cub} and O_{hex}) is predominantly due to the connectivity of the MnO_6 octahedra. O_{cub} ions are apex-shared, but O_{hex} ions are located in the shared faces linking MnO_6 octahedra. The manganese ions separated by the shared face have a close approach distance, resulting in a high degree of repulsion between them. This repulsion can be minimised by a displacement of the oxide ions composing the shared face such that they shield the manganese ions. The displacement of the

O_{hex} ions to shield the face-sharing manganese ions reduces the Mn-O bond lengths, accounting for the increase in the bond valence sum contribution of manganese to O_{hex}. The energetic penalty for the displacement of O_{hex} is an increase in the Ba-O_{hex} bond length.

4.4.2.2.1.1. Ba-O bond lengths

The barium-oxygen bonds can be separated into two classes. The oxide coordination sphere contains four barium ions (Figure 4.16). Two are located within the same layer in the *ab* plane (connected by in plane bonds) and one is located in each of the adjacent layers along the *c* axis (connected by out of plane bonds). Alternatively, each barium ion has a coordination sphere of twelve oxide anions: six connected by in plane bonds; three located in each of the adjacent layers, connected by out of plane bonds. The coordination spheres for barium ions are shown in Figure 4.18.

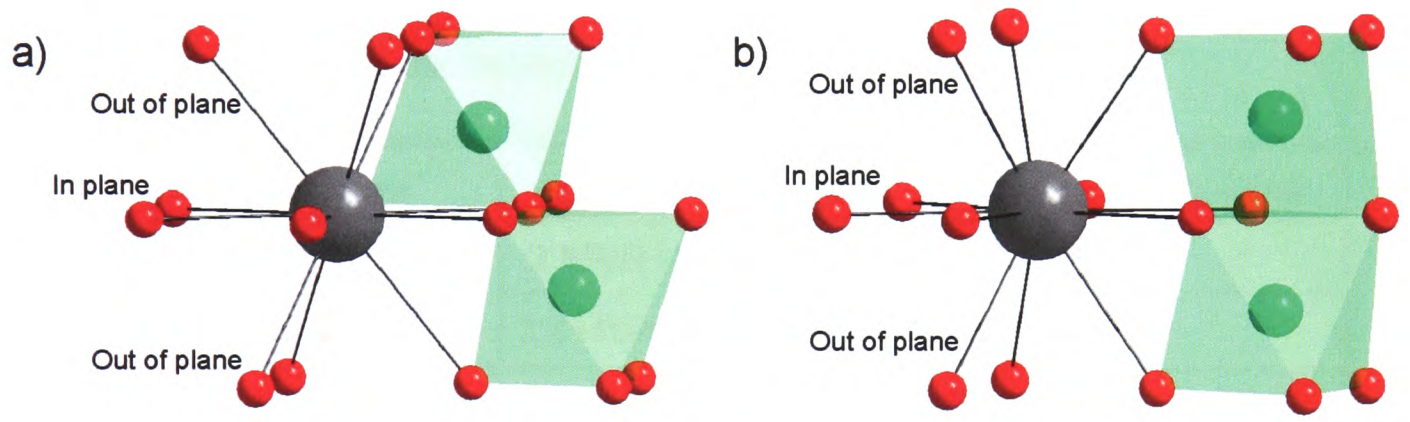


Figure 4.18 Barium coordination spheres for a) Barium ions in cubic layers and b) Barium ions in hexagonal layers.

The displacement of O_{hex} would be expected to affect the in plane Ba-O_{hex} bond length, but in fact the symmetry of the unit cell results in a much greater effect on the out of plane Ba-O_{hex} bond length. The situation is shown in Figure 4.19. For the perfect case in which hexagonal oxide ion layers are identical to the symmetric cubic oxide layers, there is no difference in bond lengths between the different layers. Displacement of the hexagonal oxide anions to provide greater shielding between face-sharing manganese ions extends the out of plane bond length to barium ions in adjacent layers, yet has a relatively small effect on the in plane bond lengths. The extreme example in Figure 4.19 accentuates the effect of the shielding.

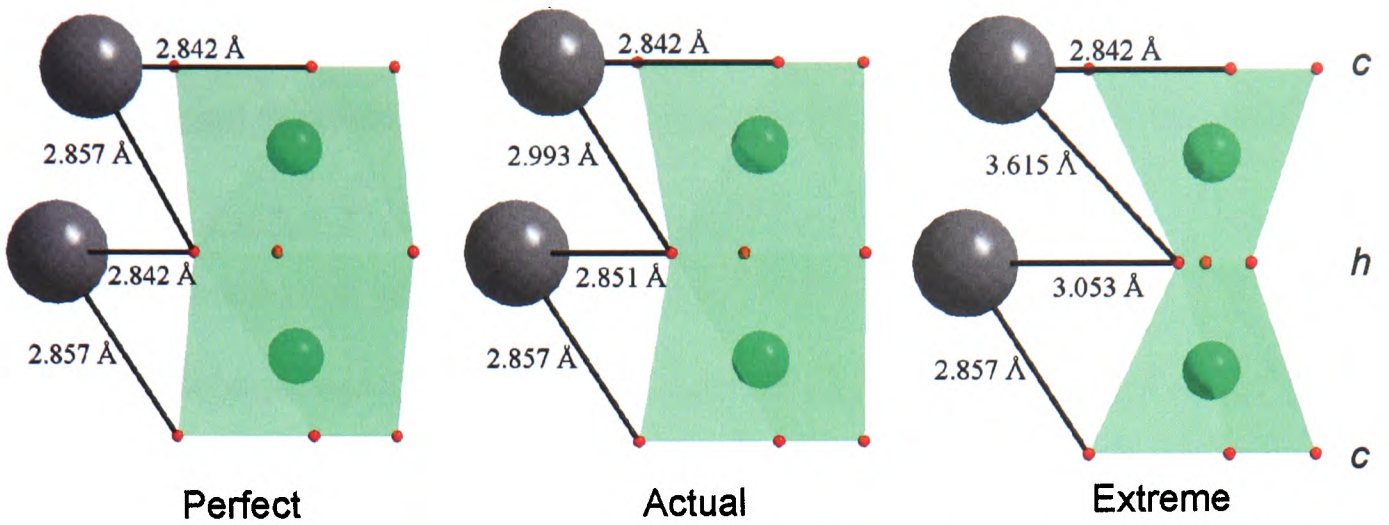


Figure 4.19 In and out of plane barium oxygen bond lengths for the 4H-$BaMnO_{2.65(1)}$ *chc* dimer. In the perfect case, the hexagonal oxide layer is displaced by exactly ($-^1/_6$, $-^1/_3$, $^1/_4$) from the cubic oxide layer. In the extreme case, the hexagonal layer provides greater shielding to the manganese ions.

Table 4.26 lists the in plane barium-oxygen bonds by plane type and confirms that all in plane barium-oxygen bonds are approximately equal regardless of the overall stacking sequence of the sample or the position of the layer within the stacking sequence. Due to the different A site cations and necessary disorder caused by this, the $Ba_{1-y}Sr_yMnO_3$ phases are excluded in order to highlight trends within the $BaMnO_{3-x}$ series.

Structure	A - *chc*	B - *hch*	C – *chh*	D - *hhh*
4H-$BaMnO_{2.65(1)}$	2.8506(1)	2.8417(1)	/	/
10H-$BaMnO_{2.91(1)}$	2.83489(8)	2.82751(6)	2.83578(8)	/
6L-$BaMnO_{2.92(1)}$	2.8390(1)	2.83129(7)	2.8396(1)	2.8361(1)
8H-$BaMnO_{2.95(1)}$	/	2.83680(5)	2.84616(7)	2.84153(6)
15R-$BaMnO_{2.99(1)}$	/	2.83956(8)	2.8492(1)	2.84445(9)
Average	**2.841**	**2.835**	**2.843**	**2.841**

Table 4.26 In plane barium-oxygen bond lengths (Å) for the different environments in $BaMnO_{3-x}$ phases.

The displacement of the oxide ions composing the shared face does have a large effect on the out of plane bond lengths. In the highly symmetric 4H structure, the two out of plane bond lengths are very different, with Ba_{cub}-O_{hex} = 2.9924(4) Å and Ba_{hex}-O_{cub} = 2.8570(9) Å. This demonstrates that the displacement of O_{hex} so as to shield the manganese greatly increases the out of plane Ba-O_{hex} bond length. Thus the displacement of O_{hex} ions reduces the Mn-O_{hex} bond length and increases the Ba-O_{hex} bond length. This increases the bond valence sum

contribution from manganese and reduces the contribution from barium, accounting for the observations used to rationalise the full occupancy of the cubic oxide sites in Section 4.4.2.2.

4.4.2.2.2. Oxide anions located in hexagonal layers

The second observation discussed in Section 4.4.2.2 in order to account for the preferred vacancy distribution was that the A site oxide ion has the smallest contribution to the bond valence sum from barium of all the O_{hex} anions. The out of plane Ba-O_{hex} bond lengths are compared in Table 4.27. This reveals that the bond lengths are longest for oxide ions located in the A site, reflecting the reduced bond valence sum contribution.

	A - *chc*	**C – *chh***		**D - *hhh***	
	<u>chc</u>	***<u>chh</u>***	***chh***	***(c)<u>hhh</u>***	***(c)hhh***
4H-$BaMnO_{2.65(1)}$	2.992	/	/	/	/
10H-$BaMnO_{2.91(1)}$	2.971	2.886	2.939	/	/
6L-$BaMnO_{2.92(1)}$	2.975	2.887	3.021	2.912	/
8H-$BaMnO_{2.95(1)}$	/	2.912	3.029	2.907	/
15R-$BaMnO_{2.99(1)}$	/	2.915	3.062	2.914	2.972
Average	**2.9794**	**2.900**	**3.013**	**2.911**	**2.972**
Average	**2.979**	**2.956**		**2.921**	

Table 4.27 Out of plane Ba-O bond lengths (Å) for different O_{hex} environments A, C and D. The oxide ion is located in the central layer of the stack, and the layers bridged by the barium-oxygen bond are underlined.

Close examination of the structures of $BaMnO_{3-x}$ phases (shown on pages 66 - 77) reveals that the non-equivalence of the out of plane Ba-O_{hex} bonds in Table 4.27 is largely a result of a displacement of the barium ions. The barium ions are always displaced away from the nearest cubic layer, where this is allowed by site symmetry. The extent of this displacement is detailed in Table 4.28, and the direction shown in Figure 4.20. In the case of a *chc* dimer, no displacement of the A site barium ions is possible due to the symmetric nature of the dimer.

Location of Barium	Ba displacement along *c* (from O plane) (Å)					
	4H	**10H**	**6H**	**9R**	**8H**	**15R**
B *(hch)*	0	0.027(2)	0.026(4)	0	0	0
C *(chh)*	/	0.123(1)	0.129(2)	0.117(3)	0.137(1)	0.136(2)
D *(hhh)*	/	/	0	/	0	0.031(2)

Table 4.28 Displacement along the *c* axis of barium ions from the oxygen layer (Å). The displacement is away from the nearest cubic layer. A value of 0 indicates no displacement is possible due to the site symmetry. The A site is excluded, as site symmetry prevents displacement of the barium ions.

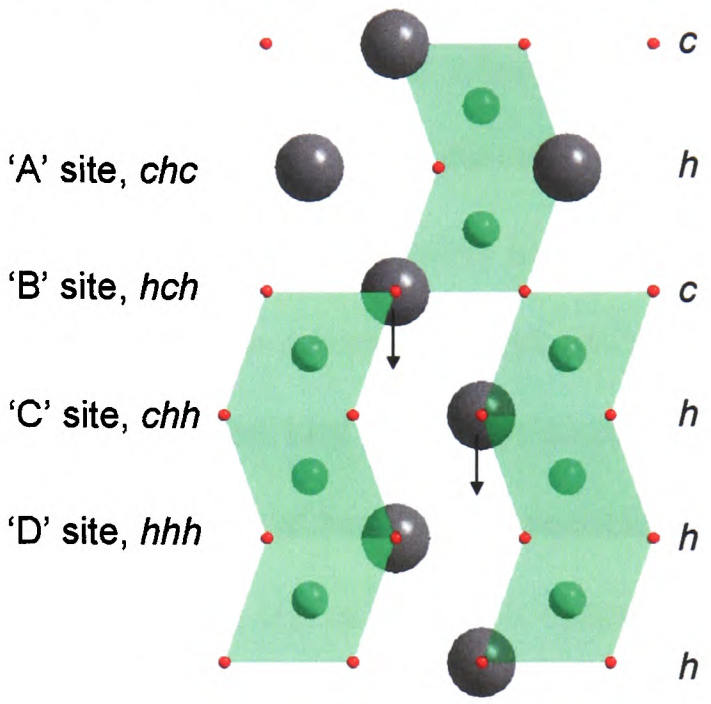


Figure 4.20 Direction of displacement of barium ions (away from the nearest cubic layer).

The effect of displacing the barium ions as shown in Figure 4.20 is to increase out of plane bond lengths of oxide ions in the A site compared to all other Ba-O_{hex} bond lengths. This accounts for the reduced bond valence sum contribution from barium to the O(A) site compared to the other O_{hex} sites.

The barium ion displacement can be rationalised by considering the effect of the cubic layers in reducing the cell volume (and thus the average barium-oxygen bond lengths, as discussed in Section 4.4.1). The contraction of the barium coordination sphere due to the introduction of cubic layers is reflected in the bond valence sums of the barium ions. These are detailed in Table 4.29.

Location of barium ion	Bond valence sum about barium ion					
	4H	4H-oxidised	10H	6L	8H	15R
A- *chc*	2.5796	2.7944	2.781	2.755	/	/
B- *hch*	2.2194	2.4328	2.479	2.488	2.486	2.466
C- *chh*	/		2.471	2.458	2.459	2.439
D- *hhh*	/		/	2.203	2.167	2.187

Table 4.29 Bond valence sums about barium ions, separated according to environment.

Table 4.29 shows that barium ions located in, or adjacent to a cubic layer (Ba(B) and Ba(C)) have a larger bond valence sum than those where the coordination sphere does not span a cubic layer (Ba(D)). Barium ions adjacent to two cubic layers (Ba(A)) have a still larger bond valence sum. The contraction of the coordination sphere indicated by the increased bond valence sum is favourable for barium ions where the coordination sphere accommodates an oxide vacancy. However, the majority of barium ions maintain their full coordination spheres, and the contraction of a full barium ion coordination sphere introduces strain which can be accommodated by displacement of the barium ion away from the cubic layer.

4.4.2.3. Manganese ion repulsion

The significance of the close approach of manganese ions which share faces has previously been alluded to. The oxide ions in the shared faces move so as to shield the manganese ions, minimising the repulsion caused by the close approach. The manganese ions may also be displaced. Mn-Mn separations are listed in Table 4.30. These are clearly much larger between adjacent MnO_6 octahedra which are separated by a cubic, apex-sharing layer than between adjacent MnO_6 octahedra which are separated by a hexagonal layer, but even between face-sharing manganese ions there is significant variation in the Mn-Mn distance. The largest separations are observed for manganese ions located in *chc* units and the smallest separations observed for those located in *hhh* units.

Layer type	Mn-Mn separation						
	4H	4H-oxidised	10H	6L	8H	15R	2H
hch	3.859(1)	3.863(1)	3.850(1)	3.854(1)	3.839(1)	3.846(1)	/
chc	2.647(1)	2.532(1)	2.547(2)	2.538(4)	/	/	/
chh	/	/	2.485(1)	2.479(3)	2.480(1)	2.467(3)	/
hhh	/	/	/	2.422(4)	2.415(1)	2.419(2)	2.4074(1)

Table 4.30 Manganese-manganese separation (Å). Manganese ions are located in the two sets of octahedral holes occurring between the three layer stacks.

In examining the separations between adjacent manganese ions it is important to consider whether the displacement of the manganese ions represents a cause or an effect of the location of the oxide anion vacancies. Average separations between face-sharing manganese ions are of the order of ~ 2.5 Å. A strong repulsion exists between the adjacent manganese ions that are this close, which can be counteracted by displacing the oxide anions composing the shared face to a more central position between the two manganese ions. As discussed above, this increases the shielding between the manganese ions at the expense of increasing the length of the Ba-O bonds. On introducing oxide vacancies into the hexagonal layers, the shielding between face-sharing manganese ions is reduced still further. This is expected to result in a displacement of manganese ions along the *c* axis, away from the shared face. This manganese ion displacement is an effect of the location of the oxide anion vacancies. However, it is likely to be favourable to locate oxide vacancies only where the increased repulsion can be relieved by manganese ion displacement. Therefore although the actual displacement of manganese ions occurs as an effect of the oxide vacancies, the potential to displace the manganese ions represents a cause of the location of the oxide anion vacancies.

When an oxide ion is removed from the shared face, both manganese ions adjacent to this face are subject to an increased repulsion, but only those which are also adjacent to a cubic layer can be displaced so as to minimise this (Table 4.31, Figure 4.21). If manganese ions share two

faces, little or no displacement can occur without increasing the overall Mn-Mn repulsion. Displacement in the *ab* plane could also minimise the Mn-Mn repulsion, but examination of the manganese displacement ellipsoids reveals no evidence of this.

Manganese environment	4H	4H-oxidised	10H	6L	9R	8H	15R
ch(c)	0.3078	0.2262	0.2403	0.229	/	/	/
ch(h)	/	/	0.2598	0.271	0.2418	0.2682	0.2591
hh(c)	/	/	0	-0.0042	0	0.0033	-0.0191
hh(h)	/	/	/	/	/	/	0

Table 4.31 Displacement of Mn along the 3-fold axis away from the epicentre of the two faces (Å). The manganese position is identified by the nature of the two adjacent BaO_3 layers. The third symbol in parentheses describes the next layer in the stacking sequence. Displacement is to the left of the three layer stacking sequence described in the manganese environment column.

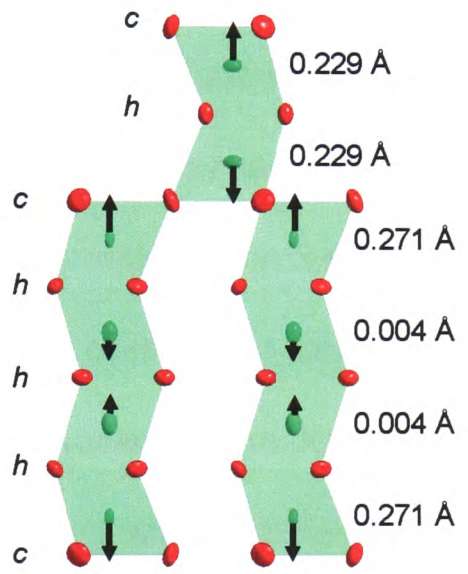


Figure 4.21 Displacement of manganese ions in the 6L structure.

Thus on placing an oxide vacancy in a hexagonal layer, it is favourable if both manganese ions are adjacent to cubic layers. This allows both manganese ions to be displaced so as to minimise the repulsion caused by the removal of the oxide ion. This provides a further rationalisation for the location of the oxide vacancies in the A site of $BaMnO_3$ stacking sequences (where this is available).

4.5. Conclusion

A new model describing oxide anion vacancy distribution in $BaMnO_{3-x}$ phases has been developed and confirmed using neutron powder diffraction techniques, in which oxide anion

vacancies are preferentially located in the A (*chc*) sites within the structure. The location of oxide vacancies in the A site can be shown to be favourable by considering the different coordination requirements of the metal ions, which can be analysed by considering their contribution to the bond valence sums of the oxide anions. Locating the vacancy in a hexagonal layer, rather than a cubic layer, is found to cause minimal disruption to the barium coordination spheres, especially if the hexagonal layer is adjacent to one or more cubic layers. Locating the vacancy in the face-sharing layers increases the repulsion between manganese ions, but if the manganese ions are both adjacent to a cubic layer, this can be minimised by displacement away from the shared face.

This new model provides an explanation for the questions unanswered by the Gonzalez-Calbet model regarding the limiting compositions of the $BaMnO_{3-x}$ stacking sequences and the conditions favouring the adoption of the 9R or 6L stacking sequences. In the presence of a high proportion of vacancies, the 6L structure is favoured over the 9R structure, as although the stacking sequence is more complex, a favourable site is provided for the location of the oxide vacancies. The discrepancies observed on using empirical rule defined in Equation 4.1 can also be accounted for if oxide vacancies are located in the A sites. When the maximum oxide vacancies are located in these sites, the Gonzalez-Calbet relationship between oxide anion vacancies and cubic layers shown in Equation 4.1 is satisfied for the 10H and 6L sequences. The 15R and 8H sequences do not contain the *chc* sites, and so fewer vacancies than predicted by Equation 4.1 are found in 15R-$BaMnO_{3-x}$ and 8H-$BaMnO_{3-x}$. The 4H structure is related to the 6L and 10H structures, but contains twice as many A sites per unit cell. 4H-$BaMnO_{3-x}$ can therefore accommodate many more anion vacancies than predicted by Equation 4.1.

Chapter 5: Magnetic characterisation of $BaMnO_{3-x}$ phases

5.1. *Introduction*

The magnetic behaviour of hexagonal perovskite phases is complex and relatively under-investigated. The mixture of cubic and hexagonal stacking results in several different magnetic exchange pathways between adjacent B cations. Magnetic coupling can occur between B cations connected by face-sharing using two different mechanisms: direct exchange, where unpaired electrons interact by direct overlap of the B cation t_{2g} orbitals (Figure 5.1a, Figure 5.2a); and a 90° superexchange, where unpaired electrons interact indirectly via the oxygen 2p orbitals (Figure 5.1b, Figure 5.2b). Magnetic coupling can occur between B cations connected by apex-sharing through 180° superexchange pathways (Figure 5.1c). B cations may also interact magnetically with those in adjacent face-sharing chains (Figure 5.1d).

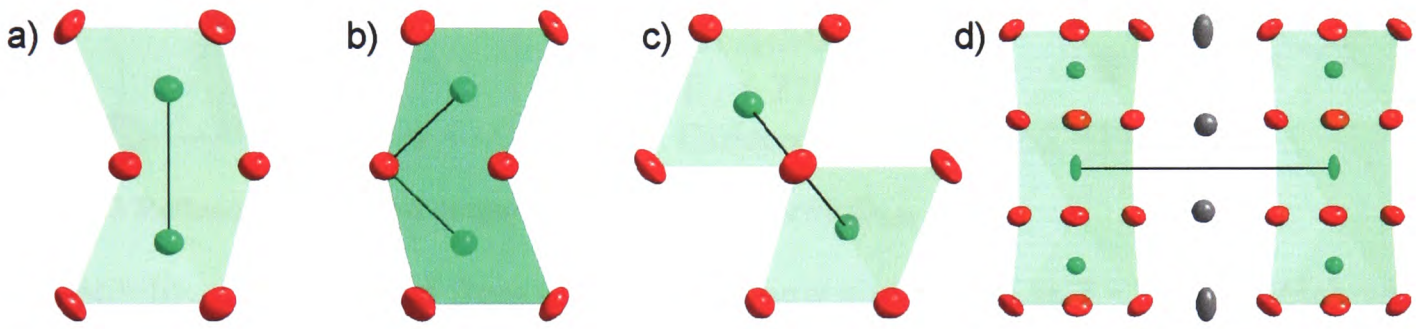


Figure 5.1 Magnetic exchange pathways in hexagonal perovskites: a) Direct exchange between face-sharing B cations; b) 90° superexchange between face-sharing B cations; c) 180° superexchange between apex-sharing B cations; d) Interchain interaction.

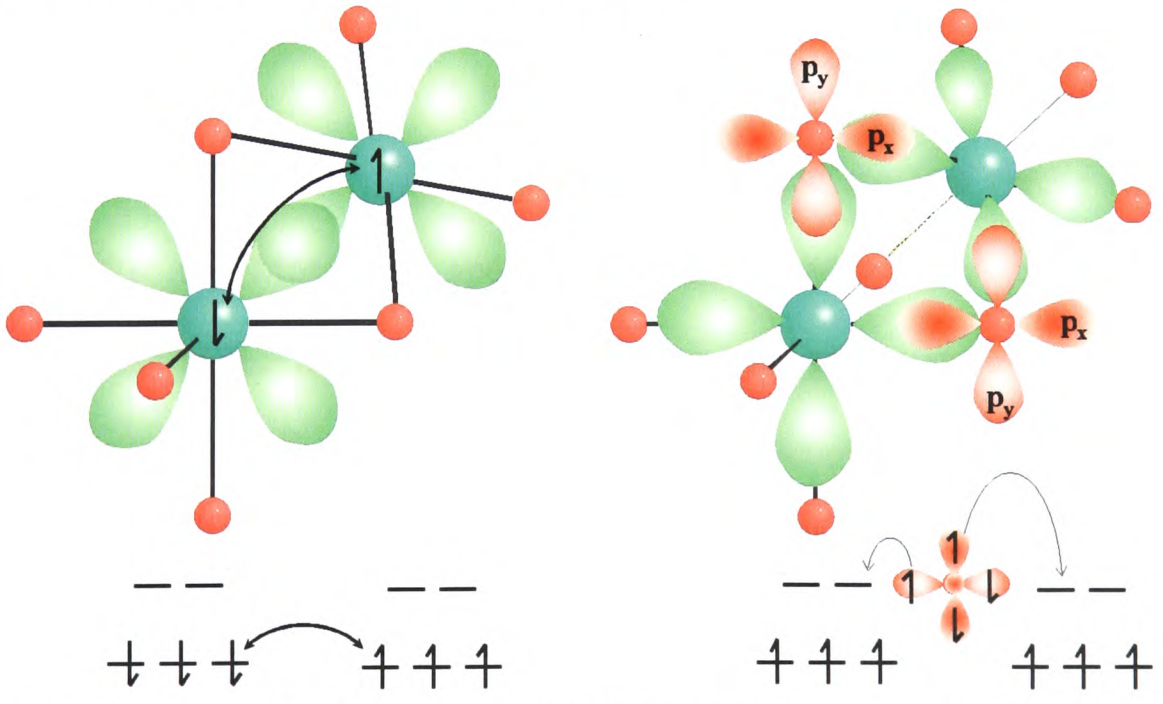


Figure 5.2 Magnetic interactions between face-sharing manganese ions: a) antiferromagnetic direct exchange between two singly occupied t_{2g} orbitals; b) ferromagnetic 90° superexchange between two empty $d_{x^2-y^2}$ orbitals.

An indication of the relative strengths of the different coupling mechanisms may be gained from previous studies on the magnetic behaviour of phases adopting hexagonal perovskite structures. In particular, the magnetic behaviour of 4H-$SrMnO_3$ and 2H-$BaMnO_3$ is both well documented and highly relevant to the Ba(Sr)MnO_{3-x} series.

5.1.1. 4H-$SrMnO_3$

The 4H structure is composed of dimers of face-sharing MnO_6 octahedra, connected to one another via apex-sharing. The structure (and magnetic model) of 4H-$SrMnO_3$ is shown in Figure 5.3.[5, 67]

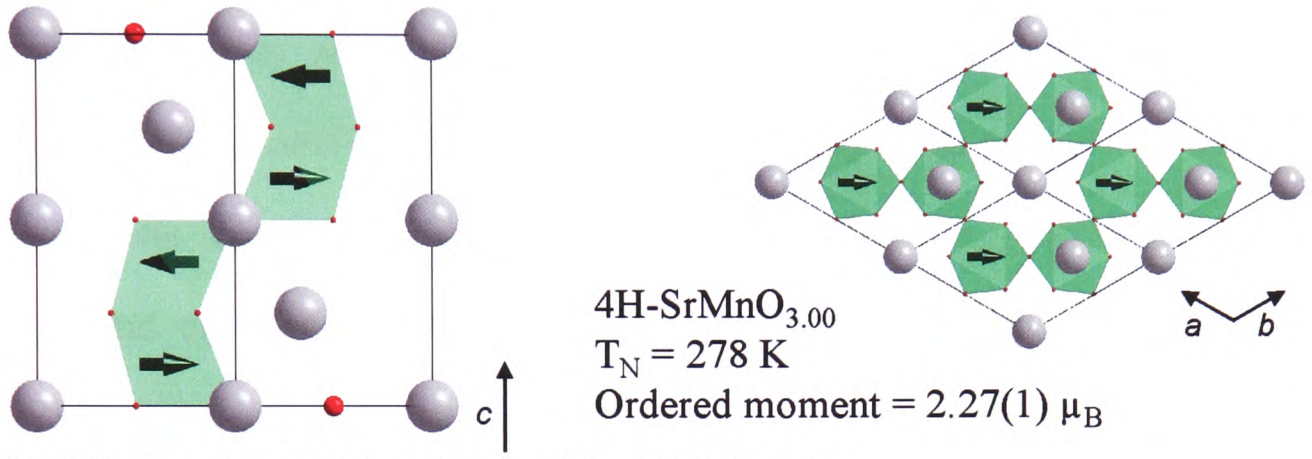


Figure 5.3 Refined nuclear and magnetic model for 4H-$SrMnO_{3.00}$.

Susceptibility data collected from 4H-$SrMnO_3$ show a transition at T ~ 350K, which was once thought to correspond to the Néel temperature.[100] This is contradicted by neutron diffraction data, which show no evidence of long-range magnetic order at 298K.[66] Variable temperature Mössbauer spectroscopy, carried out on a sample of 4H-$SrMnO_3$ in which ~ 1.3% of the manganese was substituted for ^{57}Fe, has been used to find the true Néel temperature, T_N = 278K.[5] At 278K the Mössbauer spectra split into a sextet due to hyperfine magnetic interactions related to the onset of magnetic order. This temperature also corresponds to a slight divergence between zero-field-cooled and field-cooled susceptibility data, and on cooling below 278K, additional intensity is observed in the neutron diffraction data.[66] An antiferromagnetic magnetic model based on that found for 4H-$Ba_{0.1}Sr_{0.9}MnO_{2.96}$ provides a

good fit to the additional intensity.[66, 109] In this model the magnetic moments lie in the *ab* plane and are antiferromagnetically aligned along the *c* axis.

The true Néel temperature, T_N = 278K, must be reconciled with the magnetic susceptibility data. Typically, a maximum in the susceptibility data is associated with T_N, but in susceptibility data collected from 4H-$SrMnO_3$ a maximum is observed at T ~ 350K and there is little signature of a magnetic event at 278K.

The reported magnetic behaviour has been rationalised on the basis of a model in which the manganese ions couple across the shared faces at T ~ 350K. This results in a system in which all magnetic moments are antiferromagnetically coupled (accounting for the observed transition in the susceptibility data), but there is no long-range magnetic order. This local antiferromagnetic coupling is not observable via Mössbauer spectroscopy or neutron diffraction, and the 180° superexchange interaction which connects the antiferromagnetic dimers is not strong enough to bring about long-range magnetic order at T = 350K. On cooling to T ~ 278K, the 180° superexchange interaction is strong enough to connect the antiferromagnetically coupled dimers. This results in long-range magnetic order, which is observable using neutron diffraction or Mössbauer spectroscopy. The magnetic system is shown in Figure 5.4.

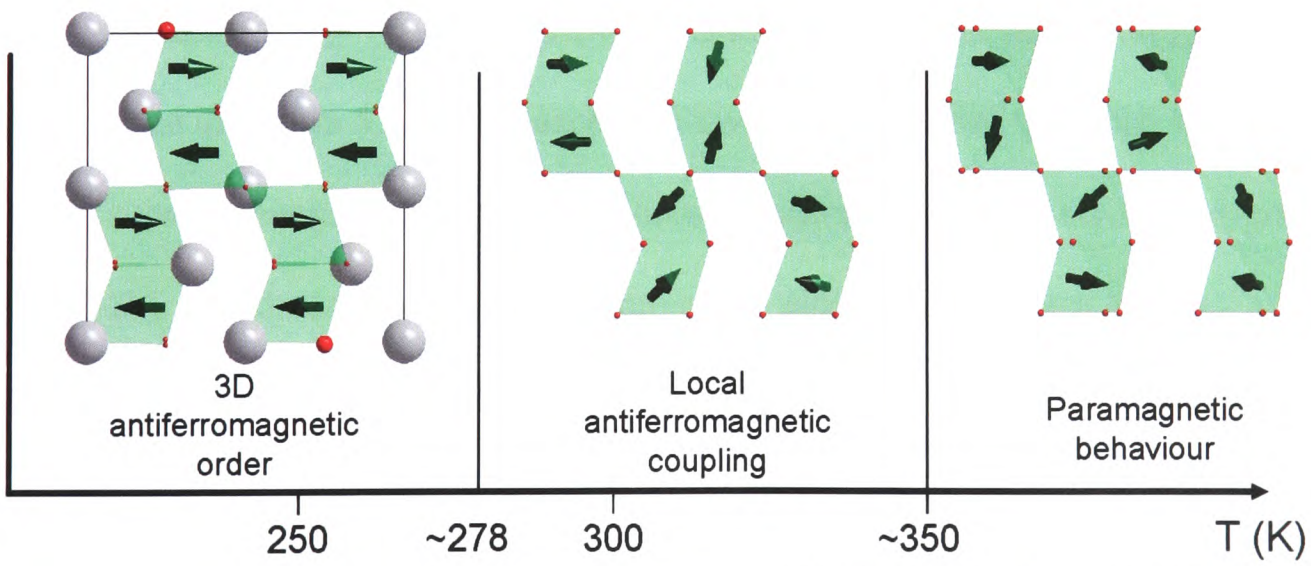


Figure 5.4 Representation of the three magnetic states of 4H-$SrMnO_3$. Above 350K, the system is expected to be paramagnetic. Below 350K, manganese ions are coupled across the shared face into antiferromagnetic pairs, but no long-range order exists. Below ~ 278K, interactions between the dimers result in a fully ordered magnetic system.

Thus the magnetic behaviour of 4H-$SrMnO_3$ can be rationalised on the basis of two magnetic interactions of different strengths. First the stronger interaction across the shared face results in local antiferromagnetic coupling. At a lower temperature the 180° superexchange interaction is strong enough to achieve long-range antiferromagnetic order.

5.1.2. 2H-$BaMnO_3$ and 2H-$BaCoO_3$

The 2H structure has no cubic stacking and so B cations are connected into isolated face-sharing chains. The different B-O-B connectivity alters the magnetic behaviour from that discussed above for 4H-$SrMnO_3$. However, reported magnetic susceptibility data collected from 2H-$BaMnO_3$ are consistent with the magnetic moments coupling antiferromagnetically in the high temperature region.[4] This is likely to be a result of strong magnetic interactions between manganese ions which share faces, as observed for 4H-$SrMnO_3$. No evidence of long-range magnetic order is observed via neutron diffraction at $T > 298K$.

2H-$BaCoO_3$ shows very different behaviour. Reported susceptibility data collected from 2H-$BaCoO_3$ can be modelled using the Curie-Weiss paramagnetic model in the range $T > 250K$. The positive Weiss constant indicates that the magnetic interactions are predominantly ferromagnetic.

The magnetic behaviour of 2H-$BaMnO_3$ and 2H-$BaCoO_3$ can be rationalised by considering the two mechanisms by which magnetic interactions between face-sharing B cations may occur, depicted in Figure 5.2. Direct exchange involves overlap of the metal t_{2g} orbitals (Figure 5.2a). 90° superexchange requires overlap between the metal e_g orbitals and oxygen p orbitals (Figure 5.2b). Octahedral Mn(IV) ions have the electronic configuration $t_{2g}^3e_g^0$, so direct exchange between the three half filled t_{2g} orbitals favours an antiferromagnetic interaction that is expected to be strong compared to the 90° superexchange interaction involving the empty e_g orbitals. The Goodenough-Kanamori-Anderson rules predict that 90° superexchange between empty e_g orbitals will result in a ferromagnetic interaction,[99] so the antiferromagnetic coupling

observed for 2H-$BaMnO_3$ and 4H-$SrMnO_3$ suggests that direct exchange is the stronger interaction for Mn(IV) systems.

The Co(IV) in 2H-$BaCoO_3$ is reported to have a low spin $t_{2g}^5 e_g^0$ configuration on the basis of band structure calculations and susceptibility data.[45, 114] As two of the t_{2g} orbitals are filled, the strength of the direct exchange interaction is greatly reduced. Paramagnetic behaviour, rather than antiferromagnetic behaviour, is reported at 300K. The Weiss constant is positive, indicating that the strongest magnetic interactions present are ferromagnetic. These interactions are presumably a result of 90° superexchange, now the strongest magnetic interaction (although not sufficient to ferromagnetically couple the magnetic moments).

No B-O-B pathway exists between the chains of face-sharing B cations in the 2H structure. Because of this, conventional exchange mechanisms suggest that compounds with 2H structures are one-dimensional magnetic systems. However, neither 2H-$BaMnO_3$ nor 2H-$BaCoO_3$ is considered a one-dimensional magnetic system as the inter-chain coupling is relatively strong. At 59K inter-chain interactions in 2H-$BaMnO_3$ bring about three-dimensional magnetic order despite the lack of Mn-O-Mn connectivity between the chains. The magnetic structure of 2H-$BaMnO_3$ is shown in Figure 5.5, in which the B cation chains are related magnetically by a 120° spin structure.

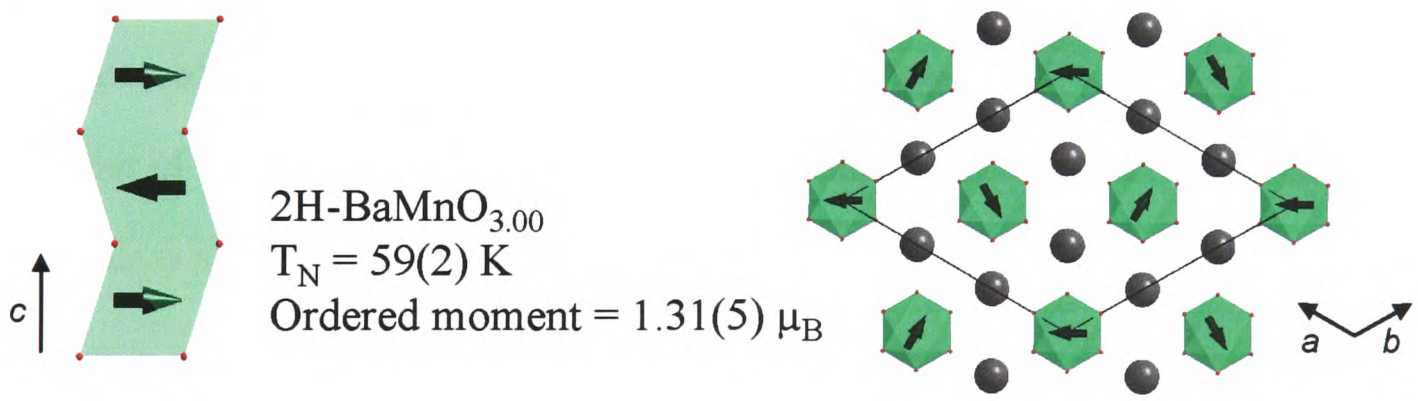


Figure 5.5 The magnetic structure of 2H-$BaMnO_3$.

The magnetic behaviour of 2H-$BaCoO_3$ is more complex. Muon-spin rotation and relaxation techniques have been used to suggest that local ferromagnetic order within the chains occurs at

T ~ 53K, and a transition to a two-dimensional antiferromagnetic state occurs at T ~ 15K.[115] Low temperature neutron diffraction reveals additional reflections attributed to the fully ordered state.[29] These reflections can also be accounted for by a 120° spin structure. However, an alternative model consistent with the neutron diffraction data is a more complex amplitude modulated structure. Muon-spin resonance results suggest that this is in fact the structure adopted.

5.2. Experimental

Neutron powder diffraction data suitable for structural refinement were collected at T ~ 1.8K from each of the $Ba(Sr)MnO_{3-x}$ phases discussed in Chapter 4. Data were collected from samples of 15R-$BaMnO_{2.99(1)}$, 8H-$BaMnO_{2.95(1)}$, 9R-$Ba_{0.875}Sr_{0.125}MnO_{3.00(1)}$, 6L-$BaMnO_{2.92(1)}$, 10H-$BaMnO_{2.91(1)}$, 4H-$BaMnO_{2.65(1)}$ and 4H-$BaMnO_{3.00(1)}$ using the POLARIS diffractometer at ISIS, U.K. Data were collected at T ~ 1.8K from samples of 4H-$Ba_{0.5}Sr_{0.5}MnO_{2.79(1)}$ and 4H-$Ba_{0.5}Sr_{0.5}MnO_{2.99(1)}$, along with an additional data set collected at 200K from 6L-$BaMnO_{2.92(1)}$, using the D2B diffractometer at the ILL, Grenoble, France.

Field-cooled and zero-field-cooled magnetisation data were collected from all samples as a function of temperature between 5 and 300K under a measuring field of 100 Oe. Field-cooled magnetisation-field isotherms were also collected between ±50000 Oe at 6K and 300K.

5.3. Results and discussion

The observed magnetic behaviour is similar for all $Ba(Sr)MnO_{3-x}$ phases. The magnetic behaviour of 6L-$BaMnO_{2.92(1)}$ will be discussed in detail in Section 5.3.1. Variations from this behaviour as a function of the change in the stacking sequence are discussed in Section 5.3.2.

5.3.1. The magnetic model of 6L-$BaMnO_{2.92(1)}$

5.3.1.1. Results

5.3.1.1.1. Magnetic Susceptibility measurements

The magnetic susceptibility data collected from 6L-$BaMnO_{2.92(1)}$ (shown in Figure 5.6) are separated into three regions by two magnetic events. For T > 250K, the overall susceptibility is

small and weakly temperature dependent. At T ~ 250K an event is observed which alters this behaviour. Below 250K, the zero-field-cooled and field-cooled data diverge but remain weakly temperature dependent until T ~ 45 K (a small discontinuity is observed at T ~ 275K, which is discussed further in Chapter 6). At T ~ 45 K there is a significant increase in the field-cooled magnetisation, consistent with the occurrence of a second magnetic transition.

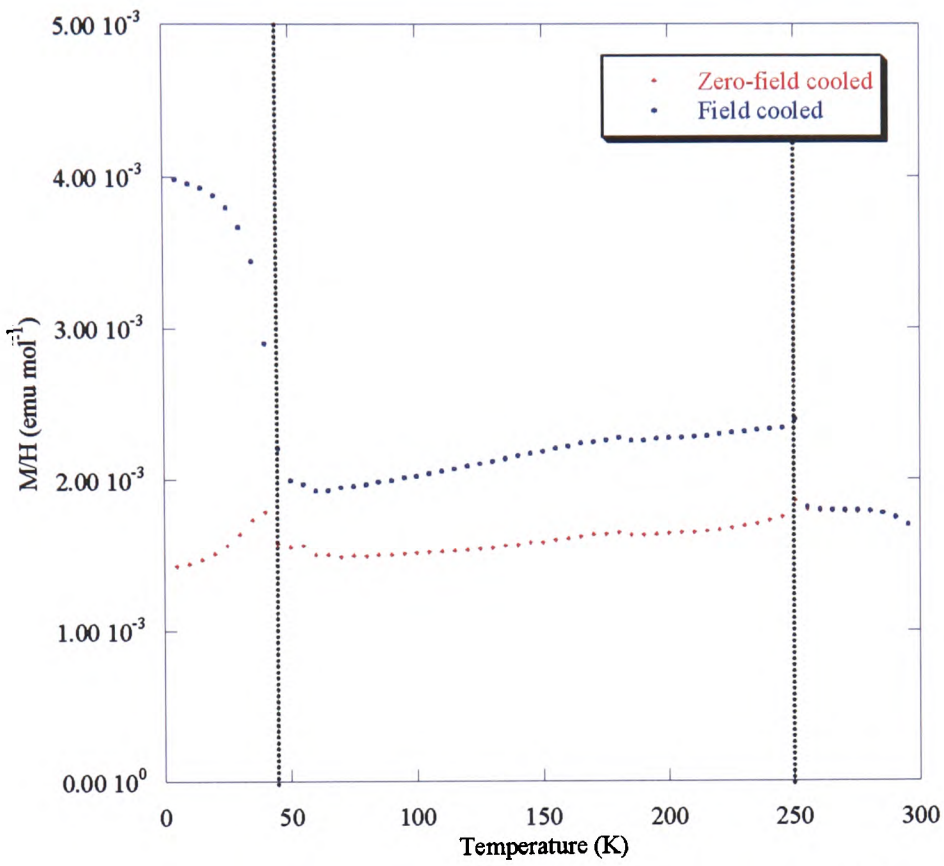


Figure 5.6 Zero-field-cooled and field-cooled magnetisation data collected from 6L-$BaMnO_{2.92(2)}$. Vertical lines indicate the magnetic events.

The 300K magnetisation-field isotherm is linear and passes through the origin. The magnetisation-field isotherm collected at 6K is nonlinear, and shows slight hysteresis (Figure 5.7). This is consistent with an extremely small ferromagnetic component to the magnetic structure. The saturated moment, obtained from the intercept of the magnetisation-field isotherm, is 0.690 emu mol^{-1} or 1.23×10^{-4} μ_B per formula unit.

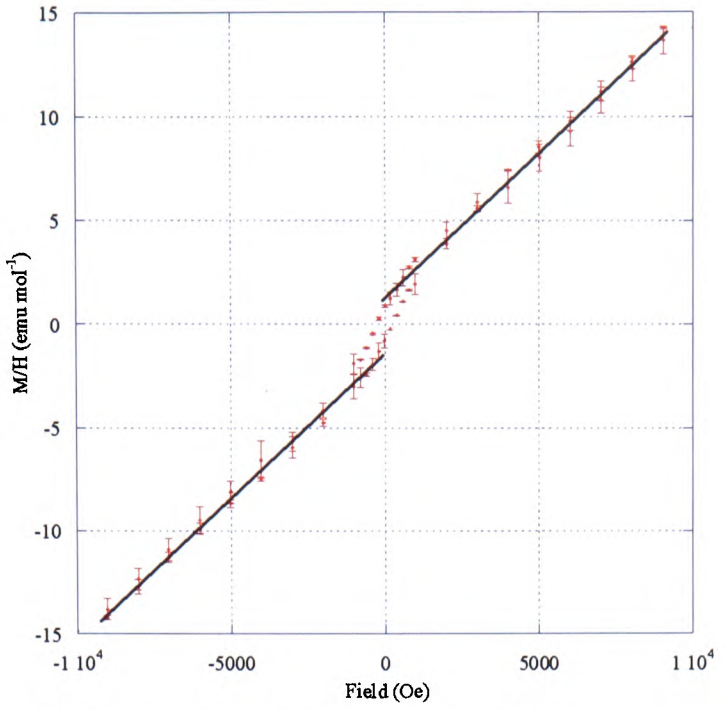


Figure 5.7 Magnetisation vs field data collected at 6K from 6L-$BaMnO_{2.92(2)}$.

5.3.1.1.2. Neutron diffraction

Neutron diffraction data collected at 298K from 6L-$BaMnO_{2.92(1)}$ were discussed in Chapter 4; no evidence of magnetic ordering was observed. The neutron powder diffraction data sets collected at 1.8K and 200K show additional diffraction intensity compared to the 298K data set (Figure 5.8), which could not be accounted for using the nuclear model. The additional scattering was assigned to the presence of long-range magnetic order. In order to account for this, a magnetic model based on that described for 4H-$Ba_{0.9}Sr_{0.1}MnO_3$ was added to the nuclear model.[109] In this model the magnetic moments of the manganese centres are constrained to lie in the *ab* plane and are antiferromagnetically coupled along the *c* axis. The magnetic and nuclear unit cell of 6L-$BaMnO_{2.92(1)}$ is shown in Figure 5.9. As the magnetic unit cell has the same dimensions as the crystallographic unit cell, there are no additional reflections, only additional intensity on reflections that were allowed previously. Refinement of the magnetic model provided a good fit to the additional intensity observed in the 200K and 1.8K data sets. All atomic positions and anisotropic displacement factors were refined. The oxygen fractional occupancy numbers were fixed to the values obtained on refinement against the 298K data set. Full details of the 1.8K refinement may be found in Table 5.1. The observed, calculated and

difference plots are shown in Figure 5.10. The ordered moment obtained on refinement was 1.85(5) μ_B for the 200K data set and 2.22(2) μ_B for the 1.8K data set.

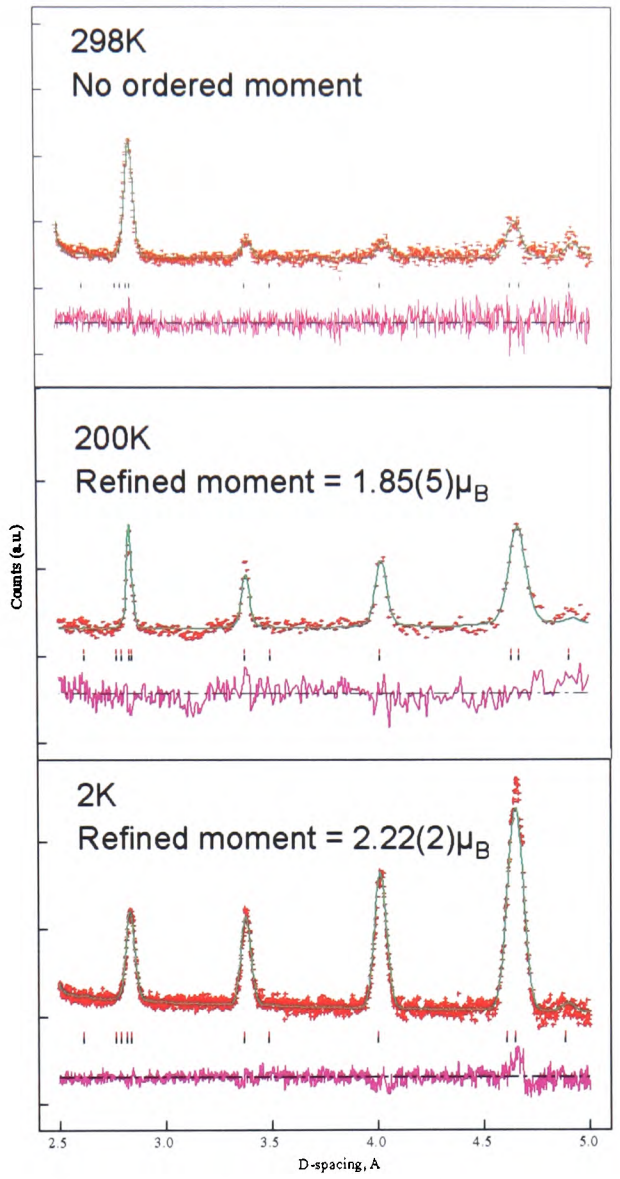


Figure 5.8 Observed, calculated and difference plots from the structural refinement of 6L-$BaMnO_{2.92(1)}$ against neutron powder diffraction data collected at 298, 200 and 1.8K. Lower tick marks represent reflection positions for the nuclear model; upper tick marks the magnetic model.

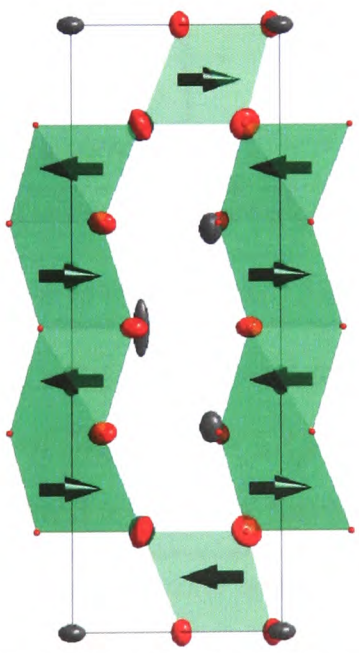


Figure 5.9 Nuclear and magnetic model of 6L-$BaMnO_{2.92(1)}$ obtained on refinement against neutron diffraction data collected at 1.8K.

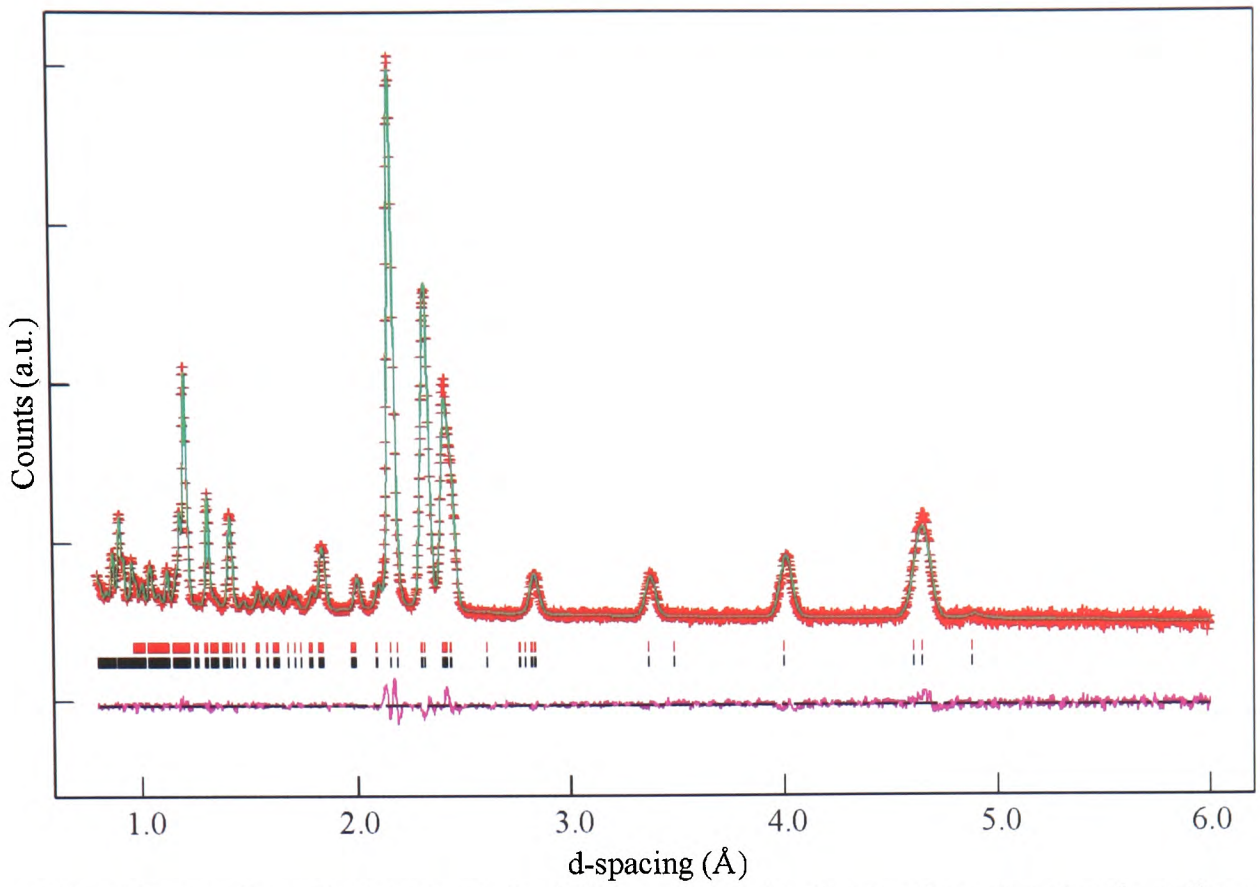


Figure 5.10 Observed, calculated and difference plots from the structural refinement of 6L-$BaMnO_{2.92(2)}$ against neutron powder diffraction data collected at 1.8K. Lower tick marks represent reflection positions for the nuclear model; upper tick marks the magnetic model.

Atom	x	y	z	Fractional Occupancy	U_{equiv}
Ba1	0	0	0	1	0.0012(1)
Ba2	⅓	⅔	½	1	0.0028(1)
Ba3	⅓	⅔	0.1669(1)	1	0.0012(1)
Ba4	⅔	⅓	0.3371(1)	1	0.0022(1)
Mn1	0	0	0.2363(1)	1	0.0019(1)
Mn2	0	0	0.4138(2)	1	0.0014(1)
Mn3	⅔	⅓	0.0913(2)	1	0.0022(1)
O1	0.5210(1)	0.4790(1)	0	0.927(6)	0.0023(1)
O2	0.8497(1)	0.8497(1)	½	0.952(8)	0.0031(1)
O3	0.8333(1)	0.8331(1)	0.1651(1)	0.998(4)	0.0039(1)
O4	0.1489(1)	0.1489(1)	0.32732(5)	0.984(6)	0.0033(1)
Space group : $P\bar{6}m2$, a = 5.6445(1) Å, c = 13.9565(2) Å					
χ^2=1.70, wRp = 1.13%, Rp = 2.27%					
Refined magnetic moment = 2.22(2)μ_B					

Table 5.1 Structural parameters refined against neutron powder diffraction data collected at 1.8K from 6L-$BaMnO_{2.92(2)}$.

5.3.1.2. Discussion

The reported magnetic behaviour of 4H-$SrMnO_3$ and 2H-$BaMnO_3$ is rationalised using models in which the strongest magnetic interaction is direct exchange between manganese ions connected by face-sharing. This results in the antiferromagnetic coupling of all manganese ions within both 2H-$BaMnO_3$ and 4H-$SrMnO_3$ above ambient temperature. A weaker magnetic interaction (the 180° superexchange interaction between manganese ions connected via apex-sharing for 4H-$SrMnO_3$ or the interchain interaction for 2H-$BaMnO_3$) brings about full three-dimensional magnetic order at a lower temperature.

The magnetic susceptibility data collected from 6L-$BaMnO_{2.92(1)}$ can be rationalised using a similar model. All diffraction features in the neutron diffraction data collected at 298K are accounted for by the nuclear model. Also, a linear relationship between magnetisation and field is observed at 300K, consistent with paramagnetic behaviour. However, the magnetic susceptibility data collected as a function of temperature are not consistent with simple paramagnetic behaviour in the range 250K < T < 300K. The weak temperature dependence and low absolute value of both field-cooled and zero-field-cooled magnetisation data suggest that there are strong antiferromagnetic interactions in this temperature range. The susceptibility data may be reconciled with the neutron diffraction data if the magnetic moments are antiferromagnetically coupled, but not antiferromagnetically ordered at T > 250K. This suggests that strong antiferromagnetic coupling exists within the face-sharing chains at T > 250K, but that no interaction takes place between the chains.

The event at T ~ 250K which results in divergence between the field-cooled and zero-field-cooled data is reminiscent of the event at the Néel temperature (T_N ~ 278K) of 4H-$SrMnO_3$. This corresponds to the magnetic ordering of antiferromagnetically coupled dimers through the 180° superexchange interaction.[5, 66] Néel temperatures are typically identified from a cusp in the susceptibility data, but as the magnetic moments of 4H-$SrMnO_3$ are antiferromagnetically

coupled prior to magnetic ordering, no anomaly is observed in the susceptibility data. It is likely that the slight divergence observed at T ~ 250K in the susceptibility data collected from 6L-$BaMnO_{2.92(1)}$ corresponds to a similar magnetic ordering event. The 200K neutron diffraction data collected from 6L-$BaMnO_{2.92(1)}$ provide supporting evidence for this. These data confirm the presence of long-range antiferromagnetic order in 6L-$BaMnO_{2.92(1)}$ at 200K. The similarity of the 6L magnetic model to that of 4H-$SrMnO_3$ suggests that the long-range magnetic order is a result of the same 180° superexchange interaction. The divergence of the zero-field-cooled and field-cooled susceptibility data suggest a slight canting of the antiferromagnetically aligned moments is associated with the transition to full magnetic order.

The second magnetic event occurs at T ~ 45K. The increased divergence between zero-field-cooled and field-cooled susceptibility data and the onset of a small degree of magnetic hysteresis are consistent with the introduction of a small ferromagnetic component to the magnetic behaviour. The cause and nature of the magnetic event at T ~ 45K are ambiguous. Possibilities include the ordering temperature of an impurity phase, a transition to a canted antiferromagnetic state, or the freezing of impurity spins not participating in the ordered magnetic structure. These possibilities are discussed further in Section 5.3.2.3.

5.3.2. Deviations in magnetic behaviour for the remaining $BaMnO_{3-x}$ phases

5.3.2.1. Susceptibility data

The field-cooled and zero-field-cooled susceptibility data for the remaining Ba(Sr)MnO_{3-x} phases are shown in Figure 5.11 - Figure 5.16. The majority of these data sets reveal the same general form as the data collected from 6L-$BaMnO_{2.92(1)}$. Three regions appear in the susceptibility data, separated by two magnetic events at T ~ 250K and T ~ 45K. The exception occurs for susceptibility data collected from 15R-$BaMnO_{2.99(1)}$. In the 15R-$BaMnO_{2.99(1)}$ data set the zero-field-cooled and field-cooled data cross at T ~ 80K and at T ~ 45K. This behaviour is discussed further in Chapter 6. All magnetisation-field isotherms collected from

$Ba(Sr)MnO_{3-x}$ phases at 300K are linear and pass through the origin. Those collected at 6K are nonlinear and show slight hysteresis.

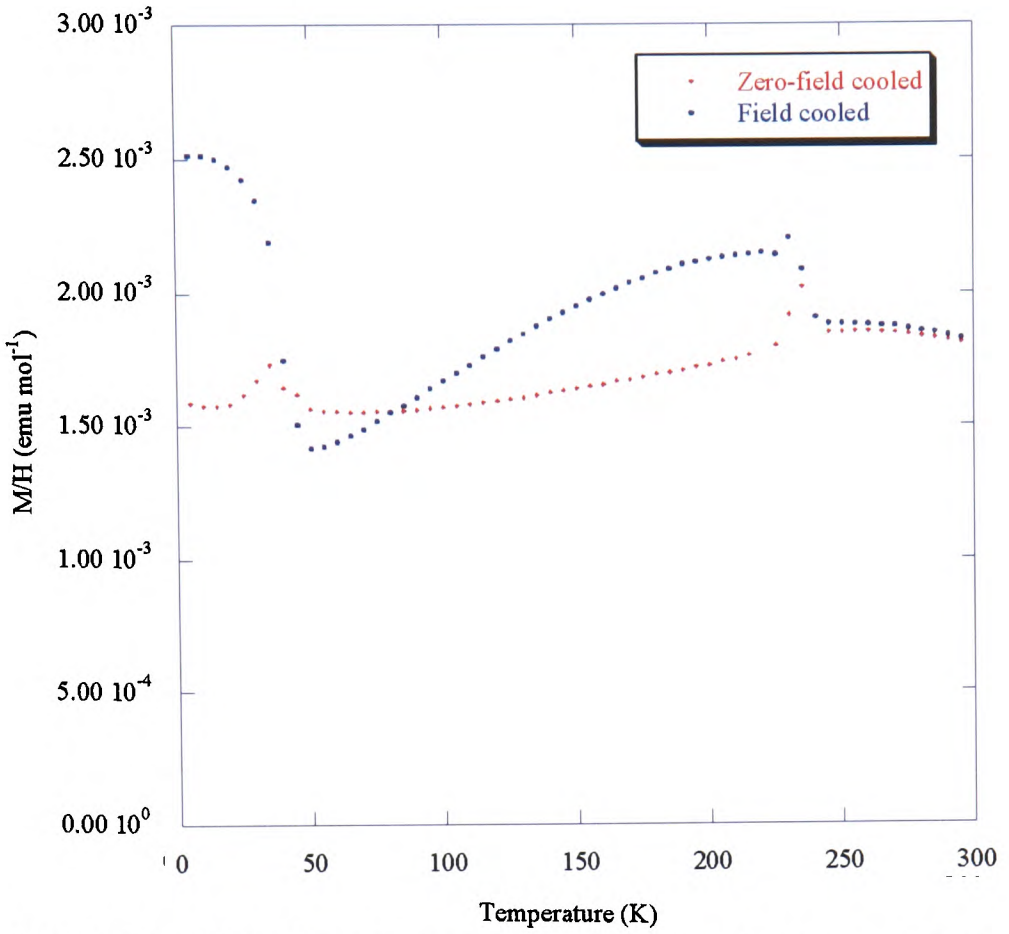


Figure 5.11 Zero-field-cooled and field-cooled magnetisation data collected from 15R-$BaMnO_{2.99(1)}$.

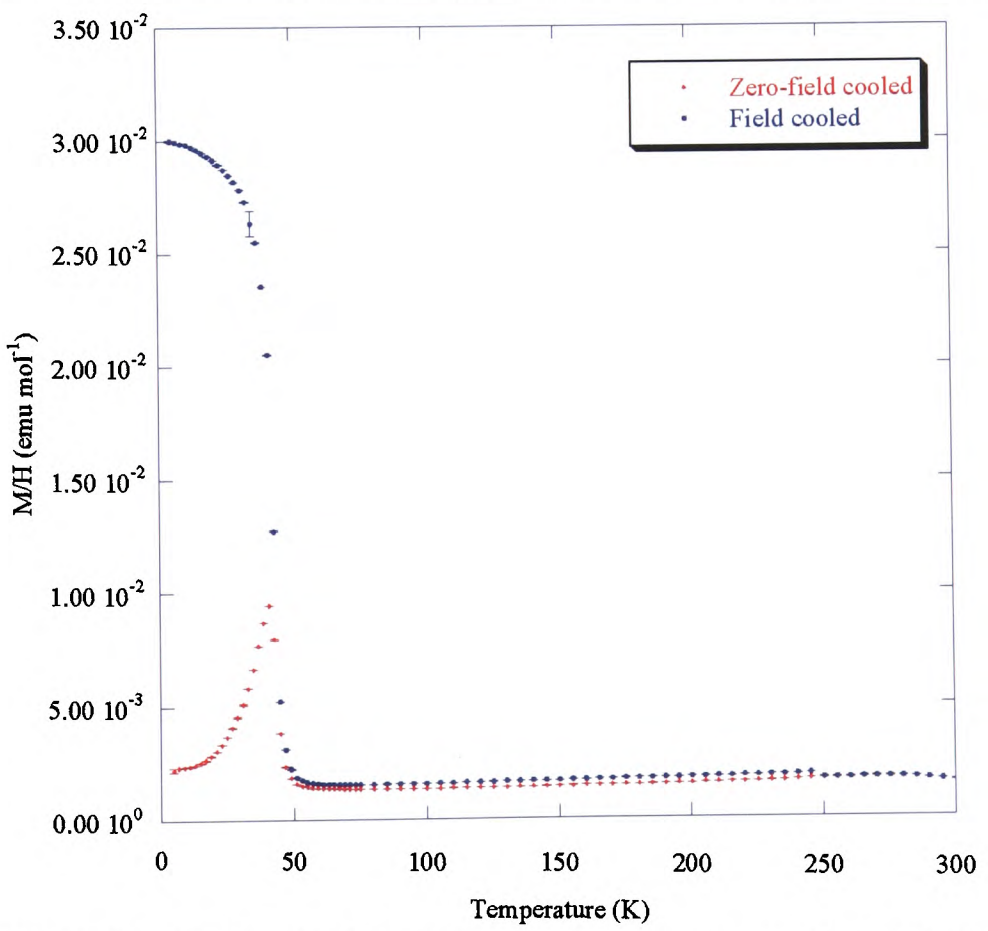


Figure 5.12 Zero-field-cooled and field-cooled magnetisation data collected from 8H-$BaMnO_{2.95(1)}$.

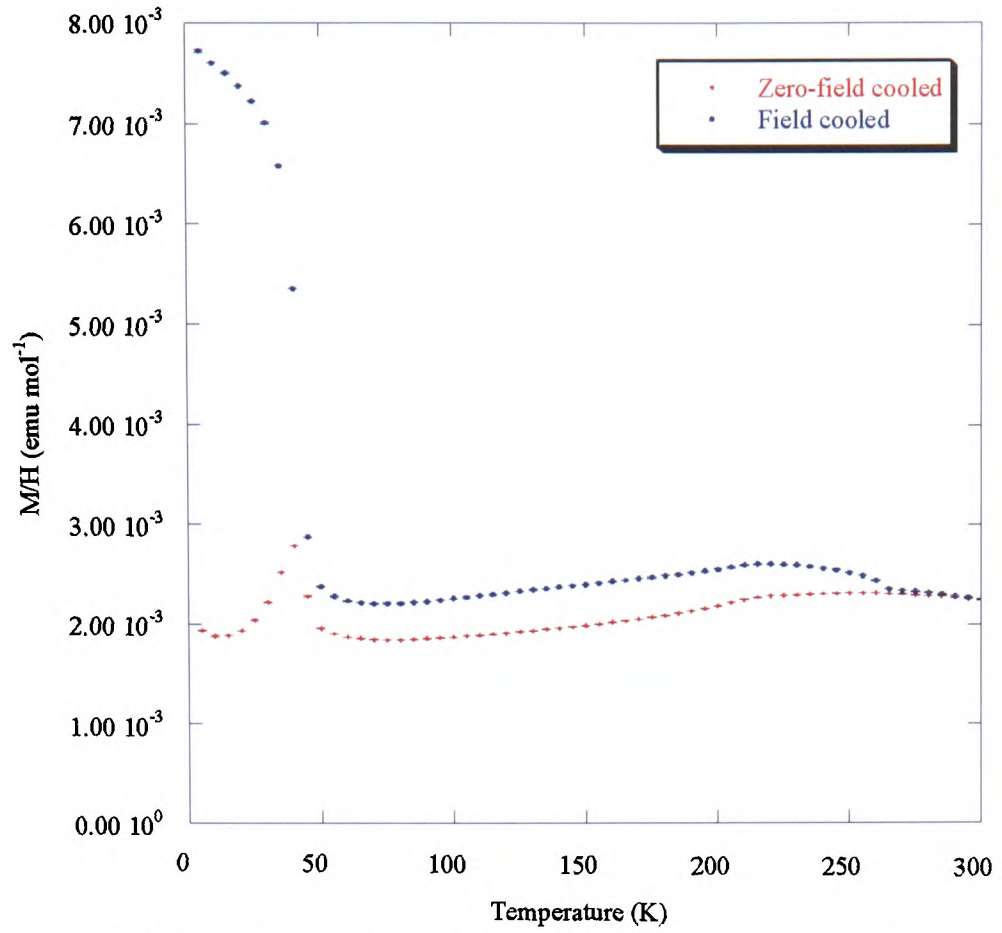


Figure 5.13 Zero-field-cooled and field-cooled magnetisation data collected from 9R-$Ba_{0.875}Sr_{0.125}MnO_{3.00(1)}$.

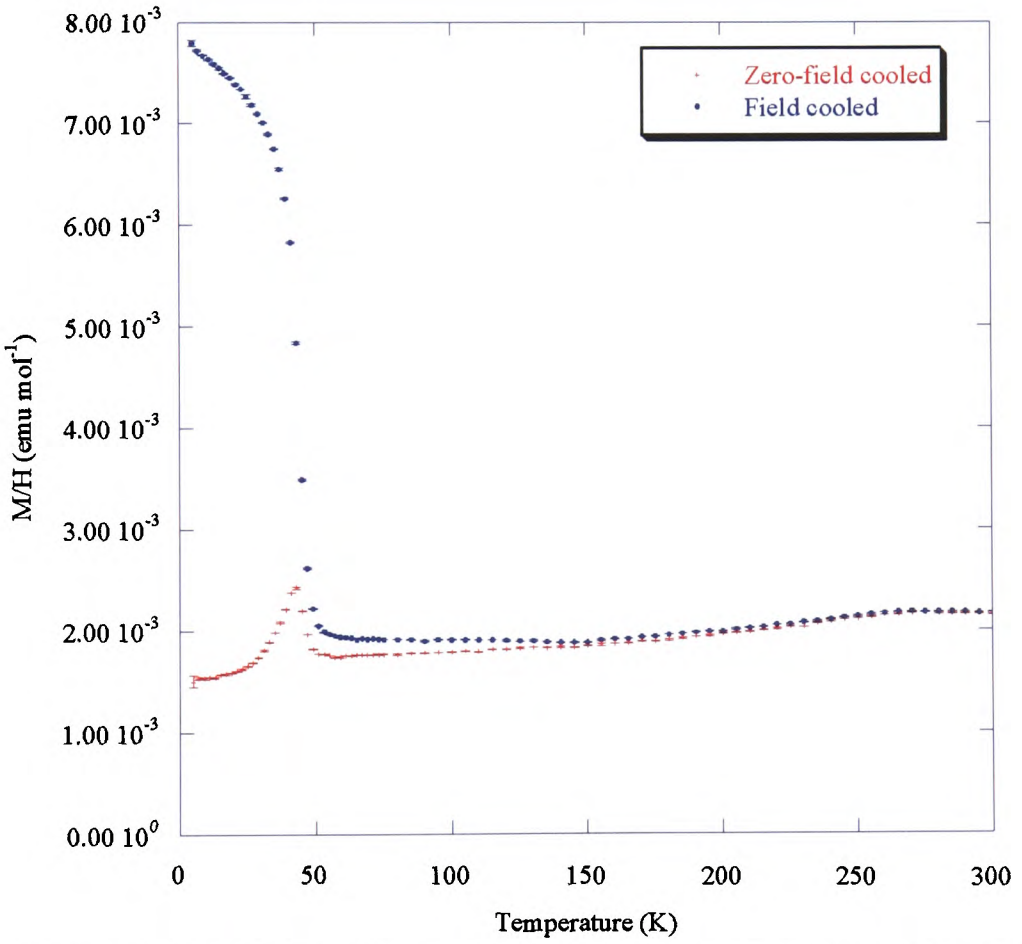


Figure 5.14 Zero-field-cooled and field-cooled magnetisation data collected from 10H-$BaMnO_{2.91(2)}$.

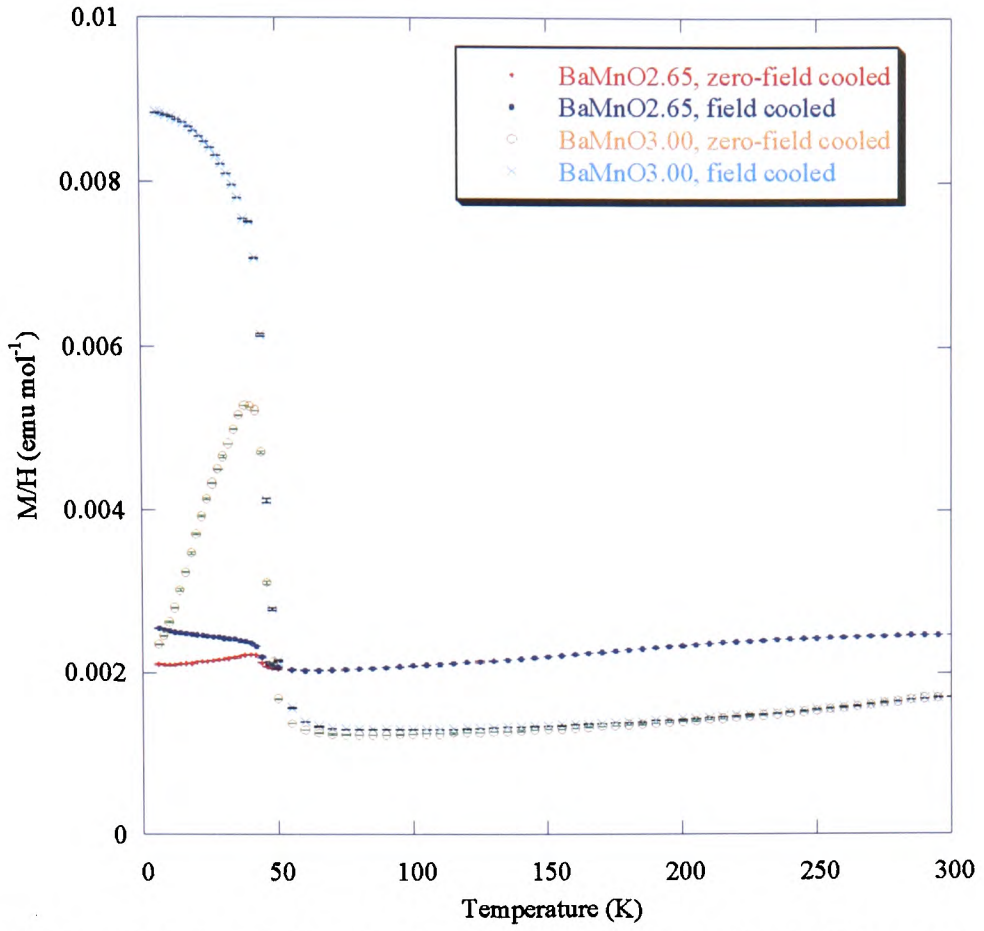


Figure 5.15 Zero-field-cooled and field-cooled magnetisation data collected from 4H-$BaMnO_{2.65(1)}$ and 4H-$BaMnO_{3.00(1)}$.

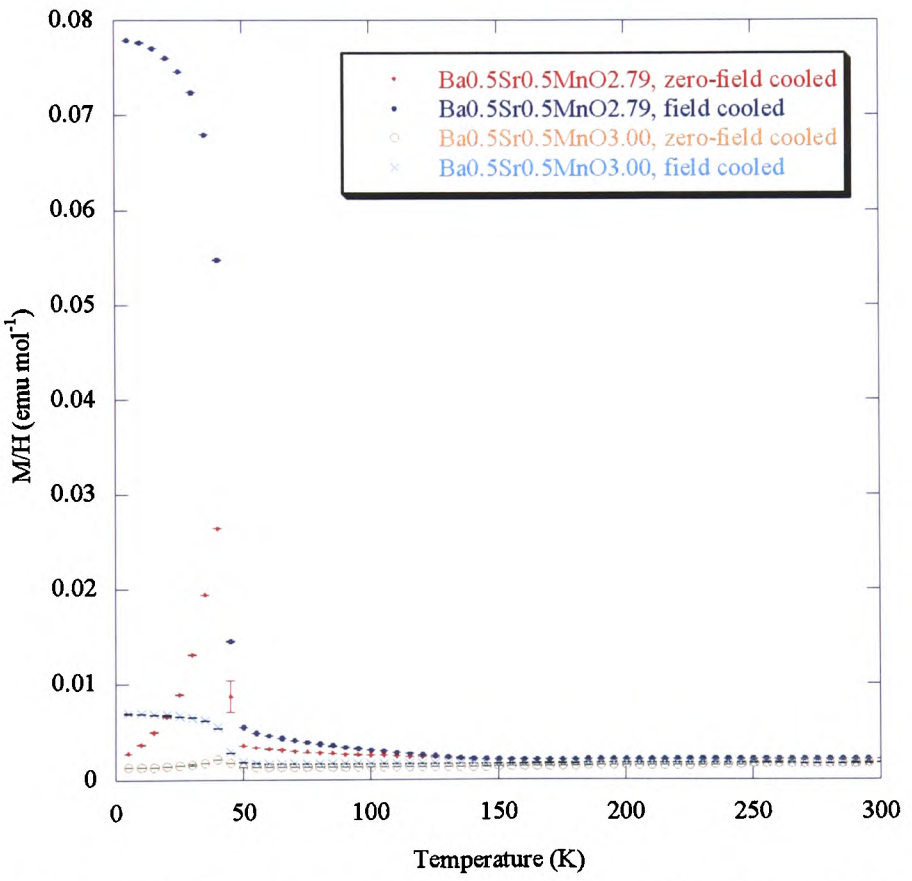


Figure 5.16 Zero-field-cooled and field-cooled magnetisation data collected from 4H-$Ba_{0.5}Sr_{0.5}MnO_{2.79(1)}$ and 4H-$Ba_{0.5}Sr_{0.5}MnO_{2.99(1)}$.

5.3.2.2. The magnetic event at T ~ 250K

The event which occurs at T ~ 250K in the susceptibility data collected from 6L-$BaMnO_{2.92(1)}$ is believed to correspond to the true Néel temperature at which the 180° superexchange

interactions couple the chains of antiferromagnetically ordered manganese ions into a fully ordered array. Above this temperature the manganese ions are believed to be antiferromagnetically coupled via direct exchange across the shared faces, forming isolated chains. An alternative model which could describe the high temperature magnetic coupling is one in which the 180° superexchange interaction, utilising the apex-sharing oxide anions, is the strongest magnetic interaction. This model would also result in antiferromagnetic coupling occurring before full magnetic ordering.

The direct exchange mechanism across the shared face couples face-sharing manganese ions into isolated chains, whereas the 180° superexchange mechanism couples apex-sharing manganese ions into isolated sheets (Figure 5.17). All manganese ions in the 4H structure have both apex-sharing and face-sharing linkages, so all are expected to couple antiferromagnetically prior to full magnetic order in either model. However the 15R, 8H, 9R, 10H and 6L stacking sequences all contain manganese sites which are solely face-sharing. The 180° superexchange pathway is not available to manganese ions in such sites and so if the 180° superexchange coupling were the stronger interaction these would be expected to behave paramagnetically in the range $250 < T\,(K) < 300$.

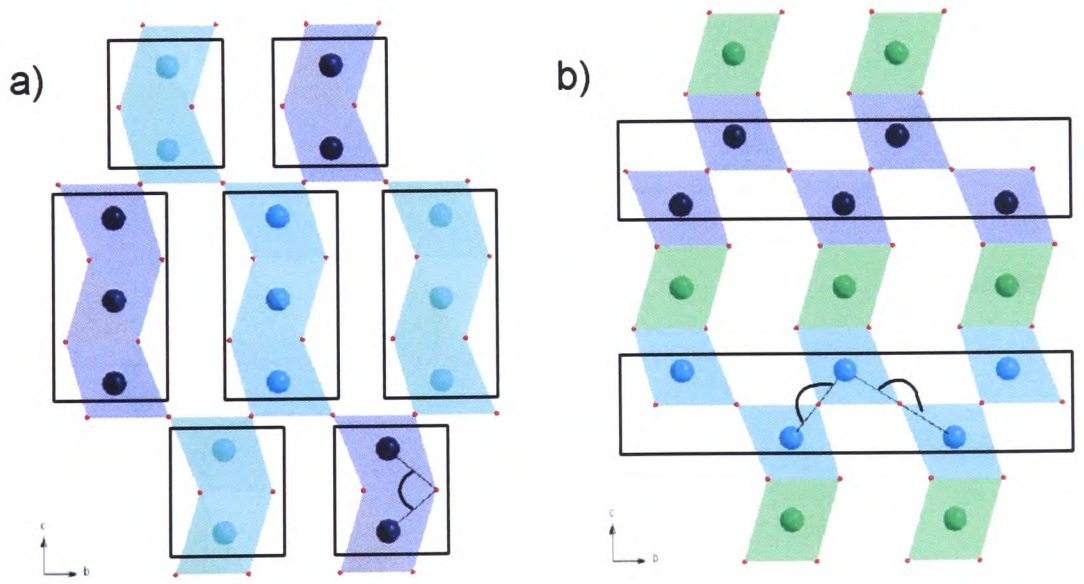


Figure 5.17 Isolated magnetic units after coupling B cations across only a) the shared face or b) the shared apex. Blue B cations are antiferromagnetically coupled. Green B cations represent those for which the relevant magnetic coupling interaction is not available.

The observed susceptibility data show similar behaviour for all $BaMnO_{3-x}$ samples in the range $270 < T\ (K) < 300$. At $T > 270K$, the low absolute magnitude and weak temperature dependence of susceptibility data collected from all $Ba(Sr)MnO_{3-x}$ samples is consistent with the antiferromagnetic coupling of the vast majority of the magnetic moments. This provides support for the model in which the direct exchange interaction is stronger than the 180° superexchange interaction.

The temperature at which the true Néel temperature occurs is indicated by divergence of the zero-field-cooled and field-cooled susceptibility data. This varies slightly across the $BaMnO_{3-x}$ series (Figure 5.18).

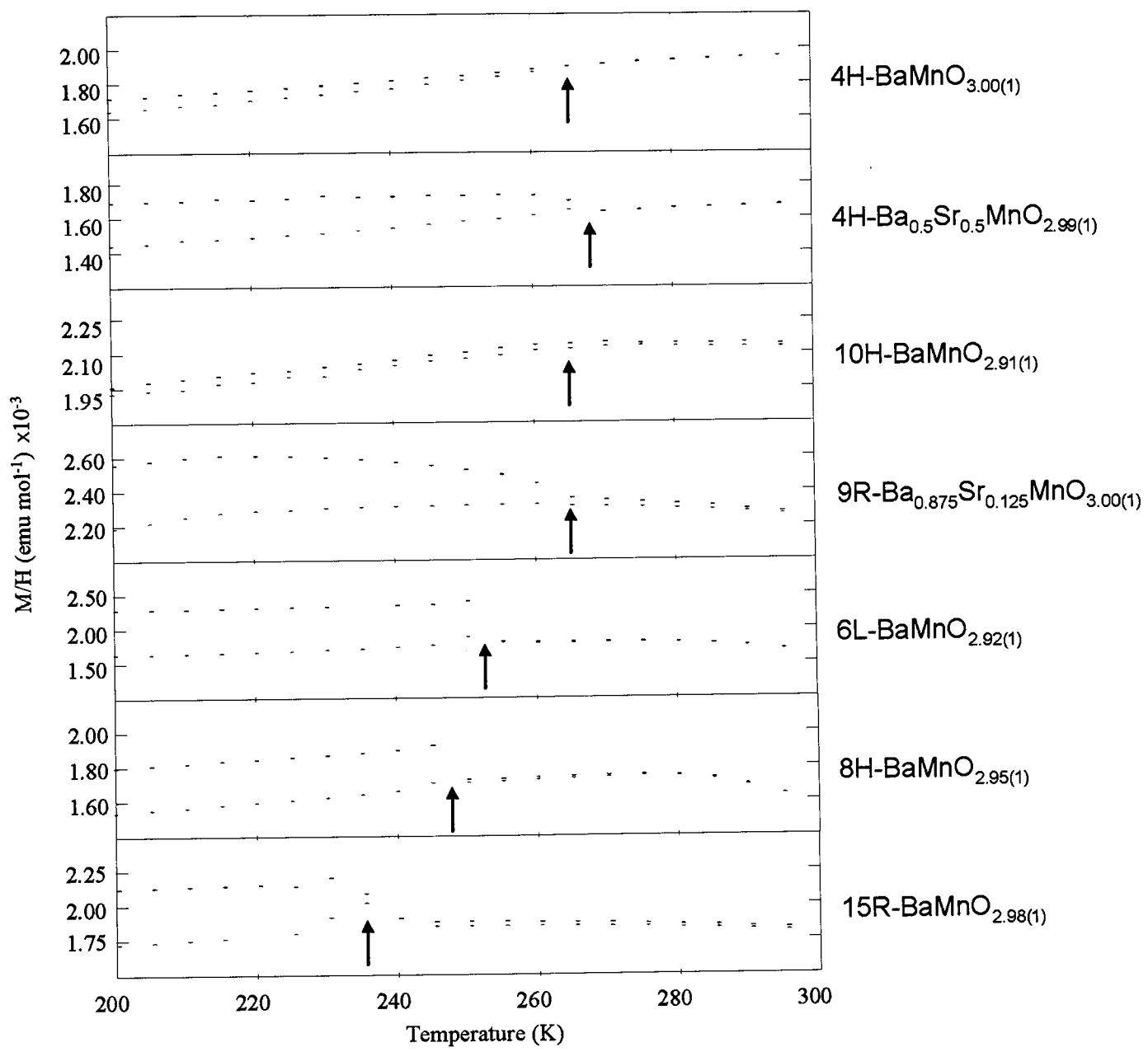


Figure 5.18 Variation in the temperature at which divergence occurs between zero-field-cooled and field-cooled susceptibility data. For $4H\text{-}BaMnO_{3.00(1)}$ and $10H\text{-}BaMnO_{2.91(1)}$, the divergence is very slight and is identified by a change in the gradient of the susceptibility.

The precise temperature of the event corresponding to T_N depends on the length of the face-sharing chains. The fewer MnO_6 octahedra in the face-sharing chains, the higher T_N is. This is consistent with the magnetic ordering event being caused by the onset of the 180° superexchange interaction. For longer face-sharing chains, there are fewer 180° Mn-O-Mn pathways per manganese ion, and thus the 180° interaction is expected to be weaker and occur at a lower temperature. The data collected from 4H-$Ba_{0.5}Sr_{0.5}MnO_{2.99(1)}$ (which contains only two manganese ions per chain) show that the transition occurs at T ~ 265K, for 15R-$BaMnO_{2.99(1)}$ with five manganese ions per chain the transition occurs at T ~ 235K. The zero-field-cooled and field-cooled susceptibility data collected from 4H-$BaMnO_{2.65(1)}$ and 4H-$Ba_{0.5}Sr_{0.5}MnO_{2.79(1)}$ are excluded from Figure 5.18 as these do not diverge or show any indication of a change in gradient in the range 200K < T < 300K. This is attributed to the high degree of charge disorder and is discussed further in Chapter 6.

5.3.2.3. Cause of the event at T ~ 45K

Possible causes of an event resulting in the small ferromagnetic component to the susceptibility were outlined previously; namely, the ordering temperature of an impurity phase, a transition to a canted antiferromagnetic state, or the freezing of impurity spins not participating in the ordered magnetic structure.

5.3.2.3.1. A ferromagnetic minority phase

A small proportion of a ferromagnetic minority phase can result in an apparently large divergence of the zero-field-cooled and field-cooled magnetisation data collected from an antiferromagnetic phase. The small size of the saturated moment (obtained from the intercept of magnetisation-field isotherms collected at 6K) is such that the proportion of a ferromagnetic phase would be undetectable using neutron powder diffraction techniques. The investigation of plausible minority phases reveals that Mn_3O_4 has a ferrimagnetic ordering temperature of 42K and can be prepared from the MnO_2 starting material under the synthesis conditions to prepare some of the Ba(Sr)MnO_{3-x} phases.[116, 117] However, a minority phase of MnO is observed in

the neutron diffraction data collected from 4H-$BaMnO_{2.65(1)}$. This suggests that the synthesis conditions used to produce 4H-$BaMnO_{2.65(1)}$ and 4H-$Ba_{0.5}Sr_{0.5}MnO_{2.79(1)}$ are too reducing to allow formation of Mn_3O_4, yet the event at T ~ 45K is still observed in susceptibility data collected from these samples. Moreover, Mn_3O_4 is readily oxidised to Mn_2O_3 on firing at 600°C under oxygen, yet the event is still observed in data collected from 4H-$BaMnO_{3.00(1)}$ and 4H-$Ba_{0.5}Sr_{0.5}MnO_{2.99(1)}$.

The lack of variation in the temperature of the magnetic event at T ~ 45K supports the idea that this may correspond to the magnetic ordering temperature of an impurity. However close examination reveals that there is in fact a slight variation in the temperature of this event. Figure 5.19 shows data collected from 4H-$BaMnO_{3.00(1)}$ and 8H-$BaMnO_{2.95(1)}$.

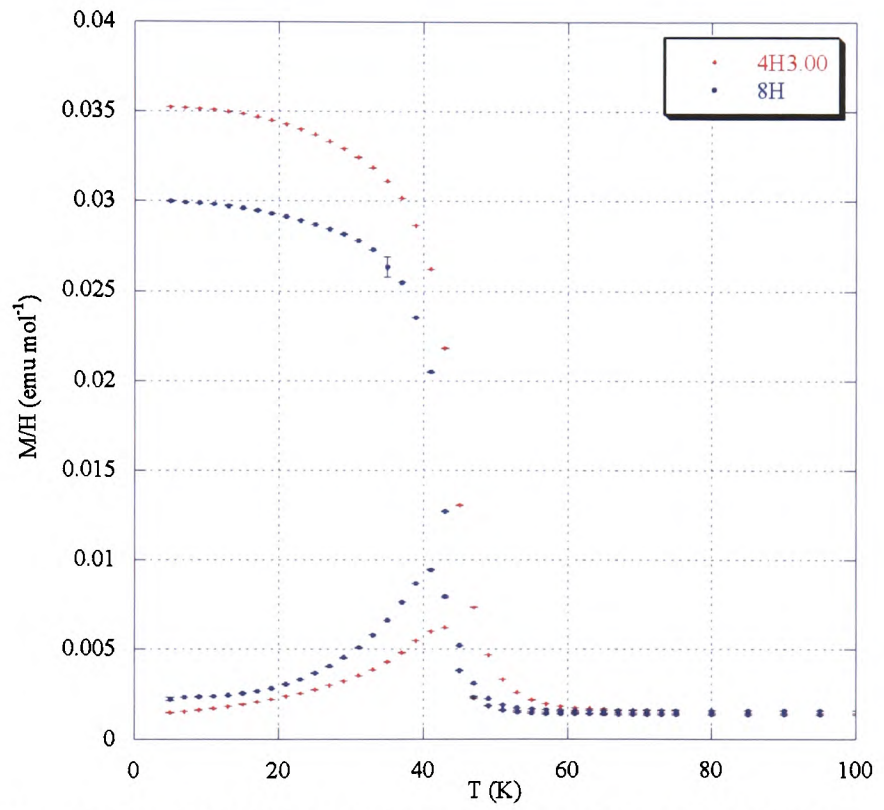


Figure 5.19 Zero-field-cooled and field-cooled magnetisation data collected from 4H-$BaMnO_{3.00(1)}$ and 8H-$BaMnO_{2.95(1)}$.

There is a clear shift in the temperature at which the zero-field-cooled and field-cooled data collected from 8H-$BaMnO_{2.95(1)}$ diverge compared to the divergence temperature of 4H-$BaMnO_{3.00(1)}$. This, coupled with the inconsistencies involving the synthesis technique and the presence of the feature in every sample of $BaMnO_{3-x}$ lends weight to the argument that the T ~ 45K event is a genuine feature of the $BaMnO_{3-x}$ phases.

5.3.2.3.2. Sample based ferromagnetism

A small ferromagnetic component to the magnetism can be caused by magnetic interactions in the sample by either a small canting angle of all the spins or the freezing of a small proportion of defect spins. The feature at T ~ 45K often dominates the susceptibility data as the major component of the magnetic moments is antiferromagnetically aligned over the entire measured temperature range.

If the small ferromagnetic moment is a result of the freezing of defect spins, the transition is expected to be glassy. A transition to a spin glass is generally indicated by asymmetric hysteresis below the freezing temperature. Examination of the magnetisation-field data collected at 6K reveals that the hysteresis (previously shown for 6L-$BaMnO_{2.92(1)}$ in Figure 5.7) is symmetric about the origin within the error of the measurement. Alternatively, the small ferromagnetic moment could be a result of a canting transition. The symmetry of the $Ba(Sr)MnO_{3-x}$ magnetic models allows canting of the magnetic moments along the *c* axis. The degree of canting required for the observed moment is negligible and would not be detectable using low temperature neutron diffraction techniques.

Four mechanisms for magnetic exchange in hexagonal perovskites were discussed in Section 5.1. Direct exchange and 180° superexchange are known to be strong interactions that result in magnetic coupling at much higher temperatures and favour antiferromagnetic ordering for Mn(IV). Either 90° superexchange or the interchain interaction could slightly modify the ordered state, resulting in a small ferromagnetic component to the magnetism.

If the transition at T ~ 45K is to a canted antiferromagnetic state, the observed data can be more readily accounted for if this is a result of interchain interactions. The interchain interaction is likely to be dependent on the interchain separation (identical to the *a* lattice parameter) and possibly on the nature of the A cation located between the chain. As neither factor changes appreciably across the measured $Ba(Sr)MnO_{3-x}$ phases, this would explain why

there is little difference in the temperature of the 45K event. It is notable that although the 45K feature is observed in all the measured $Ba(Sr)MnO_{3-x}$ phases, there is no evidence of this event in magnetisation data collected from 4H-$SrMnO_{3.00}$.[66] The transition temperature is very similar to the reported Néel temperature of 2H-$BaMnO_3$, 59(2)K. This is known to be the temperature at which the strength of the interchain interaction results in an antiferromagnetic 120° spin structure. In the remaining $Ba(Sr)MnO_{3-x}$ phases full antiferromagnetic order exists due to the 180° superexchange interaction and the 120° spin structure cannot be adopted without disrupting the antiferromagnetic ordering, but the interchain interaction could cause a canting of the antiferromagnetic moments.

5.3.2.4. 1.8K neutron diffraction

5.3.2.4.1. Results

Details of the refinements of neutron diffraction data collected at 1.8K from the remaining $Ba(Sr)MnO_{3-x}$ phases are listed in Table 5.2 - Table 5.10. Observed, calculated and difference plots are shown in Figure 5.20 - Figure 5.24. All refinements except those against data collected from 4H-$BaMnO_{2.65(1)}$ and 4H-$Ba_{0.5}Sr_{0.5}MnO_{2.79(1)}$ required a magnetic model in order to fit additional diffraction features. The magnetic unit cells are shown in Figure 5.25. All are based on that of 4H-$Ba_{0.9}Sr_{0.1}MnO_{2.96}$, in which the moments lie in the *ab* plane and are antiferromagnetically aligned along the *c* axis.[109]

Although no additional sharp diffraction features were observed in the 1.8K neutron diffraction data collected from 4H-$Ba_{0.5}Sr_{0.5}MnO_{3-x}$, close examination of the difference plots in Figure 5.24 reveals the presence of an additional broad feature compared to the 298K neutron diffraction data. This occurs at approximately $2\theta \sim 20°$ or $d \sim 4.6$ Å, corresponding to the [002] Bragg reflection, the most intense of the 4H magnetic model shown in Figure 5.25. No evidence of similar behaviour was observed in the 1.8K neutron diffraction data collected from 4H-$BaMnO_{2.65(1)}$.

Atom	x	y	z	Fractional Occupancy	U_{equiv} (Å^2)
Ba1	0	0	0	1	0.0028(1)
Ba2	0	0	0.133892(5)	1	0.0012(1)
Ba3	0	0	0.26536(4)	1	0.0002(1)
Mn1	0	0	½	1	0.0031(1)
Mn2	0	0	0.36157(5)	1	0.0005(1)
Mn3	0	0	0.43164(8)	1	0.0018(1)
O1	½	0	0	1	0.0048(1)
O2	0.18614(8)	-0.18614(8)	0.06427(2)	0.9875(1)	0.0035(1)
O3	0.48427(8)	-0.48427(8)	0.13292(3)	1	0.0035(1)
Space group : R $\bar{3}$ m, a = 5.6606(1) Å, c = 35.2349(8) Å χ^2=2.00, wRp = 1.47%, Rp = 2.69% Refined magnetic moment = 2.20(2) μ_B					

Table 5.2 Structural parameters refined against neutron powder diffraction data collected at 1.8K from 15R-$BaMnO_{2.99(1)}$. The magnetic unit cell is doubled parallel to the z-axis.

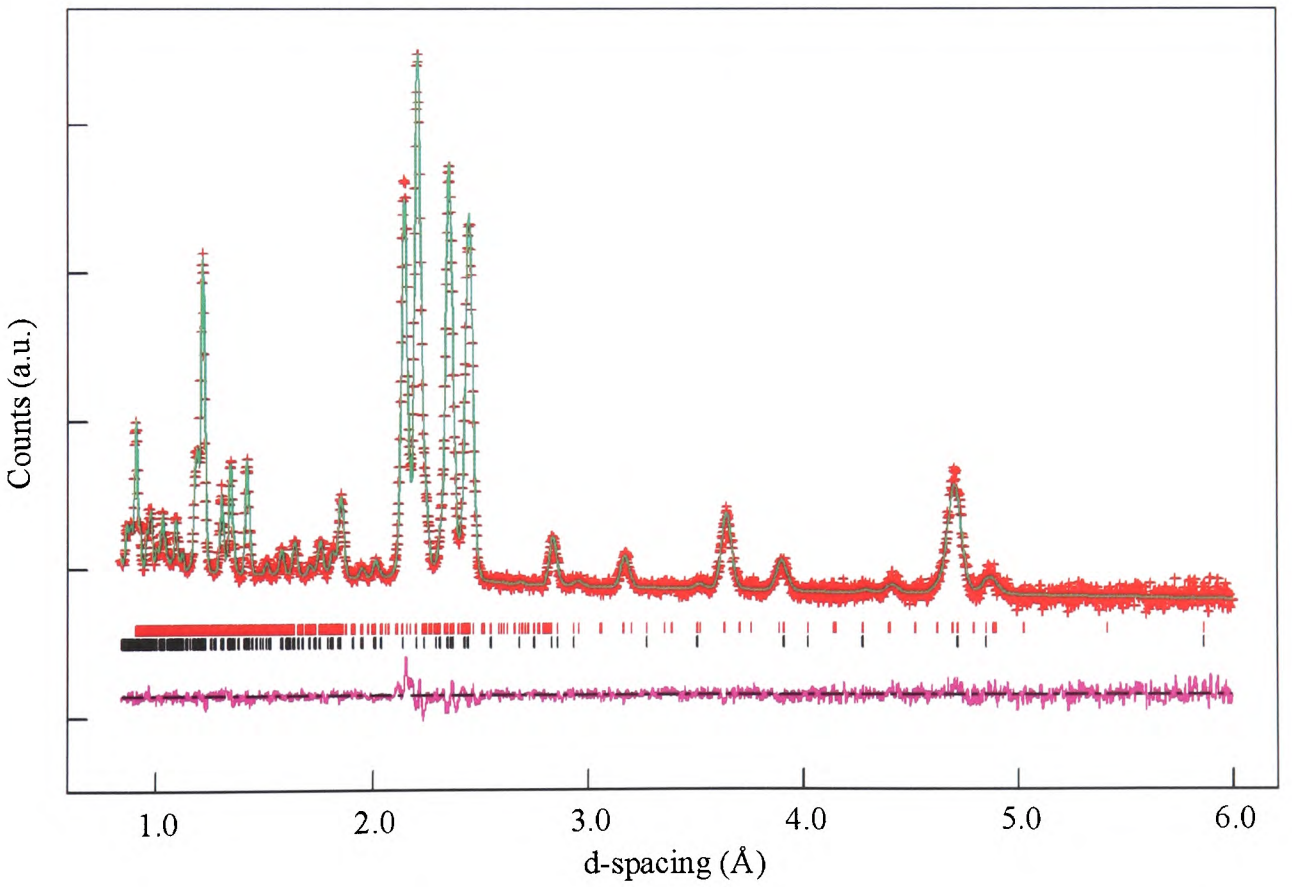


Figure 5.20 Observed, calculated and difference plots from the structural refinement of 15R-$BaMnO_{2.99(1)}$ against neutron powder diffraction data collected at 1.8K. Lower tick marks represent reflection positions for the nuclear model; upper tick marks the magnetic model.

Atom	x	y	z	Fractional Occupancy	U_{equiv} (Å^2)
Ba1	0	0	0	1	0.0020(2)
Ba2	0	0	¼	1	0.0020(2)
Ba3	⅓	⅔	0.12840(4)	1	0.0016(1)
Mn1	⅓	⅔	0.55320(5)	1	0.0022(1)
Mn2	⅓	⅔	0.68559(6)	1	0.0016(1)
O1	½	0	0	1	0.0039(1)
O2	0.51599(7)	0.0320(1)	¼	0.979(2)	0.0033(1)
O3	0.81480(4)	0.62960(8)	0.12111(2)	0.977(1)	0.0032(1)
Space group : $P6_3/mmc$, a = 5.65863(9) Å, c = 18.7082(3) Å χ^2=1.781, wRp = 1.08%, Rp = 2.03% Refined magnetic moment = 2.23(2) μ_B					

Table 5.3 Structural parameters refined against neutron powder diffraction data collected at 1.8K from 8H-$BaMnO_{2.95(1)}$.

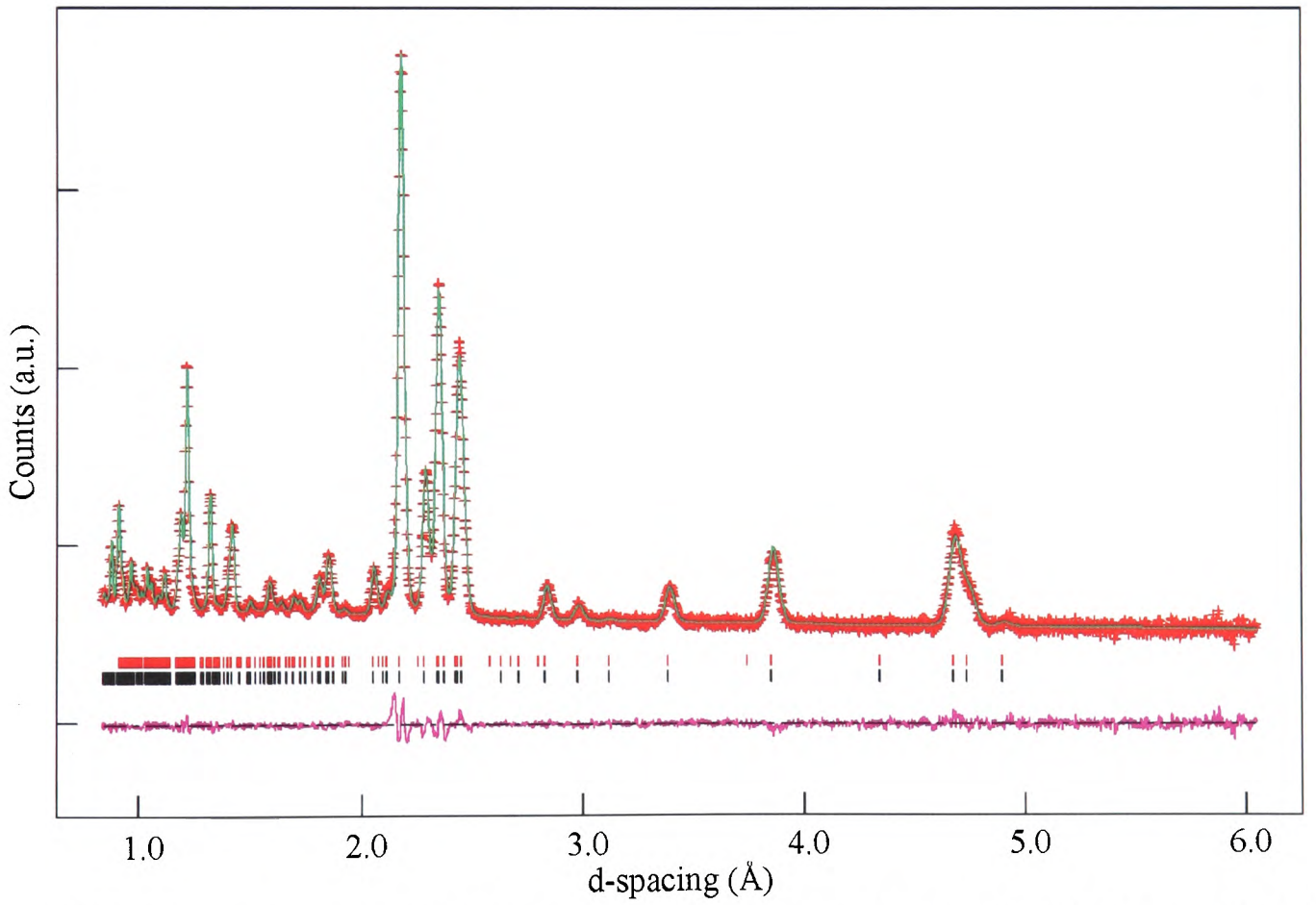


Figure 5.21 Observed, calculated and difference plots from the structural refinement of 8H-$BaMnO_{2.95(1)}$ against neutron powder diffraction data collected at 1.8K. Lower tick marks represent reflection positions for the nuclear model, upper tick marks the magnetic model.

Atom	x	y	z	Fractional Occupancy	U_{equiv} (Å^2)
Ba1/Sr1	0	0	0	0.77(1)/0.23(1)	0.0019(1)
Ba2/Sr2	0	0	0.21959(4)	0.926(5)/0.074(5)	0.0024(1)
Mn1	0	0	½	1	0.0015(1)
Mn2	0	0	0.38161(4)	1	0.0020(1)
O1	½	0	0	1	0.0041(1)
O2	0.14908(3)	-0.14908(3)	0.55830(2)	1	0.0036(1)
Space group : R-3m, a = 5.6255(1) Å, c = 20.8470(4) Å					
χ^2=2.21, wRp = 1.41%, Rp = 2.66%					
Refined magnetic moment = 2.44(3) μ_B					

Table 5.4 Structural parameters refined against neutron powder diffraction data collected at 1.8K from 9R-$Ba_{0.875}Sr_{0.125}MnO_{3.00}$. The magnetic unit cell is doubled parallel to the z-axis.

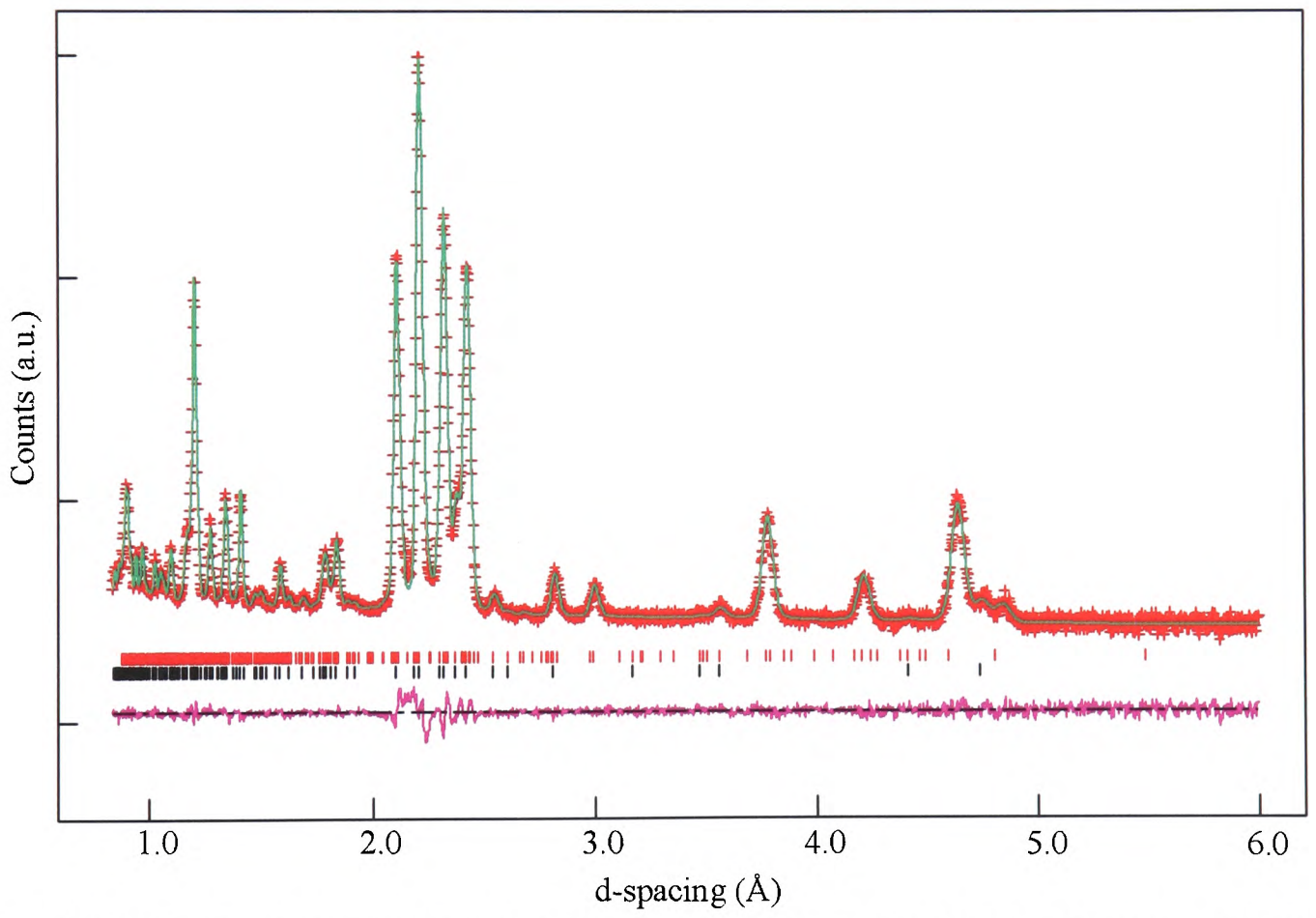


Figure 5.22 Observed, calculated and difference plots from the structural refinement of 9R-$Ba_{0.875}Sr_{0.125}MnO_{3.00}$ against neutron powder diffraction data collected at 1.8K. Lower tick marks represent reflection positions for the nuclear model; upper tick marks the magnetic model.

Atom	x	y	z	Fractional Occupancy	U_{equiv} (Å^2)
Ba1	0	0	¼	1	0.0022(1)
Ba2	⅓	⅔	0.14913(6)	1	0.0029(1)
Ba3	⅓	⅔	0.54725(5)	1	0.0019(1)
Mn1	0	0	0	1	0.0023(1)
Mn2	0	0	0.10698(6)	1	0.0023(1)
Mn3	⅓	⅔	0.69494(5)	1	0.0024(1)
O1	0.52075(8)	0.0415(2)	¼	0.933(2)	0.0039(1)
O2	0.14860(5)	0.2972(1)	0.05247(2)	0.984(2)	0.0042(1)
O3	0.83325(7)	0.6665(1)	0.15047(2)	0.979(2)	0.0045(1)
Space group : $P6_3/mmc$, a = 5.6407(1) Å, c = 23.1360(4) Å					
χ^2=1.66, wRp = 1.10%, Rp = 2.08%					
Refined magnetic moment = 2.56(2) μ_B					

Table 5.5 Structural parameters refined against neutron powder diffraction data collected at 1.8K from 10H-$BaMnO_{2.91(1)}$.

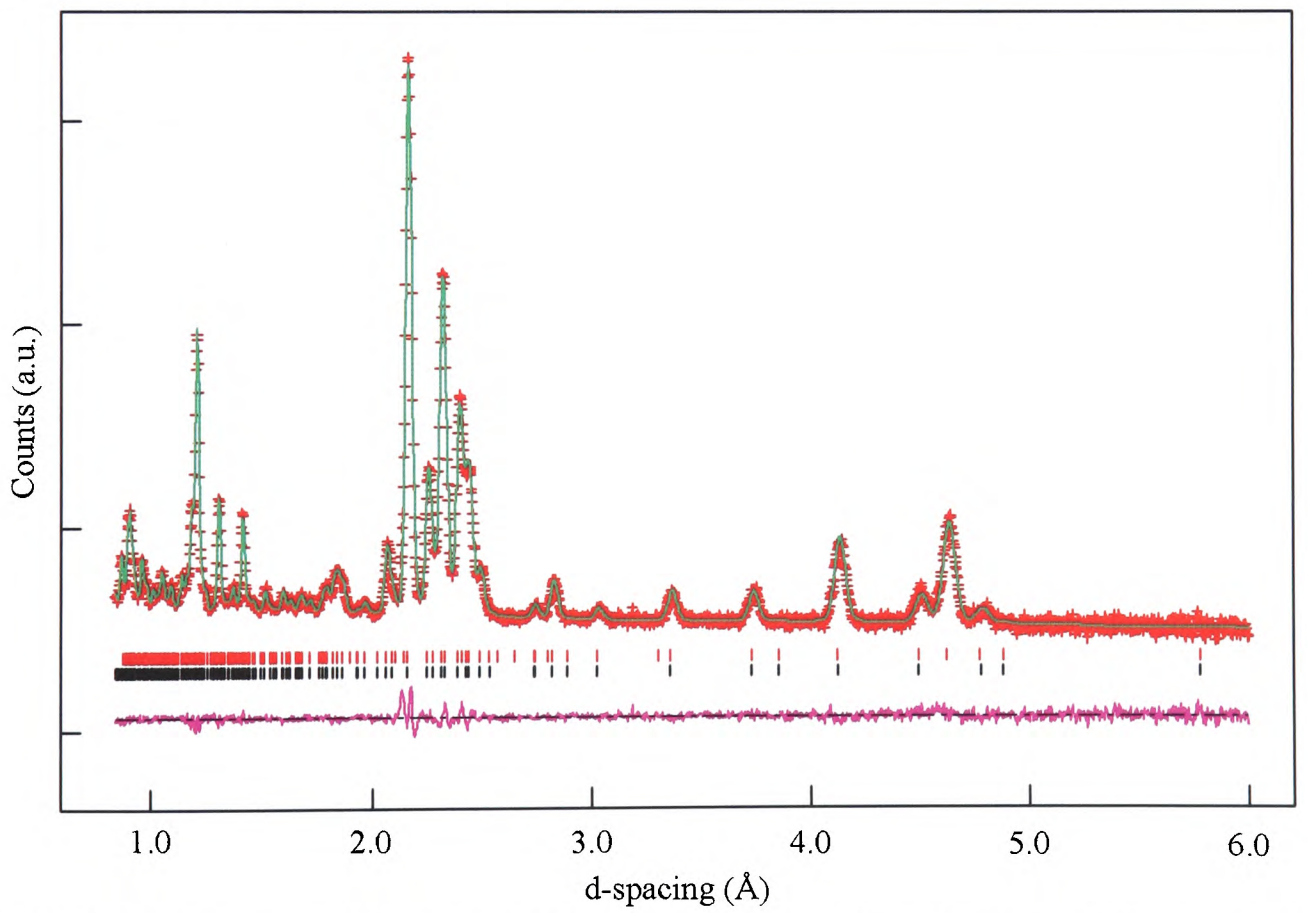


Figure 5.23 Observed, calculated and difference plots from the structural refinement of 10H-$BaMnO_{2.91(1)}$ against neutron powder diffraction data collected at 1.8K. Lower tick marks represent reflection positions for the nuclear model; upper tick marks the magnetic model.

Atom	x	y	z	Fractional Occupancy	U_{equiv} (Å^2)
Ba1	0	0	0	1	0.0183
Ba2	⅓	⅔	¼	1	0.0050
Mn1	⅓	⅔	0.60860(7)	1	0.0045
O1	½	0	0	0.971	0.0087
O2	-0.18913(5)	-0.3782(1)	¼	0.761	0.0101

Table 5.6 Structural parameters refined against neutron powder diffraction data collected at 1.8K from 4H-$BaMnO_{2.65(1)}$.

Atom	x	y	z	Fractional Occupancy	U_{equiv} (Å^2)
Ba1	0	0	0	1	0.0021
Ba2	⅓	⅔	¼	1	0.0014
Mn1	⅓	⅔	0.60855(9)	1	0.0019
O1	½	0	0	0.982(3)	0.0037
O2	-0.18677(2)		¼	0.990(2)	0.0034

Table 5.7 Structural parameters refined against neutron powder diffraction data collected at 1.8K from 4H-$BaMnO_{3.00(1)}$.

Atom	x	y	z	Fractional Occupancy	U_{equiv} (Å^2)
Ba/Sr1	0	0	0	0.67/0.33	0.0190
Ba/Sr2	⅓	⅔	¼	0.33/0.67	0.0079
Mn1	⅓	⅔	0.6097(3)	1	0.0077
O1	½	0	0	0.998	0.0149
O2	-0.1853(2)	-0.3706(4)	¼	0.850	0.0140

Table 5.8 Structural parameters refined against neutron powder diffraction data collected at 1.8K from 4H-$Ba_{0.5}Sr_{0.5}MnO_{2.79(1)}$.

Atom	x	y	z	Fractional Occupancy	U_{equiv} (Å^2)
Ba/Sr1	0	0	0	0.68/0.32	0.0059
Ba/Sr2	⅓	⅔	¼	0.32/0.68	0.0058
Mn1	⅓	⅔	0.6112(2)	1	0.0051
O1	½	0	0	1	0.0083
O2	-0.1839(1)		¼	0.994(2)	0.0051

Table 5.9 Structural parameters refined against neutron powder diffraction data collected at 1.8K from 4H-$Ba_{0.5}Sr_{0.5}MnO_{2.99(1)}$.

	4H-$BaMnO_{2.65(1)}$	4H-$BaMnO_{3.00(1)}$	4H-$Ba_{0.5}Sr_{0.5}MnO_{2.79(1)}$	4H-$Ba_{0.5}Sr_{0.5}MnO_{2.99(1)}$
***a* (Å)**	5.6651(2)	5.62732(8)	5.5722(2)	5.5390(1)
***c* (Å)**	9.3196(3)	9.2080(1)	9.1887(3)	9.1236(1)
χ^2	1.836	1.093	8.154	5.521
Rp	2.44	2.05	3.78	3.60
wRp	1.41	1.11	5.17	4.80
Refined moment	/	2.71(2) μ_B	/	2.61(2) μ_B

Table 5.10 Refinement statistics, lattice parameters and ordered magnetic moment refined against neutron powder diffraction data collected at 1.8K from 4H-$BaMnO_{2.65(1)}$, 4H-$BaMnO_{3.00(1)}$, 4H-$Ba_{0.5}Sr_{0.5}MnO_{2.79(1)}$ and 4H-$Ba_{0.5}Sr_{0.5}MnO_{2.99(1)}$. All models are in the space group $P6_3/mmc$.

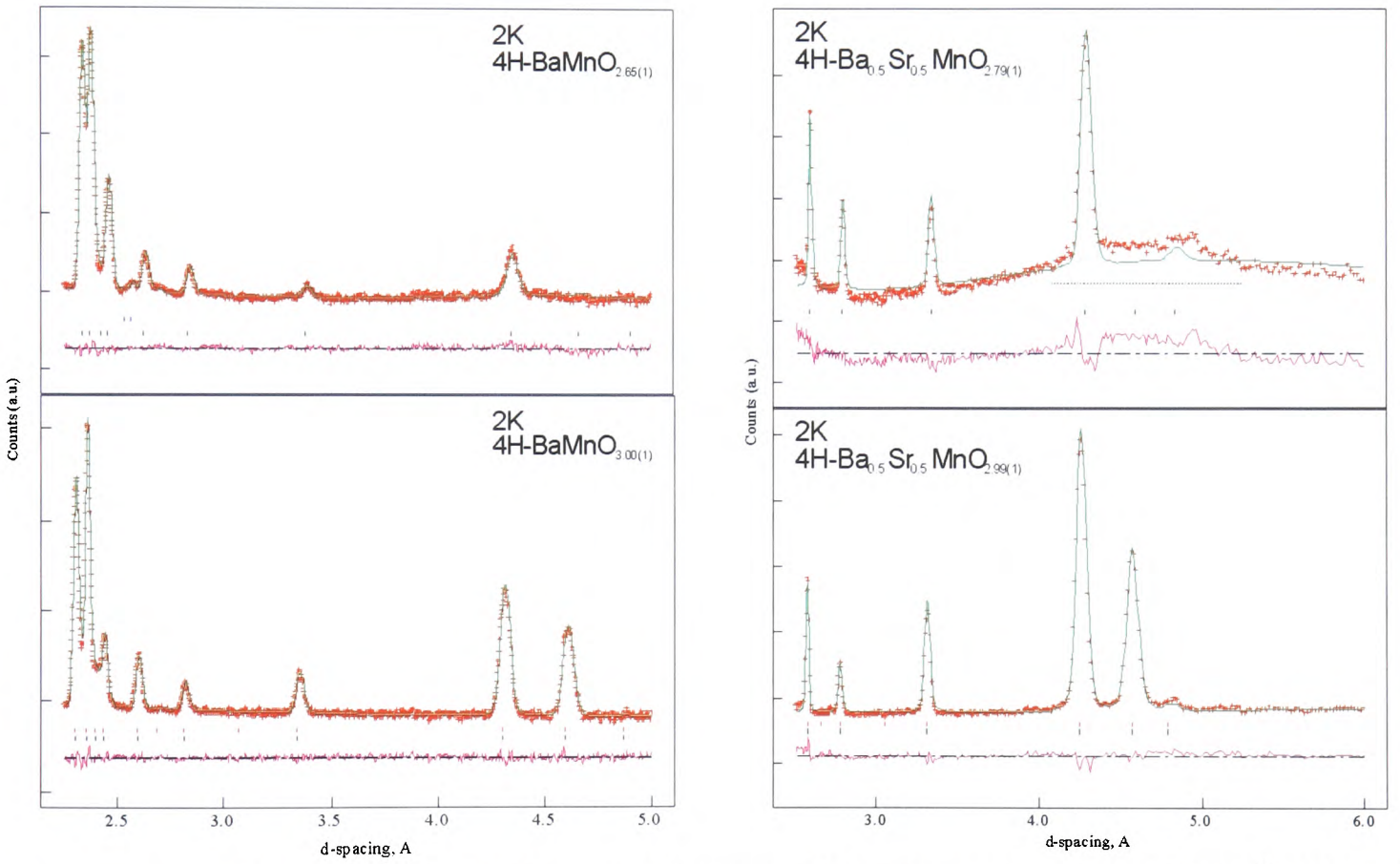


Figure 5.24 Observed, calculated and difference plots from the structural refinement of 4H-$BaMnO_{2.65(1)}$, 4H-$BaMnO_{3.00(1)}$, 4H-$Ba_{0.5}Sr_{0.5}MnO_{2.79(1)}$ and 4H-$Ba_{0.5}Sr_{0.5}MnO_{2.99(1)}$ against neutron powder diffraction data collected at 1.8K. Lower tick marks represent reflection positions for the nuclear model; upper tick marks the magnetic model. A dashed line highlights the broad feature observed in the 4H-$Ba_{0.5}Sr_{0.5}MnO_{2.79(1)}$ data.

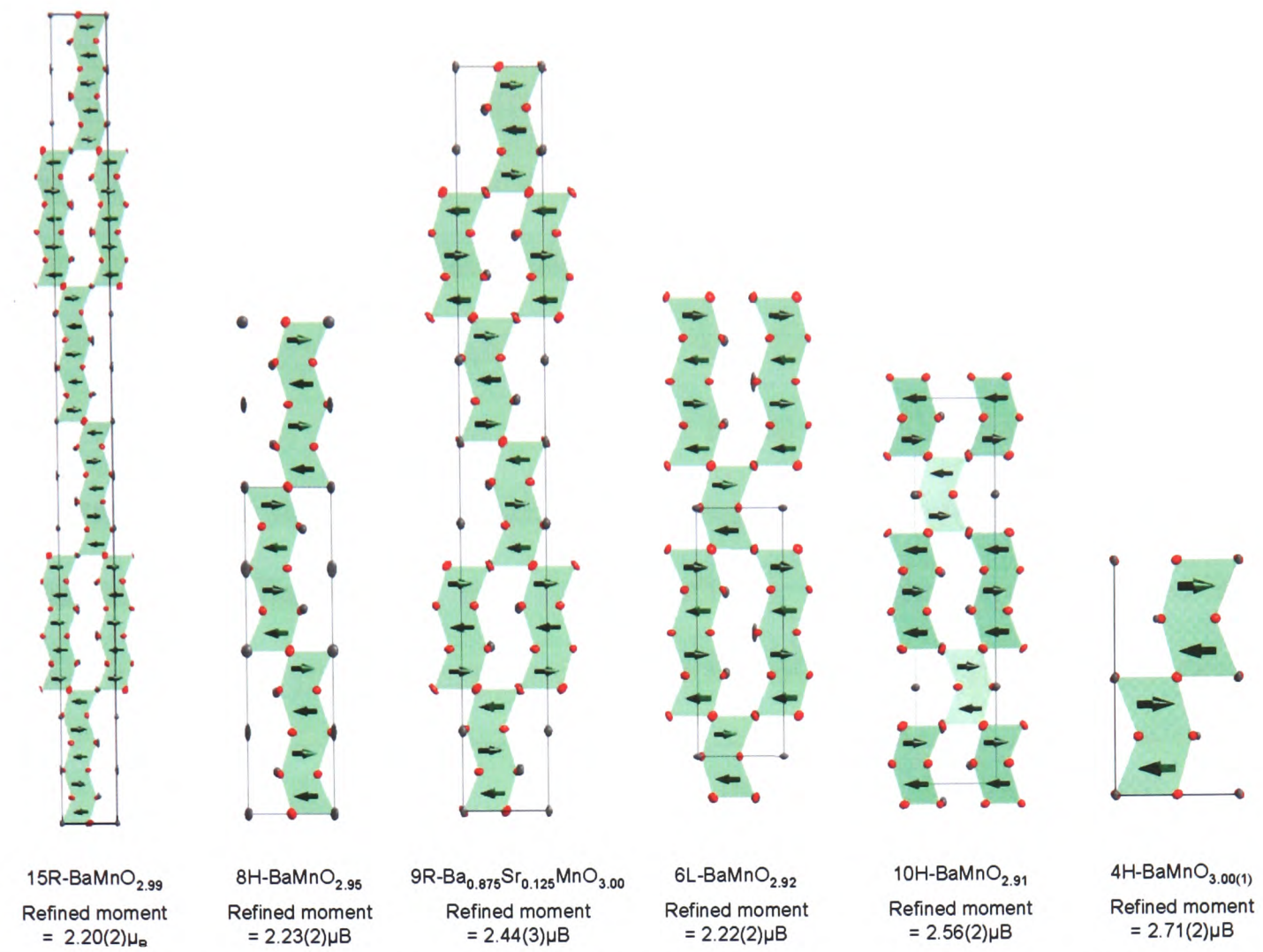


Figure 5.25 Nuclear and magnetic models obtained from refinement against neutron diffraction data collected at 1.8K. Marked cell edges correspond to the magnetic unit cell.

5.3.2.4.2. Discussion

The expected magnetic moment for a magnetically ordered Mn(IV) system is 3 μ_B. All ordered moments from refinement are significantly smaller than this. The ordered moments obtained from refinement and the percentage reductions from the expected value are listed in Table 5.11. Reported ordered moments are also lower than expected for 4H-$Ba_{0.1}Sr_{0.9}MnO_{2.96}$ (refined moment = 2.41(4) μ_B, ~ 80% of expected value), 2H-$BaMnO_3$ (refined moment = 1.31(5) μ_B, ~ 44% of expected value) and 2H-$CsVI_3$ (refined moment = 1.64(5) μ_B, ~ 54% of expected value).[4, 12, 109] This has been attributed to both zero point motion and covalency.[118] Previous work suggests zero point motion is the more significant effect as the percentage reduction is comparable for the isostructural and isoelectronic compounds 2H-$BaMnO_3$ and 2H-$CsVCl_3$.[4] The ordered moments of the $BaMnO_{3-x}$ series are consistent with this. It is reasonable to assume that the effect of covalency in reducing the ordered moment is constant across the $BaMnO_{3-x}$ series, yet greater variation in the refined magnetic moment is observed over the

$BaMnO_{3-x}$ series (Table 5.11) than between the 2H-$BaMnO_3$ and 2H-$CsVI_3$ phases discussed above. This suggests that the variation across this series is due to alterations in the zero point motion. The zero point spin deviation is related to the dimensionality of the structure, where lower dimensional structures have greater zero point motion.[119] Therefore, the closer the structure is to being one-dimensional, the greater the effect of the zero point motion in reducing the moment. This is observed to some degree in the data. The magnitude of the refined magnetic moments shows a correlation with the length of the face-sharing chains. The stacking sequences of 4H-$BaMnO_{3.00(1)}$ and 10H-$BaMnO_{2.91(1)}$ have short chains and an increased ordered moment compared to phases such as 15R-$BaMnO_{2.99(1)}$ with long face-sharing chains.

Sample	Ordered magnetic moment (μ_B)	Reduction from expected moment
15R-$BaMnO_{2.99(1)}$	2.20	73.3%
6L-$BaMnO_{2.92(1)}$	2.22	74.3%
8H-$BaMnO_{2.95(1)}$	2.23	74.4%
9R-$Ba_{0.875}Sr_{0.125}MnO_{3.00(1)}$	2.44	81.3%
10H-$BaMnO_{2.91(1)}$	2.56	85.3%
4H-$Ba_{0.5}Sr_{0.5}MnO_{2.99(1)}$	2.61	87.0%
4H-$BaMnO_{3.00(1)}$	2.71	90.3%

Table 5.11 Ordered magnetic moments from refinement of 1.8K neutron diffraction data and the percentage decrease from the theoretical value of $3\mu_B$.

5.4. Conclusion

The magnetic behaviour of $BaMnO_{3-x}$ phases has been investigated and shown to be closely related to that of the structurally related phase 4H-$SrMnO_3$. Antiferromagnetic coupling occurs above ambient temperature between manganese ions connected by a shared face using a direct exchange interaction. However, magnetic order is achieved by a weaker superexchange interaction through the apex-sharing oxide ions. The strength of this interaction is dependent on the length of the face-sharing chains, longer chains representing a weaker interaction. The

magnetic models of $BaMnO_{3-x}$ phases are similar to that of 4H-$Ba_{0.5}Sr_{0.5}MnO_{3-x}$. Magnetic moments lie in the *ab* plane and are antiferromagnetically aligned along the *c* axis. The magnitude of the ordered moment is also dependent on the length of the face-sharing chains, longer chains representing a smaller ordered moment.

Chapter 6: The effect of disorder on magnetic behaviour

6.1. *Introduction*

The previous chapter introduced a magnetic model which can be used to rationalise the magnetic behaviour of hexagonal perovskite phases in the $Ba(Sr)MnO_{3-x}$ series. In this model, there are three different magnetic interactions, shown in Figure 6.1. The strongest interaction (J_1) occurs between octahedral manganese ions connected by a shared face. This results in local antiferromagnetic coupling within face-sharing chains at an unknown temperature, $T > 300K$. The second interaction (J_2) utilises a 180° superexchange interaction between MnO_6 octahedra connected by apex-sharing. This interaction connects the locally ordered face-sharing chains, bringing about long-range magnetic order at a temperature in the range $230 \leq T\,(K) \leq 280$. The weakest magnetic interaction occurs at $T \sim 45K$. The mechanism of this interaction is not known, but it introduces a small ferromagnetic component to the susceptibility. This could represent either the freezing of spins which do not participate in the ordered structure or a transition to a canted antiferromagnetic state through an interchain interaction as shown in Figure 6.1 (J_3).

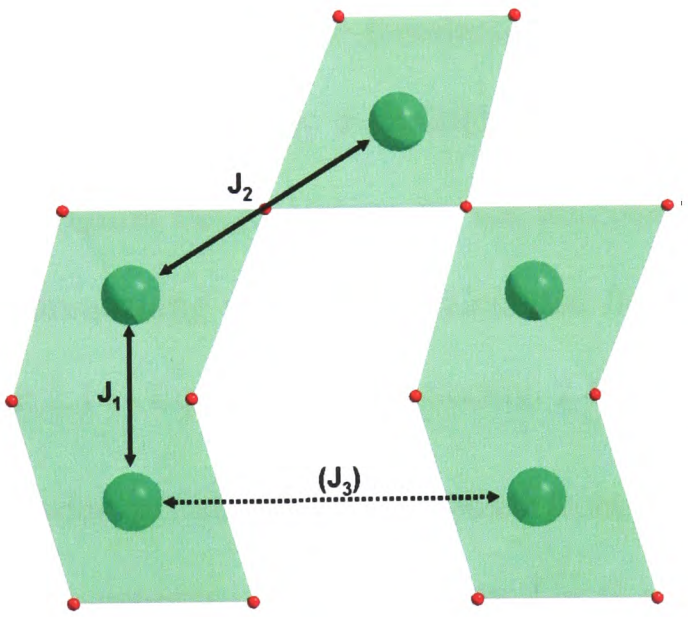


Figure 6.1 The three magnetic interactions in $BaMnO_3$ hexagonal perovskites. J_1 is the strongest, J_2 the second strongest. It is possible that the third interaction, J_3, is an interchain interaction as shown here.

The magnetic behaviour may be altered by introducing disorder into the system. There are two major types of disorder that can be introduced into $Ba(Sr)MnO_{3-x}$ phases: structural disorder and charge disorder.

6.2. *Structural disorder*

Structural disorder is prevalent in the $BaMnO_{3-x}$ phases. In their study of the series by the means of electron diffraction and electron microscopy, González-Calbet et al. observed that the electron diffraction patterns often show streaking along the c^*-axis, indicative of stacking disorder.[105, 108] Electron microscopy reveals that this is the result of disordered intergrowths of several different stacking sequences within individual crystallites.

The extent of structural disorder for a bulk sample can be monitored by measuring the peak widths of diffraction reflections. As discussed in Section 2.4, the half width of a peak is a complex function of both instrumental factors (modelled using a Gaussian function) and sample dependent factors (modelled using a Lorentzian function). The Lorentzian function is defined using two parameters, X and Y, which model broadening attributable to the particle size and microstrain respectively. Each parameter is modified by a second term, X_e or Y_e, which describes the anisotropic nature of the broadening with respect to a defined axis. The Lorentzian parameters may be separated by their different 2θ dependencies, especially if data are collected over a wide angular range. Values for the microstrain and particle size parallel and perpendicular to the broadening axis can be calculated from the four Lorentzian profile parameters using Equation 2.14 - Equation 2.17 in Section 2.4.3.

Examination of X-ray powder diffraction data collected from $Ba(Sr)MnO_{3-x}$ samples reveals that the *hk0* reflections are consistently sharper than $l \neq 0$ reflections. This indicates the presence of anisotropic broadening along the [*00l*] axis, and is consistent with the streaking along c^* observed by González-Calbet et al.. This suggests the anisotropic broadening is caused by disordered intergrowths of alternate stacking sequences.

Refinement against the neutron and X-ray powder diffraction data collected from 8H-$BaMnO_{3-x}$, 6L-$BaMnO_{3-x}$, 10H-$BaMnO_{3-x}$ and 4H-$BaMnO_{3-x}$ reveal that the anisotropic peak broadening is minimal. A greater degree of anisotropic broadening is observed in X-ray powder diffraction data collected from 15R-$BaMnO_{3-x}$ and 9R-$Ba_{0.175}Sr_{0.125}MnO_3$. The synthesis conditions for final samples of 15R-$BaMnO_{2.99(1)}$ and 9R-$Ba_{0.875}Sr_{0.125}MnO_{3.00(1)}$ discussed in Chapter 4 were chosen so as to minimise the anisotropic broadening, but X-ray powder diffraction and magnetometry data were also collected from a number of samples which were less than fully ordered.

6.2.1. 15R-$BaMnO_{2.99(1)}$ and 9R-$Ba_{0.875}Sr_{0.125}MnO_{3.00(1)}$

X-ray powder diffraction data were collected from a sample of 9R-$Ba_{0.875}Sr_{0.125}MnO_{3.00(1)}$ fired for a total of 16 days at $T \leq 1050°C$ (labelled 9R-i). The sample was then fired for a further 32 days at $T \leq 1150°C$ and further X-ray diffraction data were collected. This second sample is the 9R-$Ba_{0.875}Sr_{0.125}MnO_{3.00(1)}$ phase discussed in previous chapters (labelled 9R-ii for the purpose of this discussion). A 9R model was refined against the two data sets, with particular regard paid to the anisotropic peak broadening parameters. The structural models obtained on refinement against the two X-ray powder diffraction data sets are identical to within the resolution of the measurement, but close examination reveals differences in the peak widths of the two diffraction data sets indicative of differing degrees of crystallinity between the two samples.

Table 6.1 lists the coherent particle size and microstrain for the two samples of 9R-$Ba_{0.875}Sr_{0.125}MnO_3$, calculated from the Lorentzian profile parameters obtained on refinement. The 9R-ii sample (fired for an additional 32 days) has reduced microstrain and increased coherent particle size parallel to the [*001*] broadening axis when compared to the 9R-i sample.

Label	T (°C)	Time (days)	Size ⊥ (Å)	Size ‖ (Å)	Strain ⊥ (%)	Strain ‖ (%)
9R-i	1000 +1050	2 +14	≥ 4000	610(30)	0.15(1)	0.35(1)
9R-ii	+1100 +1150	+9 +23	5200(600)	1500(100)	0.05(1)	0.05(1)

Table 6.1 Size and strain broadening on refinement against X-ray diffraction data collected from the samples 9R-i and 9R-ii, calculated parallel and perpendicular to the *00l* axis. The coherent particle size in the *ab* plane could not be determined for 9R-i as any peak broadening due to this was negligible compared to other factors. The value of 4000 was found to be the size limit for the observation of broadening as a result of coherent particle size in the *ab* plane.

Susceptibility data show a strong dependency on the degree of anisotropic broadening observed in the X-ray diffraction data. Susceptibility data measured from 9R-i and 9R-ii are shown in Figure 6.2.

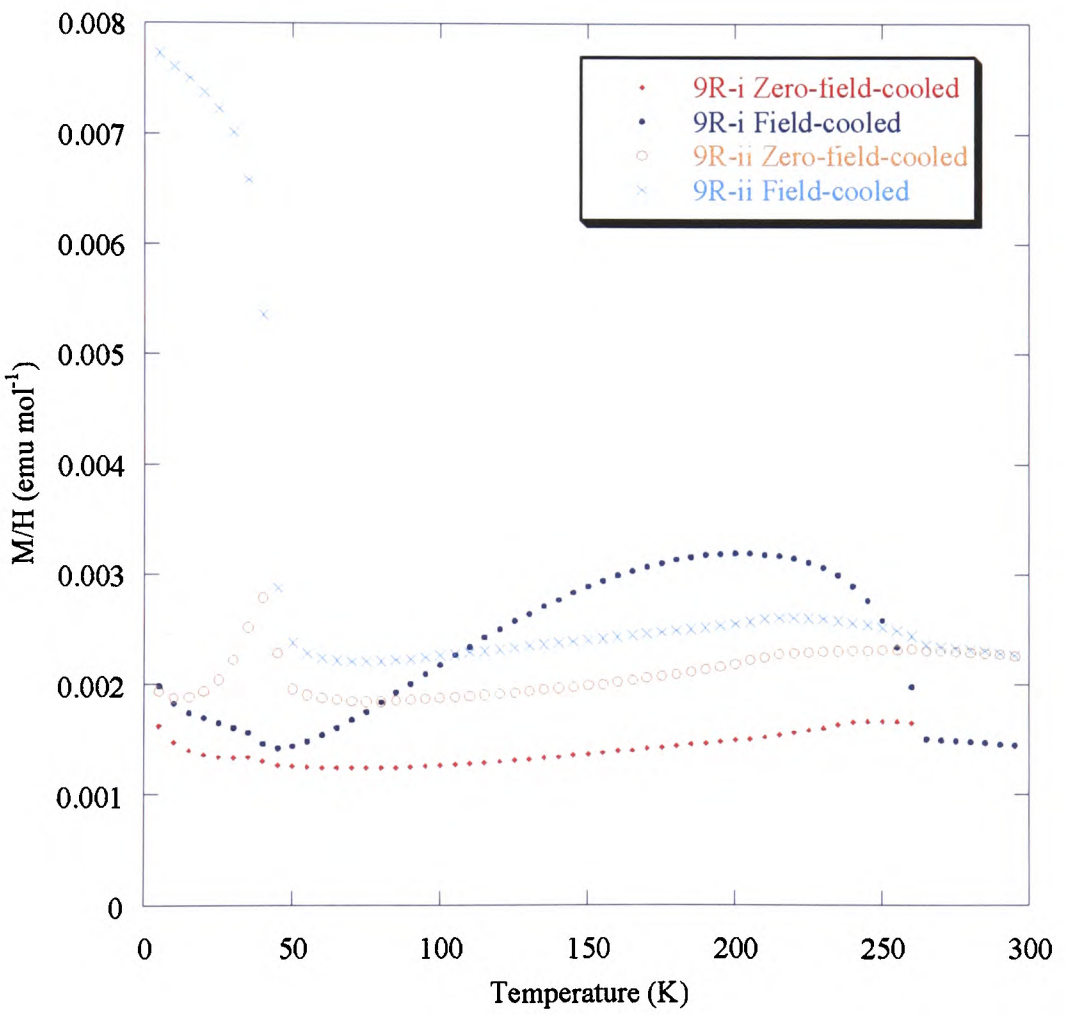


Figure 6.2 Magnetisation data collected from different samples of 9R-$Ba_{0.875}Sr_{0.125}MnO_3$.

The susceptibility data are similar in that zero-field-cooled and field-cooled data diverge at T ~ 260K and a further magnetic event occurs at T ~ 45K. They differ in that the temperature dependence in the range 45K ≤ T(K) ≤ 260K is much greater for the highly anisotropic 9R-i

sample, and the divergence at T ~ 45K is almost totally suppressed. The susceptibility data collected from the 9R-ii sample closely resemble those collected from the other $Ba(Sr)MnO_{3-x}$ samples, described in Section 5.3.1.

The increased microstrain and reduced coherent particle size observed in the 9R-i sample are believed to be due to the introduction of disordered intergrowths of alternate stacking sequences. This can be reduced by prolonged heating. The anisotropy of the sample indicated by the X-ray diffraction data clearly has an effect on the susceptibility data. X-ray diffraction data collected from 9R-i and 9R-ii are identical save for the degree of anisotropic broadening, yet susceptibility data show considerable variation. The variation is predominantly associated with the event at T ~ 45K, suggesting that this is highly dependent on the degree of structural order. However, the overall magnitudes of susceptibility data collected from both 9R-i and 9R-ii are comparable: both are relatively low. This suggests that the majority of spins are antiferromagnetically coupled in both samples, and thus that the interaction across the shared faces is not greatly affected by structural disorder.

A similar effect to that observed for 9R-$Ba_{0.875}Sr_{0.125}MnO_3$ can be observed in data collected from 15R-$BaMnO_{3-x}$ samples. A number of 15R-$BaMnO_{3-x}$ samples were prepared in the course of investigating the phase diagram of $BaMnO_{3-x}$ in Chapter 3. Figure 6.3 shows the peak widths of a 15R sample (15R-I) fired under a 33% pO_2 atmosphere at 1330°C for 200hr (15R-Ia) and from the same sample after a further 40hr firing at 1335°C and 40hr at 1345°C (15R-Ib). All *hk0* reflections are sharper than the $l \neq 0$ reflections, providing clear evidence of anisotropic peak broadening. On increasing the firing temperature there is relatively little change in the *hk0* reflections but all $l \neq 0$ reflections are sharper, indicating that the anisotropic broadening associated with disordered intergrowths is reduced.

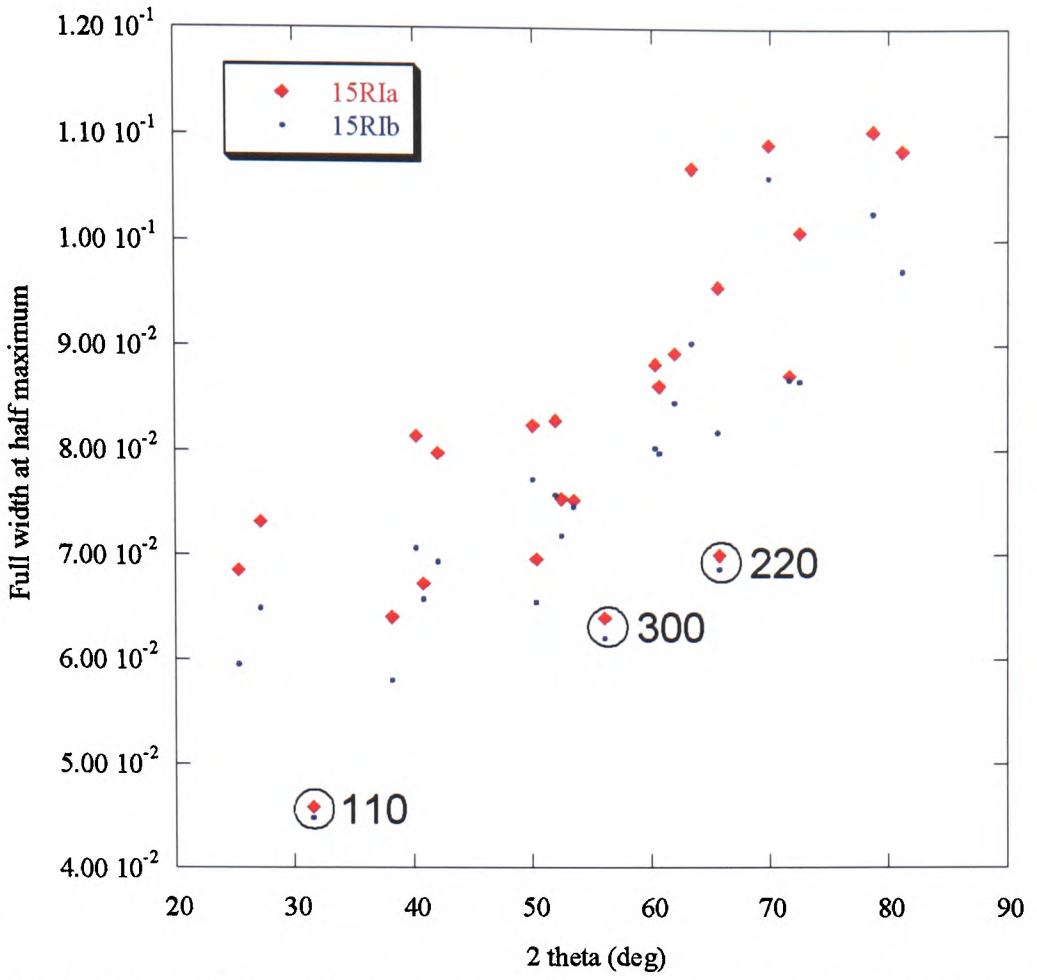


Figure 6.3 Peak widths in 15R-Ia and 15R-Ib $BaMnO_{3-x}$ samples. All *hk0* peaks are labelled.

The 15R model was refined against the X-ray diffraction data collected from 15R-Ia and 15R-Ib with particular regard paid to the anisotropic peak broadening parameters. Refinement was also carried out against data collected from a comparable 15R-$BaMnO_{3-x}$ sample (15R-II) fired in air at 1275°C. 15R-IIa was fired for 72 hours and 15R-IIb for a further 360 hours. The structural models obtained on refinement against all data sets are near identical; however, the anisotropic peak broadening parameters varied across the four samples. Values for the microstrain and particle size parallel and perpendicular to the [*00l*] axis were calculated from the Lorentzian profile parameters obtained on refinement against X-ray diffraction data using Equation 2.14 - Equation 2.17 in Section 2.4.3. Results are listed in Table 6.2.

Label	T (°C)	% O_2 (%)	Time (hr)	Size ⊥ (Å)	Size ‖ (Å)	Strain ⊥ (%)	Strain ‖ (%)
15R-Ia	1330	33.3	200	7000(1000)	1700(100)	0.03(2)	0.04(2)
15R-Ib	1335 1345		+40 +40	9000(1000)	2700(200)	0.03(1)	0.05(1)
15R-IIa	1275	21 (air)	72	8000(1000)	1900(200)	0.05(3)	0.13(1)
15R-IIb			+360	10000(1000)	2500(300)	0.04(1)	0.04(1)

Table 6.2 Microstrain and particle size for 15R-Ia, 15R-Ib, 15R-IIa and 15R-IIb. Values are calculated from the Lorentzian profile parameters obtained on refinement against X-ray powder diffraction data with an anisotropic broadening axis of *00l*.

The greatest degree of anisotropy was observed for the 15R-IIa sample fired under air at 1275°C for only 72 hours. The microstrain parallel to the *c* axis (0.13(1)%) is reduced by prolonged firing times (microstrain (15R-IIb) = 0.04(1)%), or firing at a higher temperature (microstrain (15R-Ia) = 0.04(2)%). Susceptibility data were collected from a sample showing a high degree (15R-IIa) and a low degree (15R-Ib) of anisotropic peak broadening. These data are shown in Figure 6.4.

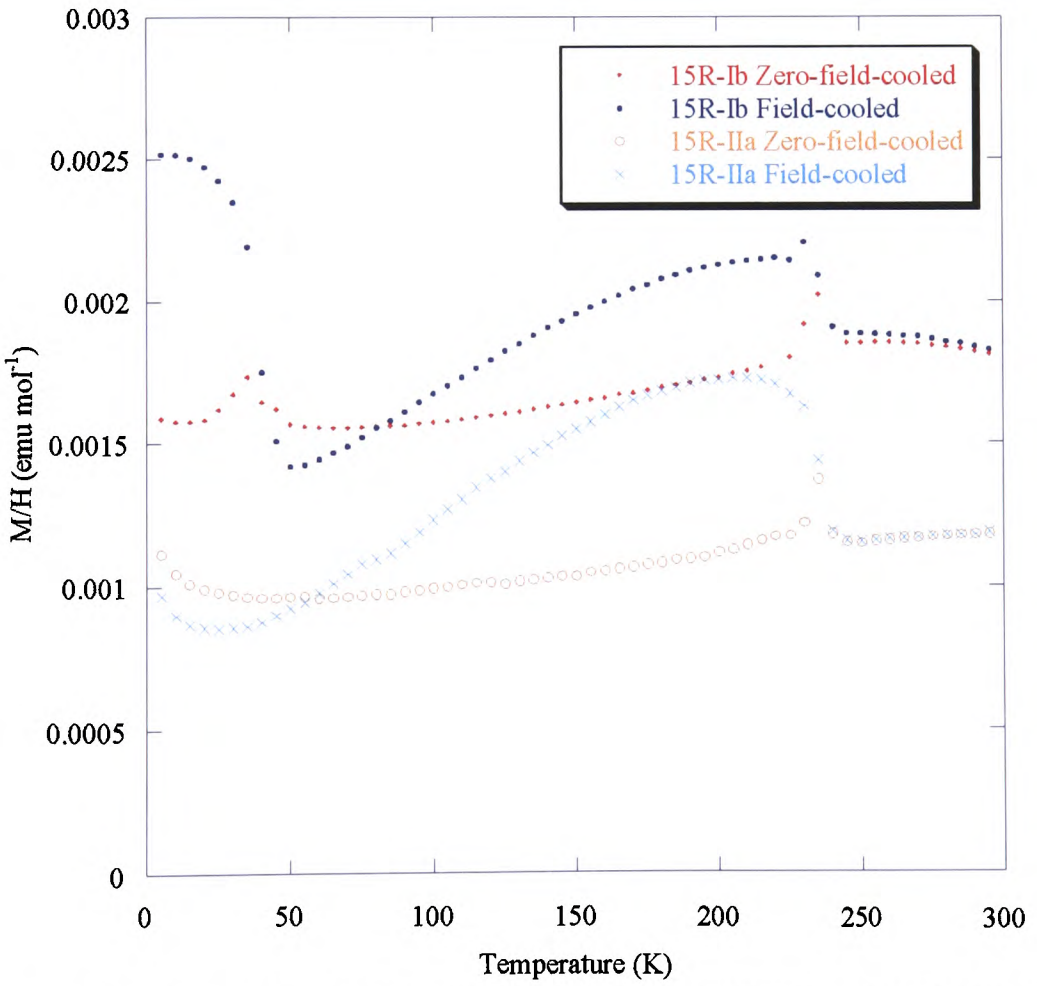


Figure 6.4 Magnetisation data collected from different samples (15R-Ib and 15R-IIa)of 15R-$BaMnO_{3-x}$.

The two 15R-$BaMnO_{3-x}$ samples 15R-Ib and 15R-IIa both show anomalous behaviour in the temperature range T < 250K. The zero-field-cooled and field-cooled data diverge below this temperature, ultimately crossing at T ~ 55K for 15R-IIa and T ~ 80K for 15R-Ib. Below these temperatures, the magnitude of the field-cooled magnetisation is lower than that of the zero-field-cooled magnetisation. The crossing of field-cooled and zero-field-cooled data suggests ferrimagnetic ordering, probably associated with disordered intergrowths of alternate stacking sequences. This is consistent with diffraction data: the anisotropic broadening thought to be associated with the presence of disordered intergrowths is reduced in data collected from 15R-Ib compared to that collected from 15R-IIa. This reduction in the proportion of disordered intergrowths results the introduction of a feature at T ~ 45K. Thus the susceptibility data collected from 15R-Ib appear similar to those collected from other Ba(Sr)MnO_{3-x} samples, as was observed for the 9R-ii sample. However the crossing of zero-field-cooled and field-cooled data still occurs, suggesting that a significant proportion of disordered intergrowths are still present. The sensitivity of the magnetic event at T ~ 45K to the presence of disorder is consistent a slight canting of the ordered moments. Such a subtle modification to the antiferromagnetic state is likely to be easily disrupted by structural disorder.

Although there are differences in the observed susceptibility data collected from 9R-i and 9R-ii or from 15R-Ib and 15R-IIa, the relatively small magnitude of these features indicates that they represent either a negligible change to the magnetic state or the behaviour of a small minority of spins (probably those which do not participate in the ordered structure). The sensitivity of the susceptibility data to the presence of disordered intergrowths is much greater than that of the diffraction data. Neutron diffraction data collected from the 15R-IIa sample at 1.8K still reveal additional intensity due to long-range magnetic order (as discussed in Section 5.3.2.4) despite the anomalous behaviour observed in susceptibility data.

6.2.2. 2H-$BaMnO_3$

The X-ray powder diffraction data collected from samples of 15R-$BaMnO_{3-x}$ and 9R-$Ba_{0.175}Sr_{0.125}MnO_3$ revealed a greater degree of anisotropic peak broadening than comparable data sets collected from 8H-$BaMnO_{3-x}$, 6L-$BaMnO_{3-x}$, 10H-$BaMnO_{3-x}$ and 4H-$BaMnO_{3-x}$ samples. One possible reason for this is the low firing temperature used in order to form 15R-$BaMnO_{3-x}$ and 9R-$Ba_{0.175}Sr_{0.125}MnO_3$. A still lower firing temperature is required for the formation of 2H-$BaMnO_3$, and so the peak widths and susceptibility data of two samples of 2H-$BaMnO_3$ were also examined for anomalous magnetic behaviour in the presence of a high degree of anisotropic peak broadening.

X-ray powder diffraction data was collected from two samples of 2H-$BaMnO_3$, 2H-I and 2H-II, using the X'pert diffractometer over the range $10 < 2\theta < 120°$. Both were fired at 1000°C in air, 2H-I for 6 days, 2H-II for 42 days. Figure 6.5 shows the peak widths of 2H-I and 2H-II.

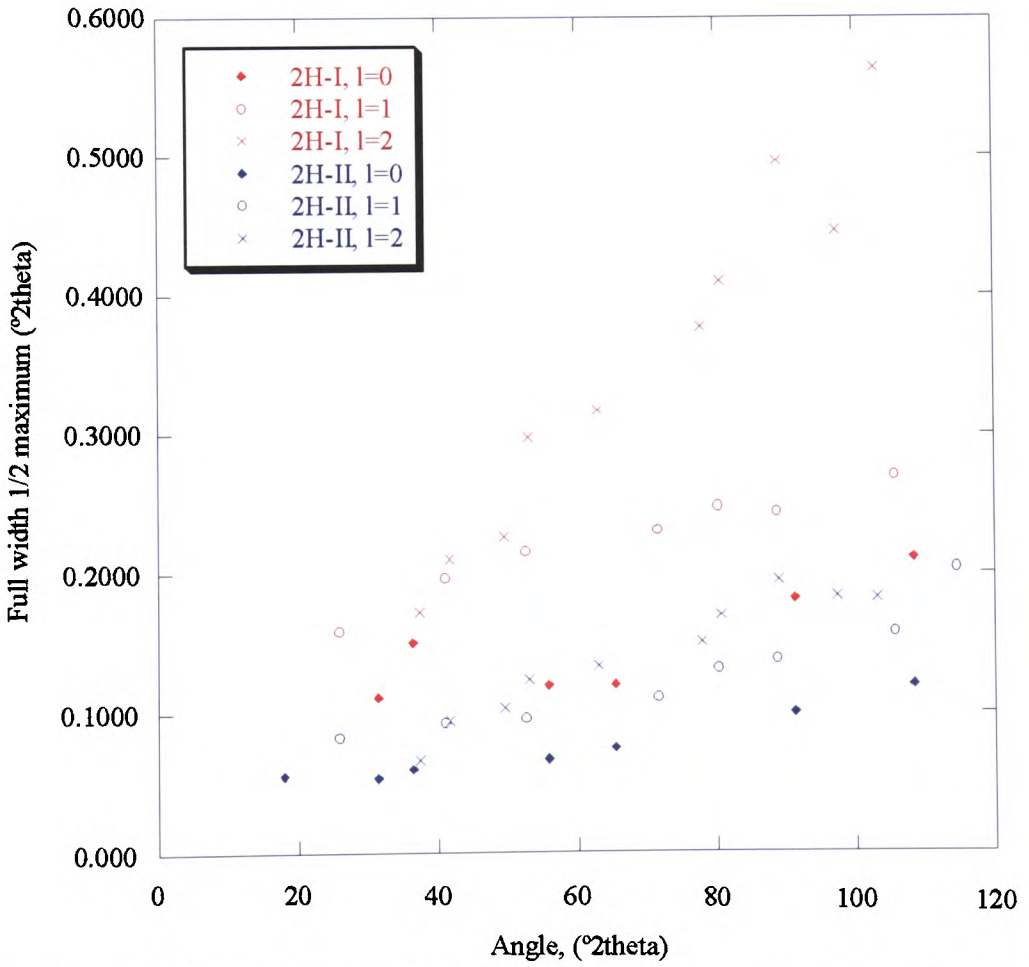


Figure 6.5 Peak width at a half maximum intensity, separated according to the value of *l* for reflections observed in X-ray diffraction data collected from two 2H-$BaMnO_3$ samples fired at 1000°C under air. 2H-I was fired for 6 days, 2H-II for 42 days.

The peak widths of both 2H-I and 2H-II show clear evidence of anisotropic peak broadening along the [*00l*] axis, where the greater the *l* value of the reflection, the broader the peak. Both the absolute peak width of all reflections and the degree of anisotropy are reduced on firing for a longer period of time.

The coherent particle size and strain parallel and perpendicular to the broadening axis (*00l*) are listed in Table 6.3, calculated from the Lorentzian profile parameters obtained from refinement.

Sample	Strain ⊥ (%)	Strain || (%)	Size ⊥ (Å)	Size || (Å)
2H-I, 6 days	0.125(5)	0.83(1)	> 10000	4600(600)
2H-II, 42 days	0	0.176(7)	> 10000	4900(300)

Table 6.3 Particle size and microstrain parallel and perpendicular to the *c* axis for 2H-$BaMnO_3$ prepared under air at 1000°C for 6 or 42 days. Sample broadening in some cases is negligible compared to the instrumental peak broadening and so undetectable. In these cases a lower limit is given.

Table 6.3 reveals that the anisotropic broadening parallel to the *c* axis is due to both a reduction in the coherent crystal length and an increase in the microstrain along this axis. The broadening due to coherent particle size does not change observably on firing for an additional 36 days, but the anisotropic microstrain is reduced from 0.83% to 0.176%.

Figure 6.6 shows the magnetisation data as a function of temperature for the two samples of 2H-$BaMnO_3$. A number of magnetic events are apparent in the susceptibility data collected from both samples. In Figure 6.6, the most notable feature is that the absolute susceptibility of 2H-I is much greater than that of 2H-II. This is largely due to the upturn in the susceptibility of 2H-I between $250 \leq T\ (K) \leq 300$. At $T \sim 250K$ there is a divergence between the zero-field-cooled and field-cooled data collected from 2H-I. The zero-field-cooled and field-cooled susceptibility data collected from the 2H-II sample diverge at the slightly lower temperature of $T \sim 230K$. In previously reported data, divergence between zero-field-cooled and field-cooled

susceptibility data occurs for T < 215K.[4] The divergence is enhanced in the data below due to the small measuring field (100 Oe).

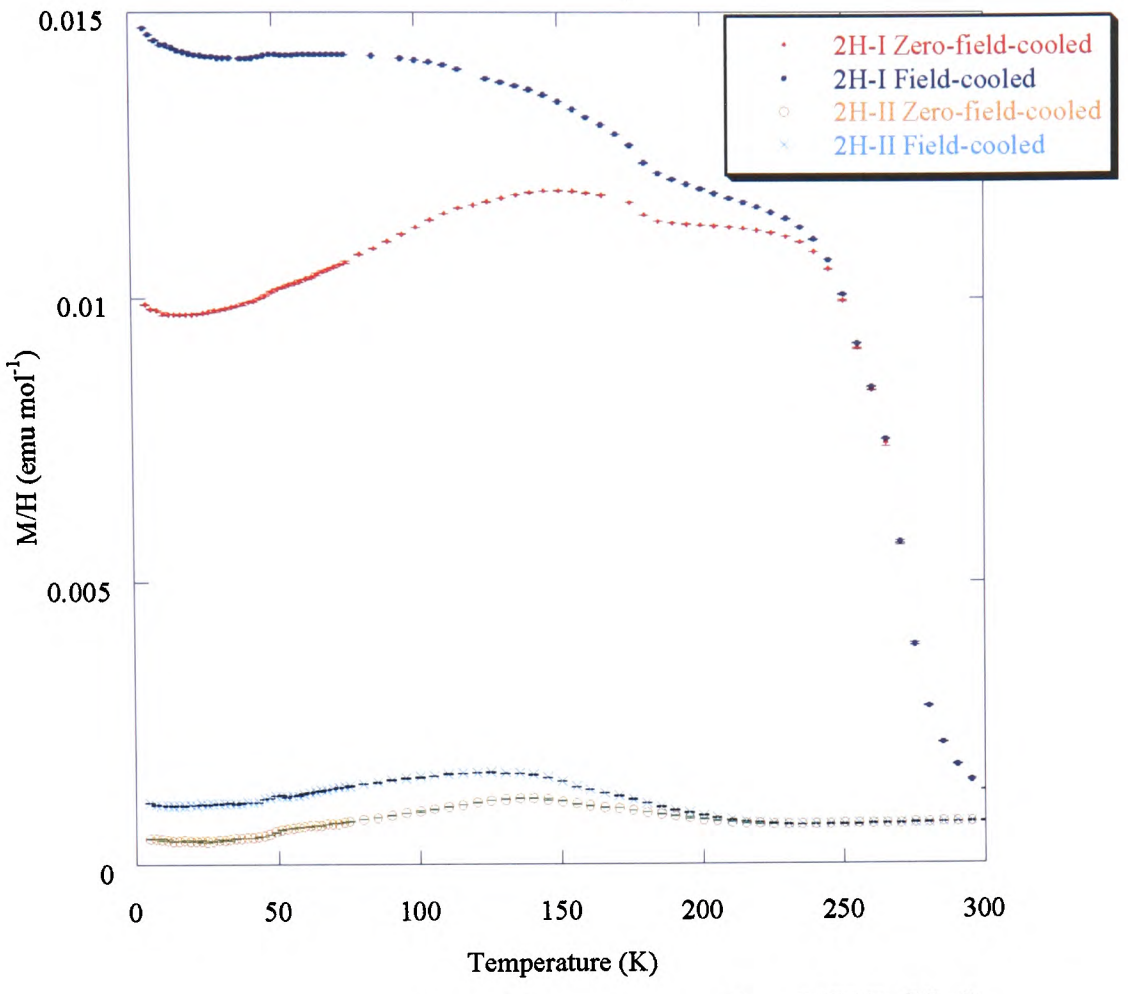


Figure 6.6 Magnetic susceptibility data collected from two samples of 2H-$BaMnO_3$.

The lowest temperature feature (observed in both data sets), is signified by discontinuity in the gradient of the field-cooled and zero-field-cooled susceptibility data at T ~ 53K (Figure 6.7). This is probably associated with the Néel temperature (T_N = 59K).

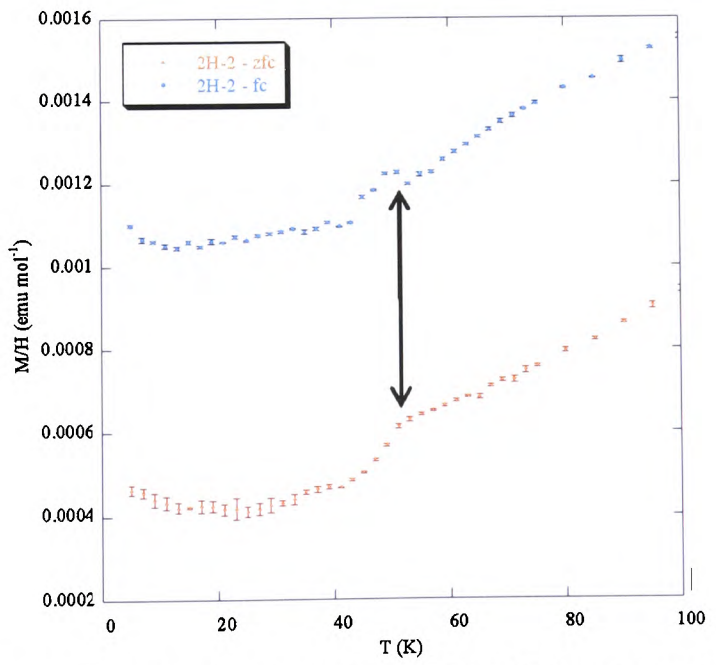


Figure 6.7 Discontinuity in gradient observed in the field-cooled and zero-field-cooled magnetisation data collected from 2H-II $BaMnO_3$ at T ~ 53K. Similar behaviour is observed for 2H-I $BaMnO_3$.

In other $BaMnO_{3-x}$ phases, a single feature occurs in the temperature range $230 \leq T\ (K) \leq 270$. Slight divergence between the zero-field-cooled and field-cooled data occurs which indicates the onset of full magnetic order utilising the 180° superexchange interaction. The ideal 2H structure has no cubic layers and so there are no 180° superexchange pathways. However, in reality most samples contain a small proportion of cubic layers. Even relatively few cubic layers disordered throughout the structure may have a large impact on the magnetic susceptibility.

The X-ray diffraction data of 2H-I suggest that there is a high degree of strain parallel to the *c* axis, indicating that 2H-I has a larger proportion of cubic layers than 2H-II. As the features observed in the susceptibility data are greatly enhanced in the 2H-I sample compared to the 2H-II sample, this suggests that these are predominantly due to the cubic layers.

6.3. *Charge disorder in 4H-$BaMnO_{2.65(1)}$ and 4H-$Ba_{0.5}Sr_{0.5}MnO_{2.79(1)}$*

It was previously noted (in Section 5.3.2.4) that the neutron diffraction data collected at 1.8K from 4H-$BaMnO_{2.65(1)}$ and 4H-$Ba_{0.5}Sr_{0.5}MnO_{2.79(1)}$ show no evidence of long-range magnetic order, although a broad feature indicative of short-range order is observed in the low temperature neutron diffraction data collected at 1.8K from 4H-$Ba_{0.5}Sr_{0.5}MnO_{2.79(1)}$. It is also notable that the hysteresis observed in magnetisation vs. field data collected at 6K from these two compounds is asymmetric with respect to the origin, whereas the hysteresis observed in comparable data collected from the remaining (magnetically ordered) $BaMnO_{3-x}$ phases is symmetric about the origin (

Figure 6.8). Asymmetric hysteresis is associated with spin glass behaviour, indicative of magnetic frustration. Therefore the magnetisation vs. field data suggests that instead of magnetic order, the magnetic moments of 4H-$BaMnO_{2.65(1)}$ and 4H-$Ba_{0.5}Sr_{0.5}MnO_{2.79(1)}$ are arranged into a glassy, frustrated system.

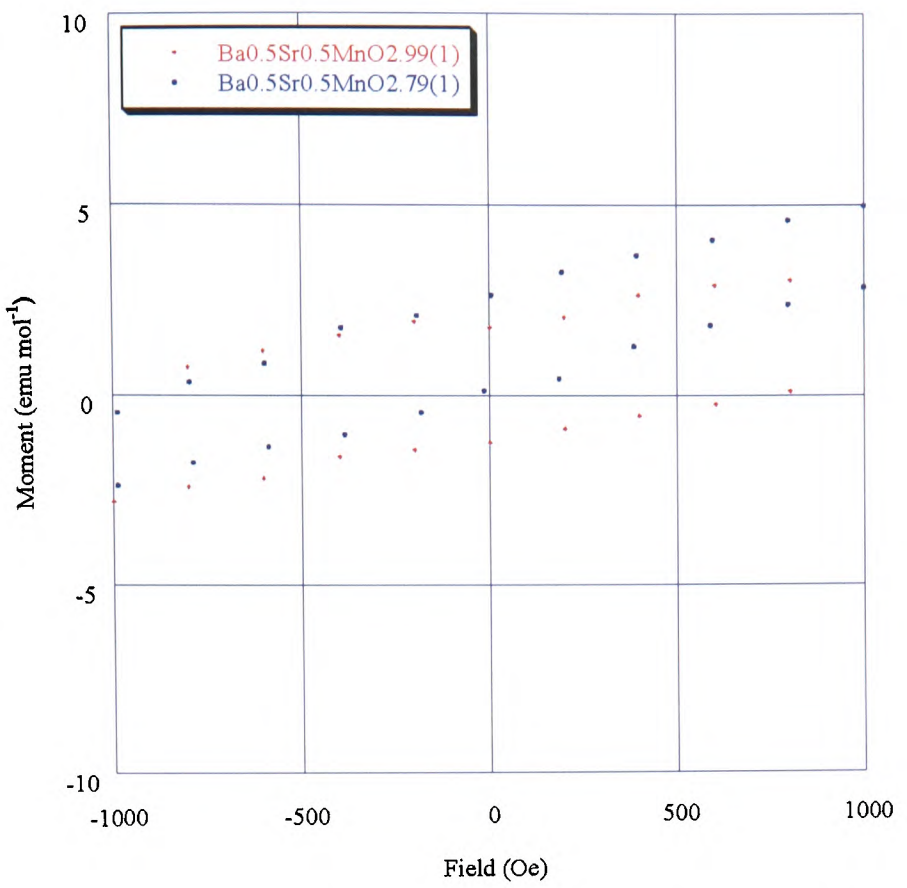


Figure 6.8 Magnetic hysteresis in 4H-$Ba_{0.5}Sr_{0.5}MnO_{2.99(1)}$ and 4H-$Ba_{0.5}Sr_{0.5}MnO_{2.79(1)}$. The hysteresis loop of 4H-$Ba_{0.5}Sr_{0.5}MnO_{2.79(1)}$ is displaced from the origin.

The 4H structure consists of an array of face-sharing Mn_2O_{9-x} dimers. The anion vacancies are disordered across the face-sharing sites, so although there is local order, where individual dimers contain either two Mn(III) or two Mn(IV) ions, there is no long-range charge order throughout the structure. The magnetisation data collected from 4H-$BaMnO_{2.65(1)}$ and 4H-$Ba_{0.5}Sr_{0.5}MnO_{2.79(1)}$ have a low absolute moment and weak temperature dependence, suggesting that antiferromagnetic coupling occurs across the shared faces. However, there is no evidence of divergence between zero-field-cooled and field-cooled data in the range $240 < T (K) < 270$. This suggests the disruption which prevents long-range magnetic order is predominantly associated with the 180° superexchange pathways.

In hexagonal perovskite structures, manganese ions adjacent to a cubic layer can couple to three neighbours via 180° superexchange pathways using the two degenerate e_g orbitals (Figure 6.9). On removing an oxide ion from the face-sharing layer, the degeneracy of the e_g orbitals is lifted. The energy of the d_{z^2} orbital is lowered relative to the $d_{x^2-y^2}$ orbital (Figure 6.10).

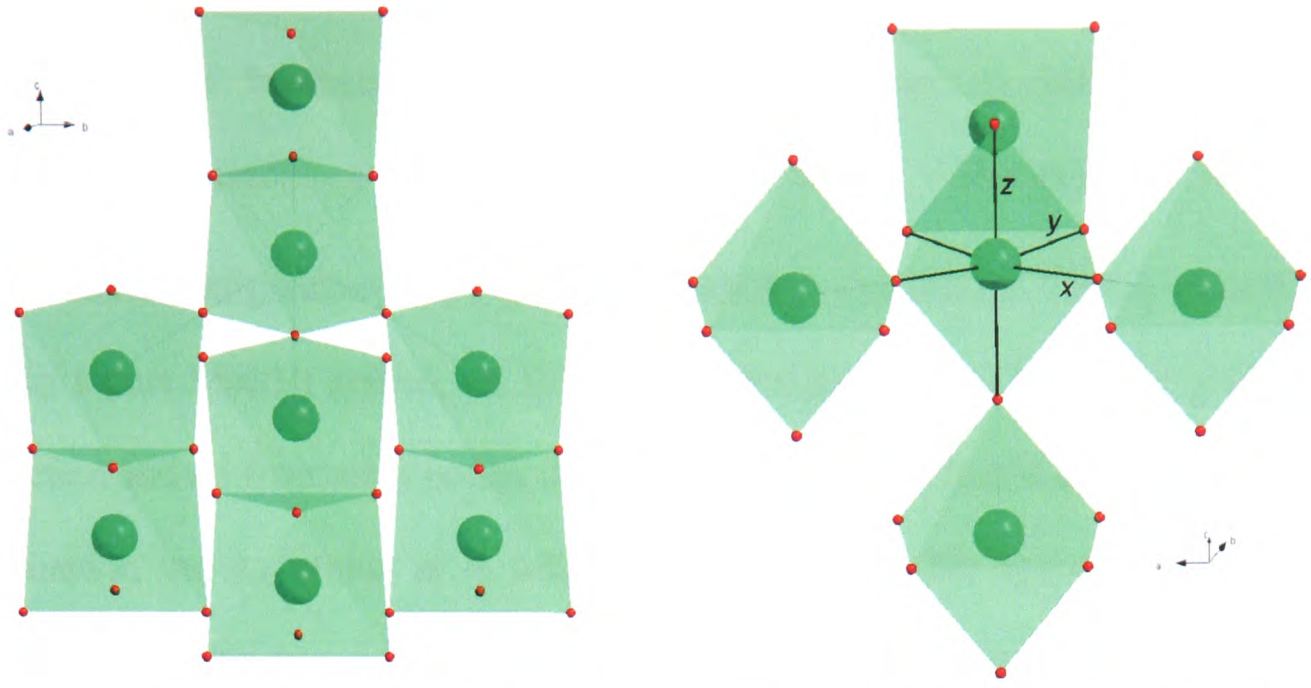


Figure 6.9 The 4H structure showing the 180° apex-sharing interactions to three adjacent manganese ions from different perspectives.

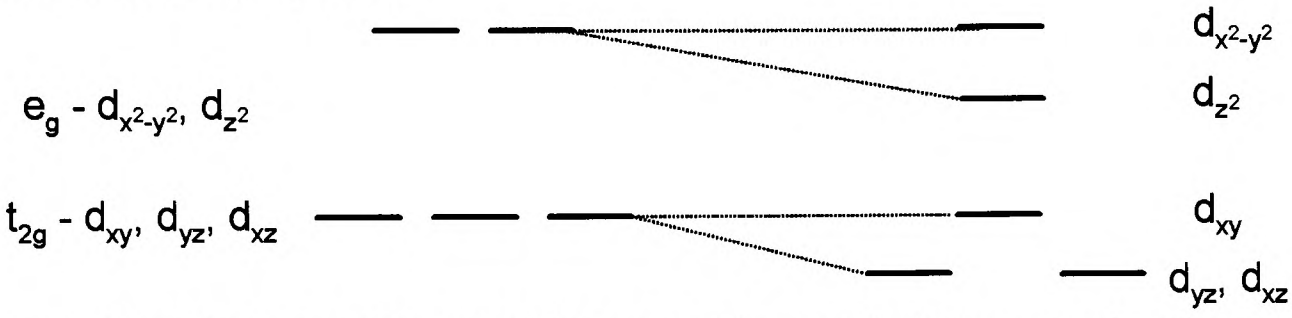


Figure 6.10 Splitting of d orbitals on lowing symmetry from octahedral to square-based pyramidal.

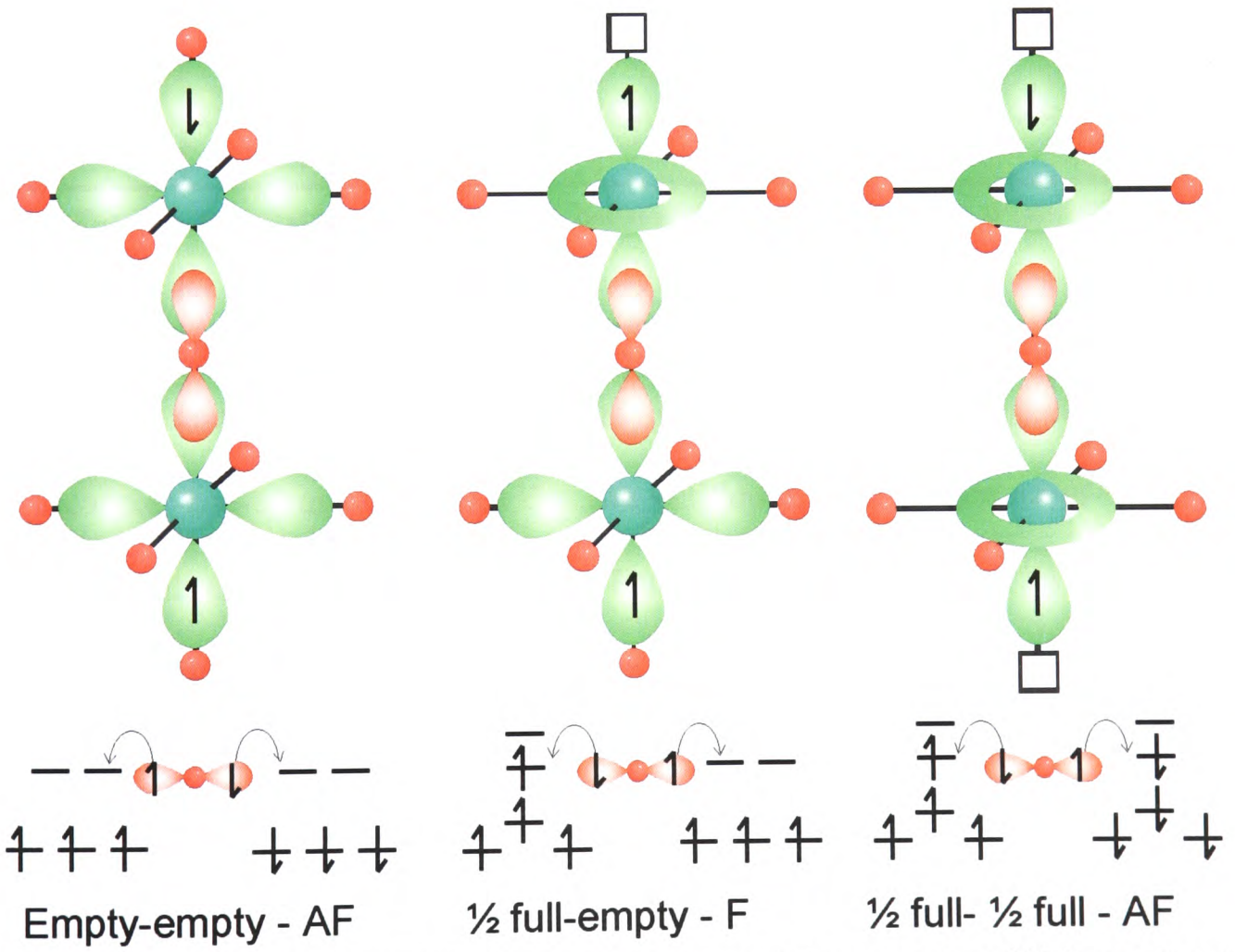


Figure 6.11 Superexchange interactions between two unoccupied manganese orbitals, an unoccupied orbital and a singly d_{z^2} occupied orbital and between two singly occupied d_{z^2} orbitals.

The Goodenough-Kanamori-Anderson rules [99] predict that 180° superexchange results in an antiferromagnetic interaction between two empty or two ½ filled e_g orbitals and a ferromagnetic interaction between an empty and a ½ filled e_g orbital (Figure 6.11).

Mn(IV) has a configuration of d^3, and so in octahedral coordination both e_g orbitals are empty. Thus in a pure Mn(IV) system, all 180° superexchange pathways favour an antiferromagnetic interaction and no frustration occurs. In contrast, Mn(III) has four d electrons so in octahedral coordination the d_{z^2} orbital is ½ full. Therefore in a Mn(III) system, 180° superexchange pathways involving two empty $d_{x^2-y^2}$ orbitals or two singly occupied d_{z^2} orbitals will favour antiferromagnetic interactions. Statistically, these are expected to account for $^5/_9$ of the total interactions (Table 6.4). Those involving both a d_{z^2} and a $d_{x^2-y^2}$ orbital will favour ferromagnetic ordering. This accounts for the remaining $^4/_9$ of the superexchange pathways.

Orbital	No. unpaired electrons	Orbital	No. unpaired electrons	Probability	Interaction
$d_{x^2-y^2}$ - ⅔	0	$d_{x^2-y^2}$ - ⅔	0	$^4/_9$	AF
$d_{x^2-y^2}$ - ⅔	0	d_{z^2} - ⅓	1	$^4/_9$	F
d_{z^2} - ⅓	1	d_{z^2} - ⅓	1	$^1/_9$	AF

Table 6.4 Possible superexchange interactions between the e_g orbitals for a d^4 ion with octahedral coordination.

The mixed ferro and antiferromagnetic interactions will result in magnetic frustration. For a purely Mn(III) containing system is relatively easy to relieve the magnetic frustration. The oxide vacancies can be arranged such that the ½ filled d_{z^2} orbitals are never involved in 180° interactions with the empty $d_{x^2-y^2}$ orbitals. For a mixed Mn(III)/Mn(IV) system, this is no longer possible without a much more complex oxide vacancy ordering scheme. If there are a large proportion of disordered oxide vacancies, resulting in sufficient competition between the ferromagnetic and antiferromagnetic interactions, the 180° magnetic coupling will be disrupted. The proportions of ferromagnetic 180° and antiferromagnetic 180° superexchange pathways expected for a random distribution of oxide vacancies within the face-sharing layers can be

calculated. 4H-$BaMnO_{2.65(1)}$ contains fractions of 0.7 Mn(III) and 0.3 Mn(IV), each with three superexchange pathways (the reduction in possible superexchange pathways due to the removal of the bridging oxide ions is neglected). The three pathways are equivalent for Mn(IV), but for Mn(III) two superexchange pathways involve the empty $d_{x^2-y^2}$ orbital and one involves the singly occupied d_{z^2} orbital. The probabilities of connecting the different manganese e_g orbitals via each possible 180° superexchange interaction are listed in Table 6.5 for 4H-$BaMnO_{2.65(1)}$ and in Table 6.6 for 4H-$Ba_{0.5}Sr_{0.5}MnO_{2.79(1)}$.

Oxidation state and fraction	**Orbital**	**Oxidation state and fraction**	**Orbital**	**Probability**	**Interaction**
Mn(III/IV) - 1	$d_{x^2-y^2}$ - ⅔	Mn(III/IV) - 1	$d_{x^2-y^2}$ - ⅔	0.444	AF
Mn(III/IV) - 1	$d_{x^2-y^2}$ - ⅔	Mn(IV) – 0.3	$^0d_{z^2}$ - ⅓	0.067×2	AF
Mn(III/IV) - 1	$d_{x^2-y^2}$ - ⅔	Mn(III) – 0.7	$^1d_{z^2}$ - ⅓	0.156×2	F
Mn(IV) – 0.3	$^0d_{z^2}$ - ⅓	Mn(IV) – 0.3	$^0d_{z^2}$ - ⅓	0.010	AF
Mn(IV) – 0.3	$^0d_{z^2}$ - ⅓	Mn(III) – 0.7	$^1d_{z^2}$ - ⅓	0.023×2	F
Mn(III) – 0.7	$^1d_{z^2}$ - ⅓	Mn(III) – 0.7	$^1d_{z^2}$ - ⅓	0.054	AF
Total AF = 64.2%				**Total F = 35.8%**	

Table 6.5 Probability of connecting different manganese orbitals via the 180° superexchange pathway for 4H-$BaMnO_{2.65(1)}$.

Oxidation state and fraction	**Orbital**	**Oxidation state and fraction**	**Orbital**	**Probability**	**Interaction**
Mn(III/IV) - 1	$d_{x^2-y^2}$ - ⅔	Mn(III/IV) - 1	$d_{x^2-y^2}$ - ⅔	0.444	AF
Mn(III/IV) - 1	$d_{x^2-y^2}$ - ⅔	Mn(IV) – 0.58	$^0d_{z^2}$ - ⅓	0.129×2	AF
Mn(III/IV) - 1	$d_{x^2-y^2}$ - ⅔	Mn(III) – 0.42	$^1d_{z^2}$ - ⅓	0.093×2	F
Mn(IV) – 0.58	$^0d_{z^2}$ - ⅓	Mn(IV) – 0.58	$^0d_{z^2}$ - ⅓	0.037	AF
Mn(IV) – 0.58	$^0d_{z^2}$ - ⅓	Mn(III) – 0.42	$^1d_{z^2}$ - ⅓	0.027×2	F
Mn(III) – 0.42	$^1d_{z^2}$ - ⅓	Mn(III) – 0.42	$^1d_{z^2}$ - ⅓	0.020	AF
Total AF = 75.9%				**Total F = 24.1%**	

Table 6.6 Probability of connecting different manganese orbitals via the 180° superexchange pathway for 4H-$Ba_{0.5}Sr_{0.5}MnO_{2.79(1)}$.

Both 4H-$BaMnO_{2.65(1)}$ and 4H-$Ba_{0.5}Sr_{0.5}MnO_{2.79(1)}$ have relatively high proportions of ferromagnetic pathways based on the random distribution of oxide vacancies, and so the glassy magnetic state at 6K is to be expected, as is the disruption of three-dimensional antiferromagnetic ordering. The broad feature attributed to short range order in the 1.8K 4H-$Ba_{0.5}Sr_{0.5}MnO_{2.79(1)}$ neutron diffraction data suggests that the proportion of Mn(III) present in this sample lies on the cusp of disrupting the three-dimensional magnetic order. Since the 180° superexchange interaction is disrupted by the Mn(III) dimers present in 4H-$BaMnO_{2.65(1)}$ and 4H-$Ba_{0.5}Sr_{0.5}MnO_{2.79(1)}$, no event is observed in the susceptibility data in the $240 < T(K) < 270$ range. However, a further magnetic event is observed at T ~ 140K in the susceptibility data of 4H-$Ba_{0.5}Sr_{0.5}MnO_{2.79(1)}$ (Figure 6.12), which causes a slight divergence of the zero-field-cooled and field-cooled magnetisation data. The temperature is such that this could not be attributed to any known manganese containing impurity phase. Close examination of the susceptibility data collected from the other $BaMnO_{3-x}$ samples remaining phases shows that a similar event occurs in data collected from 10H-$BaMnO_{2.91(1)}$ at T ~ 150K and from 6L-$BaMnO_{2.92(1)}$ at T ~ 175K (Figure 6.13). The divergence does not occur in susceptibility data collected from the oxidised 4H-$Ba_{0.5}Sr_{0.5}MnO_{2.99(1)}$ or 10H-$BaMnO_{2.96(1)}$ samples suggesting that these events are related to the Mn(III) dimers. However oxidation of 6L-$BaMnO_{2.92(1)}$ to 6L-$BaMnO_{2.99(1)}$ has little effect on the event observed at T ~ 175K, suggesting this is of a different nature, unrelated to the presence of Mn(III) dimers.

It seems likely that the additional magnetic event observed in the 6L-$BaMnO_{2.92(1)}$ and 10H-$BaMnO_{2.91(1)}$ magnetisation data is related to the presence of Mn(III) dimers and the different exchange interactions this introduces into the system.

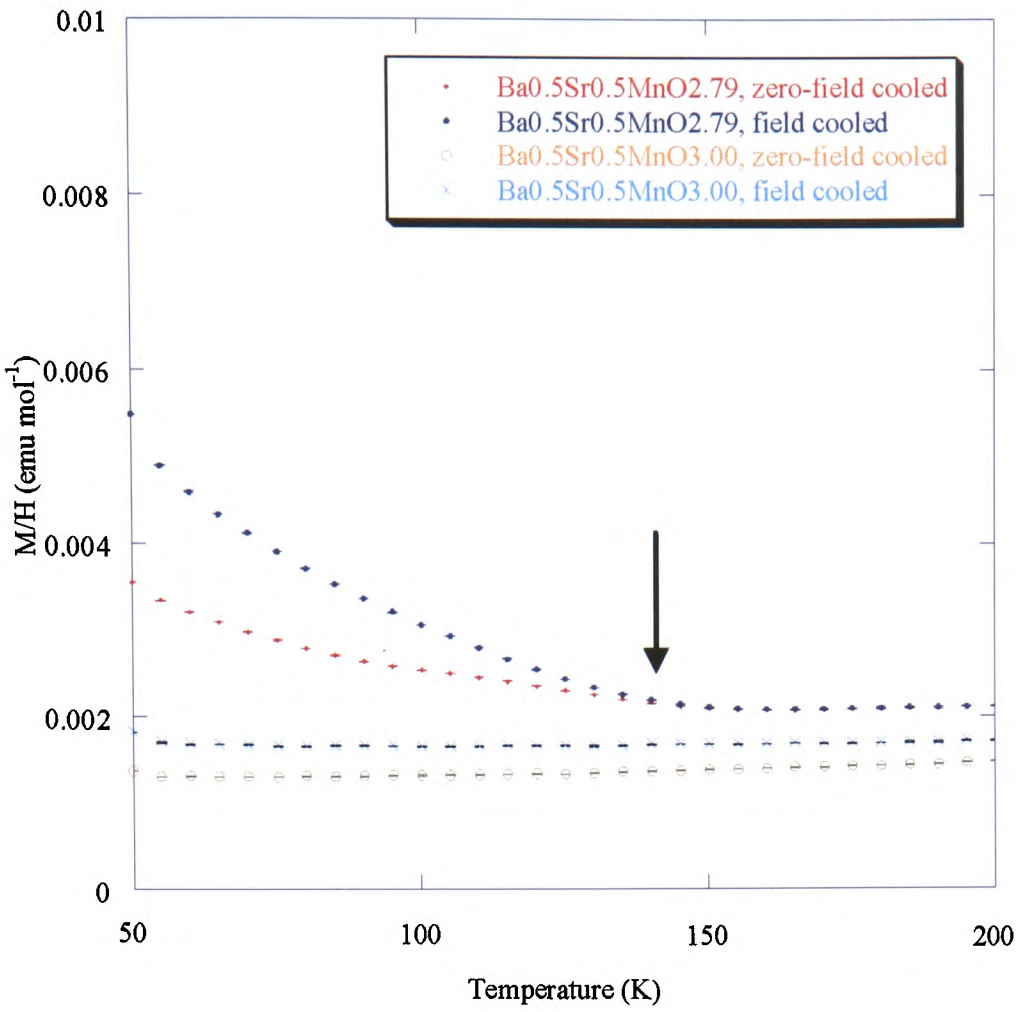


Figure 6.12 Divergence between zero-field-cooled and field-cooled magnetometry data collected from 4H-$Ba_{0.5}Sr_{0.5}MnO_{2.79(1)}$ increases when T < 140K. This does not occur for 4H-$Ba_{0.5}Sr_{0.5}MnO_{2.99(1)}$.

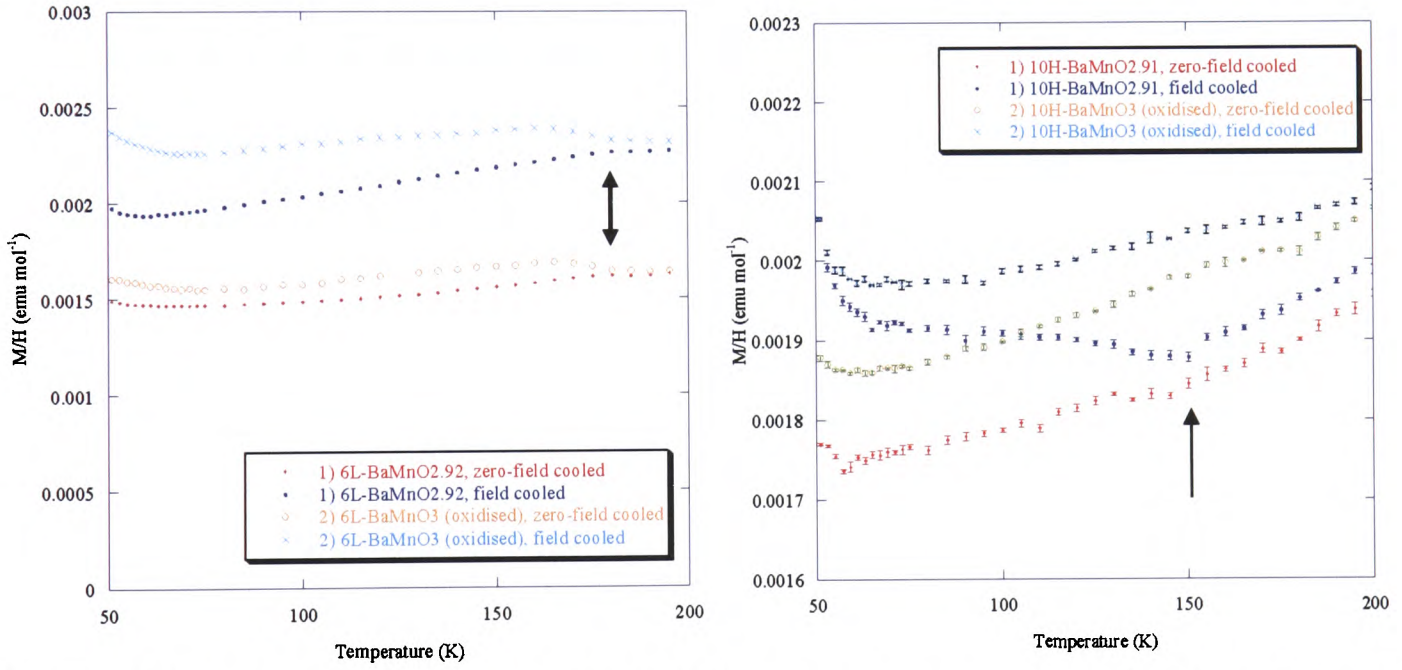


Figure 6.13 Events at T ~ 175K and T ~ 150 K observed in magnetometry data collected from 6L-$BaMnO_{2.92(1)}$ and 10H-$BaMnO_{2.91(1)}$ are affected by oxidation.

6.4. Conclusion

It is clear that both charge and structural disorder have an effect on the magnetic behaviour of the Ba(Sr)MnO_{3-x} hexagonal perovskites. Charge disorder has a profound effect with regard to the overall magnetic behaviour. A high degree of charge disorder completely disrupts the long-

range ordering of magnetic moments. The competing magnetic interactions introduced by charge disorder cannot all be satisfied so the system is frustrated.

The effect of a small degree of structural disorder is largely superficial with regard to the overall behaviour. Direct exchange is not disrupted, and strong antiferromagnetic coupling persists across the measured temperature range for all samples. Long-range magnetic order is also maintained. However, the antiferromagnetic behaviour of the majority of spins allows magnetometry data to be dominated by more subtle effects which are often greatly influenced by the degree of structural disorder.

Chapter 7: Synthesis and characterisation of $Ba(Sr)Mn_{1-z}B'_zO_{3-x}$

7.1. Introduction

7.1.1. B cation order

Introducing different cations to a system raises the possibility that these will order over different sites. Cation ordering exists in a number of structures, often caused by a large difference in either the size or the charge of the cations. The A and B cations in the perovskite structure, for example, occupy different sites on the basis of widely different sizes and charges. Different cations can also be ordered over the B site in compounds of the form $AB_{1-x}B'_xX_3$.

The ordering of different B cations within a structure often has far reaching implications for the magnetic properties. These are strongly dependent on the B cation connectivity, which is affected by B cation ordering. For example, where B and B' are disordered in a cubic perovskite based $AB_{0.5}B'_{0.5}X_3$ system there are three different 180° superexchange pathways: B-O-B, B-O-B' and B'-O-B'. However, if the B cations are arranged alternately (forming the ordered double perovskite structure) there are only B-O-B' pathways. The ordered and disordered structures are shown in Figure 7.1.

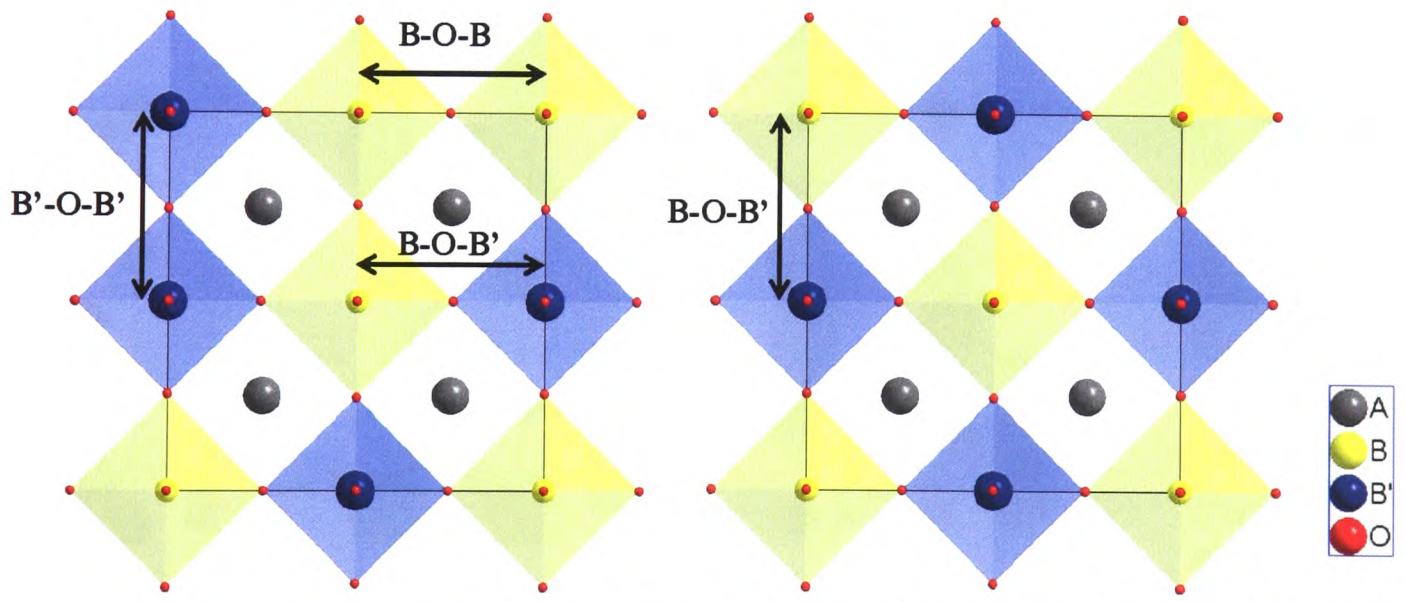


Figure 7.1 Disordered $AB_{0.5}B'_{0.5}O_3$ with B-O-B, B-O-B' and B'-O-B' linkages and the double perovskite $AB_{0.5}B'_{0.5}O_3$ with only B-O-B' linkages.

7.1.2. B cation order in the hexagonal perovskite system

There are several examples of partial B cation ordering in hexagonal perovskite systems. The ordering of B cations of different sizes can have an effect in determining the stacking sequence. As discussed in Section 1.3.3, there are three different sequences with a 1:1 ratio of cubic to hexagonal layers: 4H, 12R and 12H (shown in Figure 7.2). The simple 4H sequence is favoured in the absence of cation ordering; the 12R (3,1 or *cchh*) provides apex-sharing sites favoured by large B cations; the 12H stacking sequence provides tetrahedral sites favoured by small B cations. Thus $BaMnO_{3-x}$ adopts the 4H stacking sequence, $BaMn_{0.75}Pr_{0.25}O_3$ ($r_{Pr(IV)}$ = 0.85 Å, $r_{Mn(IV)}$ = 0.53 Å)[82] adopts the 12R sequence,[73] and $BaMn_{0.4}Co_{0.6}O_{2.83}$ ($r_{Co(IV),oct}$ = 0.53 Å)[82] adopts the 12H sequence (Mn(IV) is equally small, but gains ligand field stabilisation energy from location in an octahedral site).[83]

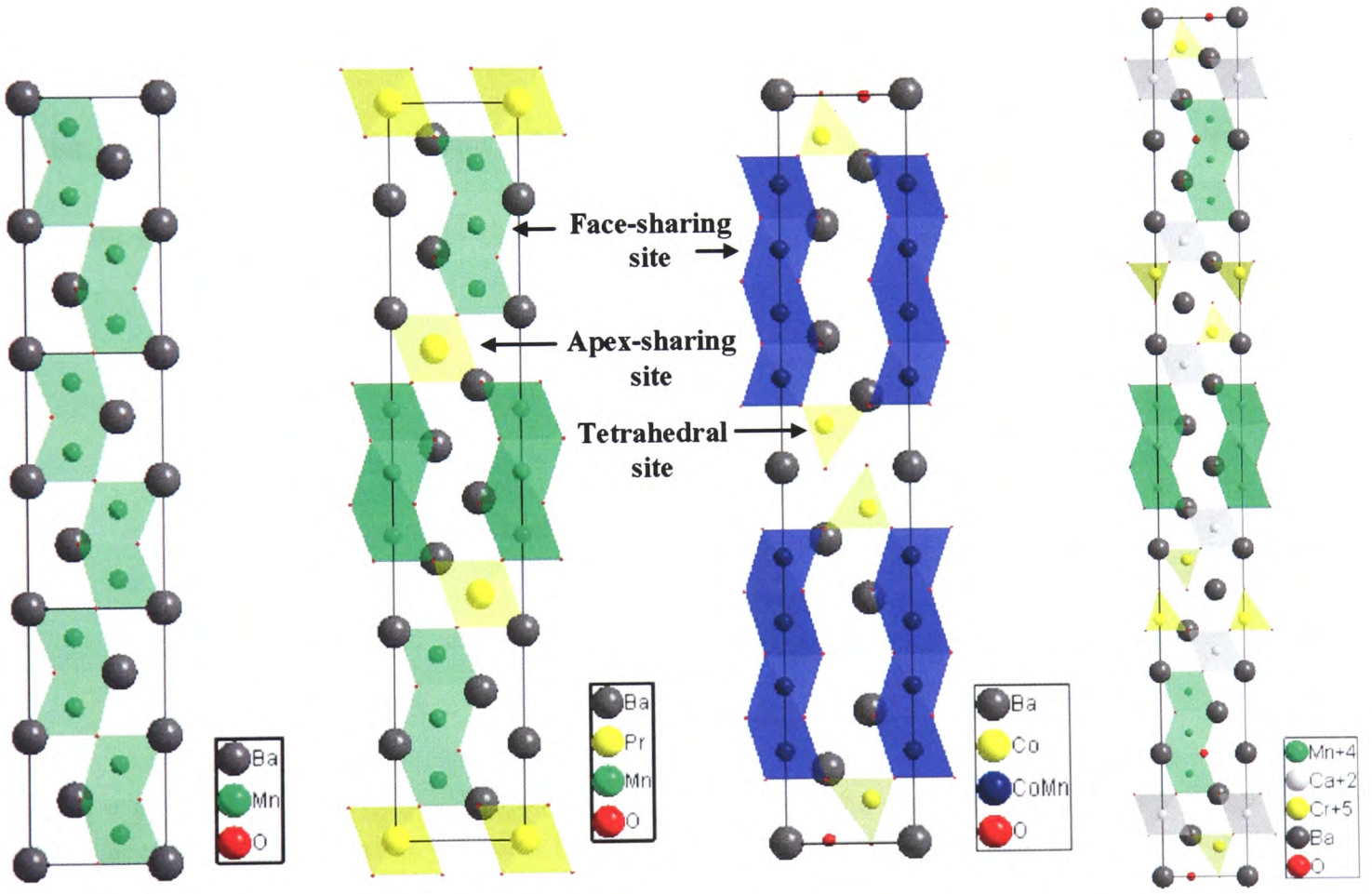


Figure 7.2 Stacking sequences involving different degrees of cation order. From left to right: 4H-$BaMnO_{3-x}$ has only one type of B cation and only one B cation site, 12R-$BaMn_{0.75}Pr_{0.25}O_3$ has two types of B cation and the larger Pr ions are located in the apex sharing sites, in 12H-$BaMn_{0.4}Co_{0.6}O_{2.83}$ the small Co(V) ions are arranged in the tetrahedral sites. 21R-$Ba_7Mn^{(IV)}_3Cr^{(V)}_2Ca^{(II)}_2O_{20}$ is shown on the right hand side; the B cations are ordered within both tetrahedral and apex sharing sites.

More complex cation ordering is observed in two compounds of the type $Ba_7Mn^{(IV)}_3B^{(V)}_2B'^{(II)}_2O_{20}$, where either B = Mn and B' = Ca, or B =Cr and B' = Mn.[79, 80]

These phases adopt a 21R (*cccccchh* or 3,1,1,1,1,1) stacking sequence (Figure 7.2). The Mn(IV) ions occupy the face sharing trimer. The smaller, highly charged B(V) ions (either Cr(V) or Mn(V)) occupy the tetrahedral sites, as in the 12H stacking sequence. The larger B(II) ions (Mn(II) or Ca(II)) are more easily accommodated in the larger apex sharing sites, as in the 12R stacking sequence. Thus different B cations are rigorously ordered on the basis of size and charge.

In the absence of a large difference in either the size or charge a statistically disordered arrangement of B cations is usually favoured due to entropic factors. However, the preferential localisation of the oxide vacancies within the face sharing hexagonal layers in the centre of Mn_2O_9 dimers (discussed in Chapter 4) suggests the potential for ordering B cations according to reducibility, even if their size and charge are similar. If the oxide vacancies are predominantly located in the dimer sites, more reducible B cations should also be located in the dimer. Less reducible B cation (B') will be located in the remaining sites, which are not adjacent to an oxide vacancy (Figure 7.3).

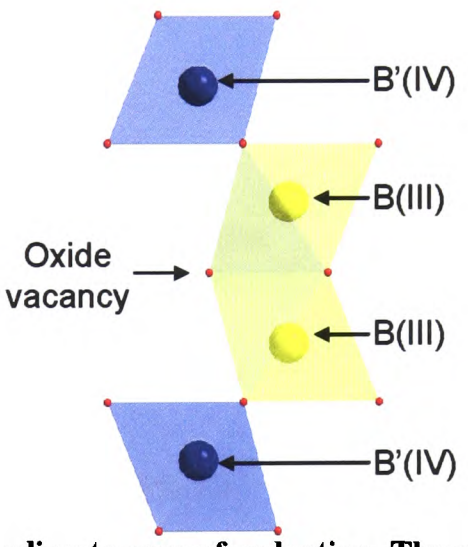


Figure 7.3 B cation ordering according to ease of reduction. The more reducible B cations are located in the face sharing dimer sites adjacent to the oxide anion vacancy. The less reducible B' cations are located in the remaining sites.

Some evidence of B cation ordering according to the location of the oxide vacancies exists in hexagonal perovskite phases. The structure of 6L-$BaMn_{0.766}Fe_{0.233}O_{2.87}$ is shown in Figure 7.4.[69] The oxide vacancies are located exclusively in the hexagonal dimer site, which is consistent with the observations in Chapter 4 and rationalises the adoption of the 6L stacking

sequence. The more reducible iron cations are also predominantly located in the dimer sites, suggesting partial ordering between the manganese and the iron cations on the basis of reducibility.

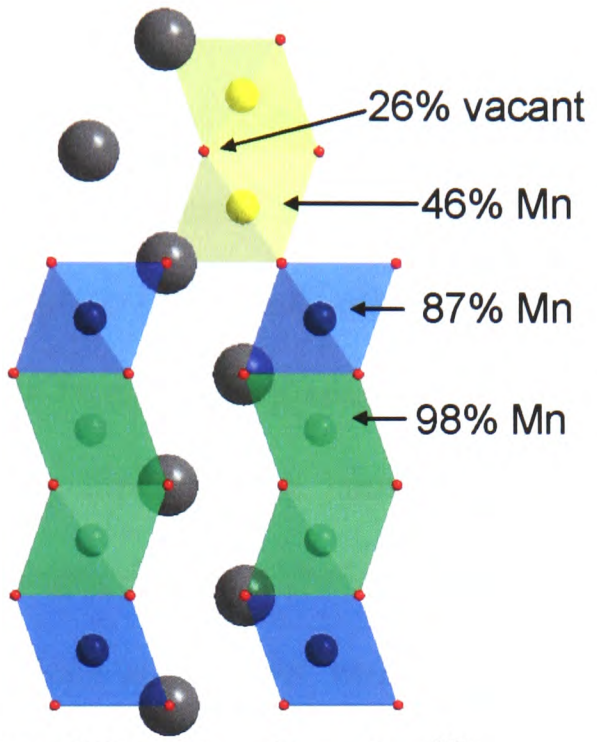


Figure 7.4 The refined structure of 6L-$BaMn_{0.766}Fe_{0.233}O_{2.87}$.[69]

Conversely, neutron diffraction studies performed on $BaTi_{0.33}Fe_{0.66}O_{2.68}$ reveal no evidence of B cation ordering. Compositions in the range $BaTi_{1-z}Fe_zO_{3-x}$ ($0.06 \leq z \leq 0.84$) adopt the 6H-$BaTiO_3$ structure (2,1 or *cch* stacking sequence), shown in Figure 7.5.[50, 55]

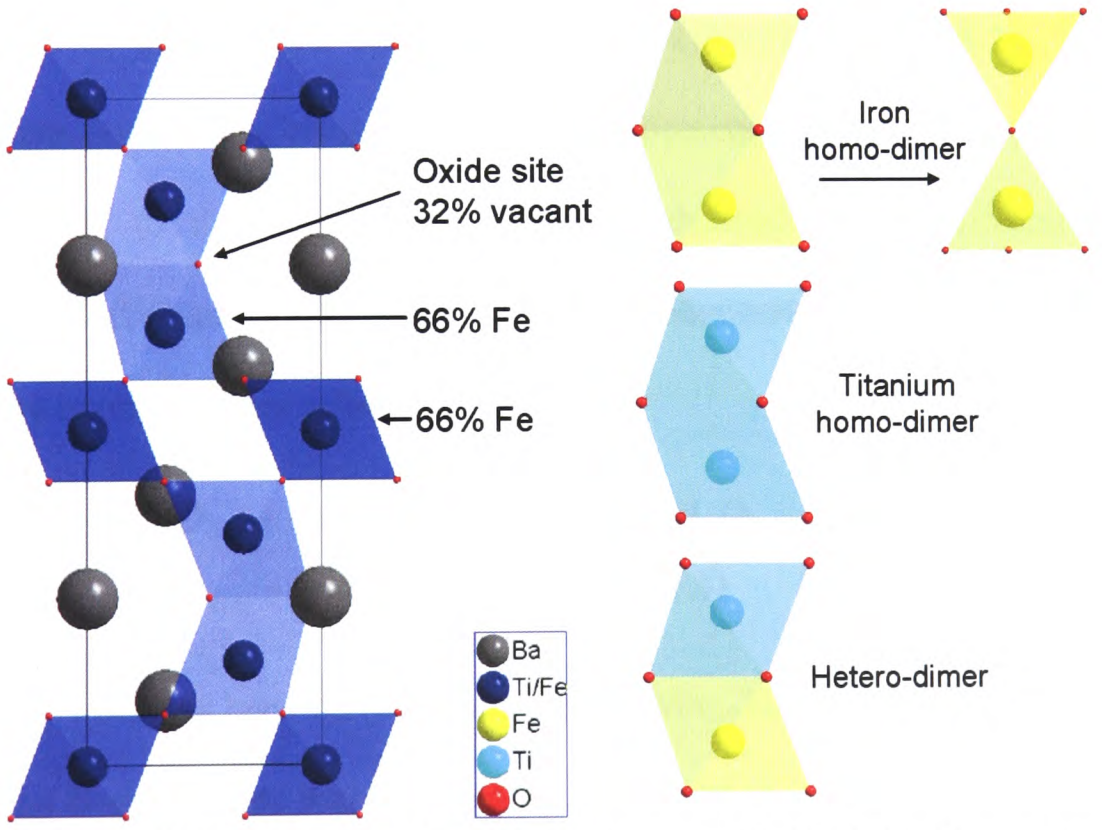


Figure 7.5 Structure of $BaTi_{0.33}Fe_{0.66}O_{2.68}$. The displacement of the Fe(III) cations suggests they are tetrahedrally coordinated. This implies local ordering within the dimers.

Although the oxide vacancies are exclusively located in the face sharing sites, a statistical distribution of iron and titanium cations is observed.[120] However, a much greater displacement from the shared face is observed for Fe than for Ti ions, consistent with tetrahedral coordination of the iron but octahedral coordination of the titanium. This suggests that the B cations are locally ordered within the dimers. Three different dimer types can be described, shown in Figure 7.5: titanium homo-dimers containing two titanium ions (Ti_2O_9); iron homo-dimers containing two iron ions (Fe_2O_9); and hetero-dimers containing an iron and a titanium ion ($TiFeO_9$). The increased displacement of Fe from the shared face suggests the vacancies are predominantly located in Fe homo-dimers. This in turn suggests that homo-dimers are favoured over hetero-dimers. If the homo-dimers are arranged randomly throughout the structure, there is no long-range order and so a statistical distribution is observed by neutron diffraction.

7.1.3. The $Ba(Sr)Mn_{1-z}Ti_zO_{3-x}$ system

The $BaMn_{1-z}Ti_zO_{3-x}$ provides a suitable system (from a chemical perspective) in which to investigate the possibilities of cation ordering according to reducibility. The ionic radius of Ti(IV) is 0.605 Å, intermediate between that of Mn(IV) (0.53 Å) and Mn(III) (0.645 Å).[82] This minimizes possible ordering due to size differences. The possibility of ordering the B cations according to the ease of reduction is enhanced by the difference between the reducibility of Mn(IV) and Ti(IV), indicated by the reduction potentials shown in Equation 7.1. The values are extracted from reference [121].

$$MnO_{2(s)} + 4H^+ + e^- \rightarrow Mn^{3+}_{(aq)} + 2H_2O \qquad E^\circ = +0.95\,V$$
$$TiO_{2(s)} + 4H^+ + e^- \rightarrow Ti^{3+}_{(aq)} + 2H_2O \qquad E^\circ = -0.666\,V$$

Equation 7.1

Some previous work has been carried out on the $BaMn_{1-z}Ti_zO_{3-\delta}$ system (where $\delta << x$). Partial ordering of the B-site cations was reported by Sinclair et al., who reported a 12R (3,1 or *cchh*) stacking sequence for $BaMn_{0.5}Ti_{0.5}O_{3.00}$.[71] The structure is shown in Figure 7.6. On the basis

of bond lengths and bond valence sum calculations, the apex-sharing octahedral sites are believed to be exclusively occupied by Ti(IV) ions, the face-sharing sites occupied by the smaller Mn(IV) ions, and a random distribution of Mn(IV) and Ti(IV) occupies the remaining sites (which contain both face and apex-sharing linkages). Thus it seems that partial B cation ordering (presumably on the basis of size) does exist in this structure. This provides a rationalisation for the adoption of the 12R stacking sequence, in preference to the simpler 4H stacking sequence.

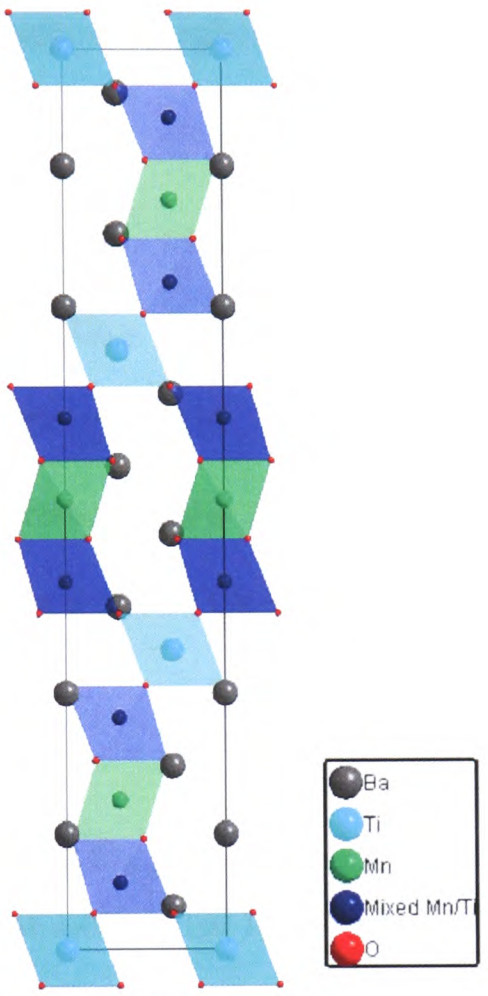


Figure 7.6 Refined structure of 12R-$BaMn_{0.5}Ti_{0.5}O_{3\ \delta}$.[71]

7.2. *Experimental*

Phases of the form $Ba_{1-y}Sr_yMn_{1-z}Ti_zO_{3-x}$ were synthesised for z = 0.50, 0.45, 0.4 and 0.33. Stoichiometric quantities of $BaCO_3$, $SrCO_3$, MnO_2 and TiO_2 were ground in an agate pestle and mortar prior to firing at 950°C (to decompose the carbonates). Samples were then reground and pressed to 2-3g pellets before firing either in air or a flow furnace under flowing argon. Samples of $BaMn_{1-z}Zr_zO_{3-x}$ were produced for z = 0.1, 0.2 and 0.25 using the same technique but substituting ZrO_2 for TiO_2. X-ray powder diffraction data suitable for refinement were

collected using the Siemens or X'pert diffractometers. Neutron powder diffraction data were collected using the Polaris diffractometer at ISIS, UK (Section 2.3.2.2.2).

Topotactic oxidation of the phases containing oxide anion vacancies was achieved by firing under flowing oxygen. Samples were heated at 10°C min^{-1} to 800°C, and held for 90 minutes. The oxidation was carried out on a thermogravimetric balance in order to monitor the mass gain. Reductive thermogravimetric analysis was also performed. Approximately 90mg samples were heated to 700°C under a flow gas of 5% H_2 in N_2. This temperature was held for up to 90 minutes in order to ensure reaction completion. All thermogravimetric measurements were corrected for the effects of buoyancy.

Magnetic susceptibility data were collected from $BaMn_{0.66}Ti_{0.33}O_{3-x}$, two forms of $BaMn_{0.5}Ti_{0.5}O_{3-x}$ and $BaMn_{0.8}Zr_{0.2}O_{3-x}$. Each of these phases was topotactically oxidised and further susceptibility data were collected. Zero-field-cooled and field-cooled data were collected as a function of temperature under a measuring field of 100 Oe. Magnetisation-field isotherms were collected between ± 50000 Oe at 6K and 300K.

7.3. *Results*

7.3.1. Synthesis

7.3.1.1. $BaMn_{1-z}Zr_zO_{3-x}$

Firing $BaMn_{0.8}Zr_{0.2}O_{3-x}$ in air at 1200°C for up to 10 days produced only a mixture of binary and ternary oxide phases, but a new $BaMn_{1-z}Zr_zO_{3-x}$ phase could be prepared on firing samples where z = 0.1, 0.2 and 0.25 under flowing argon at 1435°C for 200 hours. Sets of additional reflections were observed in the X-ray diffraction data collected from $BaMn_{0.75}Zr_{0.25}O_{3-x}$ and $BaMn_{0.9}Zr_{0.1}O_{3-x}$. These could be accounted for by minority phases of $BaZrO_3$ or 4H-$BaMnO_{3-x}$ respectively. The relative phase fractions of the minority phases (detailed in Table 7.1) suggest that the $BaMn_{1-z}Zr_zO_{3-x}$ phase occupies a narrow compositional range where $z \sim 0.15$. The majority of the reflections observed using X-ray powder diffraction could be

indexed using a hexagonal cell with lattice parameters of a = 5.739 Å and c = 14.077 Å, typical of a 6 layered stacking sequence. Refinement of a model based on that of 6H-$BaTiO_3$ provided a good fit to the data. X-ray and neutron powder diffraction data suitable for refinement were collected from the single phase 6H-$BaMn_{0.8}Zr_{0.2}O_{3-x}$ sample.

Sample	6H	a (Å)	c (Å)	4H-$BaMnO_{3-x}$	Cubic $BaZrO_3$
$BaMn_{0.9}Zr_{0.1}O_{3-x}$	0.69(3)	5.733(1)	14.068(4)	0.32(3)	0
$BaMn_{0.8}Zr_{0.2}O_{3-x}$	1	5.7341(1)	14.0643(4)	0	0
$BaMn_{0.75}Zr_{0.25}O_{3-x}$	0.86(1)	5.737(1)	14.075(3)	0	0.12(1)

Table 7.1 Fractions of minority phases 4H-$BaMnO_{3-x}$ and $BaZrO_3$ on firing $BaMn_{1-z}Zr_zO_{3-x}$ at 1435°C under flowing argon. The fractions are expressed as a proportion of the total barium content.

7.3.1.2. $Ba_{1-y}Sr_yMn_{1-z}Ti_zO_{3-x}$

The phase diagram of $BaMn_{1-z}Ti_zO_{3-x}$ is shown in Figure 7.7 as a function of z and the firing temperature. X-ray powder diffraction data were collected from each sample and indexed to obtain the size of the unit cell. Suitable models were then refined against the data to determine the stacking sequence. The observed stacking sequences are shown in Figure 7.8.

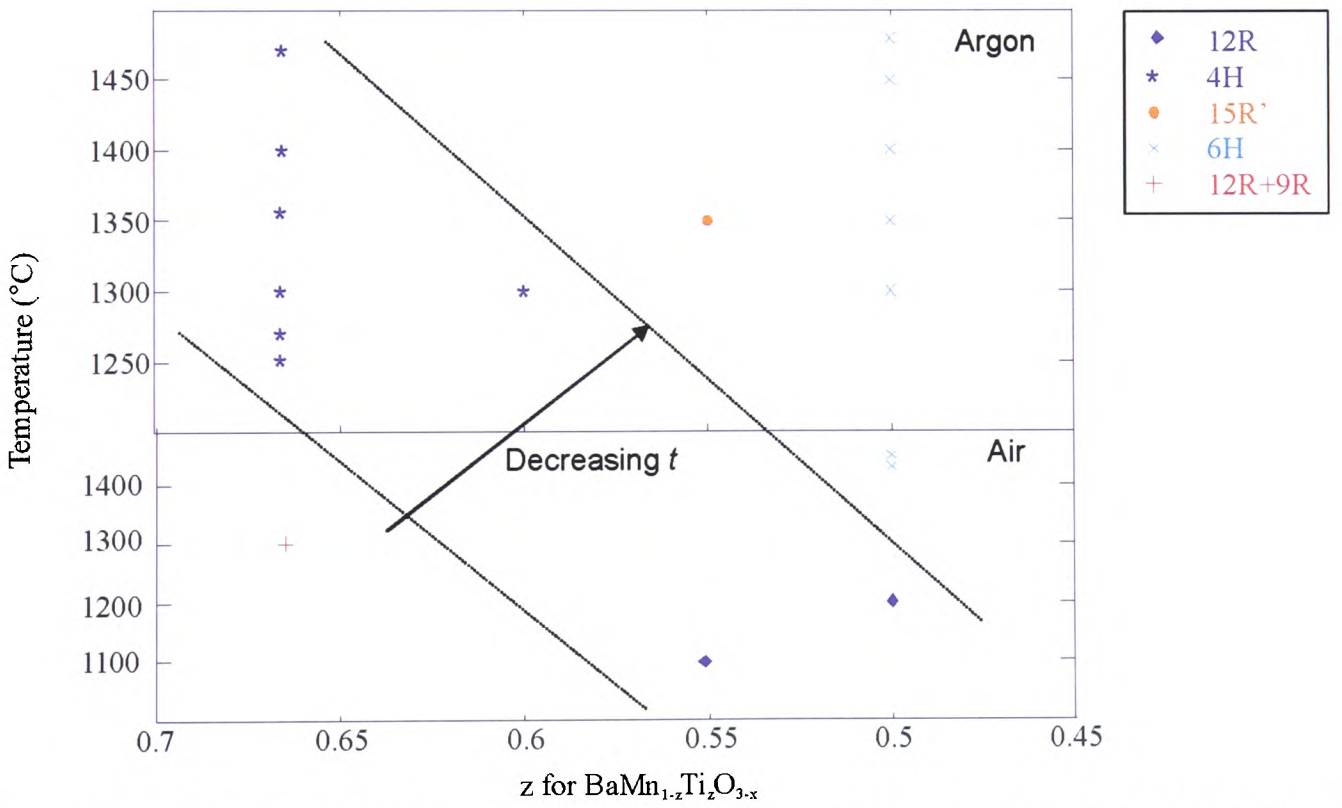


Figure 7.7 Phase diagram for $BaMn_{1-z}Ti_zO_{3-x}$ as a function of T and z. The lower portion shows the stacking sequences adopted on firing in air, the upper portion shows the stacking sequences adopted on firing under flowing argon. The lines separate the region of the phase diagram where stacking sequences containing 50% cubic layers are adopted.

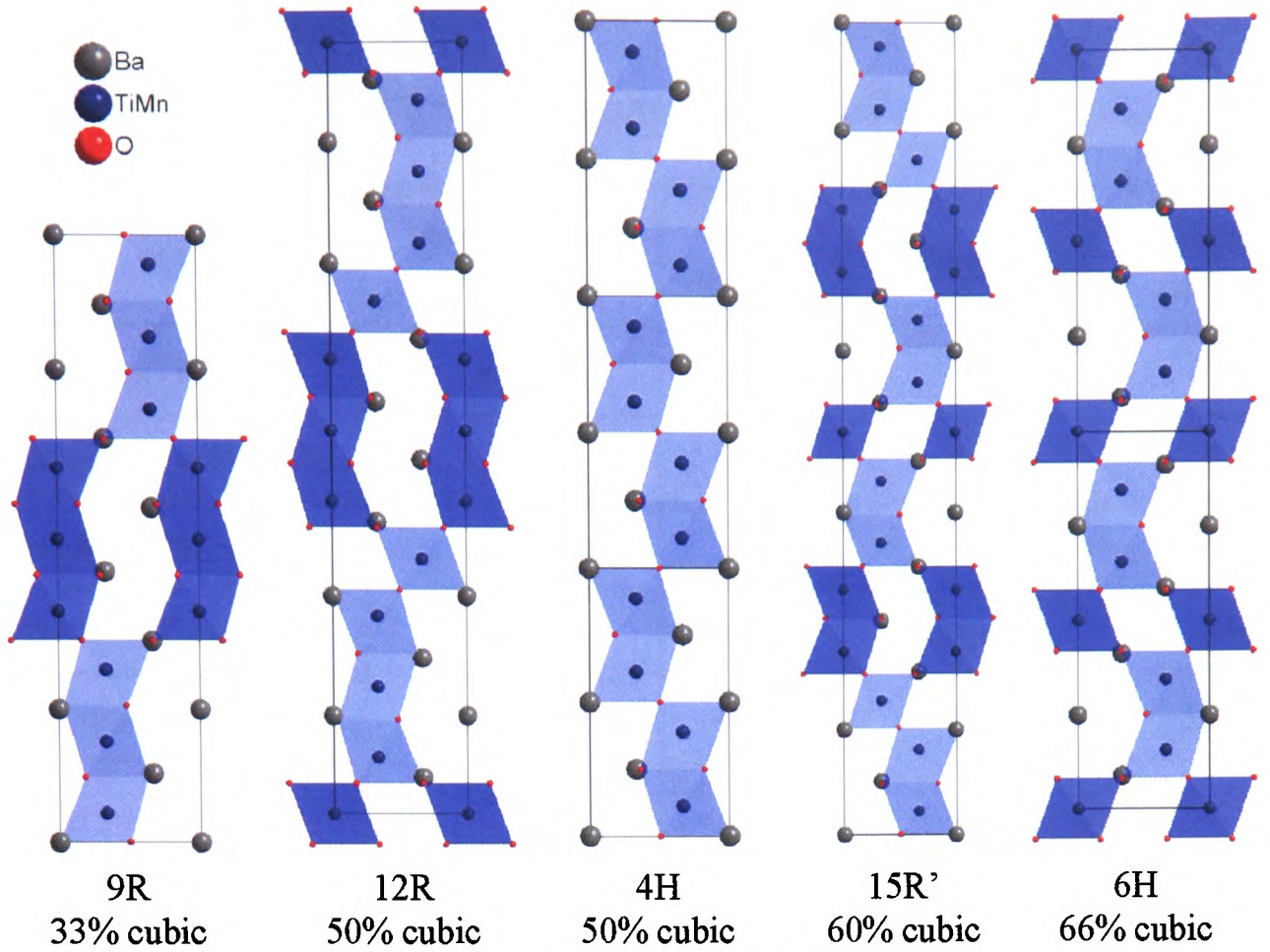


Figure 7.8 Stacking sequences observed in the $Ba_{1-y}Sr_yMn_{1-z}Ti_zO_{3-x}$ series.

The 12R-$BaMn_{0.5}Ti_{0.5}O_3$ phase formed in air at 1250°C was discussed in Section 7.1.3.[71] Increasing the temperature or firing under argon leads to reduction, which increases the average B-O bond length. This reduces the tolerance factor, favouring an increased proportion of cubic layers. Similarly, reducing the proportion of the smaller Mn(IV) ion (increasing *z*) or substitution of Sr for Ba (increasing *y*) favours an increased proportion of cubic layers (although on substituting more than 20% Sr into the sample $SrTiO_3$ is formed). The 15R' stacking sequence (2,2,1 or *chcch*) has not been previously observed in the $Ba_{1-y}Sr_yMn_{1-z}Ti_zO_{3-x}$ series. This sequence is intermediate between that of 4H (2 or *ch*) adopted by $BaMnO_{3-x}$ and 6H (2,1 or *cch*), adopted by $BaTiO_3$.

X-ray powder diffraction data suitable for structural refinement were collected from samples of 12R-$Ba_{0.8}Sr_{0.2}Mn_{0.66}Ti_{0.33}O_{3-x}$, 4H-$BaMn_{0.66}Ti_{0.33}O_{3-x}$, 15R'-$BaMn_{0.55}Ti_{0.45}O_{3-x}$, and from two 6H-$BaMn_{0.5}Ti_{0.5}O_{3-x}$ samples, prepared as detailed in Table 7.2. 6H-$BaMn_{0.5}Ti_{0.5}O_{3-x}$ was prepared with a *h*igh proportion of oxide *v*acancies (HV 6H) by firing under flowing argon at 1300°C , and a second 6H sample was prepared with a *l*ow proportion of oxide *v*acancies (LV

6H) on firing at 1400 < T(°C) < 1450 in air. Neutron powder diffraction data were collected from 4H-$BaMn_{0.66}Ti_{0.33}O_{3-x}$, HV 6H-$BaMn_{0.5}Ti_{0.5}O_{3-x}$ and LV 6H-$BaMn_{0.5}Ti_{0.5}O_{3-x}$.

	Temperature (°C)	Time (hours)	Atmosphere	Stacking sequence
$BaMn_{0.66}Ti_{0.33}O_{3-\delta}$	1300	96	Air	12R/9R
$Ba_{0.8}Sr_{0.2}Mn_{0.66}Ti_{0.33}O_{3-\delta}$	1250	384	Air	12R
$BaMn_{0.66}Ti_{0.33}O_{3-x}$	1300	96	Argon	4H
$BaMn_{0.55}Ti_{0.45}O_{3-x}$	1350	420	Argon	15R'
$BaMn_{0.5}Ti_{0.5}O_{3-\delta}$	1250	42-48	Air	12R [71]
$BaMn_{0.5}Ti_{0.5}O_{3-x}$	1400 1425 1430 1435 1440 1445 1450	24 144 768 504 336 264 72	Air	6H (LV)
$BaMn_{0.5}Ti_{0.5}O_{3-x}$	1250 1300	268 140	Argon	6H (HV)

Table 7.2 Synthesis conditions for samples prepared for structural refinement. The conditions reported for the formation of 12R-$BaMn_{0.5}Ti_{0.5}O_{3-x}$ are included for comparison.

7.3.2. Structural refinement

7.3.2.1. $BaMn_{1-z}Zr_zO_{3-x}$

A model based on that of 6H-$BaTiO_3$ was refined against neutron powder diffraction data collected from $BaMn_{0.8}Zr_{0.2}O_{3-x}$. This produced a good fit, but several weak reflections were observed that were not accounted for. These were attributed to small proportions of MnO (refined mole fraction = 1.5(1)%) and $BaZrO_3$ (refined mole fraction = 3.5(1)%). All atomic positions and anisotropic displacement ellipsoids of the 6H-$BaMn_{0.8}Zr_{0.2}O_{3-x}$ model were refined, along with the oxide fractional occupancies. The fractional occupancy of zirconium and manganese was allowed to refine across the two B cation sites, constrained such that each site remained fully occupied. The face-sharing site was found to be fully occupied by

manganese, with the zirconium located exclusively in the larger, apex-sharing site. Refinement of the manganese to zirconium ratio in this site resulted in an overall ratio of 0.7967(7) Mn to 0.2033(7) Zr, in good agreement to the synthetic composition ($BaMn_{0.8}Zr_{0.2}O_{3-x}$). The refined model is listed in Table 7.3, and selected bond lengths and angles in Table 7.4. Calculated, observed and difference plots are shown in Figure 7.9, and the structure is shown in Figure 7.10. The anisotropic displacement parameters are listed in Appendix C.

Atom	x	y	z	Fractional Occupancy	U_{equiv} (Å^2)
Ba1	0	0	¼	1	0.0084
Ba2	⅓	⅔	0.09048(8)	1	0.0096
Mn1	0	0	0	0.390(2)	0.0023
Zr1	0	0	0	0.610(2)	0.0023
Mn2	⅓	⅔	0.84299(7)	1	0.0064
O1	0.52202(8)	0.0440(2)	¼	0.821(4)	0.0145
O2	0.83097(5)	0.6619(1)	0.08356(3)	0.993(4)	0.0145
Space group : P 6_3/mmc, a = 5.73782(5)Å, c = 14.0773(2)Å					
χ^2 = 2.293, wRp = 2.73%, Rp = 4.61%					
Refined stoichiometry: $BaMn_{0.8}Zr_{0.2}O_{2.81(1)}$					

Table 7.3 Structural parameters refined against neutron powder diffraction data collected from 6H-$BaMn_{0.8}Zr_{0.2}O_{2.81(1)}$.

Bond	Bond Length(Å)/angle(°)
Ba1 – O1	2.87724(7)
Ba1 – O2	2.8830(5)
Ba2 – O1	2.926(1)
Ba2 – O2 (3x)	2.9443(9)
Ba2 – O2 (6x)	2.87067(5)
Mn1/Zr – O2	2.0507(5)
Mn2 – O1	1.9443(8)
Mn2 – O2	1.9329(8)
Mn2 – Mn2	2.618(2)
Mn2 – O2 – Mn2	79.63(4)

Table 7.4 Selected bond lengths and angles extracted from the structure of 6H-$BaMn_{0.8}Zr_{0.2}O_{2.81(1)}$.

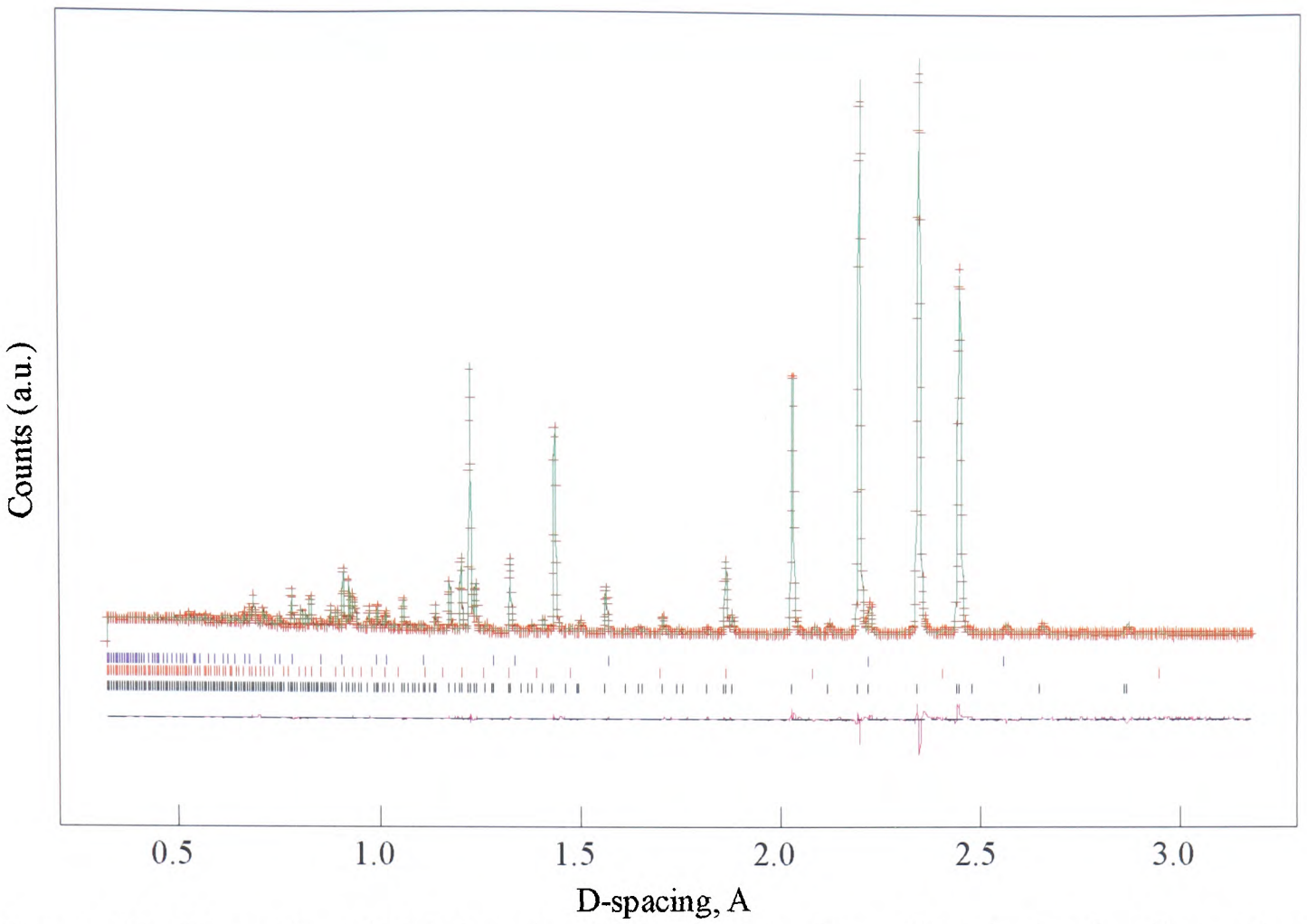


Figure 7.9 Observed, calculated and difference plots from the structural refinement of 6H-$BaMn_{0.8}Zr_{0.2}O_{2.81(1)}$ against neutron powder diffraction data collected at 298K. The upper tick marks mark reflections attributed to MnO (mole fraction of 0.015(1)), centre tick marks those attributed to $BaZrO_3$ (mole fraction of 0.035(1)) and lower tick marks 6H-$BaMn_{0.8}Zr_{0.2}O_{2.81(1)}$.

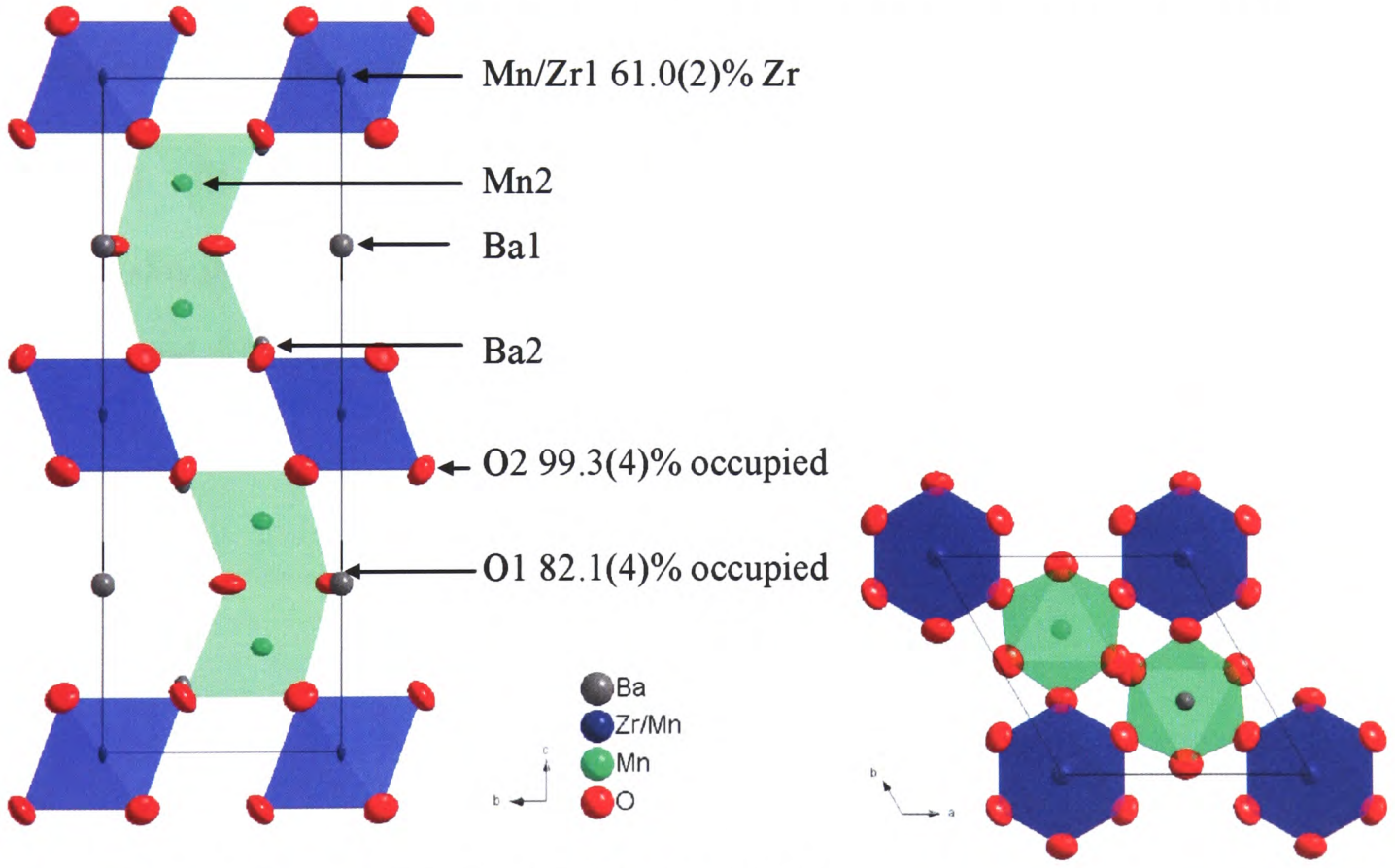


Figure 7.10 Refined structural model of 6H-$BaMn_{0.8}Zr_{0.2}O_{2.81(1)}$.

7.3.2.2. $BaMn_{1-z}Ti_zO_{3-x}$

Structural models based on those detailed in Table 7.5 were refined against the neutron and high quality X-ray diffraction data collected from the $Ba(Sr)Mn_{1-z}Ti_zO_{3-x}$ samples.

Sample	Model based on:
12R-$Ba_{0.8}Sr_{0.2}Mn_{0.66}Ti_{0.33}O_{3-\delta}$	12R-$BaMn_{0.5}Ti_{0.5}O_3$ [71]
15R'-$BaMn_{0.55}Ti_{0.45}O_{3-x}$	15R'-$SrMn_{1-x}Fe_xO_{3-\delta}$ ($x \sim 0.1$) [49]
6H-$BaMn_{0.5}Ti_{0.5}O_{3-x}$ (HV, HV-O, LV, LV-O)	6H-$BaTiO_{3-\delta}$ [50]
4H-$BaMn_{0.66}Ti_{0.33}O_{3-x}$, 4H-$BaMn_{0.66}Ti_{0.33}O_{3.00}$	4H-$BaMnO_{2.65(1)}$ [122]

Table 7.5 Basis of models refined against X-ray diffraction data.

7.3.2.2.1. 12R-$Ba_{0.8}Sr_{0.2}Mn_{0.66}Ti_{0.33}O_{3-\delta}$ and 15R'-$BaMn_{0.55}Ti_{0.45}O_{3-x}$

Due to small sample sizes only X-ray powder diffraction data were collected from 12R-$Ba_{0.8}Sr_{0.2}Mn_{0.66}Ti_{0.33}O_{3-\delta}$ and 15R'-$BaMn_{0.55}Ti_{0.45}O_{3-x}$. All atomic positions and isotropic displacement factors were refined, although oxide atomic positions were damped and refined only on the final cycles of the refinement to minimise the risk of divergence. The oxide occupancy numbers were not refined, and the displacement factors of oxide ions were constrained to take the same value (within each refinement).

A good fit was achieved to the X-ray diffraction data collected from 12R-$Ba_{0.8}Sr_{0.2}Mn_{0.66}Ti_{0.33}O_{3-\delta}$. The structural model is detailed in Table 7.6 and calculated, observed and difference plots are shown in Figure 7.11.

Atom	x	y	z	Fractional occupancy	U_{iso} ($Å^2$)
Ba/Sr1	0	0	0.2872(1)	0.75/0.25(2)	0.017(1)
Ba/Sr2	0	0	0.1277(1)	0.85/0.15(2)	0.015(1)
Mn/Ti1	0	0	½	0.66/0.33	0.014(2)
Mn/Ti2	0	0	0.4089(3)	0.66/0.33	0.028(3)
Mn/Ti2	0	0	0	0.66/0.33	0.003(2)
O1	0.149(1)	0.851(1)	0.4569(5)	1	0.005(2)
O2	0.164(2)	0.836(2)	0.6287(6)	1	
Space group : R $\bar{3}$ m, a = 5.6323(1)Å, c = 27.7267(9)Å χ^2 = 1.201, wRp = 8.14%, Rp = 6.41%					

Table 7.6 Refined structural model of 12R-$Ba_{0.8}Sr_{0.2}Mn_{0.66}Ti_{0.33}O_{3-\delta}$.

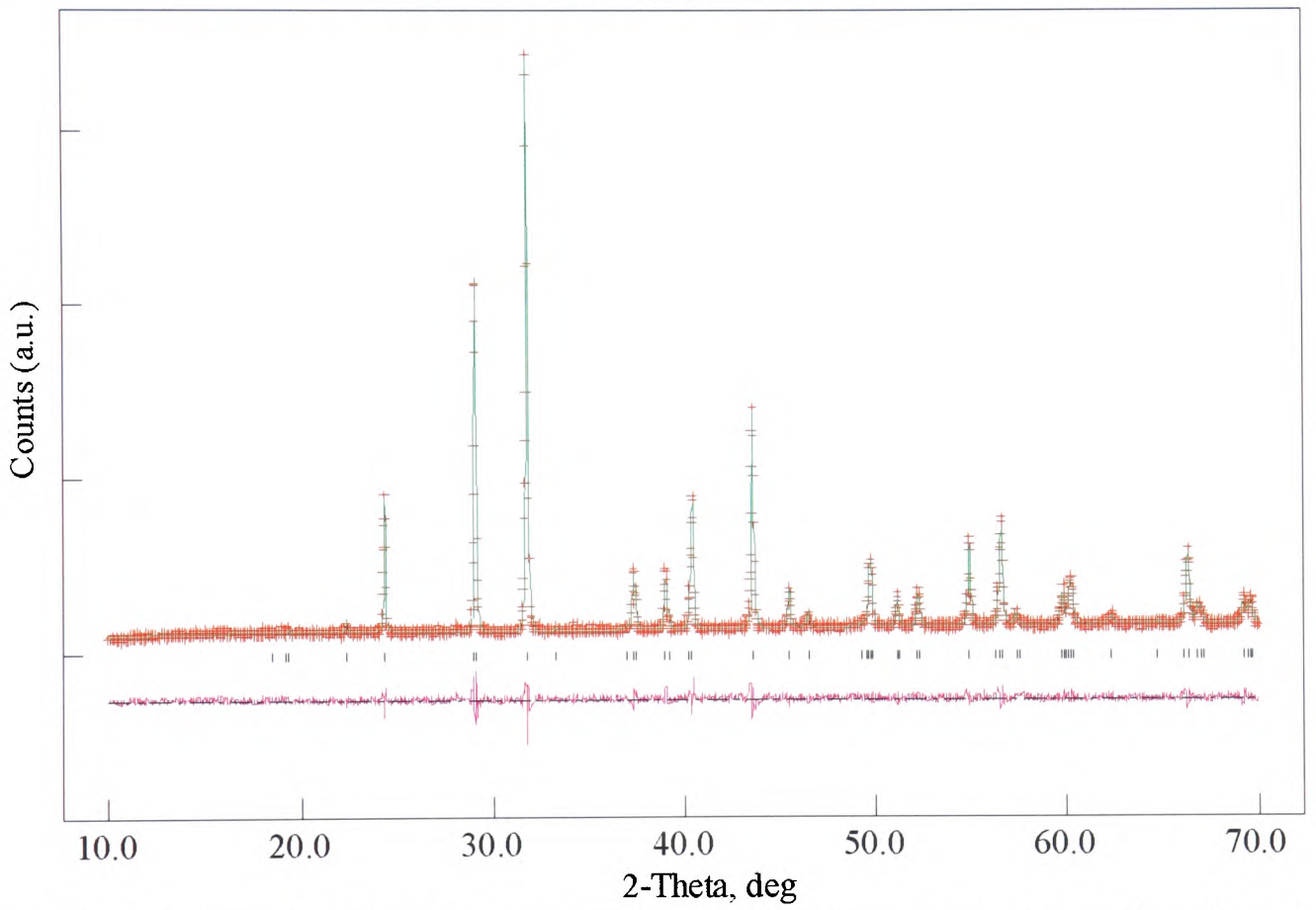


Figure 7.11 Observed, calculated and difference plots from the structural refinement of 12R-$Ba_{0.8}Sr_{0.2}Mn_{0.66}Ti_{0.33}O_{3-\delta}$ against X-ray powder diffraction data.

Close examination of X-ray powder diffraction data collected from 15R'-$BaMn_{0.55}Ti_{0.45}O_{3-x}$ revealed weak reflections attributable to a phase with the 6H stacking sequence. 6H-$BaMn_{0.55}Ti_{0.45}O_{3-x}$ was added to the refinement as a second phase, which slightly improved the fit. The weight fraction of 6H-$BaMn_{0.55}Ti_{0.45}O_{3-x}$ refined to 0.092(5). Calculated, observed

and difference plots of the refinement against 15R'-$BaMn_{0.55}Ti_{0.45}O_{3-x}$ data are shown in Figure 7.12, and the model is listed in Table 7.7.

Atom	X	y	z	U_{iso} ($Å^2$)
Ba1	0	0	0	0.005(4)
Ba2	0	0	0.1313(2)	0.001(4)
Ba3	⅓	⅔	0.2663(2)	0.007(3)
Mn/Ti1	0	0	½	0.028(1)
Mn/Ti2	⅓	⅔	0.3625(7)	0.034(7)
Mn/Ti3	⅓	⅔	0.4391(6)	0.041(6)
O1	½	0	0	0.025(4)
O2	0.836(2)	0.173(2)	0.0658(5)	
O3	0.490(3)	-0.490(3)	0.1352(6)	
Space group : $R\bar{3}$ m, a = 5.7045(2)Å, c = 35.165(1)Å				
χ^2=2.251, wRp = 6.61%, Rp = 4.94%				

Table 7.7 Structural model of 15R'-$BaMn_{0.55}Ti_{0.45}O_{3-x}$ obtained on refinement against X-ray powder diffraction data.

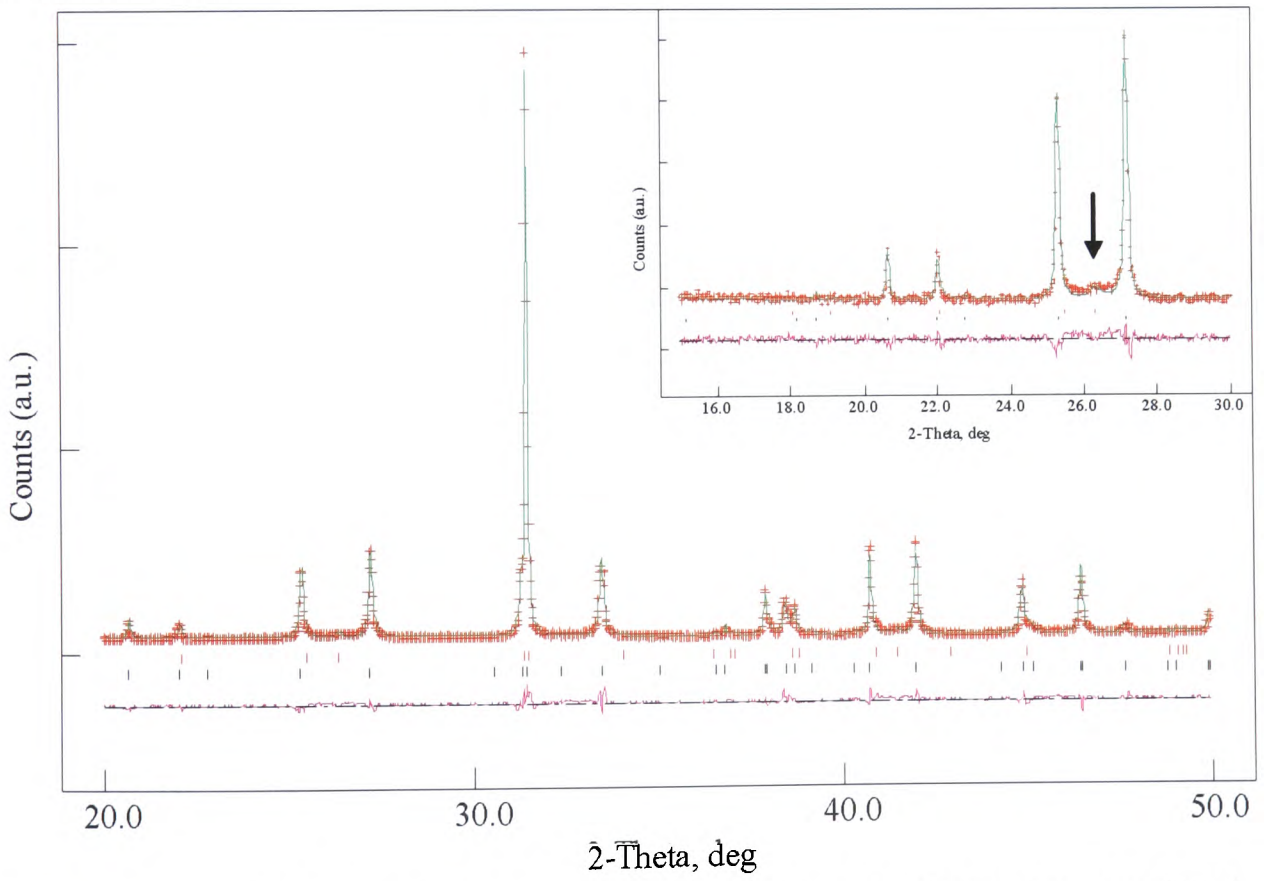


Figure 7.12 Observed, calculated and difference plots from the structural refinement of 15R-$BaMn_{0.55}Ti_{0.45}O_{3-x}$ against X-ray powder diffraction data. Lower tick marks represent reflection positions for 15R-$BaMn_{0.55}Ti_{0.45}O_{3-x}$; upper tick marks 6H-$BaMn_{0.55}Ti_{0.45}O_{3-x}$. The inset highlights the small proportion of 6H-$BaMn_{0.55}Ti_{0.45}O_{3-x}$.

7.3.2.2.2. 6H-$BaMn_{0.5}Ti_{0.5}O_{3-x}$

Neutron powder diffraction data were collected from HV and LV 6H-$BaMn_{0.5}Ti_{0.5}O_{3-x}$. A dual refinement against both X-ray and neutron diffraction data was not carried out due to slight differences in the measuring temperatures. Refinement of a model based on 6H-$BaTiO_3$ produced a good fit to the neutron diffraction data collected from both samples. No additional reflections were observed in the LV data, but weak reflections corresponding to a small proportion of a phase with the 15R' stacking sequence (refined weight fraction = 0.032(5)) were observed in the neutron powder diffraction data collected from HV 6H-$BaMn_{0.5}Ti_{0.5}O_{3-x}$, along with a small proportion of MnO (refined mole fraction = 0.035(8)). All atomic positions and anisotropic displacement ellipsoids were refined, as was the fractional occupancy of the oxide sites. The B cation distribution was not refined due to the similarity in neutron scattering lengths of manganese and titanium. The refined models are listed in Table 7.8, and selected bond lengths and angles are listed in Table 7.9. Observed, calculated and difference plots from the structural refinement are shown in Figure 7.14 and Figure 7.15, and the refined models are shown in Figure 7.13. The anisotropic displacement factors are listed in Appendix C.

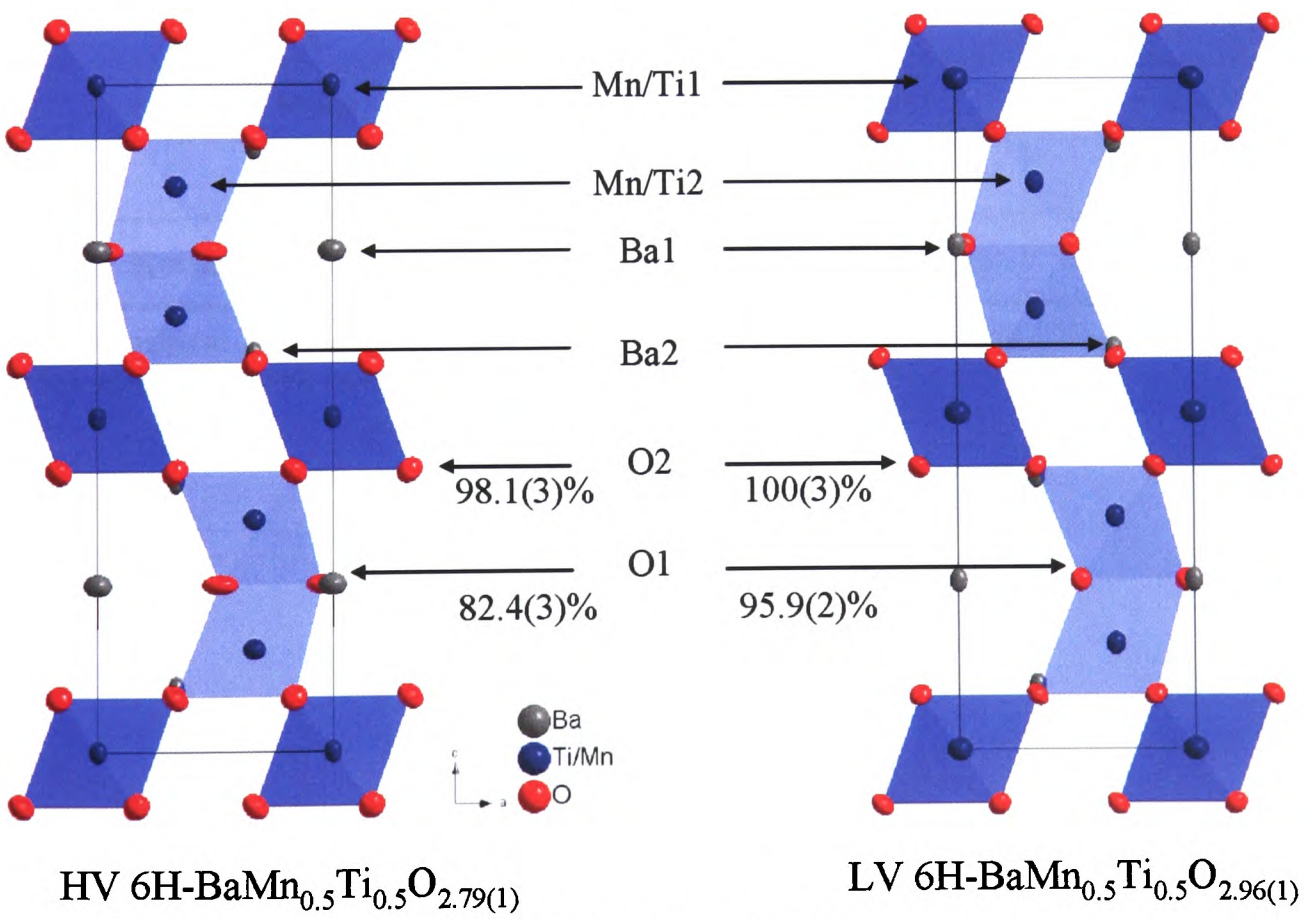


Figure 7.13 Refined structures of HV and LV 6H-$BaMn_{0.5}Ti_{0.5}O_{3-x}$.

Atom	Position	Variable	HV	LV
Ba1	2a (0,0,¼)	U_{equiv} (Å^2)	0.0102	0.0058
Ba2	4f (⅓,⅔,z)	z	0.09108(9)	0.09417(5)
		U_{equiv} (Å^2)	0.0074	0.0056
Mn/Ti1	2a (0,0,0)	U_{equiv} (Å^2)	0.0058	0.0091
Mn2	4f (⅓,⅔,z)	z	0.84679(9)	0.84480(7)
		U_{equiv} (Å^2)	0.0070	0.0060
O1	6h (x,2x,¼)	x	0.5214(1)	0.51899(5)
		Fractional Occupancy	0.824(3)	0.959(2)
		U_{equiv} (Å^2)	0.0140	0.0068
O2	12k (x,2x,z)	x	0.83501(8)	0.83399(4)
		z	0.08113(3)	0.08084(2)
		Fractional Occupancy	0.981(3)	1.004(2)
		U_{equiv} (Å^2)	0.0099	0.0069
***a* (Å)**			5.70005(5)	5.68410(4)
***c* (Å)**			13.9781(2)	13.8931(1)
χ^2			2.020	1.719
wRp			2.88%	2.45%
Rp			5.59%	4.78%
Refined stoichiometry			$BaMn_{0.5}Ti_{0.5}O_{2.79(1)}$	$BaMn_{0.5}Ti_{0.5}O_{2.959(2)}$

Table 7.8 Structural model of HV 6H-$BaMn_{0.5}Ti_{0.5}O_{3-x}$ and LV 6H-$BaMn_{0.5}Ti_{0.5}O_{3-x}$ obtained from refinement against neutron powder diffraction data.

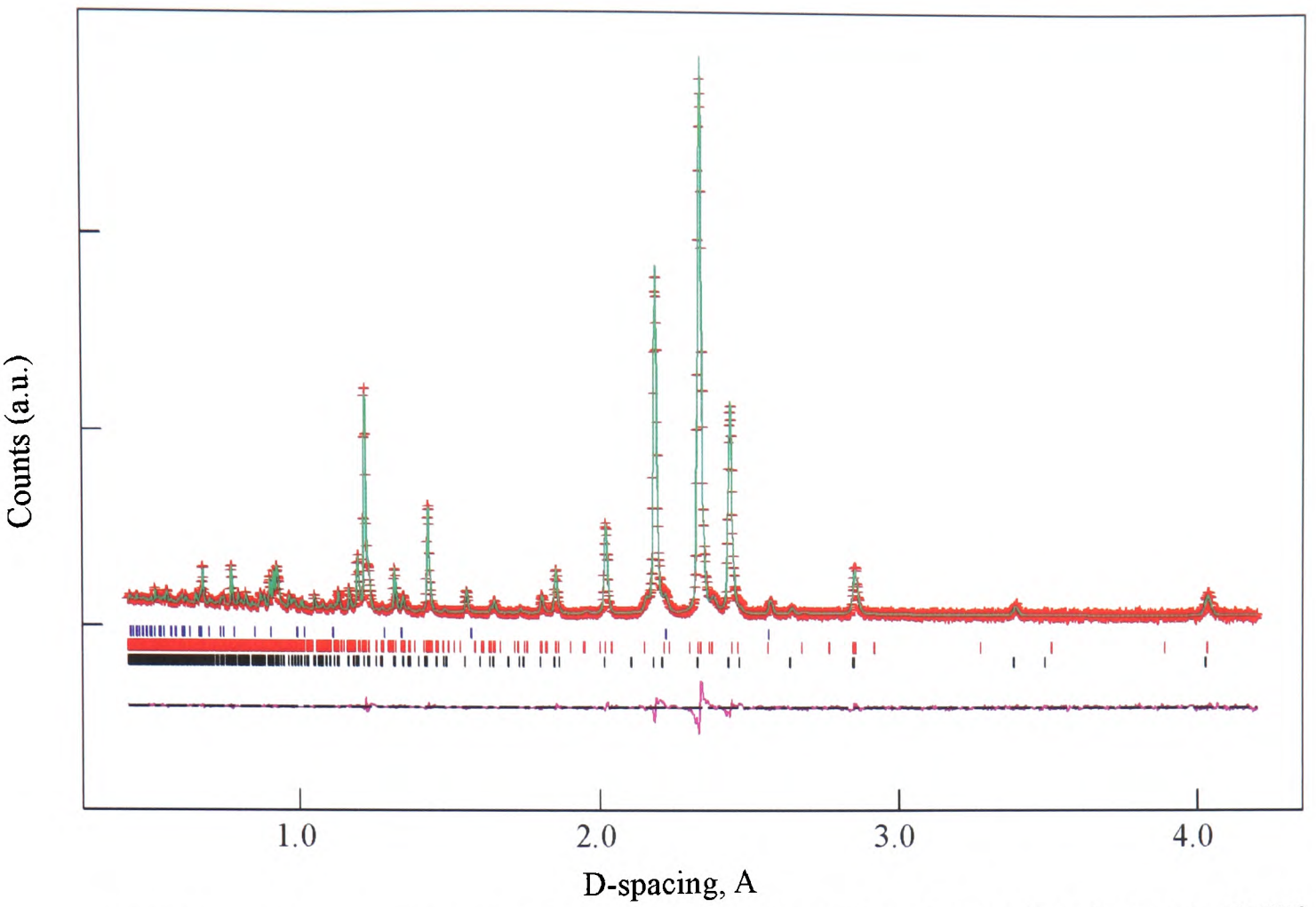


Figure 7.14 Observed, calculated and difference plots from the structural refinement of HV 6H-$BaMn_{0.5}Ti_{0.5}O_{3-x}$ against neutron powder diffraction data. Upper tick marks are MnO, middle tick marks are 15R'-$BaMn_{1-z}Ti_zO_{3-x}$, lower tick marks are 6H-$BaMn_{0.5}Ti_{0.5}O_{3-x}$.

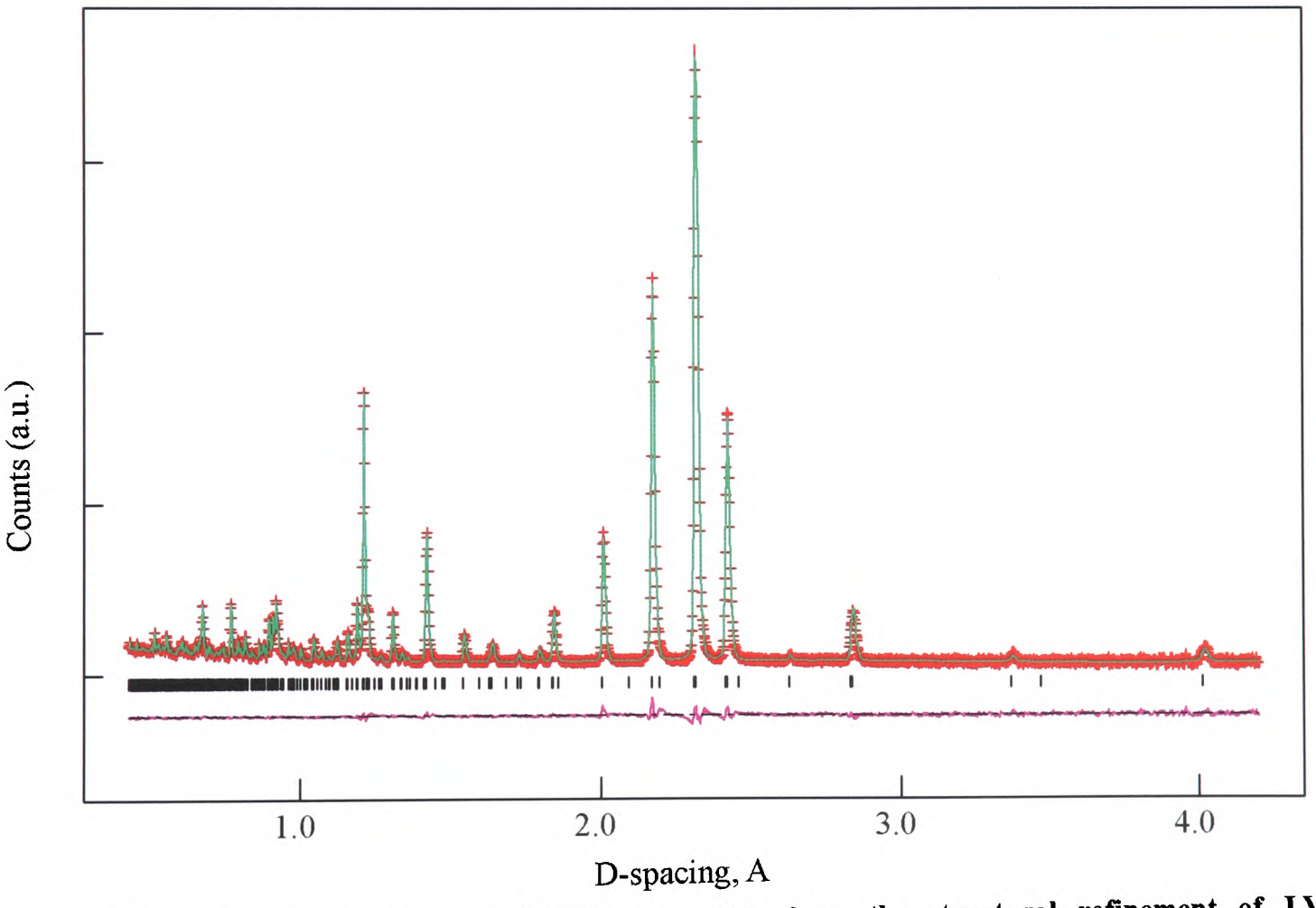


Figure 7.15 Observed, calculated and difference plots from the structural refinement of LV 6H-$BaMn_{0.5}Ti_{0.5}O_{3-x}$ against neutron powder diffraction data.

Bond	Bond Length(Å)/angle(°)	
	HV 6H-$BaMn_{0.5}Ti_{0.5}O_{3-x}$	LV 6H-$BaMn_{0.5}Ti_{0.5}O_{3-x}$
Ba1 – O1	2.85786(8)	2.84819(4)
Ba1 – O2	2.8679(6)	2.8626(3)
Ba2 – O1	2.895(1)	2.8333(7)
Ba2 – O2(3x)	2.925(1)	2.9370(7)
Ba2 – O2(6x)	2.85346(8)	2.84818(6)
Mn/Ti1 – O2	1.9848(7)	1.9831(4)
Mn2 – O1	1.972(1)	1.9618(7)
Mn2 – O2	1.944(1)	1.9444(7)
Mn2 – Mn2	2.706(2)	2.634(2)
Mn2 – O2 – Mn2	78.09(5)	79.86(4)

Table 7.9 Selected bond lengths and angles extracted from the structures of HV 6H-$BaMn_{0.5}Ti_{0.5}O_{3-x}$ and LV 6H-$BaMn_{0.5}Ti_{0.5}O_{3-x}$.

7.3.2.2.3. 4H-$BaMn_{0.66}Ti_{0.33}O_{3-x}$

On refinement of the 4H model against neutron diffraction data collected from 4H-$BaMn_{0.66}Ti_{0.33}O_{3-x}$ a small number of relatively intense reflections were revealed, which could not be accounted for. These were attributed to a second phase with the 6H stacking sequence, and a 6H-$BaMn_{0.66}Ti_{0.33}O_{3-x}$ model was added to the refinement as a second phase. The *a* lattice parameter of the 6H phase is identical to that of the 4H phase, accounting for the difficulty in identifying the second phase from X-ray diffraction data. The atomic positions, oxide occupancy numbers and anisotropic displacement factors of the 4H model were refined against the neutron diffraction data, along with oxide occupancy numbers, atomic positions and isotropic displacement factors of the 6H model. The refined mole fraction of 6H-$BaMn_{1-z}Ti_zO_{3-x}$ was 0.187(4).

Observed, calculated and difference plots of the refinement are shown in Figure 7.17. The model of 4H-$BaMn_{0.66}Ti_{0.33}O_{3-x}$, obtained on refinement against the neutron diffraction data, is detailed in Table 7.10 and is shown in Figure 7.16. Anisotropic displacement factors are listed

in Appendix C. The lattice parameters of the 6H model refined to a = 5.7113(3) Å, c = 13.9841(9) Å.

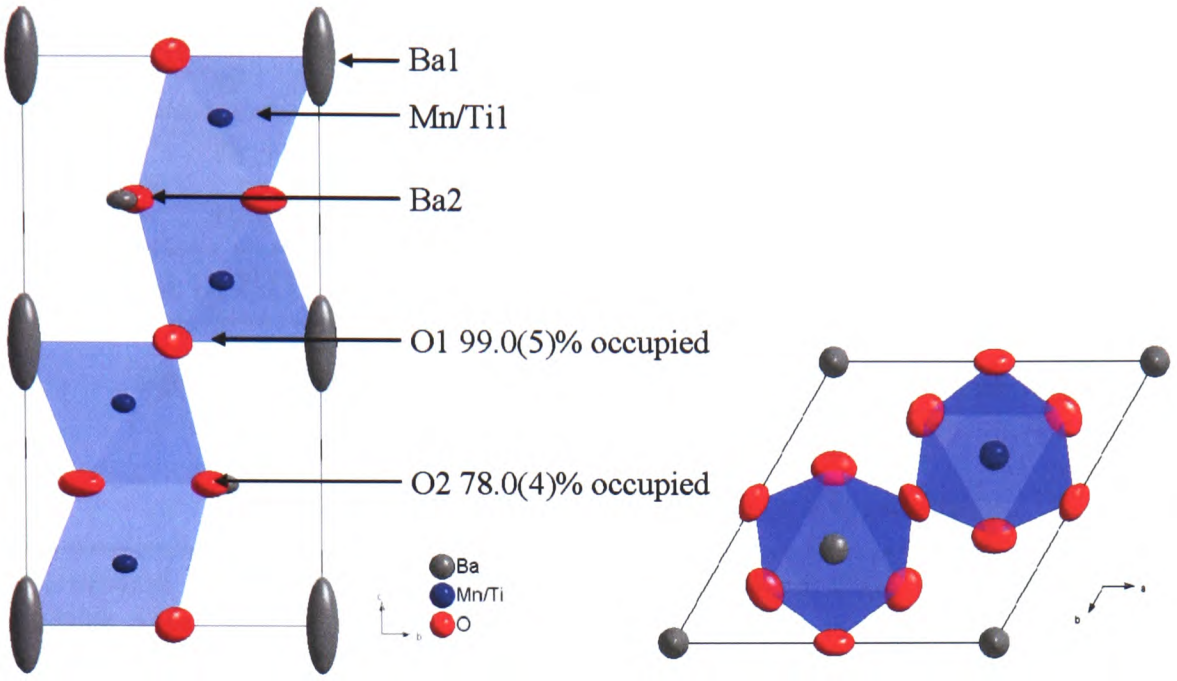


Figure 7.16 Refined structure of 4H-$BaMn_{0.66}Ti_{0.33}O_{2.66(2)}$.

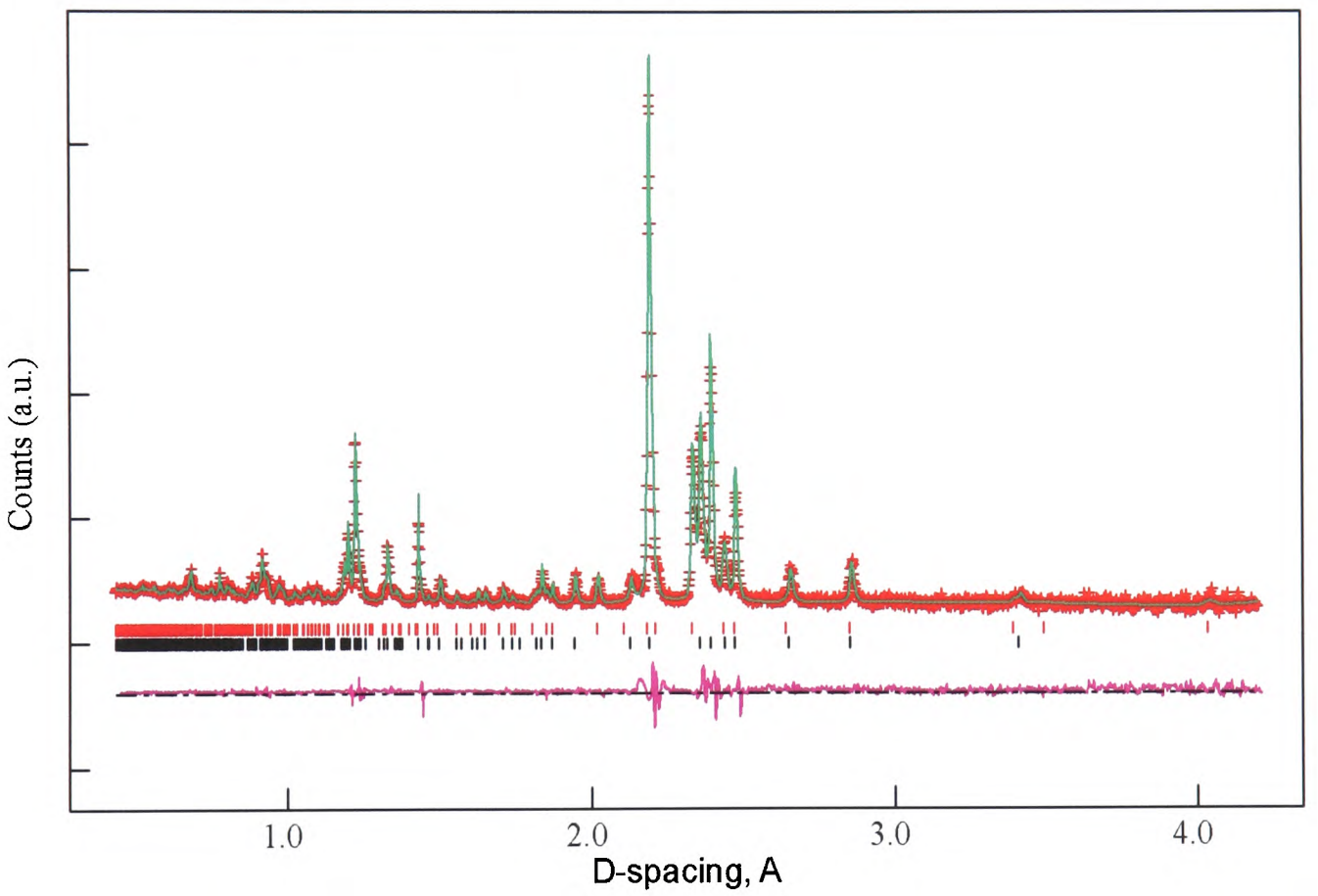


Figure 7.17 Observed, calculated and difference plots from the structural refinement of 4H-$BaMn_{0.66}Ti_{0.33}O_{2.66(2)}$ against neutron powder diffraction data. Lower tick marks represent reflection positions for 4H-$BaMn_{0.66}Ti_{0.33}O_{2.66(2)}$; upper tick marks 6H-$BaMn_{0.66}Ti_{0.33}O_{3-x}$.

Atom	x	y	z	Fractional occupancy	U_{equiv} (Å^2)
Ba1	0	0	0	1	0.0344
Ba2	⅓	⅔	¼	1	0.0071
Mn/Ti1	⅓	⅔	0.6082(2)	1	0.0050
O1	½	0	0	0.990(5)	0.0118
O2	-0.1895(1)	-0.3791(2)	¼	0.780(4)	0.0137
Space group : P 6_3/m m c, a = 5.7126(1)Å, c = 9.4338(2)Å					
χ^2=1.673, wRp = 2.34%, Rp = 4.43%					
Refined stoichiometry : $BaMn_{0.66}Ti_{0.33}O_{2.66(2)}$					

Table 7.10 Structural model of 4H-$BaMn_{0.66}Ti_{0.33}O_{2.66(2)}$ obtained from refinement against neutron powder diffraction data.

Bond	Bond Length(Å)/angle(°)
Ba1 – O1	2.85630(5)
Ba1 – O2	3.0131(8)
Ba2 – O1	2.87780(5)
Ba2 – O2	2.8652(1)
Mn/Ti1 – O1	1.9393(9)
Mn/Ti1 – O2	1.953(1)
Mn2 – Mn2	2.676(3)
Mn2 – O2 – Mn2	78.24(7)

Table 7.11 Selected bond lengths and angles extracted from the structure of 4H-$BaMn_{0.66}Ti_{0.33}O_{2.66(2)}$.

	a (Å)	c (Å)
4H-$BaMnO_{2.65(1)}$	5.6833(2)	9.3556(4)
4H-$BaMn_{1-z}Ti_zO_{2.66(2)}$	5.7126(1)	9.4338(2)

Table 7.12 Lattice parameters of 4H-$BaMn_{1-z}Ti_zO_{2.66(2)}$ and 4H-$BaMnO_{2.65(1)}$. Those of 4H-$BaMnO_{2.65(1)}$ are extracted from Table 4.19.

The relatively high proportion of a minority 6H-$BaMn_{1-z}Ti_zO_{3-x}$ phase (observed using neutron diffraction techniques) raises the possibility of segregation of the manganese and titanium between this and the 4H phase. Comparison of the lattice parameters of 4H-$BaMn_{1-z}Ti_zO_{2.66(2)}$ with those of 4H-$BaMnO_{2.65(1)}$ (Table 7.12) reveals a significant increase for

$4H\text{-}BaMn_{1-z}Ti_zO_{2.66(2)}$. Since both phases have a similar proportion of oxide vacancies, the increase in lattice parameters for $4H\text{-}BaMn_{1-z}Ti_zO_{2.66(2)}$ can only be accounted for by a relatively high value of z, suggesting that B cation segregation is minimal.

7.3.3. Electron diffraction

Electron diffraction data were collected from $4H\text{-}BaMn_{0.66}Ti_{0.33}O_{2.66(2)}$ as described in Section 2.3.3. Two patterns are shown in Figure 7.18, indexed against the 4H unit cell with $a = 5.71$ Å and $c = 9.43$ Å. The first pattern shows superstructure reflections which can only be indexed on the basis of a $\sqrt{3}$ unit cell expansion in the *ab* plane. This is the simplest expansion that maintains the hexagonal symmetry cell (shown in Figure 7.19). The second can be indexed on the basis of a 3-fold expansion of the 4H cell along the *c* axis, but is more likely to be a particle of $6H\text{-}BaMn_{0.66}Ti_{0.33}O_{3-x}$.

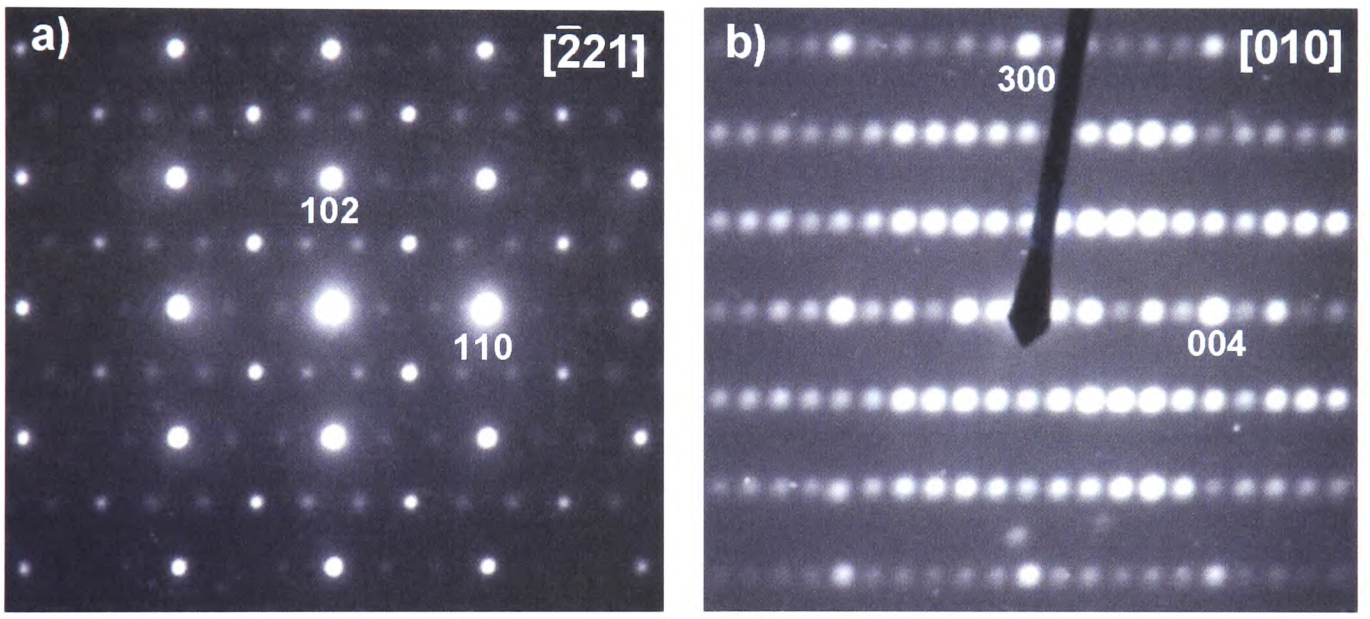


Figure 7.18 Electron diffraction data collected from $4H\text{-}BaMn_{0.66}Ti_{0.33}O_{2.66(2)}$, indexed against the 4H cell. The supercell reflections in pattern (a) can be indexed on the basis of a $\sqrt{3}$ expansion along the *a* and *b* axes. The supercell reflections in pattern (b) can be indexed on the basis of a 3-fold expansion along the *c* axis.

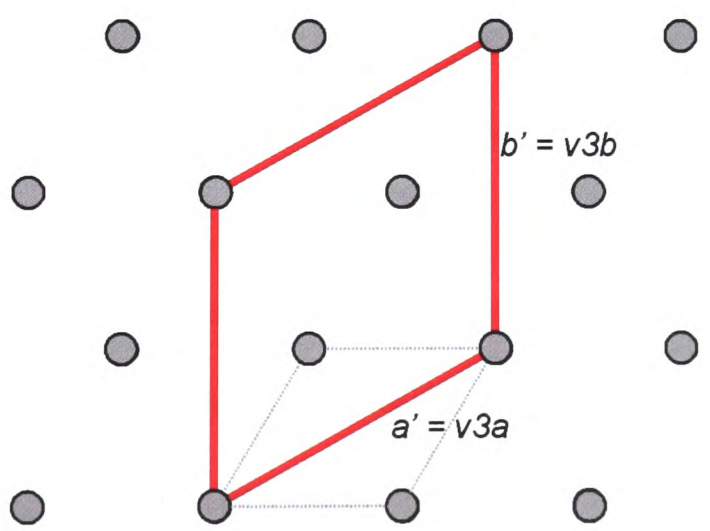


Figure 7.19 $\sqrt{3}$ expansion of a hexagonal unit cell. The new unit cell is shown in red. Hexagonal symmetry is maintained.

The $\sqrt{3}$ unit cell expansion suggests the ordering of either the B cations or of the oxide vacancies. However, the absence of any features in the X-ray and neutron diffraction data suggests that this order occurs only over a short range.

7.3.4. Chemical characterisation

Identifying the chemical composition of phases of the type $BaMn_{1-z}(Ti/Zr)_zO_{3-x}$ is more difficult than for $BaMnO_{3-x}$ phases as the insolubility of Ti(IV) and complex aqueous chemistry of zirconium rules out the use of iodiometric titrations. Some titrations were performed on $BaMn_{1-z}Ti_zO_{3-x}$ samples, but the results were not self-consistent and so were discounted.

Oxidative thermogravimetric analysis measurements were performed on the samples from which neutron powder diffraction data were collected. The results are detailed in Table 7.13, and generally show good agreement with the compositions yielded by refinement against the neutron powder diffraction data.

	6H-$BaMn_{0.8}Zr_{0.2}O_{3-x}$	**LV 6H-$BaMn_{0.5}Ti_{0.5}O_{3-x}$**	**HV 6H-$BaMn_{0.5}Ti_{0.5}O_{3-x}$**	**4H-$BaMn_{0.66}Ti_{0.33}O_{3-x}$**
TGA	0.20(2)	0.02(2)	0.18(2)	0.29(2)
Neutron diffraction	0.19(1)	0.04(2)	0.21(1)	0.34(2)

Table 7.13 Comparison of x obtained via reductive thermogravimetric analysis and neutron powder diffraction for $BaMn_{1-z}(Ti/Zr)_zO_{3-x}$.

In order to corroborate the full oxidation of HV-O and LV-O 6H-$BaMn_{0.5}Ti_{0.5}O_{3-x}$, reductive thermogravimetric analysis was also carried out on HV, HV-O, LV and LV-O 6H-$BaMn_{0.5}Ti_{0.5}O_{3-x}$. Samples were reduced under a flow gas of 5% H_2 in N_2 at 700°C. The HV-O 6H sample was assumed to be fully stoichiometric, as this phase had the smallest lattice parameters. The reductive thermogravimetric analysis carried out on this sample was used to standardise the remaining measurements, yielding compositions of HV 6H-$BaMn_{0.5}Ti_{0.5}O_{2.82(2)}$

and LV 6H-$BaMn_{0.5}Ti_{0.5}O_{2.95(1)}$ and LV-O 6H-$BaMn_{0.5}Ti_{0.5}O_{2.97(1)}$. This method assumes that the end point of all reductions is the same. Powder X-ray diffraction data were collected from all 6H-$BaMn_{0.5}Ti_{0.5}O_{3-x}$ samples after reduction in order to confirm that this was the case. The *a* lattice parameters obtained on refinement against these X-ray diffraction data sets were identical to within 0.005Å, the *c* lattice parameters to within 0.015Å. This suggests that the differences in composition after reduction are minimal.

7.3.5. Magnetometry

Zero-field-cooled and field-cooled magnetometry data were collected from four samples: 4H-$BaMn_{0.66}Ti_{0.33}O_{2.66(2)}$, LV 6H-$BaMn_{0.5}Ti_{0.5}O_{2.96(2)}$, HV 6H-$BaMn_{0.5}Ti_{0.5}O_{2.79(1)}$ and 6H-$BaMn_{0.8}Zr_{0.2}O_{2.81(1)}$. All four samples were also oxidised topotactically, and further magnetometry data sets were collected. The data sets are shown in Figure 7.20 - Figure 7.23.

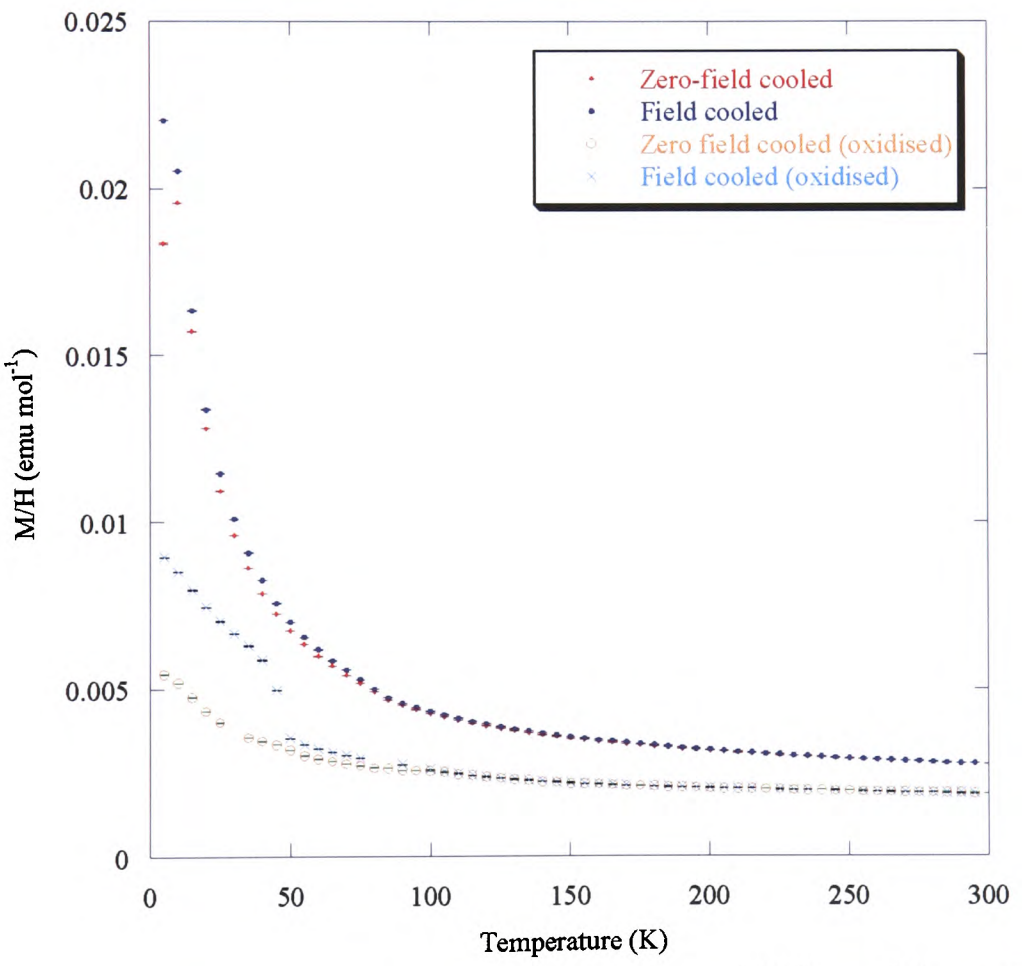


Figure 7.20 Field-cooled and zero-field-cooled susceptibility data collected from 4H-$BaMn_{0.66}Ti_{0.33}O_{2.66(2)}$ and 4H-$BaMn_{0.66}Ti_{0.33}O_3$.

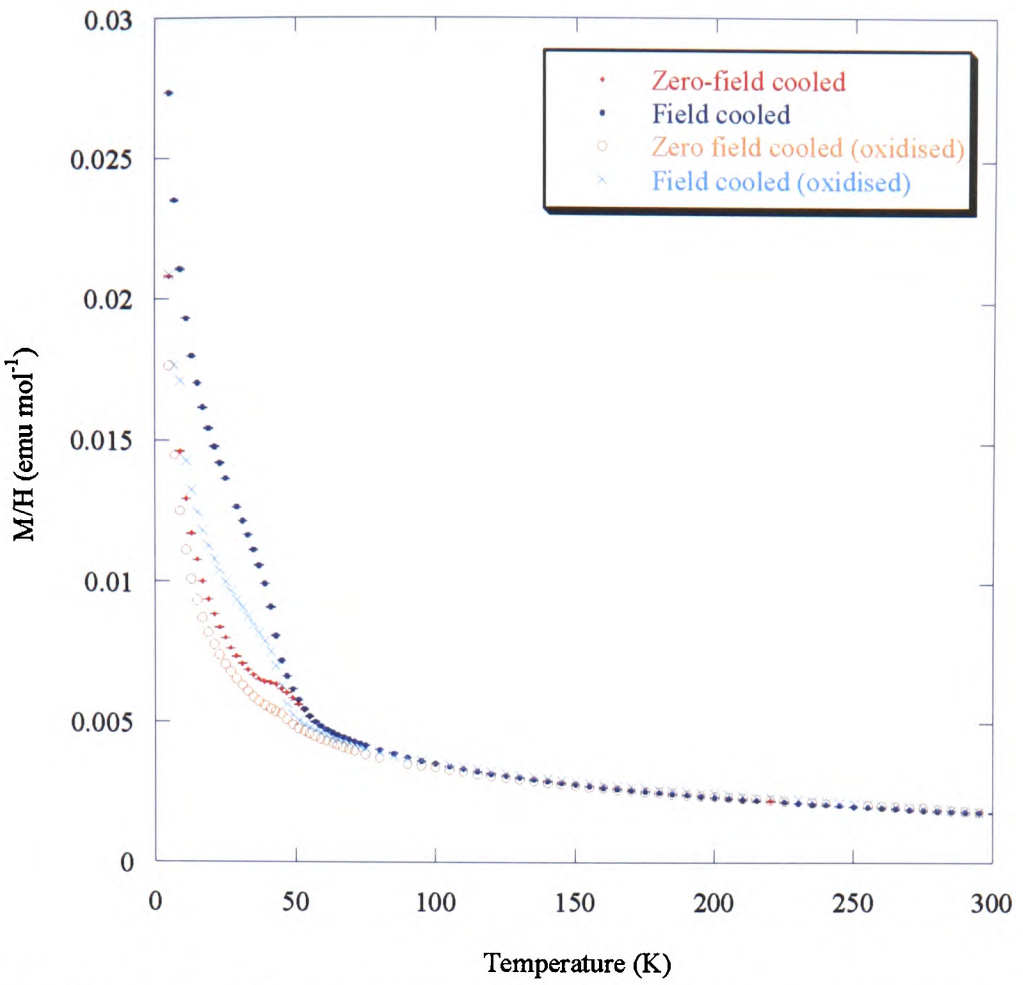


Figure 7.21 Field-cooled and zero-field-cooled susceptibility data collected from LV 6H-$BaMn_{0.5}Ti_{0.5}O_{2.96(2)}$ and LV-O 6H-$BaMn_{0.5}Ti_{0.5}O_{2.97(2)}$.

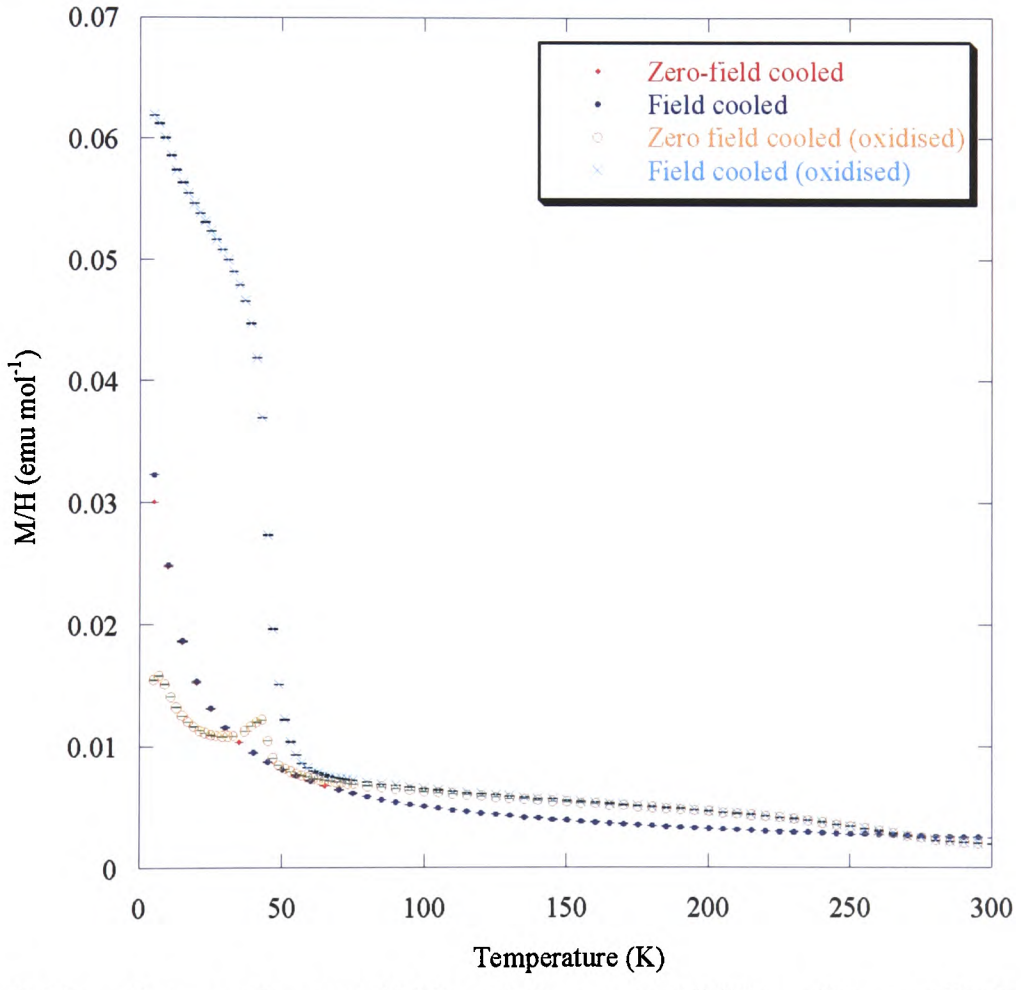


Figure 7.22 Field-cooled and zero-field-cooled susceptibility data collected from HV 6H-$BaMn_{0.5}Ti_{0.5}O_{2.79(1)}$ and HV-O 6H-$BaMn_{0.5}Ti_{0.5}O_{3.00(2)}$.

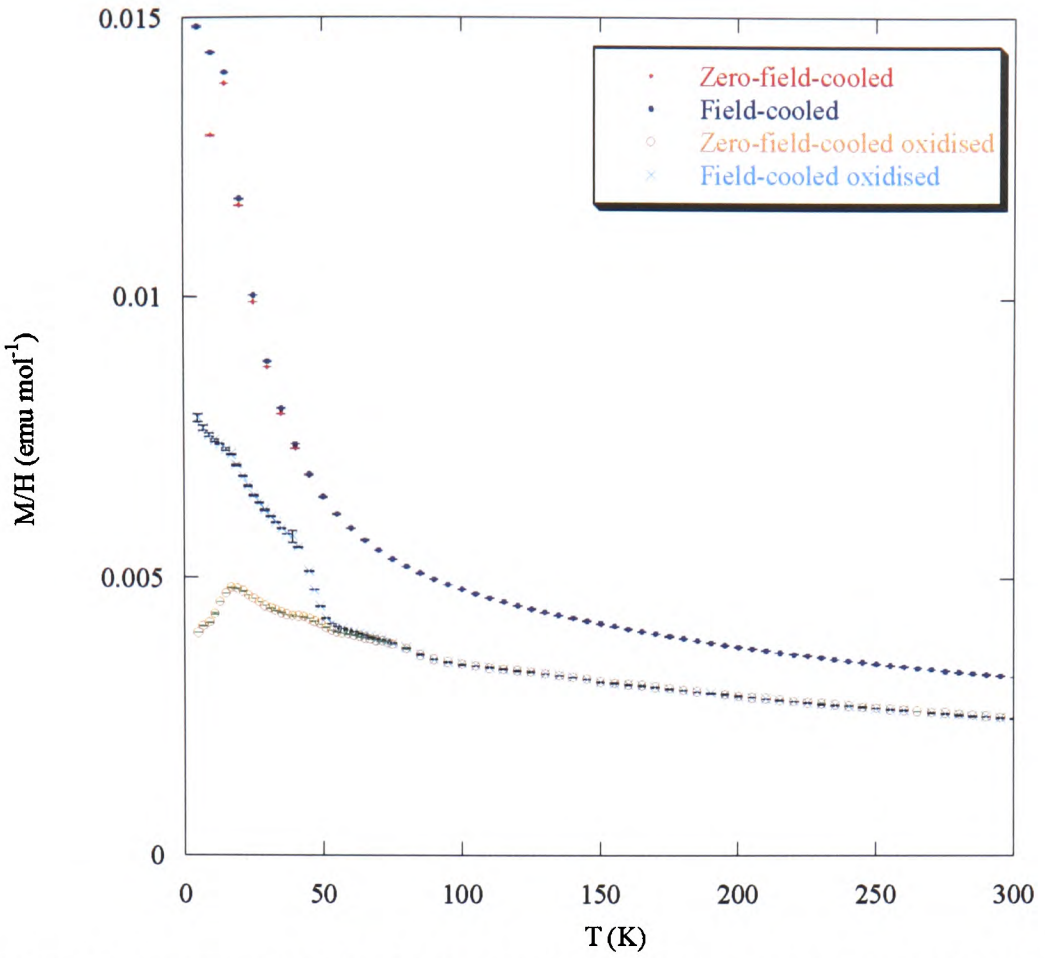


Figure 7.23 Field-cooled and zero-field-cooled susceptibility data collected from 6H-$BaMn_{0.8}Zr_{0.2}O_{2.79(1)}$ and 6H-$BaMn_{0.8}Zr_{0.2}O_{3.00(2)}$.

All the data sets collected from samples prior to oxidation contain few features. The zero-field-cooled and field-cooled data do not diverge in the range 75 < T (K) < 300, and can be fitted in this range using a Curie-Weiss model (Equation 2.26). The fitting parameters are detailed in Table 7.14, as is the fitting statistic R.

	C	Θ	K	R
4H-$BaMn_{0.66}Ti_{0.33}O_{2.66(2)}$	0.165(4)	-7(1)	0.00165(1)	0.99950
LV 6H-$BaMn_{0.5}Ti_{0.5}O_{2.96(2)}$	0.528(9)	64(1)	0.00035(2)	0.99989
HV 6H-$BaMn_{0.5}Ti_{0.5}O_{2.79(1)}$	0.543(5)	29.0(8)	0.00085(1)	0.99996
6H-$BaMn_{0.8}Zr_{0.2}O_{2.81(1)}$	0.57(2)	87(3)	0.00178(4)	0.99968

Table 7.14 Curie-Weiss fitting parameters ($\chi = (C/(T-\theta)) - K$) to susceptibility data collected from 4H-$BaMn_{0.66}Ti_{0.33}O_{2.66(2)}$, LV 6H-$BaMn_{0.5}Ti_{0.5}O_{2.96(2)}$, HV 6H-$BaMn_{0.5}Ti_{0.5}O_{2.79(1)}$ and 6H-$BaMn_{0.8}Zr_{0.2}O_{2.81(1)}$. The fitting statistic R is also shown.

An abrupt divergence between zero-field-cooled and field-cooled data sets collected from HV 6H-$BaMn_{0.5}Ti_{0.5}O_{2.79(1)}$, 4H-$BaMn_{0.66}Ti_{0.33}O_{2.66(2)}$ and 6H-$BaMn_{0.8}Zr_{0.2}O_{2.81(1)}$ is observed at T < 20K (~ 5K, ~ 10K and ~ 15K respectively). The zero-field-cooled and field-cooled data sets

collected from LV 6H-$BaMn_{0.5}Ti_{0.5}O_{2.96(2)}$ diverge at T ~ 45K, as do data sets collected from all oxidised samples. A further event resulting in a discontinuity of the gradient of the susceptibility data collected from HV-O 6H-$BaMn_{0.5}Ti_{0.5}O_{3.00(2)}$ occurs at approximately 285K.

7.4. Discussion

7.4.1. Structure

As in other hexagonal perovskite systems, the ratio of cubic to hexagonal layers in the stacking sequence of $Ba_{1-y}Sr_yMn_{1-z}B_zO_{3-x}$ phases can be rationalised on the basis of the tolerance factor, which can be manipulated by varying *x*, *y* or *z*. Tolerance factors for the four compounds from which neutron diffraction data were collected are listed in Table 7.15. These are similar for the three phases adopting the 6H stacking sequence, which clearly have the same proportion of cubic layers. $BaMn_{0.66}Ti_{0.33}O_{2.66(2)}$ has a larger tolerance factor, and adopts the 4H stacking sequence which has a smaller proportion of cubic layers.

LV 6H-$BaMn_{0.5}Ti_{0.5}O_{2.96(2)}$	**HV 6H-$BaMn_{0.5}Ti_{0.5}O_{2.79(1)}$**	**6H-$BaMn_{0.8}Zr_{0.2}O_{2.81(1)}$**	**4H-$BaMn_{0.66}Ti_{0.33}O_{2.66(2)}$**
1.031	1.034	1.036	1.055

Table 7.15 Tolerance factors calculated from the bond lengths extracted from refinement against neutron diffraction data.

As noted in the Chapter 4, the tolerance factor (*t*) can not account for the arrangement of the cubic layers within the stacking sequence. The 4H (*ch*) and 12R (*cchh*) stacking sequences contain the same proportion of cubic layers (50%). The adoption of the simple 4H sequence is expected in the absence of B cation order. However large B cations are generally accommodated within apex-sharing sites, none of which are available in the 4H sequence. As shown previously in Figure 7.2, the 12R sequence provides such sites, and so the adoption of the 12R sequence can be rationalised on the basis of partial B cation order.

$BaMn_{0.66}Ti_{0.33}O_{3.00}$ adopts a mixture of 9R (33.3% cubic) and 12R (50% cubic) stacking sequences. Reducing *t*, whether by increasing *y* (forming $Ba_{0.8}Sr_{0.2}Mn_{0.66}Ti_{0.33}O_{3-\delta}$), increasing *z* (forming $BaMn_{0.5}Ti_{0.5}O_{3-\delta}$), or increasing *x* (forming $BaMn_{0.66}Ti_{0.33}O_{2.66(2)}$) produces a single

phase with 50% cubic layers. However, while both $Ba_{0.8}Sr_{0.2}Mn_{0.66}Ti_{0.33}O_{3-\delta}$ and $BaMn_{0.5}Ti_{0.5}O_{3-\delta}$ adopt the 12R stacking sequence, the reduced phase $BaMn_{0.66}Ti_{0.33}O_{2.66(2)}$ adopts the simpler 4H stacking sequence. A possible rationalisation for the adoption of this sequence by $BaMn_{0.66}Ti_{0.33}O_{2.66(2)}$ could be increased B cation disorder due to the introduction of Mn(III) ions to the Mn/Ti(IV) system. An alternative rationalisation is that the 4H sequence provides the dimeric sites found to be favourable in the presence of a high proportion of oxide vacancies (discussed in Chapter 4). This would suggest that the energetic benefit of locating the oxide vacancies in the dimer sites is more favourable than that of locating Ti(IV) ions in apex sharing sites.

7.4.2. Susceptibility data

7.4.2.1. Similarities with the $BaMnO_{3-x}$ series

The susceptibility data collected from $BaMnO_{3-x}$ phases was discussed in Chapter 5. The low magnitude of the susceptibility data in the range $5 < T\ (K) < 300$ is accounted for by strong antiferromagnetic coupling between manganese ions connected by a shared face. An event causing a slight divergence of zero-field-cooled and field-cooled data occurs in the range $230 < T\ (K) < 280$, indicating the onset of antiferromagnetic ordering as a result of weaker antiferromagnetic coupling between apex-sharing manganese ions. A second magnetic event occurs at $T \sim 45K$.

The magnetic behaviour of the hexagonal $BaMn_{1-z}Ti_zO_{3-x}$ and 6H-$BaMn_{0.8}Zr_{0.2}O_{3-x}$ phases is likely to be closely related to that of the $BaMnO_{3-x}$ series. It is likely that face-sharing manganese ions in the $BaMn_{1-z}B'_zO_{3-x}$ system also couple antiferromagnetically over the measured temperature range ($5 \leq T\ (K) \leq 300$). This accounts for the low magnitude of the susceptibility data. The temperature of the second antiferromagnetic interaction between apex-sharing manganese ions (utilising a 180° superexchange interaction) was observed to increase with the proportion of cubic layers in $BaMnO_{3-x}$ phases (see Section 5.3.2.2). The event

observed at T ~ 285K in data collected from HV-O 6H-$BaMn_{0.5}Ti_{0.5}O_{3-x}$ is consistent with this trend.

7.4.3. Differences from the $BaMnO_{3-x}$ series

Although the magnetic behaviour of the hexagonal $BaMn_{1-z}Ti_zO_{3-x}$ phases and 6H-$BaMn_{0.8}Zr_{0.2}O_{3-x}$ is related to that of the $BaMnO_{3-x}$ series, the introduction of non-magnetic d^0 ions is expected to produce some modifications. The non-magnetic ions introduce breaks into the magnetic network, which are expected to disrupt any long-range magnetic order (although no low temperature neutron diffraction data were collected to confirm this). A further modification is expected due to the manganese-titanium hetero-dimers which may be present in $BaMn_{1-z}Ti_zO_{3-x}$ phases. Homo and hetero-dimers occurring in 6H-$BaTi_{0.33}Fe_{0.66}O_{2.68}$ were discussed in Section 7.1.2. A manganese homo-dimer contains two face-sharing manganese ions which couple antiferromagnetically. A manganese-titanium hetero-dimer contains only one manganese ion, which cannot couple antiferromagnetically across the shared face. Manganese ions in hetero-dimers are therefore magnetically isolated in the absence of a superexchange interaction between the 180° Mn-O-Mn bonds (Figure 7.24).

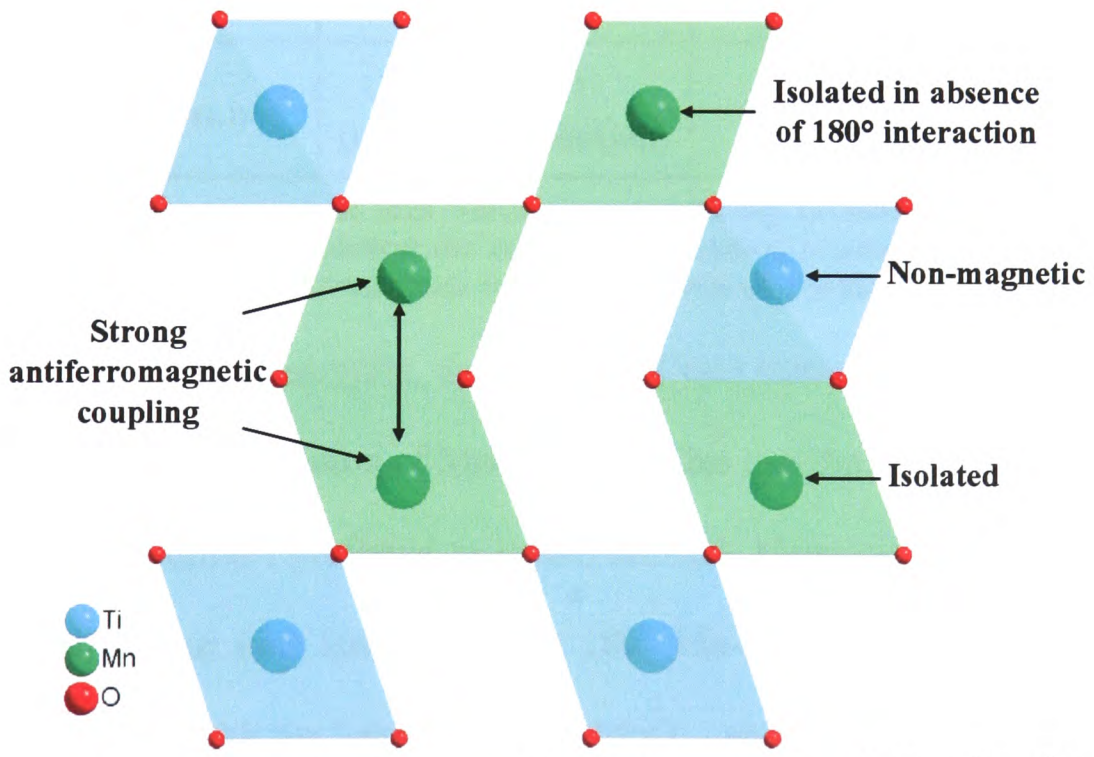


Figure 7.24 Magnetic coupling and isolation on introducing non-magnetic ions into the 6H stacking sequence.

The presence of magnetically isolated manganese ions is suggested by the susceptibility data. Unlike susceptibility data collected from $BaMnO_{3-x}$ phases, the data collected from 6H-$BaMn_{0.8}Zr_{0.2}O_{2.81(1)}$, 4H-$BaMn_{0.66}Ti_{0.33}O_{2.66(2)}$, LV 6H-$BaMn_{0.5}Ti_{0.5}O_{2.96(2)}$ and HV 6H-$BaMn_{0.5}Ti_{0.5}O_{2.79(1)}$ appear paramagnetic in the range $75 \leq T(K) \leq 300$ and can be fitted by the Curie-Weiss model. If the paramagnetic behaviour is attributable to isolated manganese ions, than an indication of the degree of local order can be obtained by comparing the measured Curie constant (from the fit to the data) and the expected Curie constant. The expected Curie constant can be calculated using Equation 2.25. For one mole of Mn(IV) C_{exp} = 1.875, for one mole of Mn(III) C_{exp} = 3.0. For comparison with the data, this must be multiplied by the proportion of manganese ions that are isolated if manganese and titanium are distributed randomly throughout the structure.

	Proportion of Mn which is isolated	**Expected C (per mole of Mn(IV))**	**Measured C (per mole of Mn)**
4H-$BaMn_{0.66}Ti_{0.33}O_{2.66(2)}$	$^1/_3$	0.625	0.330(7)
6H-$BaMn_{0.5}Ti_{0.5}O_{2.96(2)}$, (LV)	$^2/_3$	1.25	1.06(2)
6H-$BaMn_{0.5}Ti_{0.5}O_{2.79(1)}$ (HV)	$^2/_3$	1.25	1.09(1)
6H-$BaMn_{0.8}Zr_{0.2}O_{2.81(1)}$	0.1631(8) (refined distribution)	0.306	0.71(2)

Table 7.16 Fraction of the manganese ions which are magnetically isolated in the absence of a 180° superexchange interaction for a statisitcal (or refmed) distribution, expected Curie constant if these behave paramagnetically, and measured Curie constant per mole of manganese ions.

For all of the $BaMn_{1-z}Ti_zO_{3-x}$ samples, the measured Curie constant is smaller than expected on the basis of a statistical distribution of Mn(IV) ions. This may be attributed to a preference for local ordering (homo-dimers preferred to hetero-dimers). However, the statistical distribution accounts for manganese ions isolated if the 180° Mn-O-Mn superexchange interaction is neglected. Comparison with the behaviour of $BaMnO_{3-x}$ phases suggests that only those which are still magnetically isolated when the 180° Mn-O-Mn superexchange interaction is not

neglected should behave paramagnetically over the entire fitted range ($75 < T(K) < 300$). Antiferromagnetic coupling involving manganese ions in apex-sharing sites utilising the 180° superexchange pathways can also account for the reduction in Curie constant. Moreover, the data collected from 6H-$BaMn_{0.8}Zr_{0.2}O_{2.81(1)}$ suggest that the susceptibility data do not provide a reliable indication of the degree of local order. No manganese ions in 6H-$BaMn_{0.8}Zr_{0.2}O_{2.81(1)}$ are isolated when 180° superexchange interactions are taken into account, suggesting that all manganese ions should be antiferromagnetically coupled in the range $75 < T\ (K) < 200$. However, data over the entire range $75 < T(K) < 300$ can be fitted using the Curie-Weiss law with a much larger Curie constant than expected, even if the 180° superexchange interactions are assumed to be negligible and manganese ions occupying the apex-sharing sites behave paramagnetically. This suggests that a significant part of the paramagnetic behaviour occurs as a result of defect ions which do not couple antiferromagnetically despite their location in manganese homo-dimers. Thus quantitative analysis of the proportion of homo and hetero-dimers based on the fitted susceptibility data is not possible.

7.4.4. Cation ordering

In all samples, the oxide vacancies are found to be exclusively located in the hexagonal (face-sharing) layers in preference to the apex-sharing cubic layers. This is consistent with the discussion in Chapter 4, where the vacancy location in hexagonal layers was rationalised on the basis of the increased contribution to the bonding of anions located in a shared face by the B cations and thus reduced contribution from A cations. Oxide vacancy location in the face-sharing sites suggests that the more reducible manganese ions will also be located preferentially in the face-sharing sites. However, it seems unlikely that the location of oxide vacancies in the face-sharing sites has any effect on the manganese-zirconium distribution in 6H-$BaMn_{0.8}Zr_{0.2}O_{3-x}$. This can be rationalised solely on the basis of the different B cation sizes, with zirconium ions occupying the larger apex-sharing site.

Mn(IV) is smaller than Ti(IV), suggesting that the face-sharing sites of 6H-$BaMn_{0.5}Ti_{0.5}O_{3-x}$ phases will also be predominantly occupied by manganese and thus the apex sharing sites of the 6H structure will be occupied by titanium. The average B-O bond lengths of HV and LV 6H-$BaMn_{0.5}Ti_{0.5}O_{3-x}$ are shown in Figure 7.25.

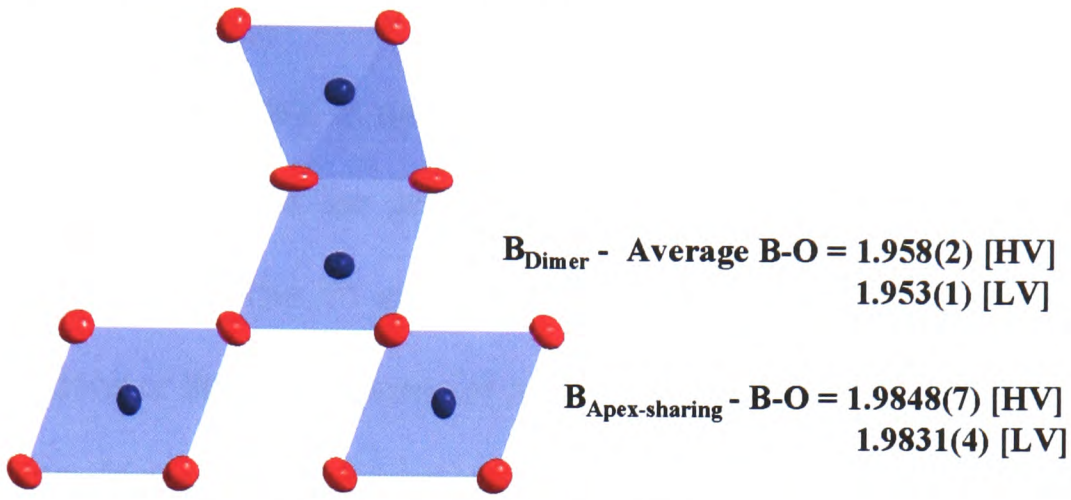


Figure 7.25 B-O bond lengths in 6H-$BaMn_{0.5}Ti_{0.5}O_{3-x}$ phases.

The average B-O bond length is larger for the apex-sharing B cation site than for the dimer site. Bond valence sum calculations were performed for Mn(IV) ions located in LV 6H-$BaMn_{0.5}Ti_{0.5}O_{2.96(2)}$ in order to compare the two sites. Only comparison is possible, as the absolute values are not meaningful for the mixed cation system. The bond valence sum relies on local bond lengths. While the average bond lengths extracted using diffraction techniques provide an approximation to these, the approximation begins to fail for sites partially occupied by several different ions. The sum for Mn(IV) in the apex-sharing site is 3.22, compared to 3.49 for the dimer site. This confirms that the apex-sharing sites are larger than the dimer sites, suggesting they will be predominantly occupied by the larger titanium cations, while Mn(IV) ions will be preferentially located in the face-sharing dimer sites.

There are not enough apex-sharing sites to account for all of the titanium ions of 6H-$BaMn_{0.5}Ti_{0.5}O_{3-x}$: some must occupy the face-sharing sites. Clearly, in 4H-$BaMn_{0.66}Ti_{0.33}O_{3-x}$ all of the titanium must occupy the face-sharing sites as these are the only sites available. There are several degrees of cation order possible in these systems. The dimers of a locally ordered system consist of Mn_2O_{9-x} (manganese homo-dimers) and Ti_2O_9

(titanium homo-dimers), with no $MnTiO_9$ dimers (hetero-dimers). Local order (a preference for homo-dimers) cannot be detected by diffraction techniques as no additional periodicity is introduced to the structure. In a fully ordered system, homo-dimers are arranged in a periodic manner throughout the structure. This is expected to result in additional diffraction features. These are not observed in the X-ray diffraction or neutron diffraction data collected from any samples, indicating that there is no long-range order of the B cations within the dimers. However, additional features are observed in electron diffraction patterns collected from 4H-$BaMn_{0.66}Ti_{0.33}O_{2.66(2)}$. The $\sqrt{3}$ expansion required to index certain patterns suggests that either the B cations or the oxide vacancies are ordered over a short-range. Short-range order of the B cations would necessarily require local order within the dimers.

However, the similarity of both diffraction and susceptibility data collected from HV and LV 6H-$BaMn_{0.5}Ti_{0.5}O_{3-x}$ indicates that in fact the proportion of oxide vacancies has little effect on the cation distribution. Any cation ordering that does occur in these systems can be rationalised on the basis of size differences between the different cations.

7.5. Conclusion

Synthesis under reducing conditions allows the formation of a series of $BaMn_{1-z}Ti_zO_{3-x}$ phases, including a novel 15R'-$BaMn_{0.55}Ti_{0.45}O_{3-x}$ phase. 6H-$BaMn_{0.8}Zr_{0.2}O_{2.81(1)}$ can also be prepared under reducing conditions. Changing the tolerance factor adjusts the proportion of cubic layers in the stacking sequence, but the proportion of oxide vacancies has a further effect. The oxide vacancies are accommodated within the face-sharing layer of B_2O_8 dimers, which favours the 4H stacking sequence for $BaMn_{0.66}Ti_{0.33}O_{2.66(2)}$. This can be compared to the 12R stacking sequence that is adopted by the related phases $BaMn_{0.5}Ti_{0.5}O_{3-\delta}$ and $Ba_{0.8}Sr_{0.2}Mn_{0.66}Ti_{0.33}O_{3-\delta}$.

There is no evidence that the oxide vacancies affect the B cation ordering within these phases. B cation ordering in these systems seems to be controlled by the size of the cations, with larger cations occupying apex-sharing sites and smaller cations occupying face-sharing sites.

Chapter 8: Topotactic reduction of 4H-Ba(Sr)MnO_{3-x}

8.1. Introduction

Previous chapters have discussed how the tolerance factor controls the proportion of cubic layers in the stacking sequence of hexagonal perovskite structures. The cubic layers often maximise their separation within the sequence (forming the simple stacking sequences discussed in Section 1.3). Complex stacking sequences (in which the cubic layers do not maximise their separation) may be adopted as a result of the ordering of either B cations or oxide vacancies.

The tolerance factor, and thus the stacking sequence, is correlated with the oxidation state of the B cations. This reduces the degree of control which can be exerted over the electrical and magnetic properties of ABO_{3-x} phases, as these are dependent both on the oxidation state of the B cation and the structure adopted. In order to overcome this problem, a technique must be found where the oxidation state of the B cation can be modified without altering the stacking sequence. This is commonly achieved by offsetting the change in tolerance factor on oxidation (or reduction) of the B cation by substituting for a larger (or smaller) A cation. However, many hexagonal perovskites contain barium as the A cation. While the tolerance factor of a $BaBX_3$ phase can easily be conserved on oxidation by substituting smaller A cations into the sample, there are no larger A(II) cations available. Moreover, the competition between stacking sequences such as 9R and 6H' (discussed in Chapter 4) or 12R and 4H (discussed in Chapter 7), shows that while A cation substitution may offset any change in the tolerance factor during oxidation or reduction and thus maintain the proportion of cubic stacking, the stacking sequence itself is not necessarily conserved.

An alternative method of decoupling the B cation oxidation state from the structure adopted is to use low temperature, topotactic reactions. In general, the oxide anions are more mobile than the metal cations at a given temperature. This has allowed low temperature topotactic

oxidations to be performed in order to increase the B cation oxidation state, as discussed in previous chapters. Topotactic reductions have been effected at low temperatures by binary metal hydrides.[123, 124] This chapter discusses the hydride reduction of 4H-Ba(Sr)MnO_{3-x} phases.

8.2. *Experimental*

8.2.1. Synthesis

4H-$BaMnO_{3-x}$ and 4H-$Ba_{0.5}Sr_{0.5}MnO_{3-x}$ starting materials were prepared as discussed in Chapter 3. Suitable proportions of binary oxides and carbonates were ground together and fired at 900°C in order to effect decarbonation. The samples were then fired at 1300-1350°C under flowing argon until X-ray powder diffraction data indicated that reaction was complete.

The starting materials were mixed with a stoichiometric double excess of either NaH or LiH in an argon filled glove box and then sealed under vacuum in glass ampoules before firing at the relevant temperature. Large samples containing LiH were fired using the pressure release system discussed in Section 2.2. Reaction completeness was monitored using data collected by the Philips diffractometer from samples contained in an air-sensitive X-ray cell (Section 2.3.1.1).

Excess hydride was washed from the samples using methanol, along with binary oxide or hydroxide by-products. Samples were then thoroughly dried on a vacuum line. Thermogravimetric analysis was used to determine if methanol remained in the samples. Any mass loss on heating in a thermogravimetric balance was attributed to the loss of methanol from the sample. Where mass loss occurred, the samples were heated gently using the pressure release system to remove the remaining methanol. Some samples were annealed after the washing procedure. These were sealed in glass ampoules under vacuum prior to firing at the relevant temperature.

8.2.2. Characterisation

X-ray powder diffraction data suitable for refinement were collected using the X-pert diffractometer from three hydride reduced phases: $Ba_{0.5}Sr_{0.5}MnO_{2.02(1)}$, $BaMnO_{2.47(1)}$ and $BaMnO_{2.06(1)}$. The air-sensitive X-ray cell was not used for these scans in order to improve the quality of the data. No significant variation in the diffraction features was observed on comparison with X-ray data collected using the air-sensitive X-ray cell, indicating that the materials are not air-sensitive over the time scale required to collect the X-ray diffraction data.

Neutron powder diffraction data were collected from $Ba_{0.5}Sr_{0.5}MnO_{2.02(1)}$, $BaMnO_{2.47(1)}$ and $BaMnO_{2.06(1)}$ using the Polaris instrument at the ISIS facility. As well as ambient temperature measurements, measurements were carried out on all samples at 1.8K, using a cryostat. For ambient and low temperature measurements samples were contained in vanadium cans, sealed under an argon atmosphere using indium wire. Data were also collected at a temperature of 373K (achieved using a furnace) from $Ba_{0.5}Sr_{0.5}MnO_{2.02(1)}$ and $BaMnO_{2.06(1)}$. For these measurements, the vanadium cans were sealed under argon using a copper gasket.

Electron diffraction data were collected from $BaMnO_{2.47(1)}$ as discussed in Section 2.3.3. High resolution electron diffraction data were collected from $BaMnO_{2.06(1)}$ by Dr. Joke Hadermann.

Chemical compositions were identified using both thermogravimetric analysis and iodiometric titrations, as discussed in Section 2.6 and 2.8.

Zero-field-cooled and field-cooled magnetic susceptibility data were collected as a function of temperature under a measuring field of 100 Oe. Magnetisation-field isotherms between ± 50000 Oe were collected at 6K and 300K.

8.3. 4H-$Ba_{0.5}Sr_{0.5}MnO_{2+x}$

8.3.1. Results

4H-$Ba_{0.5}Sr_{0.5}MnO_{3-x}$ was fired with LiH for 2 days at 350°C, washed, and dried for approximately two hours on a vacuum line. The product was then dried in the pressure venting

system for 2 hours at 175°C in order to remove any remaining methanol. Iodiometric titrations were carried out on the product, yielding a chemical composition of $Ba_{0.5}Sr_{0.5}MnO_{2.02(1)}$. Thermogravimetric analysis was also carried out. The thermogravimetric data are shown in Figure 8.1. If the final composition is taken to be 4H-$Ba_{0.5}Sr_{0.5}MnO_{3.00}$, the calculated initial composition is 4H-$Ba_{0.5}Sr_{0.5}MnO_{2.04(1)}$, in good agreement with the result obtained by titration.

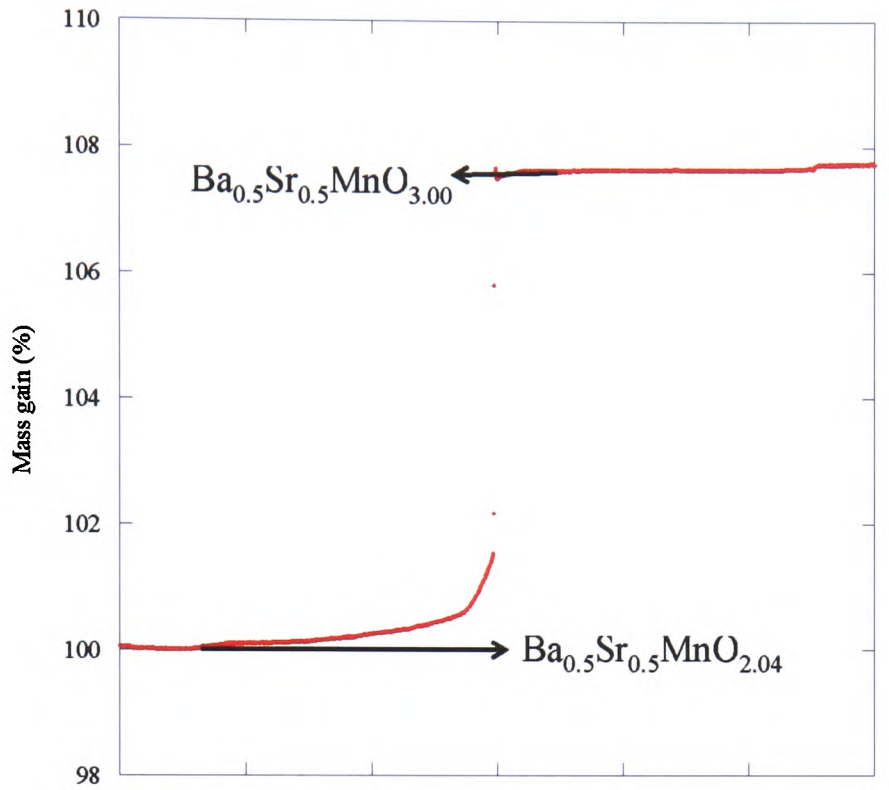


Figure 8.1 Thermogravimetric data collected from 4H-$Ba_{0.5}Sr_{0.5}MnO_{2+x}$.

8.3.1.1. Structural refinement

X-ray powder diffraction data collected from 4H-$Ba_{0.5}Sr_{0.5}MnO_{2.02(1)}$ can be indexed using a hexagonal unit cell with lattice parameters of a = 5.7153(4) Å and c = 9.4218(8) Å. Comparison with the lattice parameters of 4H-$Ba_{0.5}Sr_{0.5}MnO_{2.79(1)}$ (5.58539(8) Å and c = 9.2123(1) Å) suggests the structures are closely related. A model based on that of 4H-$Ba_{0.5}Sr_{0.5}MnO_{2.79(1)}$ was refined against the X-ray powder diffraction data collected from 4H-$Ba_{0.5}Sr_{0.5}MnO_{2.02(1)}$, producing a good fit. This confirms that the reduction is topotactic, and that the cation positions are essentially unchanged relative to the starting material.

Refinement of the 4H model against the neutron powder diffraction data collected from 4H-$Ba_{0.5}Sr_{0.5}MnO_{2.02(1)}$ at 298K did not produce a good fit. The model was unable to account

for the diffraction intensity at high *d*-spacings. Comparison with neutron diffraction data collected at 1.8K and 373K (Figure 8.2) suggests that the additional intensity is a result of magnetic ordering.

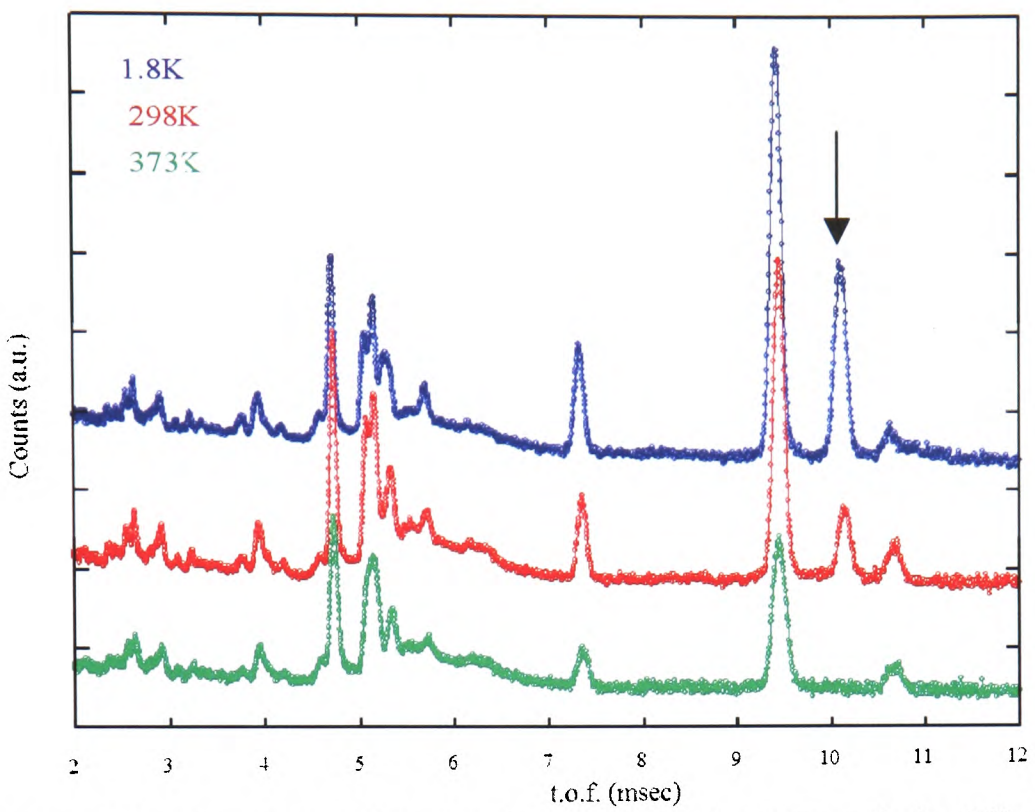


Figure 8.2 Neutron diffraction data collected using the A bank of the polaris diffractometer from $Ba_{0.5}Sr_{0.5}MnO_{2.02(1)}$ at 1.8K, 298K and 378K. The highlighted reflection can only be accounted for by magnetic scattering.

A magnetic model identical to that described for 4H-$BaMnO_{3.00(1)}$ (in Section 5.3.2.4) was added to the nuclear 4H-$Ba_{0.5}Sr_{0.5}MnO_{3-x}$ model and refined against the 298K neutron diffraction data. This produced a good fit, accounting for all of the scattered intensity. As no magnetic scattering was observed in the data collected at 373K, this data set was used to decouple the nuclear and magnetic scattering. The nuclear 4H model was refined against the 373K neutron diffraction data. All atomic positions and anisotropic displacement factors were refined, with particular attention paid to the oxide ion occupancy numbers. These were strongly correlated with the oxide displacement ellipsoids, so the oxide ion occupancy was constrained such that the composition was consistent with that obtained chemically. The barium and strontium occupancy numbers were not refined, but were set to the values obtained from the refinement against data collected from $Ba_{0.5}Sr_{0.5}MnO_{2.79(1)}$ (Table 4.20). The nuclear model obtained on refinement against the 373K data was then refined against the 298K and 1.8K data

sets. Atomic positions and anisotropic displacement factors were allowed to relax in these refinements, but the occupancy numbers were fixed. With the addition of the magnetic model a good fit was achieved which accounted for all of the intensity. Observed, calculated and difference plots from the refinements against data collected from the Polaris A (low angle) bank are shown in Figure 8.3. Models for the three refinements are detailed in Table 8.1. The model from refinement against data collected at 298K is shown in Figure 8.4, along with the magnetic model. Selected bond lengths extracted from the 298K model are listed in Table 8.2. The anisotropic displacement factors are listed in Appendix D.

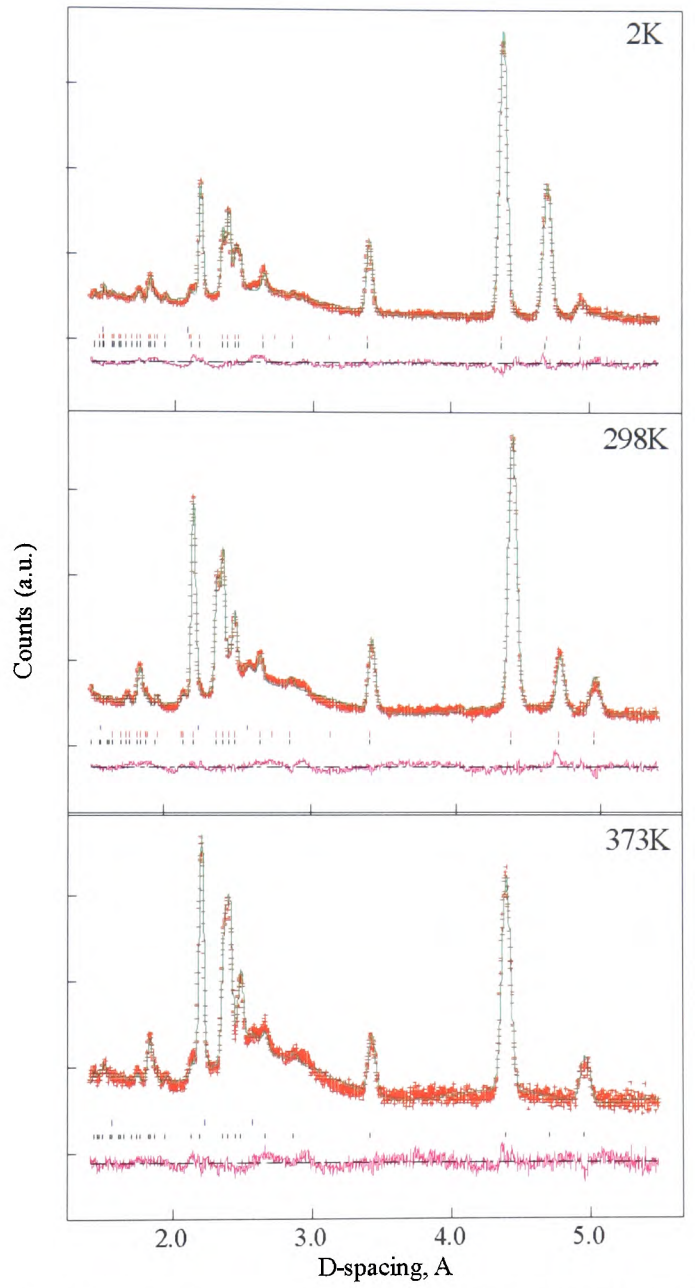


Figure 8.3 Observed, calculated and difference plots from refinement against neutron diffraction data collected at 298K from 4H-$Ba_{0.5}Sr_{0.5}MnO_{2+x}$ using the A bank of the Polaris diffractometer. Lower tick marks represent reflection positions for 4H-$Ba_{0.5}Sr_{0.5}MnO_{2+x}$; upper tick marks represent reflections due to the vanadium sample container.

Atom	Position	Variable	Temperature		
			1.8K	**298K**	**373K**
Ba/Sr1	2a (0,0,0)	Fractional Occupancy	0.67/0.33		
		U_{equiv} (Å^2)	0.0522	0.0728	0.0788
Ba/Sr2	2c (⅓,⅔,¼)	Fractional Occupancy	0.33/0.67		
		U_{equiv} (Å^2)	0.0333	0.0436	0.0473
Mn	4f (⅓,⅔,z)	z	0.6069(4)	0.6069(3)	0.6070(3)
		U_{equiv} (Å^2)	0.0123	0.0140	0.0165
		Ordered moment	3.73(3)	1.92(3)	0
O1	6g (½,0,0)	Fractional Occupancy	0.813(6)		
		U_{equiv} (Å^2)	0.1304	0.1411	0.1357
O2	6h (x,2x,¼)	x	-0.1770(5)	-0.1795(4)	-0.1778(4)
		Fractional Occupancy	0.534(6)		
		U_{equiv} (Å^2)	0.0724	0.0789	0.0784
***a* (Å)**			5.7005(3)	5.7179(6)	5.720(2)
***c* (Å)**			9.3776(5)	9.4179(9)	9.429(4)
χ^2			2.206	3.256	2.075
wRp			1.54%	1.88%	1.19%
Rp			1.71%	2.17%	1.71%

Table 8.1 Structural parameters refined against neutron powder diffraction data collected from 4H-$Ba_{0.5}Sr_{0.5}MnO_{2+x}$ at 1.8, 298 and 373K.

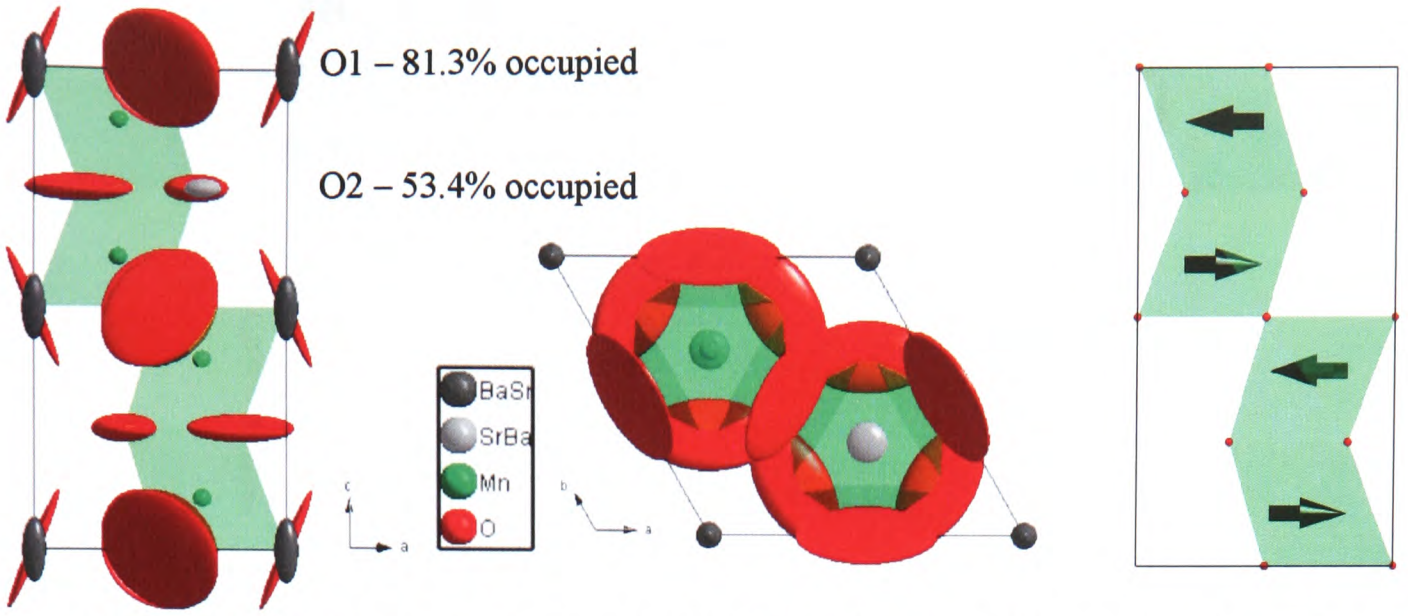


Figure 8.4 Nuclear and magnetic models of 4H $Ba_{0.5}Sr_{0.5}MnO_{3-x}$ obtained on refinement against neutron diffraction data collected at 298K.

Bond	Bond Length(Å)/angle(°)
Ba/Sr1 – O1	2.8590(3)
Ba/Sr1 – O2	2.950(2)
Ba/Sr2 – O1	2.8754(5)
Ba/Sr2 – O2	2.8618(3)
Mn1 – O1	1.933(4)
Mn1 – O2	2.034(3)
Mn2 – Mn2	2.696(5)
Mn2 – O2 – Mn2	78.24(7)

Table 8.2 Selected bond lengths and angles extracted from the structure of 4H-$Ba_{0.5}Sr_{0.5}MnO_{2.02(2)}$.

8.3.1.2. Magnetometry data

Magnetic susceptibility data collected from 4H-$Ba_{0.5}Sr_{0.5}MnO_{2.02(1)}$ are shown in Figure 8.5. The overall susceptibility is small and largely temperature independent. A slight divergence is observed between zero-field-cooled and field-cooled data, which persists across the entire measured temperature range. The convergence observed at 300K is a result of the thermal hysteresis involved in the measurement, rather than a true feature of the sample. No magnetic events are observed.

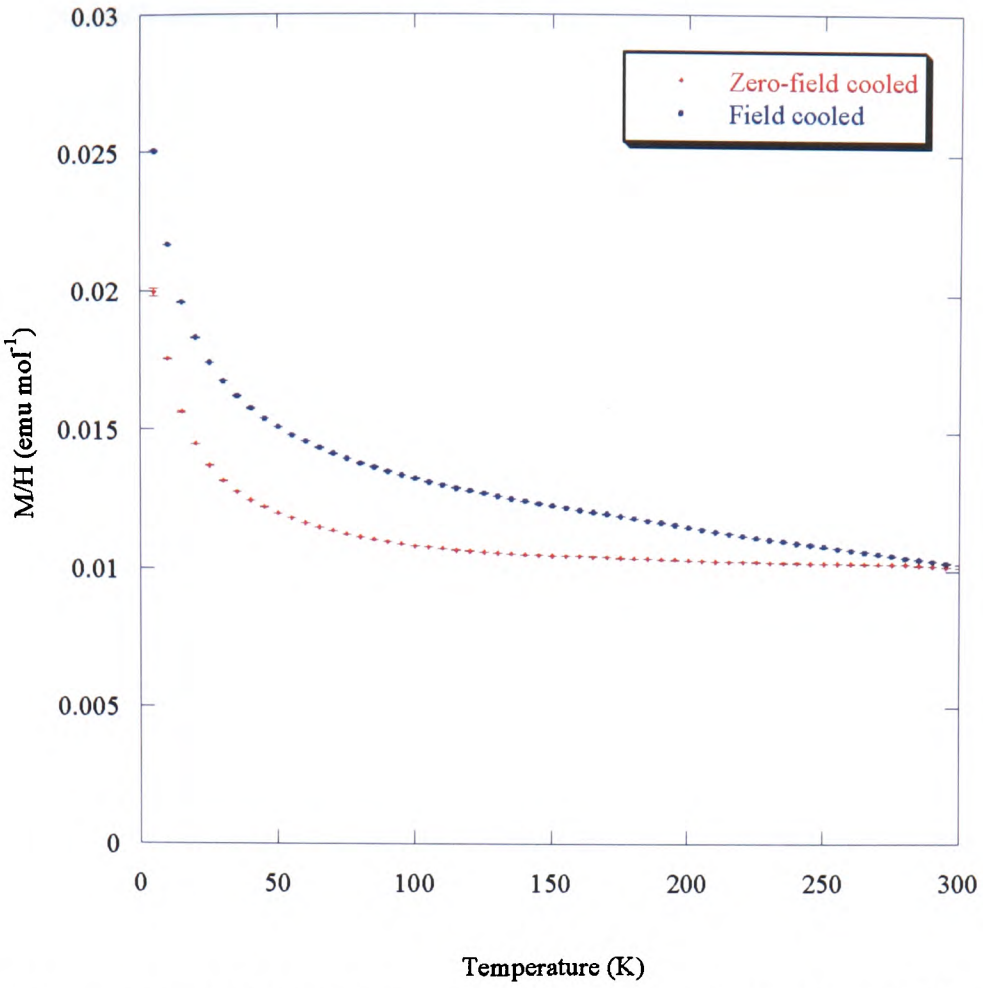


Figure 8.5 Zero-field-cooled and field-cooled magnetisation data collected from 4H-$Ba_{0.5}Sr_{0.5}MnO_{2.02(1)}$.

8.3.2. Discussion

8.3.2.1. Structure

4H-$Ba_{0.5}Sr_{0.5}MnO_{3-x}$ is readily reduced by LiH, and diffraction data show that the cation substructure, unit cell and symmetry of the reduced product are unchanged with respect to the starting material (the reduction is topotactic). In Table 8.3 the lattice parameters of 4H-$Ba_{0.5}Sr_{0.5}MnO_{2.02(1)}$ are compared with those of 4H-$Ba_{0.5}Sr_{0.5}MnO_{2.99(1)}$ and 4H-$Ba_{0.5}Sr_{0.5}MnO_{2.79(1)}$ (extracted from Table 4.20). A linear relationship is observed between the lattice parameters and x, as expected considering expansion of the Mn-O bond length on reduction and the absence of any structural transformation.

Sample	*a* (Å)	*c* (Å)	Volume (Å^3)
4H-$Ba_{0.5}Sr_{0.5}MnO_{2.02(1)}$	5.7179(6)	9.4179(9)	266.66(7)
4H-$Ba_{0.5}Sr_{0.5}MnO_{2.79(1)}$	5.58539(8)	9.2123(1)	248.89(1)
4H-$Ba_{0.5}Sr_{0.5}MnO_{2.99(1)}$	5.5528(1)	9.1471(2)	244.25(1)

Table 8.3 Lattice parameters of 4H-$Ba_{0.5}Sr_{0.5}MnO_{3-x}$ phases obtained on refinement against neutron diffraction data collected at 298K.

The oxide vacancies are predominantly, but not exclusively, located in the hexagonal layers. Approximately ½ of the hexagonal oxide sites are vacant, and approximately $^1/_6$ of the cubic oxide sites. The displacement factors of the oxide ions (shown in Figure 8.4) are extremely large. This static displacement can be attributed to the oxide ion distribution. A large number of oxide vacancies have been introduced to the structure in a relatively disordered manner. Along with the disorder associated with the oxide vacancy distribution, the oxide ions will move to accommodate variations in the local environment. If twisting of the metal-oxide polyhedra does not take place in an ordered manner, this is expected to introduce a large degree of uncertainty to the position of the oxide ions. Thus the displacement ellipsoids are large as they model a large static variation in the oxide position, not the small distribution expected due to thermal vibrations. This static distribution is not expected to change with temperature, which accounts for the lack of variation in the displacement factors on cooling. Similar displacement factors are observed for partially occupied oxide sites in other topotactically reduced phases such as $Sr_4Mn_{2.88}O_{7.04}Cu_2S_2$ and $YSr_2Mn_2O_{7-x}$.[125, 126]

8.3.2.2. Magnetism

Neutron diffraction data reveal that 4H-$Ba_{0.5}Sr_{0.5}MnO_{2.02(1)}$ is antiferromagnetically ordered at ambient temperature. The susceptibility data collected from 4H-$Ba_{0.5}Sr_{0.5}MnO_{2.02(1)}$ are essentially featureless, which is consistent with antiferromagnetic coupling over the measured temperature range. The observed susceptibility behaviour is probably a result of a relatively small number of defect spins.

Ambient temperature antiferromagnetism is unusual. Table 8.4 compares the magnetic behaviour of 4H-$Ba_{0.5}Sr_{0.5}MnO_{2.02(1)}$ to that of 4H-$Ba_{0.5}Sr_{0.5}MnO_{2.99(1)}$ and 4H-$Ba_{0.5}Sr_{0.5}MnO_{2.79(1)}$ (discussed in Chapters 5 and 6).

Sample	Mn oxidation state	Magnetic behaviour	
		Ambient temperature	1.8K
4H-$Ba_{0.5}Sr_{0.5}MnO_{2.02(1)}$	~ II	Antiferromagnetic order	Antiferromagnetic order
4H-$Ba_{0.5}Sr_{0.5}MnO_{2.79(1)}$	III/IV	Antiferromagnetic coupling	Short-range antiferromagnetic order
4H-$Ba_{0.5}Sr_{0.5}MnO_{2.99(1)}$	IV	Antiferromagnetic coupling	Antiferromagnetic order

Table 8.4 Magnetic behaviour of 4H-$Ba_{0.5}Sr_{0.5}MnO_{3-x}$ phases.

Antiferromagnetic coupling of face-sharing manganese ions occurs in all three 4H-$Ba_{0.5}Sr_{0.5}MnO_{3-x}$ phases. This is believed to occur using a direct exchange mechanism between singly occupied t_{2g} orbitals (see Chapter 5). In order for full magnetic order to be achieved, coupling must also occur between apex-sharing manganese ions. This utilises a superexchange mechanism involving the e_g orbitals. As shown in Figure 8.6, the 180° superexchange interaction is always antiferromagnetic if the e_g orbitals are either both empty (e.g. Mn(IV)) or both singly occupied (e.g. Mn(II)). Thus both 4H-$Ba_{0.5}Sr_{0.5}MnO_{2.99(1)}$ and 4H-$Ba_{0.5}Sr_{0.5}MnO_{2.02(1)}$ order antiferromagnetically.

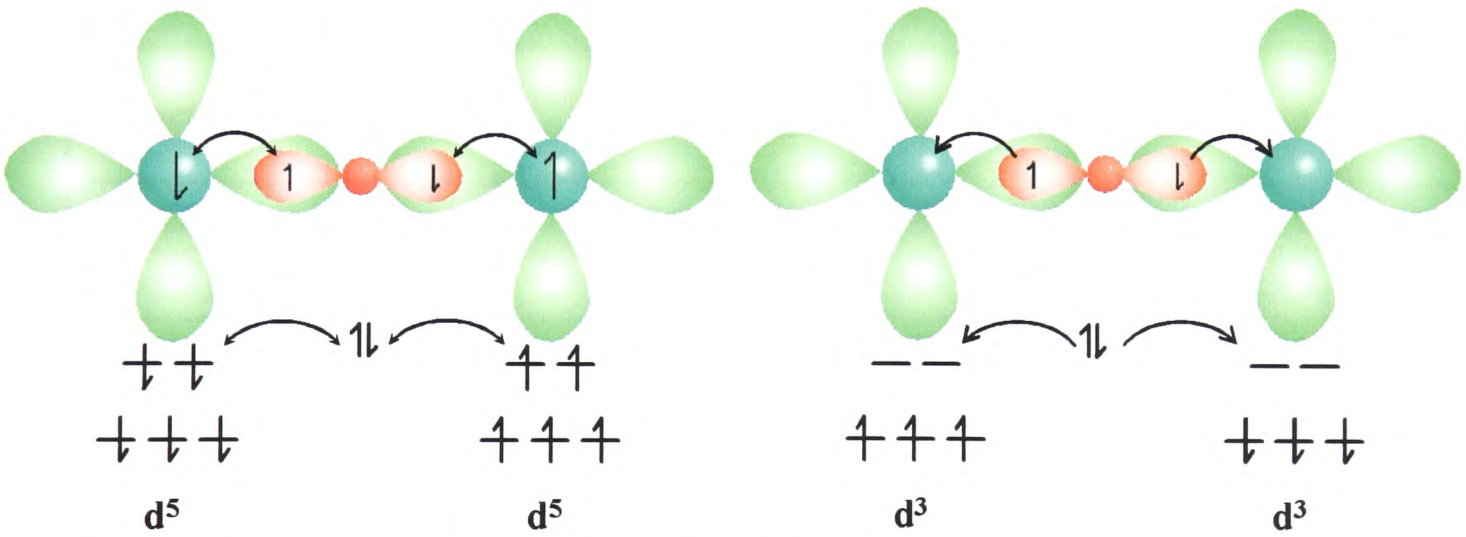


Figure 8.6 180° superexchange interaction for d^5 and d^3 systems.

A ferromagnetic interaction occurs between a singly occupied and an empty orbital. The effect of this in disrupting the magnetic ordering in 4H-$Ba_{0.5}Sr_{0.5}MnO_{2.79(1)}$ was discussed in Chapter 6. The magnetic behaviour 4H-$Ba_{0.5}Sr_{0.5}MnO_{2.02(1)}$ furthers the ideas discussed in Chapter 6 with regard to charge disorder. 4H-$Ba_{0.5}Sr_{0.5}MnO_{2.02(1)}$ shows a much higher degree of

structural disorder than 4H-$Ba_{0.5}Sr_{0.5}MnO_{2.79(1)}$, yet shows long-range magnetic order above ambient temperature. This confirms that the disruption of magnetic order in 4H-$Ba_{0.5}Sr_{0.5}MnO_{2.79(1)}$ is caused by charge disorder, rather than structural disorder.

The magnetic ordering temperature of the Mn(II) system (4H-$Ba_{0.5}Sr_{0.5}MnO_{2.02(1)}$, $295 \leq T_N$ (K) ≤ 373) is higher than that of the Mn(IV) system (4H-$Ba_{0.5}Sr_{0.5}MnO_{2.99(1)}$, $T_N \sim 270K$). The strength of the superexchange interaction is dependent on a number of factors including the covalency of the M-X bond, the *d*-electron configuration and the metal oxidation state. The interaction is expected to be stronger for the d^5 system due the increase in the number of unpaired electrons. Moreover, the 180° superexchange pathway utilises the e_g orbitals, and a stronger interaction is expected if these are singly occupied than if they are empty.

8.4. 4H-$BaMnO_{2+x}$

8.4.1. Results

8.4.1.1. Synthesis

Hydride reductions were also carried out on 4H-$BaMnO_{3-x}$. Details of the reaction conditions and products are shown in Table 8.5.

Starting material	Temperature (°C)	Hydride	Result
4H-$BaMnO_{3-x}$	≤ 250	LiH	Incomplete reaction
4H-$BaMnO_{3-x}$	275-350	LiH	Orthorhombic phase
4H-$BaMnO_{3-x}$	≥ 375	LiH	Decomposition
4H-$BaMnO_{3-x}$	150-170	NaH	Hexagonal phase
4H-$BaMnO_{3-x}$	200-225	NaH	Orthorhombic phase

Table 8.5 Reaction conditions and results on reducing 4H-$BaMnO_{3-x}$ with NaH and LiH.

4H-$BaMnO_{3-x}$ forms a continuum of hexagonal phases on reduction by NaH when $T \leq 170°C$. The lattice parameters increase steadily with temperature as the extent of reduction increases. As the temperature is increased to $170 < T$ (°C) < 200 a two phase mixture is produced, consisting of the most reduced hexagonal 4H-$BaMnO_{2+x}$ phase and a new orthorhombic

4H-$BaMnO_{2+x}$ phase. On increasing the temperature to T ~ 200°C, a single orthorhombic phase is formed. The orthorhombic 4H-$BaMnO_{2+x}$ phase decomposes on washing out the sodium containing by-products (with methanol), but a seemingly identical phase can be produced using LiH. Washing out the lithium containing by-products does not decompose the orthorhombic phase.

Two samples were prepared for structural characterisation: the orthorhombic 4H-$BaMnO_{2+x}$, and the most reduced of the hexagonal 4H-$BaMnO_{2+x}$ phases. Synthesis conditions of these samples are detailed in Table 8.6.

Sample	Structure	Hydride	T (°C)	Time
4H-$BaMnO_{2+x}$	Hexagonal	NaH	170	6 days
		Annealed	300	1 day
4H-$BaMnO_{2+x}$	Orthorhombic	LiH	290 300 340	1 day 1 day 1day
		Dried	150	2 hrs

Table 8.6 Synthesis conditions for hydride reduced phases prepared for structural characterisation.

Iodiometric titrations carried out on the hexagonal and orthorhombic $BaMnO_{2+x}$ phases yield compositions of hexagonal $BaMnO_{2.47(1)}$ and orthorhombic $BaMnO_{2.06(1)}$.

8.4.1.2. Structural analysis

8.4.1.2.1. X-ray powder diffraction

Close examination of X-ray powder diffraction data collected from $BaMnO_{2.47(1)}$ reveals that several of the reflections are split. These can be indexed on the basis of an orthorhombic unit cell. This is related to the original hexagonal cell by a distortion which removes the equivalence between the a and b lattice parameters. The relationship is made clear by considering an alternative description of the hexagonal unit cell as a C-centred orthohexagonal cell, a special case of an orthorhombic cell where $b' = \sqrt{3}a$. Distortion of the orthohexagonal cell produces a C-centred orthorhombic cell where $b' > \sqrt{3}a$ (or alternatively $b' < \sqrt{3}a$).

Projections of the *ab* plane of hexagonal, orthohexagonal and C-centred orthorhombic unit cells are shown in Figure 8.7.

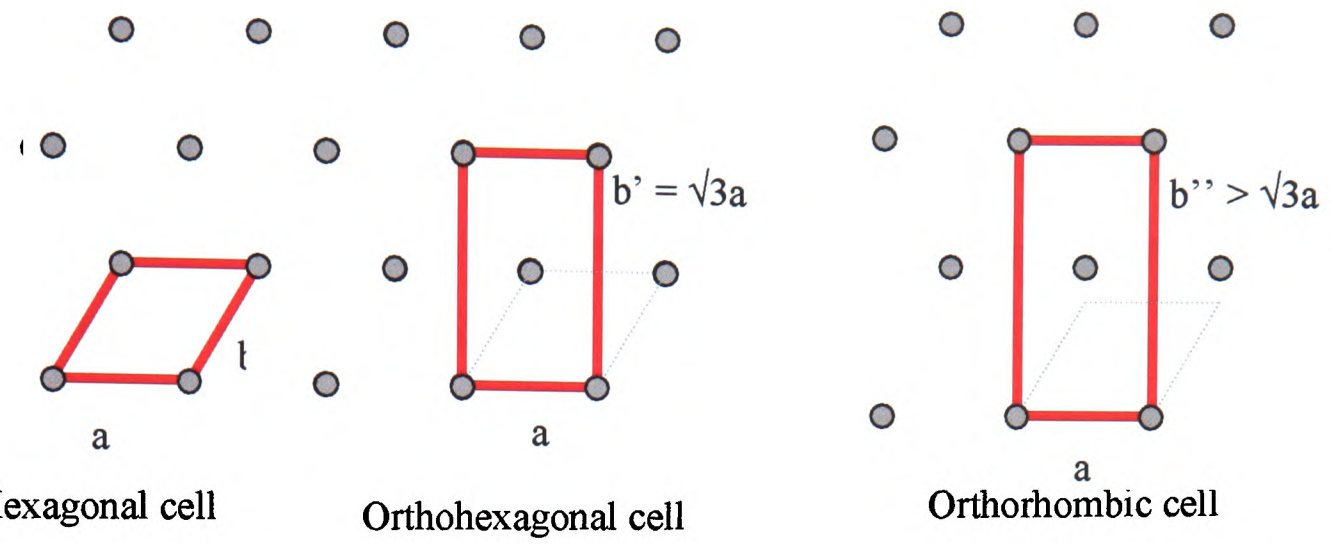


Figure 8.7 Lattice points in the *ab* plane of hexagonal, orthohexagonal and C-centred orthorhombic unit cells.

A suitable model was constructed in the space group $C222_1$, based on an orthorhombic distortion of the hexagonal 4H unit cell. The model is shown in Figure 8.8. Refinement of this model against the X-ray diffraction data collected from $BaMnO_{2.47(1)}$ produced a relatively good fit to the data, although several weak reflections were unaccounted for.

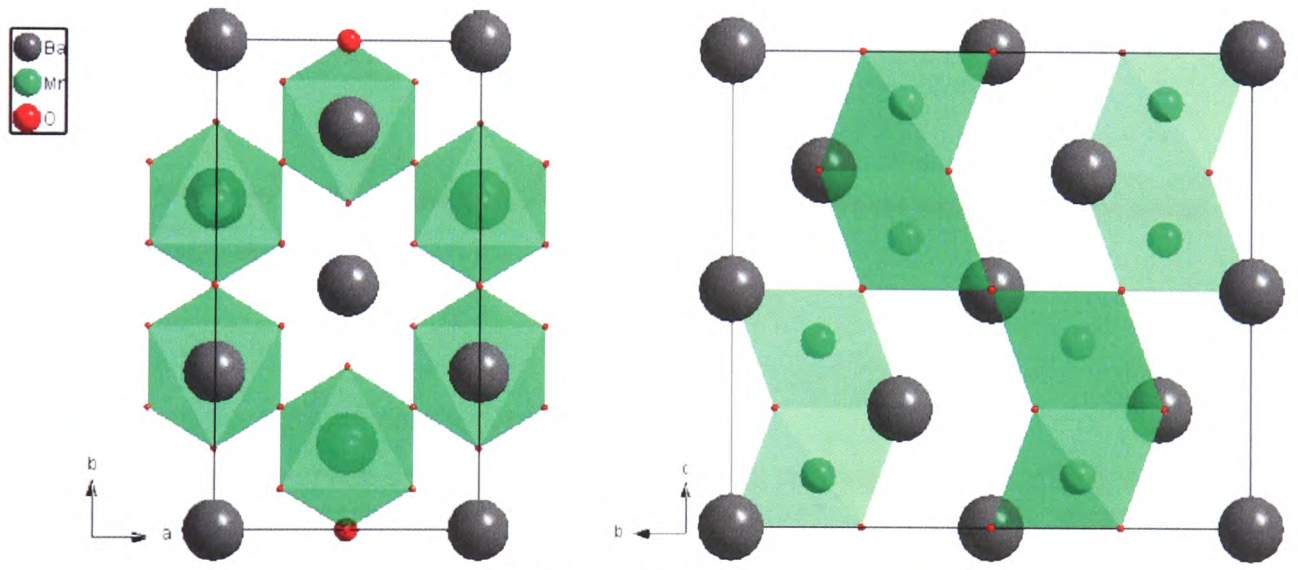


Figure 8.8 Orthorhombic model based on the 4H structure.

Refinement of the orthorhombic model against X-ray powder diffraction data collected from $BaMnO_{2.06(1)}$ also produced a good fit to the data. The extent of the orthorhombic distortion from the hexagonal cell is much greater for $BaMnO_{2.06(1)}$, and no additional reflections were observed.

8.4.1.2.2. Neutron diffraction data

8.4.1.2.2.1. $BaMnO_{2.47(1)}$

The intense reflections observed in neutron powder diffraction data collected from $BaMnO_{2.47(1)}$ can be indexed using the orthorhombic unit cell shown in Figure 8.8 with lattice parameters of $a = 5.6958(2)$ Å, $b = 9.9126(3)$ Å and $c = 9.4591(2)$ Å. However, as in the X-ray diffraction data, a number of weak reflections are unaccounted for. These could not be attributed to any of the known potential impurity phases. No cell expansion or distortion of the orthorhombic cell could be found which would account for the weak reflections. Calculated, observed and difference plots of the refinement using the orthorhombic model are shown in Figure 8.9.

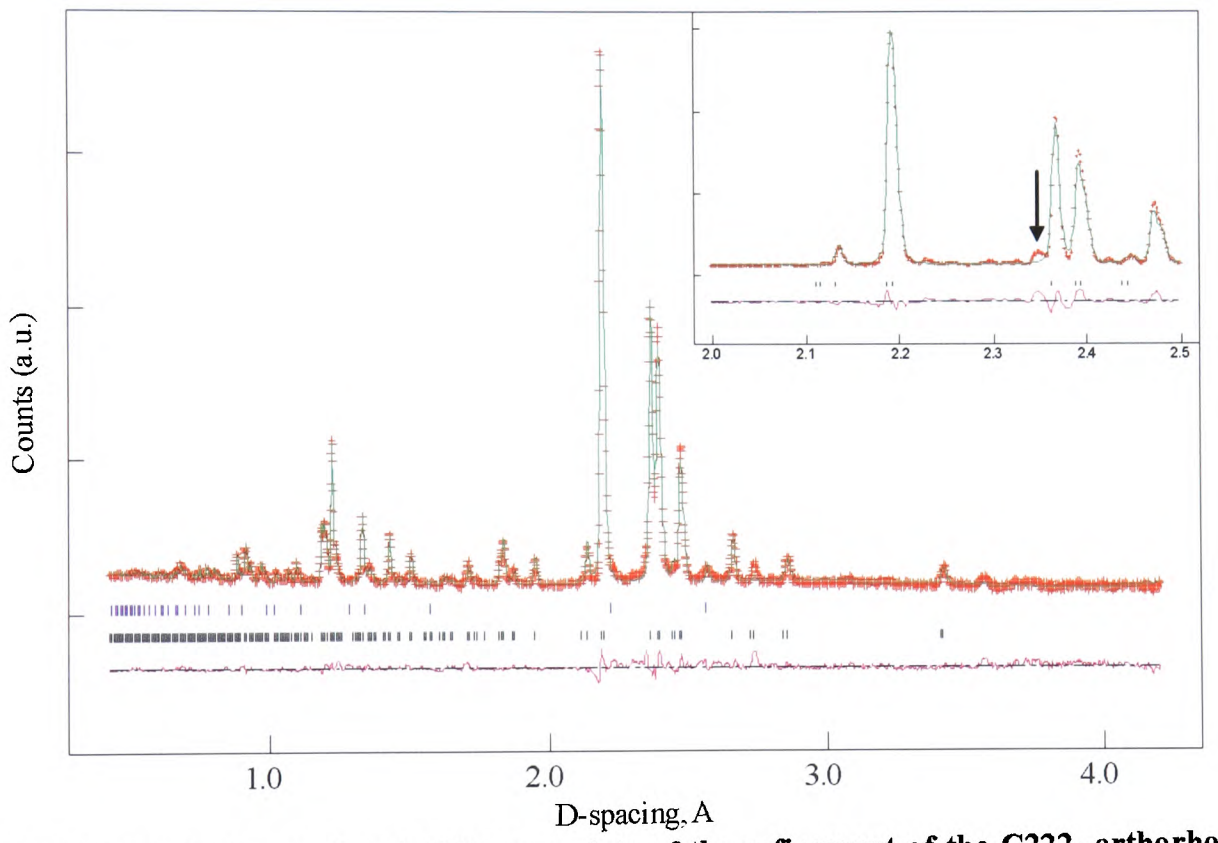


Figure 8.9 Calculated, observed and difference plots of the refinement of the $C222_1$ orthorhombic 4H model against neutron diffraction data collected from $BaMnO_{2.47(1)}$. The inset shows one of the weak reflections that is unindexed.

8.4.1.2.2.2. $BaMnO_{2.06(1)}$

The majority of the reflections observed in neutron diffraction data collected at 298K from $BaMnO_{2.06(1)}$ can also be indexed using the orthorhombic cell discussed above. Unlike the X-ray diffraction data, a number of reflections observed in the neutron diffraction data are not indexed by the orthorhombic cell. Some of these were found to correspond to those expected

for MnO, but others could not be indexed on the basis of possible impurity phases. Attempts to index the additional reflections using various cell expansions of the C-centred orthorhombic cell found that they were accounted for by a superstructure such that $a' = 2a$. Various models based on an orthorhombic cell related to the original 4H model by $a' = 2a$, $b' > \sqrt{3}a$, $c' = c$ were refined against the data. On refinement, additional intensity was observed at high *d*-spacings, similar to that observed in data collected from 4H-$Ba_{0.5}Sr_{0.5}MnO_{2.02(1)}$. The additional intensity was attributed to magnetic ordering within the sample. Neutron diffraction data were also collected at higher temperatures in order to decouple the magnetic and nuclear scattering. Data sets collected at 1.8K, 298K and 378K are shown in Figure 8.10.

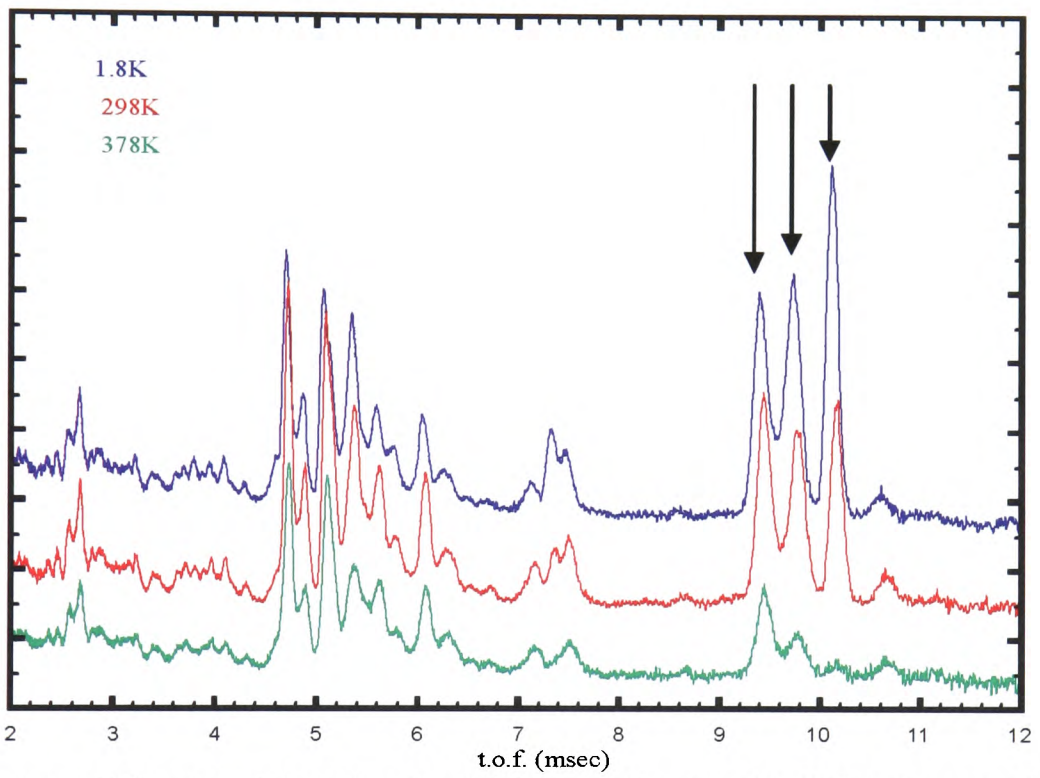


Figure 8.10 Neutron diffraction data sets collected from orthorhombic $BaMnO_{2.06(1)}$ at 1.8K, 298K and 378K, noting the intense reflections due to magnetic scattering.

Orthorhombic models related to the original hexagonal 4H cell by $a' = 2a$, $b' > \sqrt{3}a$, $c' = c$ unit cell were able to account for all of the reflections in the 378K data set. A modeless (Lebail) refinement in the space group $Pmn2_1$ produces a good fit with lattice parameters of a = 11.2799(7) Å, b = 10.3824(7) Å and c = 9.4674(4) Å. However, no model could be found which would produce an acceptable fit to the entire diffraction profile.

8.4.1.2.3. Electron diffraction

8.4.1.2.3.1. $BaMnO_{2.47(1)}$

A number of the electron diffraction patterns collected from $BaMnO_{2.47(1)}$ show additional superstructure reflections. A representative pattern is shown in Figure 8.11, indexed against an orthorhombic cell with a = 5.70 Å, b = 9.91 Å and c = 9.46 Å. The superstructure reflections observed in the first pattern require a three-fold expansion along both a and b in order to index the reflections.

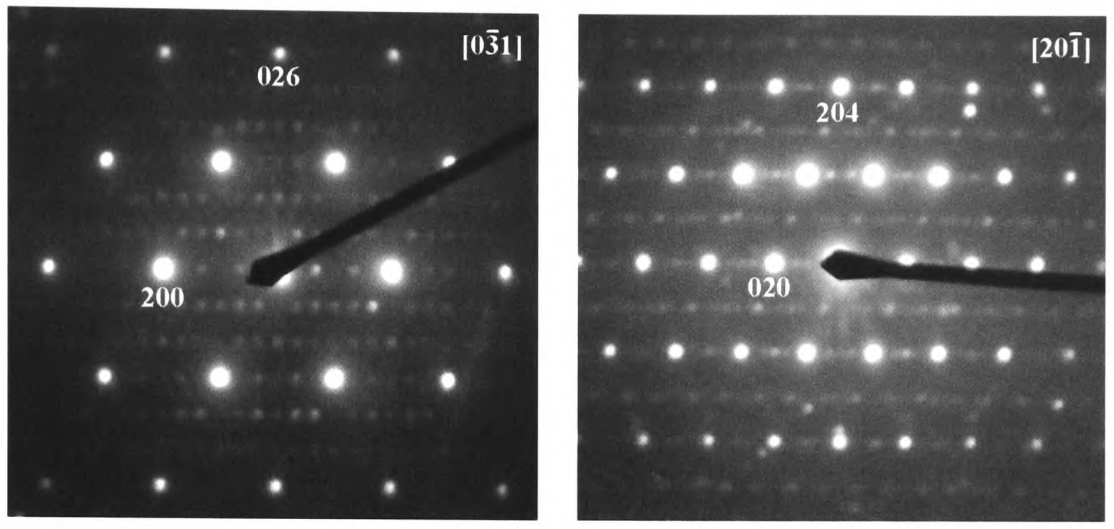


Figure 8.11 Electron diffraction data collected from $BaMnO_{2.47(1)}$, indexed against orthorhombic model. The first pattern shows additional superstructure reflections indicating a three-fold expansion along both *a* and *b*. The second requires a two-fold expansion along the *a* axis, and streaking is observed along the *b* axis.

Examination of the X-ray diffraction and neutron diffraction data provides no evidence to support a three-fold expansion of the unit cell along the a and b axis. In other electron diffraction patterns no additional reflections are observed or different expansions are required. The second pattern shown in Figure 8.11 shows superstructure reflections which can only be indexed by a two-fold expansion along the a axis, and streaking is observed along the b axis.

8.4.1.2.3.2. $BaMnO_{2.06(1)}$

Electron diffraction data were collected from $BaMnO_{2.06(1)}$ by Dr. Joke Hadermann. A selection of the data is shown in Figure 8.12, indexed against the simple orthorhombic unit cell where a = 5.64 Å, b = 10.38 Å and c = 9.47 Å.

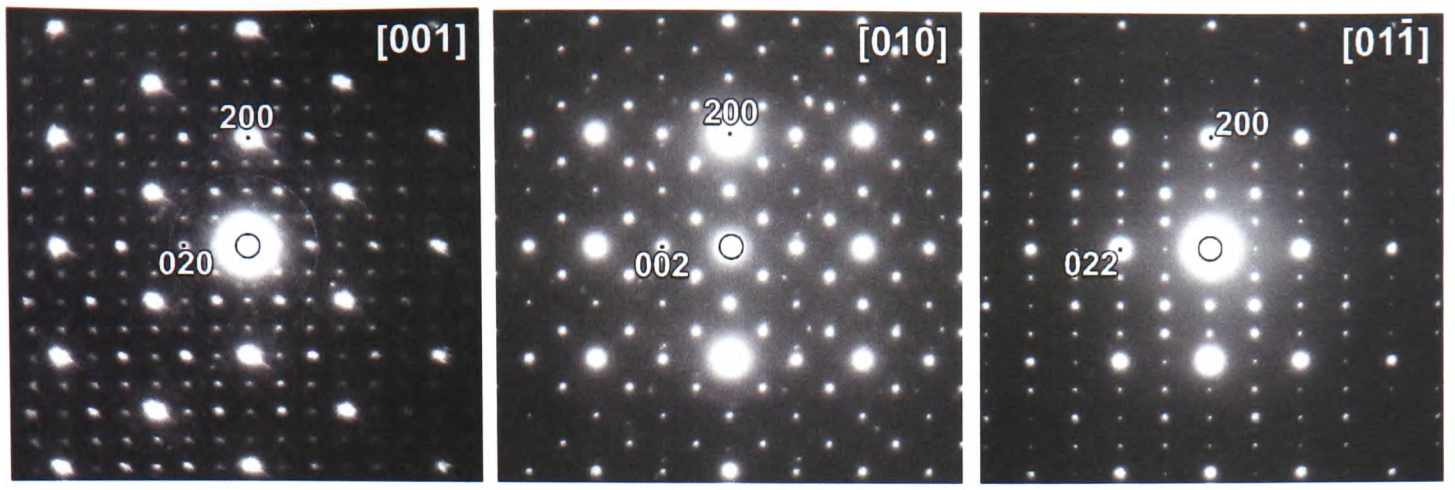


Figure 8.12 Electron diffraction data collected from orthorhombic 4H-$BaMnO_{2.06(1)}$ indexed against the orthorhombic cell related to that of the 4H structure by $a' = a$, $b' > \sqrt{3}a$, $c' = c$.

A number of superstructure reflections are apparent which confirm the 2*a* expansion of the unit cell observed in the neutron diffraction data. However, other patterns do not show evidence of this expansion. Individual crystallites were sometimes found to have domains with and without a clear superstructure.

8.4.1.3. Magnetometry

Field-cooled and zero-field-cooled magnetometry data collected from $BaMnO_{2.47(1)}$ and $BaMnO_{2.06(1)}$ are shown in Figure 8.13 and Figure 8.14.

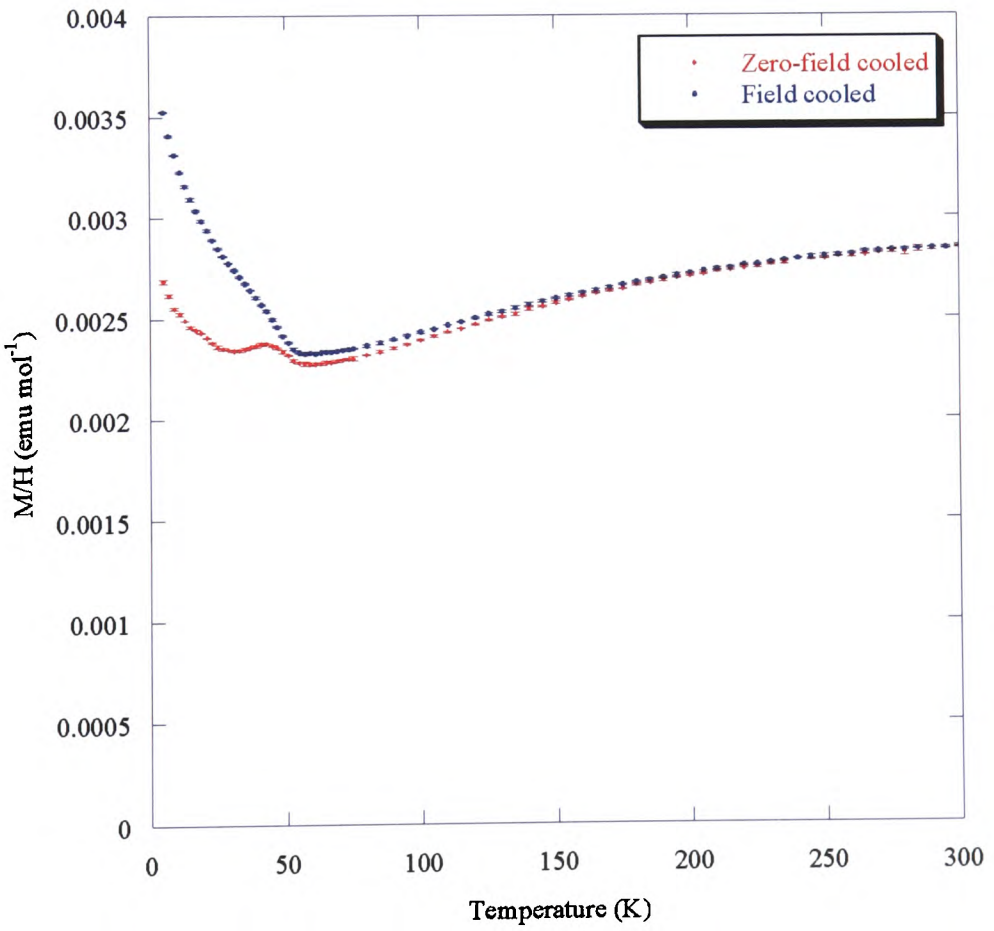


Figure 8.13 Zero-field-cooled and field-cooled magnetisation data collected from $BaMnO_{2.47(1)}$.

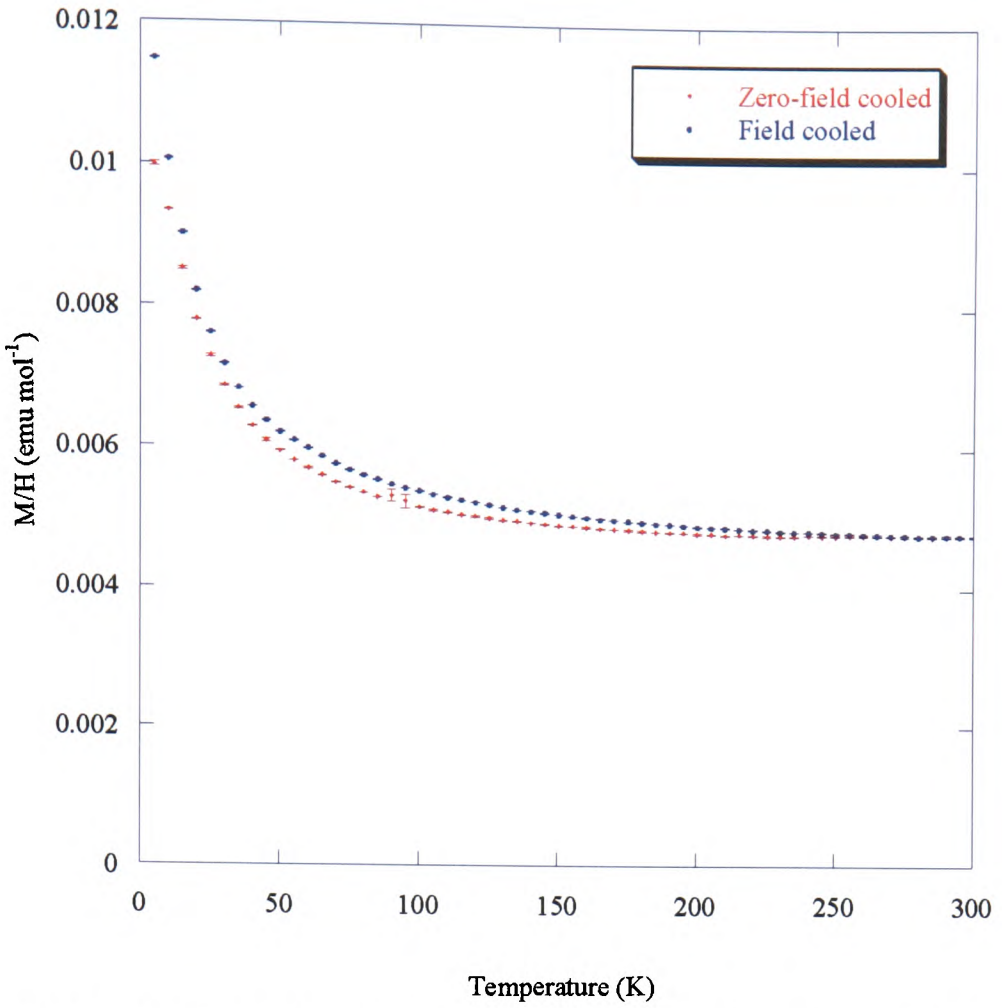


Figure 8.14 Zero-field-cooled and field-cooled magnetisation data collected from $BaMnO_{2.06(1)}$.

The susceptibility data collected from $BaMnO_{2.47(1)}$ are reminiscent of those collected from $BaMnO_{2.65(1)}$ (shown in Figure 5.15). The data collected from $BaMnO_{2.47(1)}$ show two events occur in close succession at T ~ 45K. The second of these is probably due to a small proportion of Mn_3O_4. The data collected from $BaMnO_{2.06(1)}$ are relatively featureless, and are similar to the data collected from 4H-$Ba_{0.5}Sr_{0.5}MnO_{2.02(1)}$.

8.4.2. Discussion

4H-$BaMnO_{3-x}$ is readily reduced using binary hydrides, and the diffraction data suggest that the cation substructure of $BaMnO_{2.47(1)}$ and $BaMnO_{2.06(1)}$ is largely unchanged. Although the structural model has not been determined for either phase, indexing the reflections confirms an expansion of the volume per manganese on reduction. The expansion is not linear with x as reduction is associated with a distortion which lowers the symmetry from hexagonal to orthorhombic. This behaviour provides a contrast to the retention of the hexagonal symmetry on reduction of 4H-$Ba_{0.5}Sr_{0.5}MnO_{3-x}$ to 4H-$Ba_{0.5}Sr_{0.5}MnO_{2.02(1)}$. The orthorhombic distortion is

presumably hindered in 4H-$Ba_{0.5}Sr_{0.5}MnO_{2.02(1)}$ by the disorder introduced by the mixture of A cations.

Sample	*a* (Å)	*b* (Å)	*c* (Å)	Volume (Å^3)	
				Unit cell	Per Mn
$BaMnO_{2.06(1)}$	11.2799(7)	10.3824(7)	9.4674(4)	1108.7(2)	69.29(1)
$BaMnO_{2.47(1)}$	5.6958(2)	9.9126(3)	9.4591(2)	534.06(3)	66.758(4)
4H-$BaMnO_{2.65(1)}$	5.6833(2)	/	9.3556(4)	261.70(3)	64.425(8)
4H-$BaMnO_{3.00(1)}$	5.6376(2)	/	9.2241(3)	253.89(2)	63.473(5)

Table 8.7 Lattice parameters of 4H-$BaMnO_{3-x}$, $0 \leq x \leq 1$ obtained on refinement against neutron diffraction data collected at 298K. Data for $BaMnO_{2.47(1)}$ was extracted from refinement of the simple orthorhombic model, data for $BaMnO_{2.06(1)}$ was extracted from a modelless refinement.

8.4.2.1. $BaMnO_{2.47(1)}$

The full structure of $BaMnO_{2.47(1)}$ could not be determined from the available data. The simple orthorhombic cell ($a' = a$, $b' \sim \sqrt{3}a$, $c' = c$) provides a good fit to the majority of the reflections. However X-ray, neutron and electron diffraction data all contain additional reflections that can not be indexed using the simple orthorhombic model. This suggests that a subtle modification of the orthorhombic cell occurs, probably associated with an ordered twisting of the MnO_{6-x} polyhedra.

Different electron diffraction patterns require different cell expansions to index the reflections, some patterns show streaking, and some show no cell expansion. None of the expansions required to index the electron diffraction data account for all of the additional reflections observed in the neutron diffraction data. This behaviour suggests that a number of different ordering regimes exist within the structure, the majority of which are likely to occur only over a short-range.

The magnetic behaviour of $BaMnO_{2.47(1)}$ appears to be very similar to that observed for 4H-$BaMnO_{2.65(1)}$ (discussed in Chapter 5). The susceptibility data can be rationalised using the

same model, in which moments are antiferromagnetically coupled over the measured temperature range. The only major difference is the presence of a second feature at T ~ 45K in susceptibility data collected from $BaMnO_{2.47(1)}$. This is consistent with the presence of a minority phase of Mn_3O_4 in the $BaMnO_{2.47(1)}$ sample, which supports the idea that the event observed in the 4H-$BaMnO_{2.65(1)}$ susceptibility data is a genuine feature of the sample, and not the result of a minority phase of Mn_3O_4.

8.4.2.2. $BaMnO_{2.06(1)}$

$BaMnO_{2.06(1)}$ also adopts an orthorhombic unit cell, similar to that of $BaMnO_{2.47(1)}$. Neutron and electron diffraction data reveal a two-fold expansion of the unit cell along the *a* axis. This is not observed by X-ray diffraction, suggesting the expansion is associated with a change in the anion lattice. This could either be a result of vacancy ordering, or ordered twisting of the MnO_{6-x} polyhedra. Electron diffraction reveals the presence of crystallites which do not show the additional features, suggesting that the $BaMnO_{2.06(1)}$ sample consists of two phases: one where the polyhedral twisting is ordered and one in which it is disordered. This accounts for the difficulty encountered in finding a model to fit the diffraction data.

The magnetic behaviour of orthorhombic $BaMnO_{2.06(1)}$ appears very similar to that of 4H-$Ba_{0.5}Sr_{0.5}MnO_{2.02(1)}$. Neutron diffraction data collected at 298K reveal intensity due to magnetic order. The susceptibility data have a low magnitude and weak temperature dependence, indicating that the ordering is antiferromagnetic in nature. As the magnetic moments are antiferromagnetically aligned over the temperature range from which susceptibility data were collected, the observed susceptibility of 4H-$BaMnO_{2.06(1)}$ is probably dominated by defect spins.

Without a nuclear model the magnetic model cannot be refined, but as the difference between data collected at 1.8K and that collected 378K represents the scattering intensity due to magnetic ordering, comparison of this to simulations of magnetic models can provide some

insight into the nature of the magnetic structure. The simulations and difference plot are shown in Figure 8.15. These suggests the magnetic moments are aligned along the *a* axis.

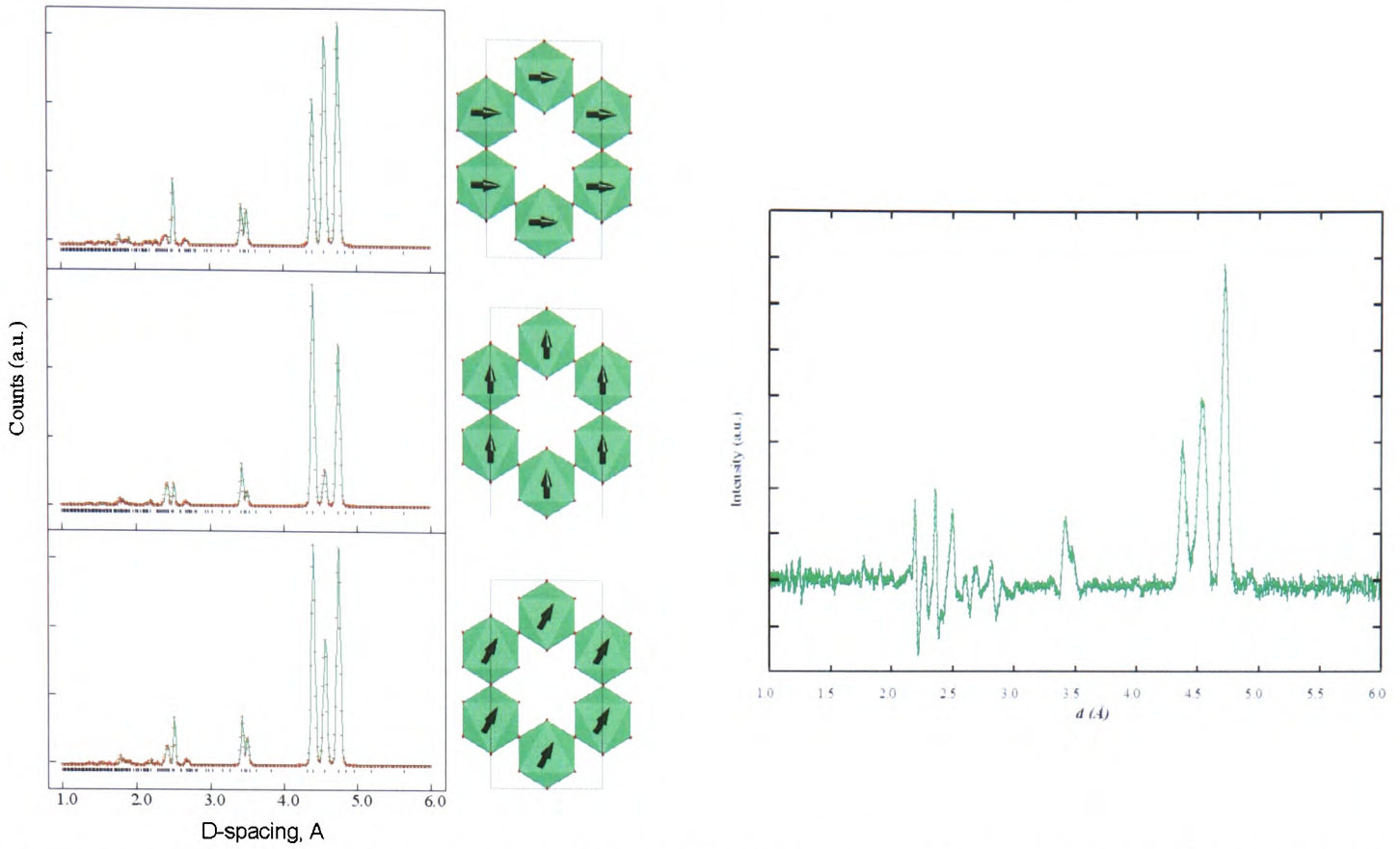


Figure 8.15 Simulations of magnetic models in which the magnetic moment is aligned along the orthorhombic *a*, *b* or *a* = *b* axis, and then antiferromagnetically coupled along the *c* axis. The difference plot of neutron diffraction data collected at 1.8K and data collected at 378K is also shown. This shows the closest similarity to the model in which magnetic moments are aligned along the *a* axis.

8.5. Conclusion

It has been shown that binary metal hydrides can effect topotactic reduction of 4H-$Ba_{0.5}Sr_{0.5}MnO_{3-x}$ to 4H-$Ba_{0.5}Sr_{0.5}MnO_{2.02(1)}$. The hexagonal unit cell is retained on reduction, and the oxide vacancies are predominantly, but not exclusively, located in the hexagonal (face-sharing) sites. On reduction from Mn(IV) to Mn(II) the magnetic interaction utilising the 180° superexchange pathway is strengthened, and antiferromagnetic order is achieved above ambient temperature in the range $298 \leq T\,(K) \leq 378$.

4H-$BaMnO_{2.65(1)}$ can also be reduced topotactically. A partial reduction can be carried out, producing $BaMnO_{2.47(1)}$. Full reduction produces $BaMnO_{2.06(1)}$. Unlike $4Ba_{0.5}Sr_{0.5}MnO_{2.02(1)}$, the hexagonal symmetry of both reduced $BaMnO_{2+x}$ unit cells is reduced to orthorhombic symmetry. The two orthorhombic $BaMnO_{2+x}$ phases undergo a further distortion or expansion, probably caused by an ordered twisting of the MnO_{6-x} octahedra. This distortion does not

appear to persist throughout the entire sample, and the complexity of the multi-phase system prevented the nature of the twisting from being determined.

The magnetic behaviour of the Mn(III) system, $BaMnO_{2.47(1)}$, is closely related to that of 4H-$BaMnO_{2.65(1)}$. The magnetic behaviour of the Mn(II) system, $BaMnO_{2.06(1)}$, is similar to that of 4H-$Ba_{0.5}Sr_{0.5}MnO_{2.02(1)}$. Antiferromagnetic ordering occurs above ambient temperature, in the range $300 < T\ (K) < 373$.

Bibliography

[1] H. D. Megaw, *Proceedings of the Physical Society, London* **58** (1946) 133.

[2] H. J. A. Koopmanns, G. M. H. van de Velde and P. J. Gellings, *Acta Crystallographica C* **39** (1983) 1323.

[3] K. R. Poeppelmeier, et al., *Journal of Solid State Chemistry* **45** (1982) 71.

[4] E. J. Cussen and P. D. Battle, *Chemistry of Materials* **12** (2000) 831.

[5] P. D. Battle, T. C. Gibb and C. W. Jones, *Journal of Solid State Chemistry* **74** (1988) 60.

[6] L. Katz and R. Ward, *Inorganic Chemistry* **3** (1963) 205.

[7] B. L. Chamberland, *Inorganic Chemistry* **8** (1968) 286.

[8] G. Meyer and U. Packruhn, *Zeitschrift fuer Anorganische und Allgemeine Chemie* **524** (1985) 90.

[9] A. Hauser, et al., *Journal of Solid State Chemistry* **56** (1985) 343.

[10] M. Harada, *Journal of the Physical Society of Japan* **52** (1983) 1646.

[11] N. Jouini, L. Guen and M. Tournoux, *Materials Research Bulletin* **17** (1982) 1421.

[12] H. W. Zandbergen, *Journal of Solid State Chemistry* **37** (1981) 308.

[13] G. L. McPherson, A. M. McPherson and J. L. Atwood, *Journal of Physics and Chemistry of Solids* **41** (1980) 495.

[14] H. J. Seifert and K. H. Kischka, *Thermochimica Acta* **27** (1978) 85.

[15] M. Niel, et al., *Materials Research Bulletin* **11** (1976) 827.

[16] H. J. Seifert and H. Fink, *Revue de Chimie Minerale* **12** (1975) 466.

[17] C. J. Kroese, W. J. A. Maaskant and G. C. Verschoor, *Acta Crystallographica B* **30** (1974) 1053.

[18] V. J. Minkiewi, D. E. Cox and G. Shirane, *Solid State Communications* **8** (1970) 1001.

[19] R. W. Asmussen, T. K. Larsen and H. Soling, *Acta Chemica Scandinavica* **23** (1969) 2055.

[20] A. Hardy, *Acta Crystallographica* **15** (1962) 179.

[21] B. E. Gushee, L. Katz and R. Ward, *Journal of the American Chemical Society* **79** (1957) 5601.

[22] J. J. Lander, *Acta Crystallographica* **4** (1951) 148.

[23] N. J. Poulsen, *Materials Research Bulletin* **32** (1997) 1673.

[24] J. Huster, *Zeitschrift fuer Naturforschung, Teil B. Anorganische Chemie, Organische Chemie* **35** (1980) 775.

[25] R. A. Gardner, M. Vlasse and A. Wold, *Inorganic Chemistry* **8** (1969) 2784.

[26] R. A. Gardner, M. Vlasse and A. Wold, *Acta Crystallographica B* **25** (1969) 781.

[27] D. Visser, G. C. Verschoor and D. J. W. Ijdo, *Acta Crystallographica B* **36** (1980) 28.

[28] J. J. Randall and L. Katz, *Acta Crystallographica* **12** (1959) 519.

[29] H. Nozaki, et al., *Physical Review B* **76** (2007) 014402.

[30] T. Negas and R. S. Roth, *Journal of Solid State Chemistry* **3** (1971) 323.

[31] Y. Syono and S.-i. Akimoto, *Journal of the Physical Society of Japan* **26** (1969) 993.

[32] P. Donahue, L. Katz and R. Ward, *Inorganic Chemistry* **4** (1965) 306.

[33] P. C. Donahue, L. Katz and R. Ward, *Inorganic Chemistry* **4** (1965) 306.

[34] T. Siegrist and B. L. Chamberland, *Journal of the less-common metals* **170** (1991) 93.

[35] N. A. Jordan and P. D. Battle, *Journal of Materials Chemistry* **13** (2003) 2220.

[36] P. C. Donahue, L. Katz and R. Ward, *Inorganic Chemistry* **5** (1966) 339.

[37] I. Gil de Muro, et al., *Journal of Solid State Chemistry* **178** (2005) 1712.

[38] J. F. Vente and P. D. Battle, *Journal of Solid State Chemistry* **152** (2000) 361.

[39] K. Yamaura, et al., *Journal of Solid State Chemistry* **158** (2001) 175.

[40] J. M. Longo and J. A. Kafalas, *Materials Research Bulletin* **3** (1968) 687.

[41] P. C. Donahue, L. Katz and R. Ward, *Inorganic Chemistry* **5** (1966) 335.

[42] T. Negas and R. S. Roth, *Journal of Solid State Chemistry* **1** (1970) 409.

[43] B. L. Chamberland, *Journal of Solid State Chemistry* **43** (1982) 309.

[44] B. L. Chamberland and J. B. Anderson, *Journal of Solid State Chemistry* **39** (1981) 114.

[45] J. T. Rijssenbeek, et al., *Physical Review B* **59** (1999) 4561.

[46] P. S. Haradem, B. L. Chamberland and L. Katz, *Journal of Solid State Chemistry* **34** (1980) 59.

[47] B. L. Chamberland and L. Katz, *Acta Crystallographica B* **38** (1982) 54.

[48] N. A. Jordan, et al., *Journal of Materials Chemistry* **13** (2003) 2617.

[49] E. J. Cussen, et al., *Inorganic Chemistry* **37** (1998) 6071.

[50] R. D. Burbank and H. T. j. Evans, *Acta Crystallographica* **1** (1948) 330.

[51] H. W. Zandbergen and D. J. W. Ijdo, *Acta Crystallographica C* **40** (1984) 919.

[52] J. T. Rijssenbeek, et al., *Physical Review B* **58** (1998) 10315.

[53] B. L. Chamberland, *Journal of Solid State Chemistry* **48** (1983) 318.

[54] O. Muller, W. B. White and R. Roy, *Journal of Inorganic and Nuclear Chemistry* **26** (1964) 2075.

[55] T. A. Vanderah, J. M. Loezos and R. S. Roth, *Journal of Solid State Chemistry* **121** (1996) 38.

[56] H. Mueller-Buschbaum and B. Mertens, *Zeitschrift fuer Naturforschung, Teil B. Anorganische Chemie, Organische Chemie* **51** (1996) 79.

[57] M. Shikano, et al., *Journal of Solid State Chemistry* **120** (1995) 238.

[58] K. E. Stitzer, et al., *Journal of Solid State Chemistry* **175** (2003) 39.

[59] T. Negas, et al., *Journal of Solid State Chemistry* **8** (1973) 1.

[60] J. H. Choy, S. T. Hong and K. S. Choi, *Journal of the Chemical Society. Faraday Transactions* **92** (1996) 1051.

[61] J. H. Choy, et al., *Japanese Journal of Applied Physics, Part 1* **32** (1993) 4628.

[62] P. D. Battle, et al., *Journal of Materials Chemistry* **6** (1996) 1187.

[63] R. V. Shpanchenko, et al., *Journal of Solid State Chemistry* **118** (1995) 180.

[64] X. J. Kuang, et al., *Chemistry of Materials* **14** (2002) 4359.

[65] E. Quarez, F. Abraham and O. Mentre, *Journal of Solid State Chemistry* **176** (2003) 137.

[66] A. Daoud-Aladine, et al., *Physical Review B* **75** (2007) 104417.

[67] R. Søndenå, P. Ravindran and S. Stølen, *Physical Review B* **74** (2006) 144102.

[68] S.-T. Hong and A. W. Sleight, *Journal of Solid State Chemistry* **128** (1997) 251.

[69] V. Caignaert, et al., *Journal of Solid State Chemistry* **73** (1988) 107.

[70] N. Tancret, P. Roussel and F. Abraham, *Journal of Solid State Chemistry* **178** (2005) 3066.

[71] D. C. Sinclair, et al., *Chemistry of Materials* **16** (2004) 2007.

[72] N. Creon, et al., *Solid state Sciences* **5** (2003) 243.

[73] A. F. Fuentes, K. Boulahya and U. Amador, *Journal of Solid State Chemistry* **177** (2004) 714.

[74] C. H. de Vreugd, H. W. Zandbergen and D. J. W. Ijdo, *Acta Crystallographica C* **40** (1984) 1987.

[75] V. A. Cherepanov, et al., *Journal of Solid State Chemistry* **153** (2000) 205.

[76] A. J. Jacobson and J. L. Hutchinson, *Journal of Solid State Chemistry* **35** (1980) 334.

[77] G. Liu and J. E. Greedan, *Journal of Solid State Chemistry* **110** (1994) 274.

[78] N. Floros, et al., *Chemistry of Materials* **12** (2000) 3197.

[79] N. Floros, et al., *Journal of Solid State Chemistry* **168** (2002) 11.

[80] S. J. Dunstone, J. H. Clark and M. A. Hayward, *Chemical Communications* (2007) 1905.

[81] X. Kuang, et al., *Chemistry of Materials* **19** (2007) 2884.

[82] R. D. Shannon, *Acta Crystallographica A* **32** (1976) 751.

[83] L. Miranda, et al., *Chemistry of Materials* **19** (2007) 1503.

[84] T. C. Gibb, *Journal of Materials Chemistry* **2** (1992) 387.

[85] C. Hammond, *The Basics of Crystallography and Diffraction*, 2nd Edition, Oxford University Press (2001).

[86] Institut Laue-Langevin, *The ILL Yellow Book*, (2001).

[87] *Institut Laue-Langevin*, http://www.ill.fr/d2b/home/ (2007)

[88] R. M. Ibberson, W. I. F. David and K. S. Knight, *The High Resolution Powder Diffractometer (HRPD) - A User Guide*, (1992),

[89] R. I. Smith and S. Hull, *User Guide for the Polaris Powder Diffractometer at ISIS*, (1997),

[90] H. M. Rietveld, *Journal of Applied Crystallography* **2** (1969) 65.

[91] A. C. Larson and R. B. Von Dreele, *GSAS Manual*, (2000).

[92] P. Thompson, D. E. Cox and J. B. Hastings, *Journal of Applied Crystallography* **20** (1987) 79.

[93] R. A. Young, *The Rietveld Method*, Oxford University Press (1993).

[94] A. C. Larson and R. B. Von Dreele, *General Structure Analysis System*, Los Alamos National Laboratory, (2000).

[95] N. E. Brese and M. O'Keefe, *Acta Crystallographica B* **47** (1991) 192.

[96] I. D. Brown, *Acta Crystallographica B* **48** (1992) 553.

[97] I. D. Brown and D. Altermatt, *Acta Crystallographica B* **41** (1985) 244.

[98] *SQUID Magnetometer* http://hyperphysics.phy-astr.gsu.edu/hbase/solids/squid.html (2007)

[99] J. B. Goodenough, *Magnetism and the Chemical Bond*, Interscience Publishers (1963).

[100] B. L. Chamberland, A. W. Sleight and J. F. Weiher, *Journal of Solid State Chemistry* **1** (1970) 506.

[101] K. Uematsu, et al., *Journal of the American Ceramic Society* **60** (1977) 466.

[102] A. D. Potoff, B. L. Chamberland and L. Katz, *Journal of Solid State Chemistry* **8** (1973) 234.

[103] S. Frenzen and H. Mueller-Buschbaum, *Zeitschrift fuer Naturforschung, Teil B. Anorganische Chemie, Organische Chemie* **50** (1995) 585.

[104] T. Negas, *Journal of Solid State Chemistry* **6** (1973) 136.

[105] J. M. Gonzalez-Calbet, et al., *Journal of Solid State Chemistry* **117** (1995) 21.

[106] J. M. Gonzalez-Calbet, et al., *Journal of Solid State Chemistry* **113** (1994) 78.

[107] J. M. Gonzalez-Calbet, et al., *Journal of Solid State Chemistry* **111** (1994) 202.

[108] J. M. Gonzalez-Calbet, et al., *Journal of Solid State Chemistry* **106** (1993) 99.

[109] A. J. Jacobson and A. J. W. Horrox, *Acta Crystallographica B* **32** (1976) 1003.

[110] H. Taguchi, et al., *Acta Crystallographica B* **33** (1977) 1298.

[111] Y. Takeda, et al., *Acta Crystallographica B* **32** (1976) 2464.

[112] M. O'Malley, M. Lockett and M. A. Hayward, *Journal of Solid State Chemistry* **180** (2007) 2851.

[113] M. A. Hayward, *Chemical Communications* (2004) 170.

[114] C. Felser, K. Yamaura and R. J. Cava, *Journal of Solid State Chemistry* **146** (1999) 411.

[115] J. Sugiyama, et al., *Physical Review B* **72** (2005) 064418.

[116] P. Ghinga, et al., *Physical Review B* **73** (2006) 184402.

[117] K. Dwight and N. Menyuk, *Physical Review* **119** (1960) 1470.

[118] H. Kadowaki, K. Hirakawa and K. Ubukoshi, *Journal of the Physical Society of Japan* **52** (1983) 1799.

[119] P. W. Anderson, *Physical Review* **86** (1952) 694.

[120] I. E. Grey, L. M. D. Cranswick and C. Li, *Journal of Applied Crystallography* **31** (1998) 692.

[121] A. Bard, R. Parsons and J. Jordan, *Standard potentials in aqueous solution*, IUPAC (Marcel Dekker), New York (1985).

[122] J. Adkin and M. Hayward, *Journal of Solid State Chemistry* **178** (2005) 3829.

[123] M. A. Hayward and M. J. Rosseinsky, *Chemistry of Materials* **12** (2000) 2182.

[124] M. A. Hayward, et al., *Journal of the American Chemical Society* **121** (1999) 8843.

[125] G. Hyett, et al., *Journal of the American Chemical Society* **129** (2007) 11192.

[126] M. A. Hayward, *Chemistry of Materials* (2006) 321.

Appendix A

The number of repeats of the stacking sequence (r) required to form a unit cell is always either 1, 2 or 3, and may be determined from the stacking sequence using the following logic:

There are three equivalent crystallographic sites in the *ab* plane of hexagonal perovskite structures in which the metal ions may be located. These are at (0, 0, z), (⅓, ⅔, z) and (⅔, ⅓, z). These positions are represented by the symbols α, β and γ in Figure A.1.

The A cations are arranged in layers (x) along the c axis; the B cations are located between the AO_3 layers (x').

Each layer x_i must contain one A cation, each layer x_i' must contain one B cation.

If a position α, β or γ contains an A cation in layer x_i, it cannot contain an A cation in layer x_{i+1} (A cations in the same *ab* position must be separated by two layers), nor can it contain a B cation in layer x_i' or x_{i-1}' (A cations must be separated by 1.5 layers from B cations in the same *ab* position).

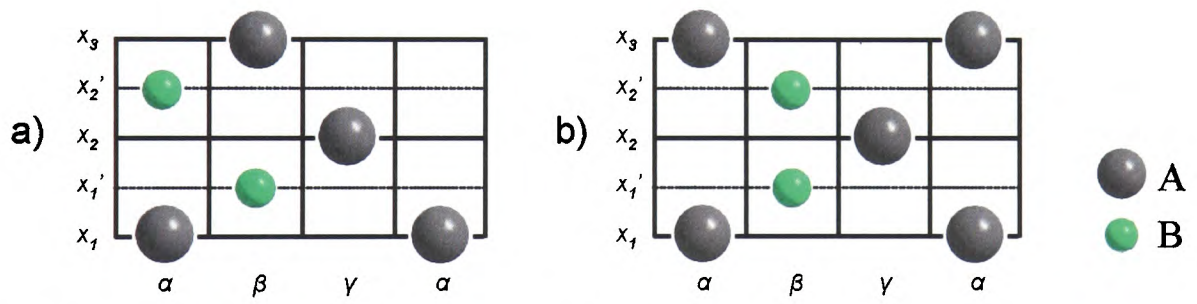


Figure A.1 A and B cation locations in a hexagonal perovskite cell.

These principles may be utilised to build a structure. In Figure A.1 (a and b), the A cation in layer x_1 has been arbitrarily located in the α position. The B cation in layer x_1' may not be located in the α position (rule 4), so must be located in β or γ. The choice between β or γ is arbitrary. Having located the x_1' B cation in the β position, the location of the x_2 A cation is predetermined by the 4th rule; it must be located in the γ position. At this point, a choice must be made. The next B cation in layer x_2' may be located in the α or β position. This is

determined by the stacking sequence. Placing the x_2' B cation directly above the x_1' B cation (in the β position) creates a hexagonal layer, and the BO_6 octahedra will be connected by a shared face. Placing the x_2' B cation in the α position creates a cubic layer, and the BO_6 octahedra will share an apex. The position of the x_3 A cation is predetermined, but a choice must again be made for the x_3' B cation position.

Obeying these structural rules only results in a choice when a new B cation is added to the sequence: either to insert a cubic layer and begin a new chain (Figure A.1a); or add another hexagonal layer and continue the face-sharing chain (Figure A.1b). Since a given stacking sequence determines the length of each face-sharing chain, the stacking sequence describes the entire structure. The number of repeat units, r, and therefore the number of layers in the unit cell N are predetermined from the stacking sequence.

In order to easily identify the number of repeat units in a unit cell, further rules were determined. If a face-sharing chain contains an even number of manganese ions (an even chain), the chains above and below must both be located in the same position (α, β or γ) in the xy plane (Figure A.2a). If the face-sharing chain contains an odd number of manganese ions (an odd chain), then the chains above and below must be located in different positions (α, β or γ) in the xy plane (Figure A.2b).

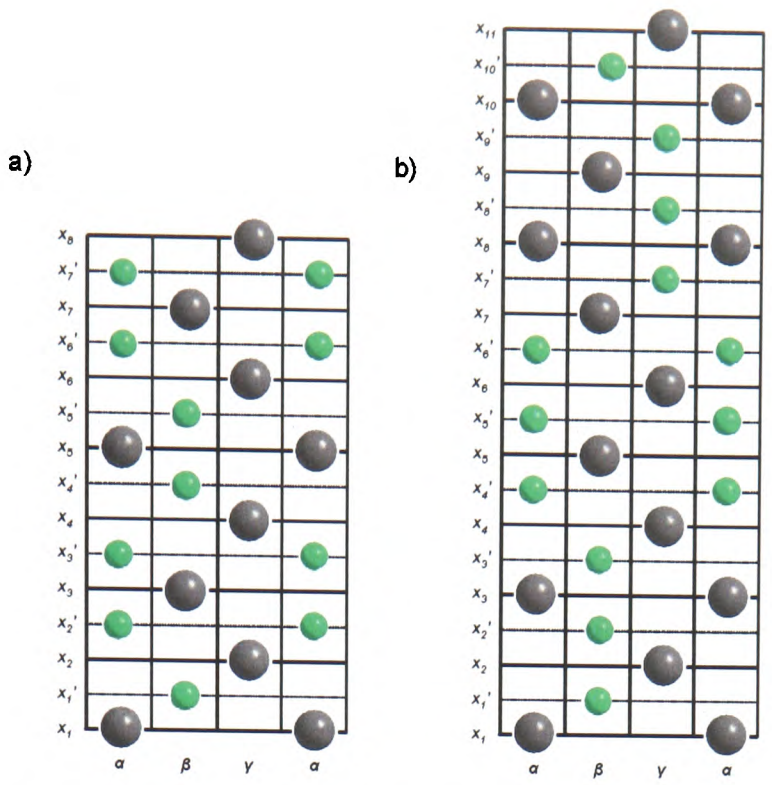


Figure A.2 Repeat units for even (a) and odd (b) manganese chains.

When the sequence is more complex, it becomes harder to identify the number of repeat units in the unit cell on a case by case basis. In order to do this more simply, the following logic was employed.

Firstly, six possible chain types were identified:

1. B cation chain in position α, next chain starts at β

2. B cation chain in position α, next chain starts at γ

3. B cation chain in position β, next chain starts at α

4. B cation chain in position β, next chain starts at γ

5. B cation chain in position γ, next chain starts at α

6. B cation chain in position γ, next chain starts at β

The structure was assumed to start with a chain type 1. The next chain is therefore 3 (if the first chain is even) or 4 (if the first chain is odd). The results for different chains are detailed in Table A.1.

Starting position	1	2	3	4	5	6
Next chain for even block	3	5	1	6	2	4
Next chain for odd block	4	6	2	5	1	3

Table A.1 Results of starting chains in positions 1 - 6 for odd or even blocks.

In order to generate *r*, the number of repeat units, the starting position of each chain in the sequence is identified. Then the sequence is repeated until the first chain in the sequence starts at position 1. The number of times it is necessary to repeat the sequence gives the value of *r*. For example, in a 2,2,1 stacking sequence, the first chain of 2 is type 1, by definition. As 2 is even, the second chain of 2 is type 3. Again this is an even chain, and so the chain of 1 is type 1. This is an odd chain, so on the second repeat of the stacking sequence, the first chain of 2 is now type 4. It is necessary to repeat the sequence three times before the first chain is type 1 again, and so in this case $r = 3$. A computer program was constructed by Dr. Daniel Goodman to automate the technique.

Appendix B

Atom	U11	U22	U33	U12	U13	U23
Ba1	0.0057(5)	0.0057(5)	0.0057(8)	0.0029(2)	0	0
Ba2	0.0024(3)	0.0024(3)	0.0193(7)	0.0012(1)		
Ba3	0.0047(3)	0.0047(3)	0.0049(6)	0.0023(1)		
Mn1	0.0047(6)	0.0047(6)	0.006(1)	0.0024(3)	0	0
Mn2	0.0016(3)	0.0016(3)	0.0015(6)	0.0008(2)		
Mn3	0.0023(2)	0.0023(2)	0.0050(5)	0.0011(1)	0	0
O1	0.0072(3)	0.0021(3)	0.0105(4)	0.0010(1)	0.0006(1)	0.0038(3)
O2	0.0055(2)	0.0055(2)	0.0062(2)	0.0042(2)	-0.00068(8)	0.00068(8)
O3	0.0068(2)	0.0068(2)	0.0055(3)	0.0036(2)	0.0006(1)	-0.0006(1)

Table B.1 Anisotropic displacement parameters ($Å^2$) refined against neutron powder diffraction data collected from 15R $BaMnO_{2.99(1)}$ at 298K.

Atom	U11	U22	U33	U12	U13	U23
Ba1	0.0047(3)	0.0047(3)	0.0108(6)	-0.0002(2)	0	0
Ba2	0.0025(3)	0.0025(3)	0.0198(7)	-0.0013(1)	0	0
Ba3	0.0051(1)	0.0051(1)	0.0064(3)	0.0025(8)	0	0
Mn1	0.0037(2)	0.0037(2)	0.0021(3)	0.00184(9)	0	0
Mn2	0.0032(2)	0.0032(2)	0.0061(3)	0.00157(9)	0	0
O1	0.0071(2)	0.0043(2)	0.0089(2)	0.00213(9)	-0.00102(7)	-0.0020(1)
O2	0.0078(2)	0.0051(2)	0.0047(2)	0.0026(1)	0	0
O3	0.0063(1)	0.0043(1)	0.0057(1)	0.00217(6)	0.00037(6)	0.0007(1)

Table B.2 Anisotropic displacement parameters ($Å^2$) refined against neutron powder diffraction data collected from 8H-$BaMnO_{2.95(1)}$ at 298K.

Atom	U11	U22	U33	U12	U13	U23
Ba/Sr1	0.0033(2)	0.0033(2)	0.0097(4)	0.0017(1)	0	0
Ba/Sr2	0.0051(1)	0.0051(1)	0.0092(3)	0.00254(7)	0	0
Mn1	0.0026(2)	0.0026(2)	0.0048(4)	0.0013(1)	0	0
Mn2	0.0044(1)	0.0044(1)	0.0010(3)	0.00220(8)	0	0
O1	0.0071(1)	0.0061(2)	0.0085(2)	0.00307(9)	0.00229(7)	0.0046(1)
O2	0.00708(9)	0.00708(9)	0.0049(1)	0.0047(1)	0.00012(4)	-0.00012(4)

Table B.3 Anisotropic displacement parameters ($Å^2$) refined against neutron powder diffraction data collected from 9R-$Ba_{0.875}Sr_{0.125}MnO_{3.00(1)}$ at 298K.

Atom	U11	U22	U33	U12	U13	U23
Ba1	0.00654(5)	0.00654(5)	0.0027(7)	0.0033(2)	0	0
Ba2	0.0022(5)	0.0022(5)	0.028(2)	0.0011(3)	0	0
Ba3	0.0060(4)	0.0060(4)	0.0077(6)	0.0030(2)	0	0
Ba4	0.0045(4)	0.0045(4)	0.0081(7)	0.0022(2)	0	0
Mn1	0.0013(4)	0.0013(4)	0.0044(6)	0.0006(2)	0	0
Mn2	0.0032(3)	0.0032(3)	0.0074(6)	0.0016(1)	0	0
Mn3	0.0047(4)	0.0047(4)	0.0021(6)	0.0024(2)	0	0
O1	0.0036(3)	0.0036(3)	0.0062(4)	0.0019(4)	0	0
O2	0.0063(3)	0.0063(3)	0.0036(4)	0.0030(4)	0	0
O3	0.0076(2)	0.0076(2)	0.0084(2)	0.0056(2)	-0.00103(7)	0.00103(7)
O4	0.0067(3)	0.0067(3)	0.0044(3)	0.0047(3)	0.00053(8)	-0.00053(8)

Table B.4 Anisotropic displacement parameters ($Å^2$) refined against neutron powder diffraction data collected from 6L-$BaMnO_{2.92(1)}$ at 298K.

Atom	U11	U22	U33	U12	U13	U23
Ba1	0.0056(3)	0.0056(3)	0.0044(4)	0.0028(1)	0	0
Ba2	0.0038(2)	0.0038(2)	0.0141(4)	0.00190(9)	0	0
Ba3	0.0047(2)	0.0047(2)	0.0063(3)	0.0024(1)	0	0
Mn1	0.0012(3)	0.0012(3)	0.0079(6)	0.0092(1)	0	0
Mn2	0.0030(2)	0.0030(2)	0.0034(4)	0.0015(1)	0	0
Mn3	0.0047(2)	0.0047(2)	0.0031(3)	0.0023(1)	0	0
O1	0.0063(2)	0.0059(2)	0.0045(2)	0.0029(1)	0	0
O2	0.00702(1)	0.0050(2)	0.0053(1)	0.00250(8)	0.00039(6)	0.00077(1)
O3	0.0080(1)	0.0056(1)	0.0069(1)	0.00281(7)	0.00154(5)	0.0031(1)

Table B.5 Anisotropic displacement parameters ($Å^2$) refined against neutron powder diffraction data collected from 10H-$BaMnO_{2.91(1)}$ at 298K.

Atom	U11	U22	U33	U12	U13	U23
Ba1	0.0107(4)	0.0107(4)	0.0507(9)	0.0054(2)	0	0
Ba2	0.0131(4)	0.0131(4)	0.0074(6)	0.0066(2)	0	0
Mn1	0.0086(3)	0.0086(3)	0.0082(5)	0.0043(2)	0	0
O1	0.0175(2)	0.0116(3)	0.0131(2)	0.0058(2)	0.0002(1)	0.0003(3)
O2	0.0210(4)	0.0125(4)	0.0091(4)	0.0063(2)	0	0

Table B.6 Anisotropic displacement parameters ($Å^2$) refined against neutron powder diffraction data collected from 4H-$BaMnO_{2.65(1)}$ at 298K.

Atom	U11	U22	U33	U12	U13	U23
Ba1	0.0085(5)	0.0085(5)	0.0167(7)	0.0042(3)	0	0
Ba2	0.0088(4)	0.0088(4)	0.0088(7)	0.0044(2)	0	0
Mn1	0.0057(4)	0.0057(4)	0.0130(5)	0.0029(2)	0	0
O1	0.0118(4)	0.0103(4)	0.0105(4)	0.0052(2)	-0.0007(1)	-0.0014(2)
O2	0.00114(4)	0.0098(4)	0.0105(4)	0.0049(2)	0	0

Table B.7 Anisotropic displacement parameters ($Å^2$) refined against neutron powder diffraction data collected from 4H-$BaMnO_{3.00(1)}$ at 298K.

Atom	U11	U22	U33	U12	U13	U23
Ba/Sr1	0.011(1)	0.011(1)	0.064(3)	0.0053(5)	0	0
Ba/Sr2	0.0173(9)	0.0173(9)	0.0085(1)	0.0087(5)	0	0
Mn1	0.0106(8)	0.0106(8)	0.007(1)	0.0053(4)	0	0
O1	0.0233(6)	0.0157(9)	0.0157(7)	0.0078(5)	-0.0030(3)	0.0060(7)
O2	0.0212(8)	0.0109(9)	0.0120(7)	0.0055(4)	0	0

Table B.8 Anisotropic displacement parameters ($Å^2$) refined against neutron powder diffraction data collected from 4H-$Ba_{0.5}Sr_{0.5}MnO_{2.79(1)}$ at 298K.

Atom	U11	U22	U33	U12	U13	U23
Ba/Sr1	0.0100(9)	0.0100(9)	0.014(1)	0.0050(5)	0	0
Ba/Sr2	0.0110(8)	0.0110(8)	0.006(1)	0.0055(4)	0	0
Mn1	0.0106(7)	0.0106(7)	0.002(1)	0.0053(3)	0	0
O1	0.0149(5)	0.0088(8)	0.0083(6)	0.0044(4)	-0.0016(3)	0.0032(6)
O2	0.0118(5)	0.0072(6)	0.0077(6)	0.0036(3)	0	0

Table B.9 Anisotropic displacement parameters ($Å^2$) refined against neutron powder diffraction data collected from 4H-$Ba_{0.5}Sr_{0.5}MnO_{2.99(1)}$ at 298K.

Appendix C

Atom	U11	U22	U33	U12	U13	U23
Ba1	0.0084(4)	0.0084(4)	0.0083(8)	0.0042(2)	0	0
Ba2	0.0056(4)	0.0056(4)	0.0177(6)	0.0028(1)	0	0
Mn/Zr1	0.0009(4)	0.0009(4)	0.0052(9)	0.0004(2)	0	0
Mn2	0.0071(2)	0.0071(2)	0.0050(4)	0.0035(1)	0	0
O1	0.0195(4)	0.0157(4)	0.0069(4)	0.0079(2)	0	0
O2	0.0172(2)	0.0112(2)	0.0131(2)	0.0056(1)	0.0022(1)	0.0044(2)

Table C.1 Anisotropic displacement parameters ($Å^2$) refined against neutron powder diffraction data collected from 6H-$BaMn_{0.8}Zr_{0.2}O_{2.81(1)}$ at 298K.

Atom	U11	U22	U33	U12	U13	U23
Ba1	0.0116(6)	0.0116(6)	0.007(1)	0.0058(3)	0	0
Ba2	0.0045(2)	0.0045(2)	0.0133(5)	0.0023(1)	0	0
Mn/Ti1	0.0050(6)	0.0050(6)	0.007(1)	0.0025(3)	0	0
Mn/Ti2	0.0074(3)	0.0074(3)	0.0062(5)	0.0037(1)	0	0
O1	0.0192(4)	0.0162(6)	0.0056(5)	0.0081(3)	0	0
O2	0.0105(2)	0.0097(2)	0.0094(2)	0.0048(1)	0.00108(9)	0.0022(2)

Table C.2 Anisotropic displacement parameters ($Å^2$) refined against neutron powder diffraction data collected from HV 6H-$BaMn_{0.5}Ti_{0.5}O_{2.79(1)}$ at 298K.

Atom	U11	U22	U33	U12	U13	U23
Ba1	0.0045(3)	0.0045(3)	0.0082(6)	0.0023(1)	0	0
Ba2	0.0043(1)	0.0043(1)	0.0082(3)	0.00215(7)	0	0
Mn/Ti1	0.0098(5)	0.0098(5)	0.0075(8)	0.0049(3)	0	0
Mn/Ti2	0.0049(2)	0.0049(2)	0.0074(3)	0.00207(9)	0	0
O1	0.0063(2)	0.0065(2)	0.0075(2)	0.0032(1)	0	0
O2	0.00716(9)	0.0069(1)	0.0066(1)	0.00342(7)	0.00094(5)	0.0019(1)

Table C.3 Anisotropic displacement parameters ($Å^2$) refined against neutron powder diffraction data collected from LV 6H-$BaMn_{0.5}Ti_{0.5}O_{2.96(1)}$ at 298K.

Atom	U11	U22	U33	U12	U13	U23
Ba1	0.0095(7)	0.0095(7)	0.084(2)	0.0048(4)	0	0
Ba2	0.0089(6)	0.0089(6)	0.0035(8)	0.0044(3)	0	0
Mn/Ti1	0.0058(5)	0.0058(5)	0.0033(6)	0.0029(2)	0	0
O1	0.0148(4)	0.0072(4)	0.0110(4)	0.0036(2)	-0.0010(2)	-0.0020(4)
O2	0.0195(5)	0.0127(6)	0.0068(5)	0.0064(3)	0	0

Table C.4 Anisotropic displacement parameters ($Å^2$) refined against neutron powder diffraction data collected from 4H-$BaMn_{0.66}Ti_{0.33}O_{2.96(1)}$ at 298K.

Appendix D

Atom	U11	U22	U33	U12	U13	U23
Ba/Sr1	0.023(1)	0.023(1)	0.172(5)	0.00117(5)	0	0
Ba/Sr2	0.058(1)	0.058(1)	0.0015(1)	0.00289(7)	0	0
Mn1	0.0151(7)	0.0151(7)	0.012(1)	0.00075(3)	0	0
O1	0.170(3)	0.034(1)	0.174(3)	0.00172(6)	-0.050(4)	0.075(6)
O2	0.144(3)	0.054(3)	0.009(1)	0.027(1)	0	0

Table D.1 Anisotropic displacement parameters ($Å^2$) refined against neutron powder diffraction data collected from 4H-$Ba_{0.5}Sr_{0.5}MnO_{2.02(1)}$ at 298K.